TECHNISCHE UNIVERSITÄT MÜNCHEN
Lehrstuhl für experimentelle Halbleiterphysik E25
Walter Schottky Institut

Spin effects in self-assembled semiconductor quantum dots

Florian Klotz

Vollständiger Abdruck der von der Fakultät für Physik der Technischen Universität München zur Erlangung des akademischen Grades eines

Doktors der Naturwissenschaften

genehmigten Dissertation.

Vorsitzender: Univ.-Prof. Dr. P. Vogl

Prüfer der Dissertation:

1. apl. Prof. Dr. M.S. Brandt
2. Univ.-Prof. J.J. Finley, Ph.D.

Die Dissertation wurde am 26.7.2012 bei der Technischen Universität München eingereicht und durch die Fakultät für Physik am 13.9.2012 angenommen.

The difference by xkcd.com

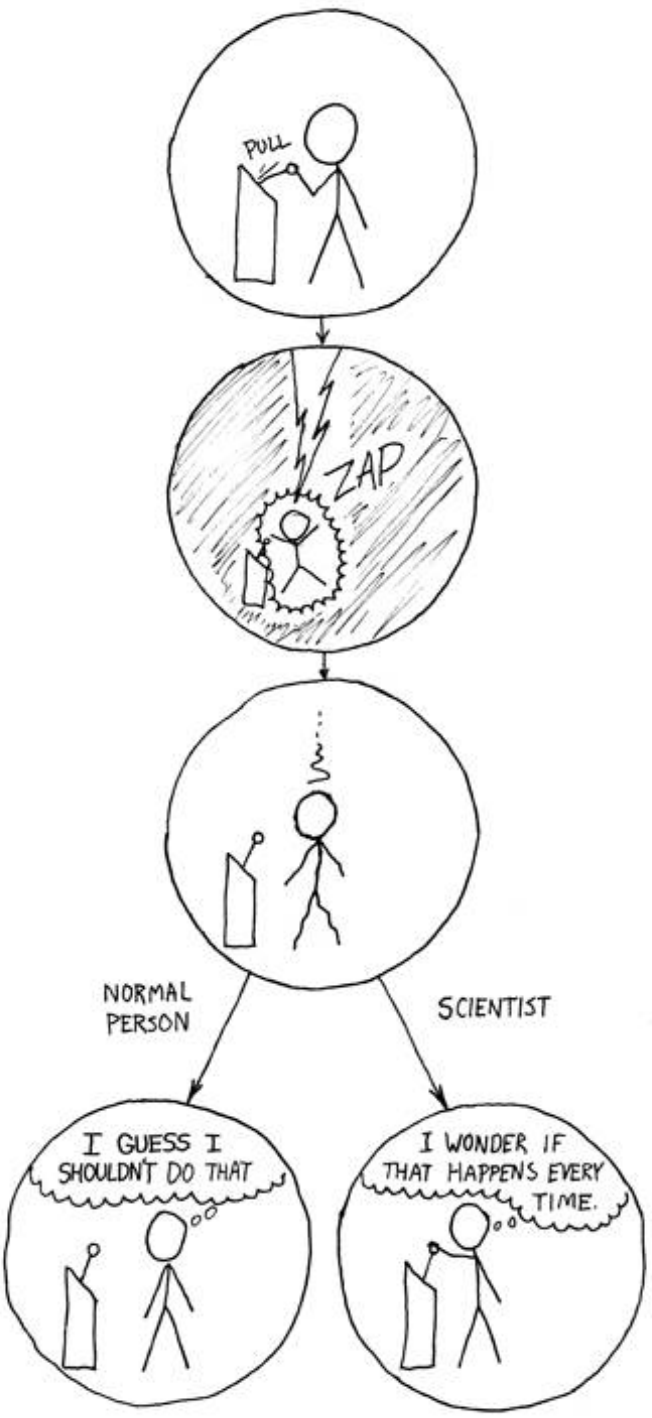

Abstract

The two level system formed by the spin of an electron confined in a quantum dot is considered a potential candidate for quantum information processing as first suggested by *Loss* and *DiVincenzo* in 1998 [Los98]. Ever since this proposal, the system has attracted considerable attention and was subject to numerous experimental and theoretical studies [Haw98; War00; Tar04; Kro04; Kop06; Now07; Kop08; Kro08b; Kla06; Oul07; Pre10; Urb12].

In this thesis, several aspects of self-assembled InGaAs quantum dots with regard to their use as fundamental building blocks in quantum computation, so called qubits, are addressed. The main aspects investigated include the tuning of the g-factor of charge carriers confined in a quantum dot, the experimental and theoretical examination of hyperfine-mediated optical pumping of the local nuclear spin ensemble and the development of integrated on-chip microwave delivery structures for electron spin control in single quantum dot experiments.

For the investigation of single quantum dots performed in the framework of this thesis, a sample consisting of a single layer of self-assembled InGaAs quantum dots embedded in the intrinsic region of an electric field-tunable n-i-Schottky photodiode was used. Single dot spectroscopy was performed at liquid helium temperature with magnetic fields up to 15 T applied in Faraday geometry. To examine the phenomena of interest, both photoluminescence as well as photocurrent measurements were carried out using resonant and non-resonant optical excitation schemes of the quantum dot nanostructures.

One of the topics addressed in this thesis is electric field control of the g-factor in these single quantum dots. The possibility to manipulate the g-factor of a confined charge carrier yields many applications and dynamical control can even provide a method for spin manipulation. Since high-frequency electric fields are nowadays routinely applied in single quantum dot experiments, an electrically tunable g-factor would open a promising path to realize such an approach. In contrast to previous works [Nak07; Rie08] where only a small change of the excitonic g-factor (< 15 %) as a function of the applied electric field was found, a large tunability up to 250 % from $g_{\mathrm{ex}} = 0.12$ to 0.42 is demonstrated in this thesis by varying the electric field from 54 kV/cm to 22 kV/cm [Klo10b]. The results were obtained by photoluminescence and photocurrent spectroscopy of single quantum dots and are presented in chapter 3 of this work.

Further detailed experimental and theoretical investigations carried out by *Jovanov et al.* and *Eisfelller et al.*, respectively, allowed to identify the mechanism leading to the observed strong tunability. The effect could be attributed to the hole whose g-factor is strongly modified by electric field-induced quenching of its angular momentum. The electron on the other hand is found to have only little impact on the total shift [Jov11; Jov12b; Jov12a; Eis12b]. The results of these studies are incorporated in sections 3.5 and 3.6.

The main scope of this thesis is on the hyperfine coupling of a confined electron to the nuclear spins of the constituent atoms of the quantum dot, an effect that is of crucial relevance for spin dynamics in such nanostructures and was identified as the major source of decoherence for an electron spin-based quantum dot qubit using III-V semiconductor materials [Bur99a; Erl01; Mer02; Coi04; Joh05; Han08; Blu11]. Consequently, a detailed understanding of the underlying mechanisms that might allow the development of reliable strategies to control the nuclear spin system via electro-optical methods and maybe even harness the mesoscopic spin ensemble as a potential resource [Tay03] is of paramount interest.

To date, the vast majority of experiments in this intensively studied field have been carried out on charged quantum dots containing an electron. However, these systems are subject to fast depolarization processes that are typically mediated by the trapped electron [Mal07]. Comparatively few studies have been performed on neutral dots for which lifetimes of optically pumped nuclear polarization up to hours are found [Mal09; Lat11; Klo12].

The measurements performed in the framework of this thesis reveal pumping of the nuclear spin bath in an uncharged self-assembled quantum dot via a hitherto unobserved mechanism. The results of the experimental and theoretical investigation of this pumping are presented and discussed in chapter 4.

By detecting the photocurrent arising from strictly resonant optical excitation of the Zeeman-split neutral exciton states, new information is obtained about the dynamic nuclear spin pumping in such systems. Hyperfine-mediated electron-nuclear flip-flop processes can occur that polarize the nuclear spin bath, creating an Overhauser magnetic field B_n. The size of B_n is measured via the energy shift δ_n of the exciton states caused by the additional Zeeman energy. In this type of experiments, highly efficient nuclear spin pumping with a maximum Overhauser shift of $\delta_\mathrm{n} = 135\ \mu$eV, corresponding to a large polarization of the nuclear spin bath up to 54 % [Ebl06] is observed. Remarkably, a pronounced *asymmetry* in the efficiency of optically pumped nuclear spin polarization is found for pumping the two Zeeman levels with the effect being much stronger following excitation of the higher energy state. This surprising behavior is found to persist over the whole parameter range for which nuclear spin pumping occurs. Furthermore, a strong dependence on the applied magnetic field B_ext is observed in which B_n was found to be always oriented in the same direction, regardless of the Zeeman state used to generate it.

To gain a deeper insight into the fundamental processes of the effect, a master equation

model based on the neutral exciton level structure of the system was developed that fully accounts for the observed behavior. The approach makes use of the strongly differing time scales between the fast excitonic and slow nuclear dynamics allowing to consider the exciton as experiencing a quasi-static Overhauser field of the nuclei. A steady state is quickly reached as determined by optical driving, tunneling out of the dot, and the hyperfine coupling. The mechanism is shown to arise from hyperfine-mediated spin flip transitions between the bright and dark states of the neutral exciton manifold where the striking features of *asymmetric* and *unidirectional* nuclear spin pumping as well as its magnetic field dependence emerge naturally in the numerical simulations performed on the basis of the model using typical parameters for self-assembled quantum dots.

Furthermore, time-resolved measurements were performed to quantitatively study the temporal evolution of the nuclear spin polarization under resonant optical cw-excitation of the dot. Recording of the time-dependent photocurrent signal enables to directly monitor the buildup of the Overhauser field in real-time via the Zeeman-shift introduced to the states by B_n. Since both the absolute number as well as the dwell time of the excitons in the quantum dot are known in photocurrent measurements, these experiments allow to deduce the net rate of electron-nuclear flip-flop processes and, thus, the strength of the hyperfine interaction in the system. Evaluation of the obtained data shows that even in the magnetic field region around $B_\mathrm{ext} = 5$ T where the highest nuclear spin polarization was achieved only one out of 10^6 electrons pumped through the dot undergoes a net flip-flop process with a nuclear spin.

In chapter 5, the work on the development and testing of on-chip coplanar stripline antennas for integration in single quantum dot photoluminescence measurements is reported. The antenna structures are designed to allow performing coherent control of individual confined electron spins. Furthermore, they are multi-functional in the sense that they serve not only as microwave delivery but also as electrical top gate and shadow mask for the single quantum dot spectroscopy.

The feasibility of electron spin manipulation using the in-plane component of the oscillating magnetic field created by a coplanar stripline antenna was demonstrated by performing electrically detected magnetic resonance on hydrogenated amorphous silicon. The use of the in-plane field component is due to the particular requirements of the quantum dot spectroscopy on the experimental geometry. Reference measurements on the same sample using a commercial electron spin resonance setup in combination with finite element calculations simulating the relative field distribution in the structure allows to determine the amplitude of the in-plane magnetic field component at the site where the quantum dots will be integrated into the device in future experiments. The obtained value of ≈ 0.12 mT for continuous wave excitation at a moderate microwave power of ≈ 120 mW corresponds to a π-pulse time of ≈ 0.5 μs for self-assembled InGaAs QDs with $|g_\mathrm{e}| = 0.6$. This is sufficiently short to allow coherent spin manipulation in single self-assembled quantum dots and meets the requirements set by the high sensitivity optical spin read-out scheme developed for this purpose [Hei10; Hei08a].

However, even shorter π-pulse times are possible by employing pulsed excitation schemes that allow for the application of significantly higher microwave powers.

Zusammenfassung

Wie von *Loss* und *DiVincenzo* 1998 vorgeschlagen, stellt das Zweiniveausystem, welches vom Spin eines Elektrons in einem Quantenpunkt gebildet wird, einen aussichtsreichen Kandidaten für Anwendungen in der Quanteninformationsverarbeitung dar [Los98]. Seit dem Erscheinen dieser Arbeit vor ca. 15 Jahren war das Thema Gegenstand zahlreicher experimenteller und theoretischer Untersuchungen [Haw98; War00; Tar04; Kro04; Kop06; Now07; Kop08; Kro08b; Kla06; Oul07; Pre10; Urb12].

Die vorliegende Arbeit befasst sich mit verschiedenen Aspekten selbstorganisierter Quantenpunkte hinsichtlich deren Verwendung als Grundbausteine für Quantencomputer, sogenannter Qubits. Die Themen umfassen die gezielte Beeinflussung des g-Faktors von Ladungsträgern in Quantenpunkten, experimentelle und theoretische Untersuchungen des optischen Pumpens des Kernspinsystems mittels hyperfeinwechselwirkungsbasierter Prozesse sowie die Entwicklung von on-chip Mikrowellenstrukturen zur Manipulation von Elektronenspins in Einzelquantenpunktexperimenten.

Für die Untersuchungen an Einzelquantenpunkten wurde eine Probe mit einer einzelnen, in die intrinsische Region einer n-i-Schottky Fotodiode eingebetteten, Lage selbstorganisierter InGaAs-Quantenpunkte verwendet. Die Spektroskopie einzelner Quantenpunkte wurde bei Flüssigheliumtemperatur und in Magnetfeldern bis 15 T durchgeführt.

Eines der Hauptthemen dieser Arbeit ist die Untersuchung der elektrischen Kontrolle des g-Faktors in einzelnen Quantenpunkten. Ein Verfahren den g-Faktor von Ladungsträgern in Quantenpunkten gezielt zu manipulieren, würde zahlreiche Anwendungsmöglichkeiten eröffnen, wobei eine dynamische Kontrolle sogar als eine Methode zur Spinmanipulation dienen kann. Da hochfrequente elektrische Felder mittlerweile standardmäßig in Quantenpunktexperimenten angewendet werden, könnte ein elektrisch kontrollierbarer g-Faktor eine solche dynamische elektrische Spinkontrolle ermöglichen.

Im Gegensatz zu früheren Untersuchungen, bei denen nur eine geringe Abhängigkeit des exzitonischen g-Faktors von elektrischen Feldern gefunden wurde, zeigen die in dieser Arbeit durchgeführten Messungen eine starke Änderung von bis zu 250 % von $g_{\mathrm{ex}} = 0.12$ auf 0.42 bei einer Variation des elektrischen Feldes von 54 kV/cm bis 22 kV/cm [Klo10b]. Die Ergebnisse wurden mittels Fotolumineszenz- und Fotostrommessungen erzielt und sind in Kapitel 3 dieser Arbeit diskutiert.

Durch weiterführende experimentelle und theoretische Untersuchungen, die von *Jovanov et al.* und *Eisfelller et al.* durchgeführt wurden, konnten die Mechanismen identifiziert werden, die der beobachteten starken elektrischen Feldabhängigkeit des g-Faktors zu Grunde liegen. Dabei konnte der Effekt eindeutig einer Variation des Loch-g-Faktors zugeordnet werden, die durch ein Quenchen des Drehimpulses hervorgerufen wird. Der Elektronen-g-Faktor trägt hingegen nur geringfügig zum Gesamteffekt bei [Jov11; Jov12b; Jov12a; Eis12b]. Die Ergebnisse dieser Untersuchungen sind in der vorliegenden Arbeit in den Abschnitten 3.5 und 3.6 zusammengefasst.

Hauptthema dieser Arbeit ist jedoch die hyperfeinwechselwirkungsbasierte Kopplung von Ladungsträgern in Quantenpunkten an die Kernspins der umgebenden Atome, eine Wechselwirkung, die entscheidenden Einfluss auf die Spindynamik in solchen Nanostrukturen hat und als Hauptursache von Dekohärenz spinbasierter Qubits in III-V-Halbleitern identifiziert wurde [Bur99a; Erl01; Mer02; Coi04; Joh05; Han08; Blu11]. Aus diesem Grund ist ein umfassendes Verständnis der zu Grunde liegenden Mechanismen von großem Interesse, da es Voraussetzung für die Entwicklung verlässlicher Methoden zur kontrollierten Beeinflussung des Kernspinsystems eines Quantenpunktes ist. Bisher wurde der Großteil aller Experimente zu diesem Thema an elektrisch geladenen Quantenpunkten vorgenommen, die mit einem oder mehreren Elektronen besetzt sind. In diesen Systemen finden jedoch meist schnelle Depolarisationsprozesse statt, die typischerweise durch das vorhandene Elektron verursacht werden [Mal07]. Im Vergleich dazu sind in ungeladenen Quantenpunkten sehr stabile Kernspinpolarisationen mit Lebensdauern im Bereich von Stunden beobachtet worden [Mal09; Lat11; Klo12].

In der vorliegenden Arbeit wird optisch-induzierte Kernspinpolarisation in resonant angeregten Quantenpunkten demonstriert, die auf einem bisher unbeobachteten Mechanismus beruht. Neben umfangreichen Experimenten wurde ein theoretisches Modell entwickelt. Die Ergebnisse sind in Kapitel 4 dargestellt.

Mittels resonanter Fotostromspektroskopie an den beiden durch die Zeemanaufspaltung getrennten Grundzuständen des neutralen Exzitons wurden neue Erkenntnisse hinsichtlich optisch erzeugter Kernspinpolarisation in selbstorganisierten Quantenpunkten gewonnen. Durch hyperfeinwechselwirkungsbasierte Elektron-Kernspin Flip-Flop-Prozesse kann ein Aufpolarisieren des Kernspinsystems und die Entstehung des damit verbundenen Overhauser-Feldes B_n erfolgen. Die Stärke dieses effektiven Magnetfeldes wird dabei durch die von ihm erzeugte zusätzliche Zeemanaufspaltung gemessen. In Experimenten solcher Art wurde im Rahmen dieser Arbeit ein maximaler Overhauser-Shift von $\delta_\mathrm{n} = 135\ \mu$eV beobachtet der einem Polarisationsgrad des Kernspinbades von 54 % entspricht [Ebl06]. Erstaunlicherweise wurde dabei eine ausgeprägte Asymmetrie hinsichtlich der Stärke des Effekts zwischen den beiden Grundzuständen des neutralen Exzitons beobachtet. Die Messungen zeigen, dass eine resonante Anregung des höherenergetischen Zeemanzweiges zu deutlich stärkeren Polarisationen des Kernspinensembles im Quantenpunkt führt als des niederenergetischen Zustands. Dieses überraschende Ergebnis wird über den gesamten Magnetfeldbereich beobachtet, in dem

Kernspinpolarisation stattfindet. Des Weiteren wurde eine starke Abhängigkeit des erzeugbaren Polarisationsgrades vom angelegten Magnetfeld festgestellt sowie, dass das erzeugte Kernspinfeld immer die gleiche Orientierung besitzt, unabhängig vom Zustand der zu seiner Erzeugung verwendet wird.

Um ein besseres Verständnis der fundamentalen Prozesse zu erlangen, die dem Effekt zu Grunde liegen, wurde ein Modell entwickelt, dass auf dem Energiespektrum des neutralen Exzitonenzustands beruht und die experimentellen Beobachtungen weitgehend zu erklären vermag. Der auf einer Mastergleichung basierende Ansatz nutzt dabei aus, dass die schnellen exzitonischen Prozesse und die langsame Kernspindynamik auf unterschiedlichen Zeitskalen stattfinden. Folglich kann für das Exziton ein quasi-statisches Overhauser-Feld der Kernspins angenommen werden, wobei sich nach kurzer Zeit durch optische Anregung, Tunnelprozesse und Hyperfeinkopplung ein Gleichgewichtszustand einstellt. Dabei zeigte sich, dass der Effekt auf hyperfeinwechselwirkungsbasierten Spin-Flip-Prozessen beruht, der Übergänge zwischen den optisch aktiven und inaktiven Zuständen des neutralen Exzitons induziert. Numerische Simulationen basierend auf dem Modell und typischen Parametern für selbstorganisierte Quantenpunkte reproduzieren dabei die charakteristischen Eigenschaften optisch erzeugter Kernspinpolarisierung, wie sie im Experiment beobachtet werden.

Des Weiteren wurden zeitaufgelöste Messungen durchgeführt, um die zeitliche Entwicklung der Kernspinpolarisation unter resonanter Dauerstrichanregung des Quantenpunktes quantitativ zu bestimmen. Durch die Messung des zeitabhängigen Overhauser-Shifts erlauben es diese Experimente, den Aufbau des Overhauser-Feldes in Echtzeit zu beobachten. Da bei Fotostrommessungen sowohl die absolute Anzahl der optisch erzeugten Ladungsträgern als auch deren Verweildauer im Quantenpunkt bekannt ist, ist es möglich, die Wahrscheinlichkeit zu bestimmen, mit der ein Flip-Flop-Prozess zwischen einem Elektronen- und einem Kernspin stattfindet, und somit Aussagen über die Stärke der Hyperfeinkopplung im System zu treffen. Eine quantitative Auswertung dieser Daten ergibt, dass selbst bei einem Magnetfeld von $B_{\text{ext}} = 5$ T, bei dem der Effekt optisch generierter Kernspinpolarisation am ausgeprägtesten ist, lediglich eines von 10^6 Elektronen, die durch den Quantenpunkt gepumpt werden, einen solchen Flip-Flop-Prozess mit einem Kernspin unterliegt.

In Kapitel 5 wird die Entwicklung von koplanaren on-chip Wellenleiterantennen vorgestellt, die im Rahmen dieser Arbeit durchgeführt wurde. Die Antennenstrukturen wurden konstruiert, um in Photolumineszenzexperimenten an Einzelquantenpunkten integriert zu werden, und dienen zusätzlich zu ihrer eigentlichen Funktion als Mikrowellenleiter außerdem als elektrische Kontakte und Schattenmaske für die optische Spektroskopie.

Die Leistungsfähigkeit der Strukturen wurde durch Testmessungen an amorphem Silizium demonstriert. Dabei wurden Messungen elektrisch detektierter magnetischer Resonanz durchgeführt, die mittels der horizontalen Komponente des oszillierenden Magnetfeldes der koplanaren Mikrowellenantenne angeregt wurde. Die Notwendigkeit

zur Verwendung der horizontalen Komponente des Magnetfeldes ergibt sich aus den speziellen Anforderungen der optischen Quantenpunktspektroskopie. Vergleichsmessungen an derselben Probe in einem kommerziellen Aufbau für Elektronenspinresonanz in Kombination mit Finite-Elemente-Simulationen zur Berechnung der relativen Feldverteilung erlauben die Bestimmung der Magnetfeldamplitude am Ort, an dem die Quantenpunkte in späteren Experimenten in der Probe integriert werden. Der ermittelte Wert von ≈ 0.12 mT bei Dauerstrichanregung bei einer moderater Mikrowellenleistung von ca. 120 mW entspricht einer π-Puls Zeit von etwa 0.5 μs für einen elektronischen g-Faktor von $|g_e| = 0.6$, typisch für selbstorganisierte InGaAs Quantenpunkte ist. Diese Zeitspanne ist lang genug, um kohärente Spinmanipulation in selbst organisierten Quantenpunkten durchzuführen, und erfüllt die Anforderungen der hochempfindlichen optischen Auslesetechnik, die für entsprechende Experimente entwickelt wurde [Hei10; Hei08a]. Durch die Verwendung gepulster Techniken sind jedoch noch wesentlich kürzere Spin-Flip Zeiten möglich, da in diesem Fall deutlich höhere Mikrowellenleistungen verwendet werden können.

Contents

Abstract i

Zusammenfassung v

1 Introduction and motivation 1

2 Properties of self-assembled quantum dots and experimental methods 11
2.1 Growth of self-assembled quantum dots 12
2.1.1 Stranski-Krastanow growth mode 12
2.1.2 Structural characterization 15
2.1.3 Partially capped overgrowth with *indium-flush* 17
2.2 Basic properties of self assembled quantum dots 20
2.2.1 Quantum dot model 20
2.2.2 Optical selection rules and fine structure 23
2.2.3 Quantum dots in magnetic and electric fields 25
2.2.4 Influence of the nuclear spin system 30
2.3 Experimental setup and characterization of single quantum dot devices 36
2.3.1 Single quantum dot device design 36
2.3.2 Experimental methods 41
2.4 Basic characterization of single quantum dots 44
2.4.1 Single Quantum Dots 44
2.5 Single quantum dot molecules 49
2.5.1 Basic properties of self-assembled quantum dot molecules 49
2.5.2 Basic charactertisation of single quantum dot molecules 53
2.6 Summary 55

3 Electrical tuning of the exciton g-factor 57
3.1 Experimental setup and method 59
3.2 Sample characterization 65
3.3 Tuning of the fine structure splitting 68
3.4 Observation of electrical g-factor tuning and non-linear Zeeman splitting 70
3.4.1 Electrical field dependent exciton g-factors 71
3.4.2 Non-linear Zeeman splittings 73
3.5 Explanation of non-linear Zeeman splitting 74

3.6 Explanation of electrical *g*-factor tuning . . . 78
3.7 Summary . . . 82

4 Dynamic nuclear polarization in neutral quantum dots 83
4.1 Steady-state photocurrent bias sweeps . . . 85
4.1.1 Magnetic field dependence . . . 90
4.1.2 Pumping power dependence . . . 93
4.1.3 Electric field dependence . . . 96
4.2 Model and numerical simulation . . . 98
4.2.1 Model . . . 98
4.2.2 Numerical simulations . . . 104
4.2.3 Comparison of simulation and experiment . . . 107
4.3 Dynamics . . . 112
4.3.1 Polarization dynamics . . . 112
4.3.2 Depolarization dynamics . . . 125
4.4 Towards DNP in a single quantum dot molecule . . . 130
4.5 Summary . . . 133

5 Development and testing of an on-chip coplanar stripline antenna structure 135
5.1 Design criteria for the CPS antenna . . . 137
5.2 Finite element simulation of the structure . . . 140
5.3 Setup and experimental results . . . 142
5.4 Applicability for spin control . . . 145
5.5 Experimental challenges using on-chip CPS antennas . . . 148
5.6 Summary . . . 151

6 Conclusive remarks and future work 153
6.1 Electron spin resonance . . . 153
6.1.1 Prospects . . . 153
6.1.2 Challenges . . . 154
6.2 Nuclear magnetic resonance . . . 156
6.2.1 Prospects . . . 156
6.2.2 Challenges . . . 157
6.3 Dynamic nuclear polarization . . . 159
6.3.1 DNP in single quantum dot molecules . . . 159
6.3.2 DNP in single quantum dots . . . 160

List of Constants and Abbreviation 163

Bibliography 167

List of Publications 193

Danksagung 195

1
Introduction and motivation

Quantum computing

Sparked by a proposal by Richard Feynman in 1982 [Fey82], the field of quantum information technology has evolved into a widely and extensively pursued area of research and development. Generally spoken, a quantum computer is a device that relies on quantum mechanical principles such as superposition or entanglement for data processing. In contrast to classical computers, the fundamental building blocks are not digital bits but operations are carried out on so-called qubits formed by the states of a quantum mechanical system [Nag06].

Since the emergence of the field three decades ago, many potential uses have been suggested, quantum algorithms have been developed and fundamental proof-of-principle experiments have been conducted demonstrating the feasibility of quantum computation. However, practical applications of quantum information processing are still missing. One of the key issues in this context is the exploration and identification of suitable physical systems fulfilling all necessary requirements [DiV00; Lad10] as well as holding the potential for practical use beyond fundamental research.

A very felicitous picture illustrating the possible future role of quantum information processing was employed by *Ladd et al.* by drawing an analogy to the laser, another, more familiar quantum technology [Lad10]: "Before the invention of the laser we had technological advances in making light: fire, the lantern, the lightbulb. Until the laser, however, this light was always 'incoherent', meaning that the many electromagnetic waves generated by the source were emitted at completely random times with respect to each other. Quantum mechanical effects, however, allow these waves to be generated in phase, and the light source engineered to exploit this concept was the laser. Lasers are routine devices today, but they do not replace light bulbs for most applications. Their

different kind of light - coherent light - is useful for thousands of applications from eye surgery to toys for cats, most of which were unimagined by the first laser physicists. Likewise, a quantum computer will not be a faster, bigger or smaller version of an ordinary computer. Rather, it will be a different kind of computer, engineered to control coherent quantum mechanical waves for different applications."

Until today, several algorithms based on quantum phenomena have been developed. The first quantum algorithm that was shown to solve a problem faster then any classical counterpart was proposed by *Deutsch* and *Josza* [Deu92; Cle98] in 1992, demonstrating for the first time the potential of quantum computation to outperform classical information processing for particular tasks. The most prominent examples for quantum algorithms are probably Shor´s algorithm for prime factorization [Sho94; Eke96; Sho97] and Grover´s algorithm to search unsorted databases [Gro96]. Both algorithms allow a substantial speedup in performance as they enable to compute their respective tasks in significantly less (an exponential reduction for the Shor and a quadratic one for the Grover algorithm) steps than any known classical algorithm [Sho94; Sho97; Gro96]. Over the last decade, several quantum algorithms have been implemented in groundbreaking experiments. Shor´s algorithm was used to factorize the number 15 into its prime factors three and five using a quantum computer consisting of 7 qubits formed by a perfluorobutadienyl iron complex molecule that could be manipulated using liquid state room-temperature nuclear magnetic resonance techniques [Van01]. Since this first demonstration, the algorithm has also been realized employing photon based qubits [Lu07; Lan07]. Other than by using the NMR approach [Chu98], the Deutsch-Josza algorithm was also successfully carried out on an ion-trap based system [Gul03].

Although very desirable, the probably most potent possible field of application for quantum computing is not the reduction of the number of calculation steps in information processing via quantum algorithms but the efficient simulation of quantum mechanical systems which was the motivation for Feynman´s original proposal. As pointed out by Feynman in his talk, the simulation of quantum mechanical systems with classical computers yields difficulties due to the large number of variables that have to be computed, a number that grows exponentially with the size of the system modeled [Fey82]. Together with the existence of effects specific to quantum mechanics that cannot be simulated accurately by classical means this represents a fundamental drawback for classical computing with limited resources for modeling of quantum systems. Feynman suggested that using a computation device based on the same principles of quantum mechanics as the system or phenomena to be examined should allow to perform this task very efficiently since the nature of the object of interest is a property of the simulation device itself. Due to the growing impact of nanotechnology on various technologies, the modeling and understanding of such systems is a matter of growing importance.

In order to perform quantum computation or simulation, the physical system used for implementation has to fulfill a set of criteria. A comprehensive survey and discussion of the requirements was performed by *DiVincenzo* in 2000 [DiV00]. Among others, the

system must be scalable and has to provide well defined qubits in which a desired state can be initialized, manipulated and read out. Furthermore, the decoherence time must be sufficiently longer than the time needed to perform logical operations. While the systems chosen for the first experiments mentioned above allowed to demonstrate the feasibility of of quantum information processing, the issue of scalability is a major challenge.

To date, a large number of physical systems such as trapped ions or atoms [Win98; And07; Bla08], liquid molecule nuclear spins [Van01; Neg06], superconducting circuits [Nak99; Mar02; Chi03], electron or hole spins confined in quantum dots [Los98; Kro04; Elz04; Han05; Han07; Kop08], photons [Kni01; O'B07; Pol09], NV-centers in diamond [Gru97; Niz04; Har06], or the nuclear spin of single donors in semiconductors [Kan98] have been proposed as qubits. Every of these approaches has different advantages and disadvantages for their use in quantum computing regarding particular aspects. An overview of the different systems and a direct comparison of their properties can be found e.g. in Ref. [Lad10]. The identification of the most suitable system(s) and development of corresponding techniques to perform information processing is a work in progress and the question which system(s) will prevail and eventually be established for quantum information processing is still open.

Quantum dots for quantum information processing

One of the promising candidates for physical realization of a qubit is the spin of an electron confined in a quantum dot (QD) as suggested by *Loss* and *DiVincenzo* [Los98]. Since this proposal in 1998, intensive effort has been made to investigate spin dynamics and develop methods for spin control in such nanostructures [Kop06; Now07; Kop08; Kro08b] as well as to optimize QD properties with regard to their use in quantum information processing [Kla06; Oul07].

The term 'quantum dot' was established by *Reed* [Ree86; Ree88] in the mid 1980s. It generally refers to nanostructures, commonly fabricated from semiconductor materials, that form a three-dimensional confinement for charge carriers [Ara82]. The spatial restriction to the nanometer scale leads to a discrete energy level spectrum [Zre94; Mar94; Nor96; Ban99]. The properties of the confinement potential can be tailored by choice of material, fabrication technique and design of the structure. This way, QDs that allow to trap either electrons, holes or excitons can be generated and basic characteristics such as the level spacing, ionization energy, inter particle interactions or the lifetime of confined charge carriers can be engineered. As a result of the zero-dimensional density of states [Efr82; Bru84; Zre94; Nor96; Ali96] QDs exhibit many atom-like properties [Mic00; Hoe04] which is why they are often referred to as 'artificial atoms' [Ash96].

Besides numerous other possible applications such as single photon sources [Mic00], LEDs [Col94; Kwa12], photodetectors [Kon06; Cli08] or photovoltaic media in solar cells [Gre03; Gur05], the spin of a charge carrier confined in a dot, as mentioned above,

forms a natural quantum mechanical two-level system with great potential to serve as a qubit. In contrast to semiconductor bulk material [Zut04; Cla76], the coupling of electrons to the solid-state environment in a QD is strongly suppressed due to the strong three-dimensional confinement [Ara82]. This results in a significant increase in spin lifetimes and decoherence times [Tar04; Kro04; Kop08] as desired for quantum computing. Furthermore, techniques for coherent spin control such as electron spin resonance (ESR) are well established and widely used in many areas of solid-state physics, chemistry, bio-chemistry, and materials science [Gor36; Zav45; Poo83; Wei07]. Although spin control and read-out on the single particle level is extremely challenging, great improvements were achieved in this field providing different approaches for full quantum-level control in QDs [Kop06; Kop08; Kro08b].

Two quantum dot systems have been studied intensively in this context over the last decade and important steps have been made in understanding the spin dynamics of charge carriers confined in such semiconductor nanostructures: (i) The first type are electrostatically defined QDs that are formed by metal gates on top of a two-dimensional electron gas (2DEG) [Cio00; Han07]. Application of a voltage allows to generate a depletion region underneath the gates and forms a confinement potential whose exact properties are determined by the geometry of the contacts, the distance from the 2DEG and the bias applied. An additional plunger gate allows to tune the tunnel coupling to the leads and control the charge state of the dot. Since these structures are not optically active, they are probed by electrical transport spectroscopy. The first experimental achievement of a gated QD reaching the single electron limit was reported in 2000 by *Ciorga et al.* using resonant current transport through the QD structure as a read-out [Cio00]. Later, a more reliable technique to determine the charge occupancy of the QD was developed using a quantum point contact placed next to the dot [Elz03]. The precise control of the properties of the system and the improved fabrication techniques allowed to perform very sophisticated experiments on gate-defined structures such as detection of the spin orientation of a single confined electron, a task for which even single shot read-out was achieved [Elz04; Han05], coupling of two and three QDs [Sch07; Han07] and coherent manipulation of single electron spins using electron spin resonance [Kop06] as well as high-frequency electric field modulation [Now07]. Latest works regarding the use of electrically defined quantum dots as spin qubits aim at materials engineering to increase the coherence time. This can be achieved e.g. by using isotopically purified ^{28}Si in order to obtain a nuclear spin free environment eliminating the major source of decoherence from the system [Wil12]. A comprehensive overview of spin physics in gate-defined QD structures can be found in Ref. [Han07]. (ii) The second type are self-assembled QDs that are also the subject of investigation in this thesis. They form in a strain-driven process during epitaxial growth of lattice-mismatched layers. In these structures, the confinement potential is generated by the different band gaps of the material within the QD material and the surrounding bulk matrix and modified by strain and the inhomogeneous chemical composition. An overview of the basic properties of these QDs is given in chapter 2. Although at present, the experimental

techniques on gated quantum dots are more advanced as compared to self-assembled structures, there are several advantages in the use of the latter as qubits. In contrast to gate defined structures, self-assembled QDs do not require temperatures in the milli-Kelvin regime [Kop06; Pot03; Kog04] but can be operated at much higher temperatures up to 70 K [Duc04]. The stronger quantization results in a stronger decoupling from the environment and, consequently, in longer spin lifetimes [Kha01]. Furthermore, they are optically active allowing to address the charge and spin states of the QD using optical techniques. Lastly, the confinement in self-assembled QDs allows to trap electrons and holes opening the possibility to explore the potential of hole spins qubits [Kro03; Dal06; Hei08b; Ger08; Bru09]. The use of holes can be advantageous as the hyperfine coupling to the nuclear spin environment is strongly suppressed due to the p-type wavefunction of heavy holes [Bur08] (cf. section 2.2.4). At the moment, hole-based devices are not available for gated QDs as the mobility of *p*-doped structures and the quality of the Schottky gates is not sufficient to allow reliable operation in the single hole regime [Kom08].

Due to the large potential of these structures for quantum information processing, self-assembled QDs were studied intensively over the last decade and many breakthroughs have been made in the development of methods for initialization [Ata06; Ger08; Hei08a], manipulation [Kro08b; Ber08; Pre10] and read out [Ata00; Hei08a; Hei10; Nic09; Vam10; Jov12c] of spins in single self-assembled QDs. In addition to that, great efforts have been made to optimize the conditions for quantum computing with QDs by engineering the parameters of the system such as controlling the interactions to the solid-state environment [Kla06; Oul07]. Recent work in this field focuses on the interaction of confined charge carriers with the local nuclear spin system, its impact on electron spin dynamics and the development of methods to overcome the related issues [Mer02; Kha02; Sch03; Bra05b; Gre07; Oul07; Mak08a; Vin09; Urb12]. This topic is also addressed in this thesis in experiments employing resonant photocurrent spectroscopy in combination with a theoretical model and numerical simulations. The results of these studies are presented in chapter 4. Another active area of research in the field of quantum dot qubits is the scaling of the QD approach to large systems by employing strongly coupled systems [Bay01; Ort03; Kre05b; Sti06; Sch08; Mue12a], a subject this thesis also studied by investigating nuclear spin effects in such structures (cf. section 4.4).

Tuning of the g-factor in quantum dots

If the charge carriers trapped in a QD carry a net spin, they couple to magnetic fields via the Zeeman effect. The strength of this interaction is characterized by the Landé g-factor which is in fact generally a tensor for electrons and holes confined in such nanostructures [Kat03; Ale06; Pry06; Wit11; Dea11]. Therefore, control of the g-factor of charge carriers confined in QDs offers a large range of possible applications and has recently attracted much attention [Nak04; Nak07; Bjo05; Tes08; Rie08; She07; She09; And09b; Pry06; Klo10b; Jov11; Jov12b].

The possibility to increase the exciton g-factor would generally be advantageous in experiments where a large Zeeman splitting of the spin states is desired in order to achieve suppression of unwanted off-resonant laser coupling as for example in measurements employing resonant QD excitation [Ata06]. The modification of the g-factor can also be used to tune the interaction strength of charge carriers confined within the QD with magnetic fields. In this respect, a reduction of the electron g-factor could be used to decrease the hyperfine coupling to nuclear spins in the QD which generate a fluctuating magnetic field representing the dominant source of decoherence in InGaAs quantum dots and limiting the time for coherent operations [Kha02; Kop08].

Besides tuning of the coupling strength to externally applied and intrinsic magnetic fields to the magnitude most favorable for a particular task, high frequency g-factor modulation could serve as an alternative technique for spin manipulation without employing an oscillating magnetic field [Sal01; Kat03; Dot06; Nak07; Pin08; And09b]. Such a technique could be enabled by an electrically tunable g-factor since high frequency oscillating electric fields can routinely be generated using mesoscopic metallic gates [Yua02; McF09; Nan10; Nan12]. Another advantage of this approach arises from the need to selectively manipulate a specific spin qubit within a quantum register in order to perform logical quantum operations. This task of selective addressing individual spins could be performed by applying time-dependent highly local ($\sim$ 100 nm) electric fields. The feasibility of this approach has been successfully demonstrated using parabolically composition-graded AlGaAs quantum wells [Sal01].

One possibility to statically control the g-factor is achieved by variation of the quantum dot parameters such as size or choice and composition of material. This technique has been studied in theory before [Sti99; Pry06; Nak04] but was only realized recently in experiments [Nak05; Kim09; Kle09; Rud09; Jov12a]. Although providing a useful tool to engineer magnetic properties of confined charge carriers, this method does not allow for in-situ adjustment of the g-factor during or between measurements or for dynamical manipulation.

Until now, only a weak dependence of the g-factor on applied electric fields was observed in single QDs. Employing in-plane fields a maximum change of the g-factor by 8 % was achieved [Nak07]. Using a method based on modifying the built-in vertical electric field, a change of 15 % was demonstrated [Rie08]. An appreciable electric control of the g-factor was previously only realized in quantum dot molecules, a system formed by two coupled QDs located at close proximity [Dot06]. In this case electric field-induced hybridization of the single particle wavefunctions across the two dots was the cause of the variation of the g-factor.

In this thesis, the effect of electric and magnetic field-tuning of the exciton g-factor is investigated in self-assembled InGaAs quantum dots. The results are presented and discussed in chapter 3. For the samples examined, a previously unobserved strong dependence of the exciton g-factor is found with tunabilities (defined as $|(g_{max} - g_{min}) / g_{min}|$)

up to 250 % [Klo10b]. The influence of the single particle contributions to and the underlying mechanism of this large g-factor tunability was studied using a theoretical model. The calculations revealed that the effect is caused by angular momentum quenching of the hole wavefunction with the changes of the electron state only contributing weakly [Jov11]. In combination with fast gate electrodes, this tunability can potentially be used for high-frequency g-factor modulation and could allow spin control with electric fields.

Dynamical nuclear polarization in quantum dots

Another essential aspect of the use of QDs as fundamental building blocks in quantum computation is the coupling between confined charge carriers and the solid-state environment. Via hyperfine interaction, the spin of a confined electron couples to the nuclear spins of the $10^4 - 10^5$ atoms forming the QD [Sch03; Coi09]. This coupling plays a major role for spin dynamics in QDs. It also opens the possibility to address the nuclear spin system, allowing to generate optically induced nuclear spin orientation, an effect called dynamical nuclear polarization. Studies of this phenomena in bulk material date back to the 1950s [Car53; Car56; Abr78; Mei84]. Lately, optically active quantum dots opened up new ways to gain insights into nuclear spin physics in semiconductor nanostructures resulting in many experimental and theoretical works [Coi09; Tay03; Kha02; Oul07; Xu09; Mal07; Ebl06; Bra05; Gam01; Tar07; Yok05; Mos09; Mal09; Mak08a; Mak08b; Che11d; Blu11].

The hyperfine coupling between an electron and the crystal lattice might offer a way to employ the local nuclear spin ensemble for quantum information applications. Due to the weak interaction strength between the nuclear spins and the possibility for optoelectronic control of the electron spin in the dot this system has the potential to be used as a long-lived memory for mesoscopic quantum bits [Tay03].

On the other hand, the fluctuating random nuclear spin system was identified as the main source of spin decoherence for electrons confined in QDs [Bur99a; Erl01; Kha02; Mer02; Coi04; Pet05; Kop05; Joh05; Han08; Blu11]. This appears to be a drawback for the use of quantum dots as physical systems for qubits since it limits the time for logic operations, particularly for the extensively researched optically active III-V semiconductors where all nuclei carry a non-zero angular momentum [Gra72]. In order to overcome this issue a deeper insight into the coupling between charge carriers confined in QDs and the resident nuclear spin bath is needed. A profound understanding of the relevant processes and dynamical mechanisms might allow to develop strategies to manipulate the nuclear spin bath and control the interactions. This motivation has lead to many experimental [Pet05; Kop05; Bru09] and theoretical [Bur99a; Erl01; Kha02; Mer02; Coi04; Fis08; Tes09] works in the field of dynamical nuclear polarization (DNP) on quantum dots.

It was shown in fundamental experiments that fluctuations of the nuclear spin polarization can be suppressed employing hyperfine-mediated transfer of angular momentum between an electron and a nuclear spin via electron-nuclear spin flip-flop processes [Gre07; Oul07; Rei08; Lat09; Vin09; Xu09]. Repeated application of this process allows

to prepare the nuclear spin system in a highly polarized, non-thermal equilibrium state [Bro96; Urb12]. This effect of DNP in combination with the appropriate magnetic fields applied was theoretically predicted and recently experimentally demonstrated to have a stabilizing influence on the electron spin polarization and extend the relaxation as well as the dephasing time [Mer98; Oul07; Cyw09a; Cyw09b; Xu09; Blu11]. DNP can even serve to lock the states of a QD to the energy of an excitation laser [Lat09] or to the resonance condition with a microwave field in an electron spin resonance experiment [Vin09]. Very recently, coherent control of the nuclear spin ensemble in self-assembled QDs was achieved using nuclear magnetic resonance techniques [Mak11] opening a path to a whole new class of DNP-based experiments.

This topic of dynamical nuclear polarization is the main focus of this thesis. The results are presented and discussed in chapter 4. Subject of investigation was the pumping of the nuclear spin system upon resonant optical excitation of the lowest orbital states of an uncharged QD in the photocurrent regime where optically generated charge carriers are rapidly extracted from the QD via tunneling escape due to the application of high electric fields. The resonant excitation in at high electric fields reveals a hitherto unobserved nuclear spin pumping mechanism exhibiting characteristic features and dependencies on experimental parameters such as the applied magnetic field or the excitation rate. Furthermore, a pronounced *asymmetry* was found for pumping the two neutral exciton Zeeman levels with dynamic nuclear polarization being much more efficient for excitation of the higher energy state than for the lower one. Due to this constellation, one level can be used to pump the nuclear spin ensemble and the other one to probe the polarization. This allows to measure effects like the free decay of nuclear spin polarization giving insight into the diffusion of nuclear polarization in strained nanostructures. It even enables fast switching between resonant QD excitation with and without pumping of the nuclear spin bath by shifting either of the two states in or out of resonance with a laser by employing the so-called quantum confined Stark effect [Mil84; Fry00b; Fin01a] which describes the variation of the QD transition energies as a function of an applied electric field. In order to obtain deeper insight into the underlying processes leading to the observed effects, a theoretical model was developed. Numerical calculations based on the model allow to simulate the actual experimental procedure and produce results that are in good agreement with the experimental data. The characteristic properties of the resonantly generated DNP such as the *asymmetry* upon pumping of the two neutral exciton states and the magnetic field dependence emerge naturally within the model. The theoretical investigations allow to develop an understanding of the nuclear pumping mechanism and to identify the relevant processes. These experimental and theoretical studies of DNP are of relevance as they provide new information on the coupling of charge carriers confined in QD to the nuclei of the solid-state matrix. In contrast to the majority of previous works in this field that were carried out on charged QDs containing one electron [Mal07; Ebl06; Bra05a] the experiments performed here were conducted in uncharged QDs for which only comparatively few studies have been

reported [Gam01; Tar07; Yok05; Mos09; Mal09; Mak08b; Kor99; Hoe12]. However, this system is of particular interest for the use of QDs in quantum information processing as it provides significantly longer lifetimes of the state of the nuclear spin system prepared as compared to charged QDs which are subject to rapid depolarization processes typically mediated by the resident electron.

Besides the potential use for quantum computing, a single electron confined in a semiconductor quantum dot coupled to a mesoscopic nuclear spin ensemble also yields the possibility to address further question of interest. It allows, for example, to study the central spin problem as it provides a model system for that configuration where one central spin is coupled to an ensemble of spins not interacting with each other. For this and similar purposes, QDs have the further advantage that the number of involved spins of $10^4 - 10^5$ is small in comparison to typical bulk solid state effects.

Spin control in quantum dots using ESR techniques

The most common and widely used technique for coherent manipulation of electron spins is electron spin resonance (ESR) where the oscillating magnetic field component of a microwave field is used to resonantly drive transitions between the two states of opposite spin orientation that are split by the Zeeman interaction. However, this well established method is usually employed on large ensembles of spins and straight forward downscaling of the usual detection schemes is not possible. This makes ESR on a single electron spin in a QD an experimentally very challenging task. Elaborate methods are necessary to probe the polarization of a single electron spin after manipulation. Until now, a small number of techniques where demonstrated to be suitable to achieve the high sensitivity needed. They include spin to charge conversion where the spin orientation of the electron is mapped onto the charge occupancy of the dot in a spin-selective charging process [Kop06; Hei08a; Hei10], energy selective readout [Elz04; Mor10] or optical readout [Hei08a; Hei10; Nic09; Vam10; Jov12c]. So far, only one successful experiment using ESR on a single self-assembled QD has been reported [Kro08b]. However, coherent control was not achieved in this case. Only very recently, this task was accomplished by *Press et al.*, however, using an optical technique for spin manipulation [Pre10]. For electrostatically defined QDs on the other hand, a number of measurements using microwaves have been demonstrated [Kop06; Kop08; Vin09]. For these experiments, coplanar stripline antennas on top of the sample structure electrically isolated from the gate contacts by a dielectric layer were used to generate the necessary oscillating magnetic field at the site of the dot.

One of the scopes of this thesis was the development of coplanar stripline antennas suitable for coherent spin manipulation in single self-assembled QDs. For this, the technology successfully used on gated QDs was modified according to the particular requirements for optical measurements on single self-assembled QDs. Furthermore, the coplanar stripline structure was multi-functionalized in the sense that it not only delivers microwaves to the site of the QD but at the same time also serves as an electrical gate to

the sample and a shadow mask for the optical single dot spectroscopy. The results of that work are presented in chapter 5. The on-chip microwave antennas were successfully tested in an electrically detected magnetic resonance experiment on a thin film of amorphous silicon. Comparison of these measurement with finite element simulations of the structure show that the achieved amplitude of the magnetic component of the microwave field necessary is sufficient to enable coherent electron spin manipulation within the coherence time typically found in self-assembled QDs and the restrictions set by the experimental technique used [Klo11b].

2

Properties of self-assembled quantum dots and experimental methods

The term 'quantum dot' generally refers to nanostructures, commonly fabricated from semiconductor materials, that confine charge carriers in all spatial dimensions. The expression was first coined by *Reed* in the late 1980's [Ree86; Ree88]. The first experimental realization was achieved by *Ekimov et al.* as CuCl nanocrystals grown in a transparent dielectric matrix [Eki81]. By design, choice of material and fabrication techniques, it is possible to engineer QDs that can trap electrons, holes or excitons, a complex of a conduction band electron bound to a valence band hole. Quantum dots have been realized and investigated in a number of physical systems such as local thickness fluctuations in quantum wells [Zre94], semiconductor nanocrystals, colloidal QDs synthesized from precursor compounds dissolved in solutions [Ros83; Baw90; Bru91], electrostatically defined QDs formed by electrical gates on top of a two-dimensional electron gas [Kou91; Cio00; Elz04], artificially patterned QDs via etching and/or photolithographically structuring of the substrate [For88] or self assembled QDs using metal-organic vapor deposition or molecular beam epitaxy of lattice mismatched materials [Sch83; Gol85; Eag90; Leo93; Sol96]. The spatial restriction to the nanometer scale leads to a zero-dimensional (0D) density of states [Efr82; Bru84; Zre94; Nor96; Ali96; Ban99] resulting in many fundamental atom-like properties of QDs such as a discrete energy spectrum [Mar94], photon antibunching [Mic00] and a radiative-lifetime-limited Lorentzian absorption lineshape [Hoe04] of optical transitions. As a result of this, quantum dots are often referred to as 'artificial atoms' [Ash96]. However, basic differences between QDs and atoms are found, e.g. in hyperfine interactions due to the coupling of the spin of confined charge carriers to the mesoscopic nuclear spin ensemble of the QD [Pet05; Bra05b]. Investigation of the nature of this hyperfine interaction and associated

effects are the main scope of this thesis and are discussed in detail in chapter 4.

In this chapter, the basic properties and fabrication techniques of self-assembled InGaAs quantum dots as well as the experimental techniques used for their investigation are introduced giving a very general overview of the topic as it can be found in many textbooks, review articles, and theses e.g. [Haw98; Gyw09; Hei09a; Kre05a]. In section 2.1, the formation of self-assembled QDs based on the growth of lattice mismatched materials, their structural characteristics and techniques to tailor the dot height are discussed. Based on a simple QD model, the electronic properties of the dot, interactions of confined charge carriers with external electric and magnetic fields as well as coupling to the nuclear spin bath in the dot are described in section 2.2. Section 2.3 deals with the growth, fabrication, processing, and characteristics of the particular samples investigated in chapters 3 and 4. In section 2.4, the basic characterization of a single QD is demonstrated exemplarily. In the last section 2.5, quantum dot molecules (QDMs), a system consisting of a pair of coupled quantum dots, are introduced. Structural properties and fundamental characteristics are discussed and typical PL spectra are presented.

2.1 Growth of self-assembled quantum dots

2.1.1 Stranski-Krastanow growth mode

Self-assembly of quantum dots can be achieved in heteroepitaxial lattice mismatched systems where strain-induced island formation takes place, the so-called Stranski-Krastanow growth mode [Str37; Str38]. The self-assembly is driven by a thermodynamic instability during the two-dimensional growth and can be used to grow e.g. $In_xGa_{1-x}As$ islands on a GaAs substrate [Sch83; Leo93; Sol96]. The lattice mismatch in this system varies from 7.2 % for $x = 0$ to 3.5 % for $x = 0.5$ where the requirements for Stranski-Krastanow growth are still met and which was used for growth of the QDs investigated in this thesis.

The Stranski-Krastanow mode self-assembly process is illustrated in figure 2.1. When InGaAs is deposited on a GaAs substrate, a thin strained film, commonly referred to as the wetting layer (WL), is building up under biaxial compression (figure 2.1(b)). When the film thickness exceeds a critical value of 1 - 3 monolayers, the strain partially relaxes and three-dimensional (3D) islands start to form on top of the wetting layer [Sch83; Gol85]. During the formation of the QDs, the total free energy of the system is minimized as the increase in surface energy is overcompensated by the reduction in strain energy (figure 2.1(c)) [Sta04]. This process generates dislocation free dots [Eag90; Leo93] enabling their use for optical applications. By adjusting growth parameters such as temperature, time, and material flux it is possible to control basic QD properties like shape [Leo94; Sol95b], material composition or dot density [Sol95a], which, however, are all subject to a certain level of fluctuation due to the statistical

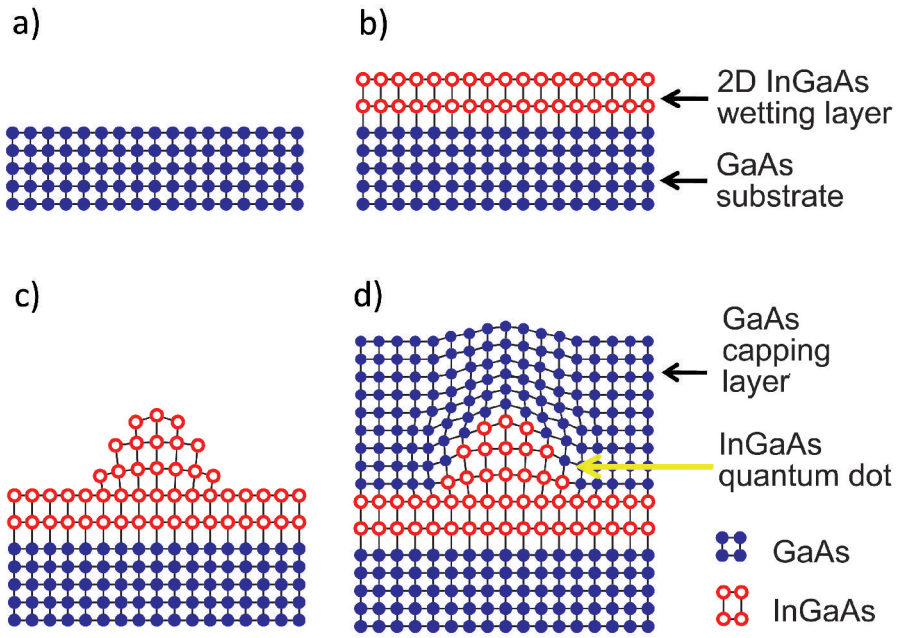

Figure 2.1. *Schematic illustration of the Stranski-Krastanow growth mode of self-assembled QDs. (a) & (b) Deposition of InGaAs onto an atomically flat GaAs substrate leads to growth of a biaxially strained InGaAs layer. (c) When a critical layer thickness is reached, partial strain relaxation minimizes the free energy of the system resulting in the formation of nano-scale islands on top of a wetting layer. (d) The quantum dots are capped with intrinsic GaAs to form fully encapsulated InGaAs islands with three-dimensional confinement. Diagram adapted from [Hei09a].*

nature of the self-assembly process. The nucleation site can not be controlled without further pre-processing of the substrate and the QDs arrange randomly on the surface. Subsequently, the dots are overgrown with the substrate material GaAs to achieve electronic confinement in all spatial directions by fully encapsulating the dots with a wider bandgap material (figure 2.1(d)). Additionally, the epitaxially grown GaAs capping layer isolates the QDs from surface states, efficiently inhibiting non-radiative recombination processes due to charge separation on the surface which would cause a degradation of the optical properties. The capping layer in combination with the perfect crystal structure formed during the self-assembly lead to quantum dots with high optical quality.

Self-assembled QDs can be obtained from either metal-organic vapor phase deposition [Osh94; Rea94] or molecular beam epitaxy (MBE) [Gol85; Gru95]. The latter was used to grow the dots investigated in this thesis and shall, therefore, be briefly discussed here. MBE allows to grow semiconductor heterostructures with high material purity, high crystal quality and precise control of the material deposition on a atomic monolayer

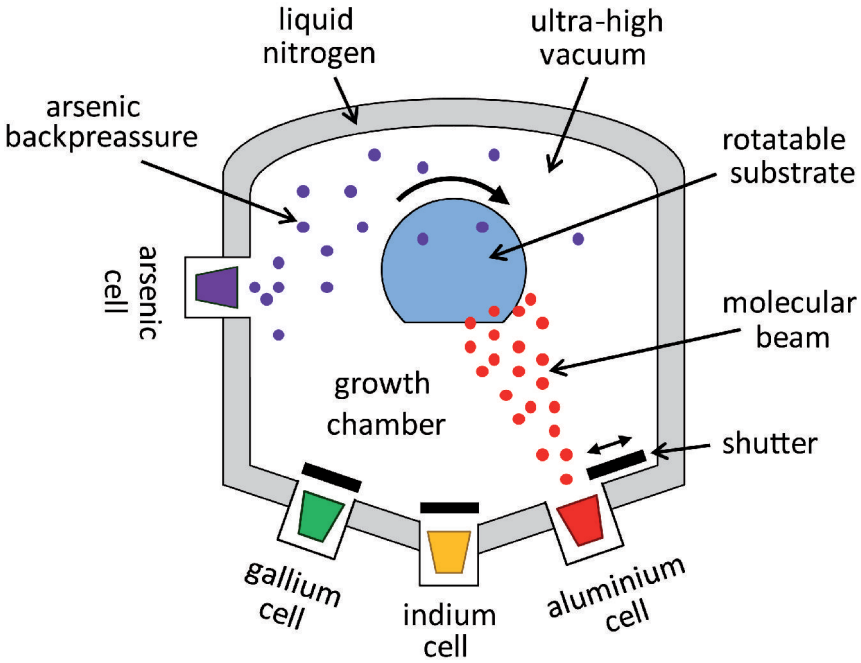

Figure 2.2. *Schematic representation of a molecular beam epitaxy system used to grow the InGaAs self-assembled QDs investigated in this thesis. Indium, gallium and aluminum are directly applied to the substrate in molecular beams whilst the arsenic flux is controlled via the arsenic back pressure in the chamber. The wafer can be rotated and heated during growth. Diagram adapted from [Hei09a].*

scale [Cho70; Cho71]. The resulting defect free growth is desirable as it further improves the optical quality of the obtained QDs.

The basic working principle of an MBE system is illustrated in figure 2.2. The substrate wafer is positioned on a rotatable and heatable holder in a growth chamber that is kept under ultra-high vacuum condition (pressure$< 10^{-10}$ mbar) by permanent cryo-pumping to ensure a minimum number of impurity atoms reaching the substrate during growth. The wafer is facing a set of effusion cells each containing a different elemental material. The cells are equipped with a shutter enabling fast switching between different materials and can be heated independently to allow adjustment of the material flux impinging on the substrate. To achieve a homogeneous coverage of the surface, the wafer is rotated during the growth. The properties of the grown layers depend on the substrate temperature, material flux and composition. The temperature determines both the diffusion length as well as the desorption rate of atoms from the surface. Due to the high crystal quality and availability of direct band gap semiconductors using III-V compound materials, MBE technology is, besides in the field of research, mainly used in the production of optoelectronic devices, e.g. light emitting diodes or quantum cascade lasers.

For the InGaAs quantum dot samples studied in this thesis, indium, gallium, and aluminum were applied to the substrate from effusion cells in direct molecular beams,

whilst incorporation of arsenic was controlled via the arsenic back pressure in the chamber. During growth of buffer and capping layers, the wafer was spinning at seven rotations per minute. For the QD growth, rotation was stopped to achieve a gradient in material coverage resulting in a variation of the quantum dot density and properties across the wafer as discussed below.

2.1.2 Structural characterization

Several microscopic techniques are available to structurally characterize the self-assembled QDs. If the dots are left uncapped, atomic force microscopy (AFM) allowing to map surfaces with a nanometer resolution [Bin86] can be employed to investigate their shape, size and density [Moi94]. Figures 2.3(a) and (b) show such AFM surface scans of an ensemble and a single QD, respectively [Jov10]. Depending on the exact growth parameters, QD structures with a height of 3-10 nm and base width of 10-30 nm are typically observed [Leo93; Pet94]. The image clearly shows the random nature of the dot distribution on the surface.

Capping the dots after the self-assembly can introduce significant changes to the geometry as well as the materials composition and distribution [Xie94; Gar97; Mir97; Lia98]. Cross-sectional transmission electron microscopy (X-TEM) enables examination of the dots after they have been overgrown [Chu99; Bru03; Kre05c]. For this technique, the sample is cleaved in situ in the TEM chamber under ultra-high vacuum normal to the growth surface exposing buried structures on the "cross-sectional surface" which is then

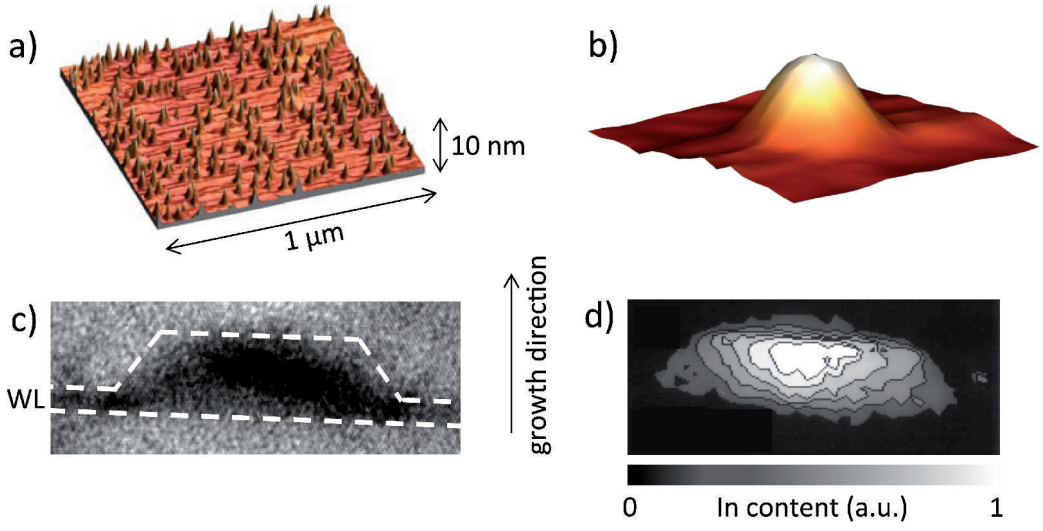

Figure 2.3. *a) Atomic force microscopy on (a) an ensemble of and (b) a single uncapped self-assembled InAs quantum dot [Jov10]. (c) Cross-sectional transmission electron microscopy, revealing the truncated pyramid shape of a single capped QD. Adapted from [Kre05c]. (d) Indium distribution of a capped dot determined from cross-sectional scanning transmission spectroscopy. Adapted from [Liu00].*

probed. A typical X-TEM image of a single capped QD is shown in figure 2.3(c), clearly showing the truncated pyramid-shaped cross-section of the dot and the 2D wetting layer [Kre05c]. In figure 2.3(d), the indium distribution within the QD is presented. The In profile was obtained from cross-sectional scanning transmission microscopy (X-STM), a technique with chemical specificity, and reveals a strongly inhomogeneous composition with an indium-rich region at the apex of the QD that has an inverted cone shape with its downward-pointing tip at the center of the dot base [Liu00; Bru02]. This In distribution as also confirmed by x-ray diffraction measurements [Keg01]. The observed material gradient in both lateral and vertical direction and the resulting non-uniform strain distribution result in a strong modification of electronic properties such as g-factors of electrons and holes or the energy level structure and has to be taken into account for realistic models to make reasonable theoretical predictions.

As mentioned above, characteristics such as size, materials composition, and density of the dots strongly depend on the materials flux during growth. Finding the exact combination of parameters for all materials needed for the growth in order to obtain QDs with the desired properties is non-trivial. To facilitate this process, the method of non-rotated growth is commonly employed which generates composition gradient across the wafer realizing a large set of growth parameters simultaneously. As indicated in figure 2.2, flux of indium, gallium, and aluminum varies across the wafer and is largest in the region facing the corresponding effusion cell. To obtain a homogeneous coverage

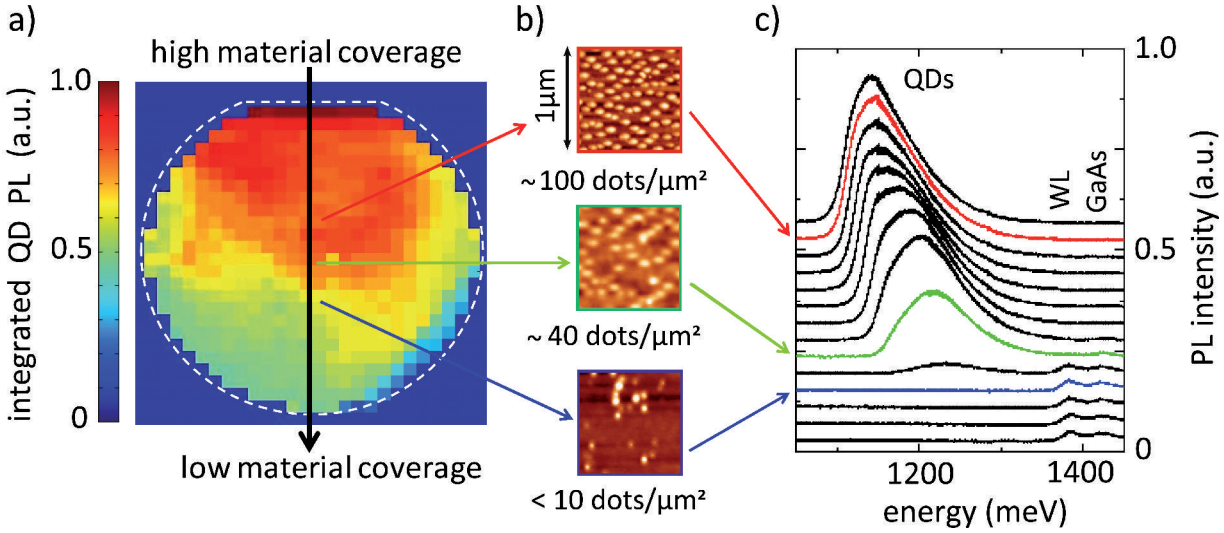

Figure 2.4. *Characterization of a wafer with self-assembled QDs grown via molecular beam epitaxy without rotation. (a) Spatially resolved color-coded integrated PL intensity of the QD emission. (b) Atomic force microscopy on three different areas of the wafer [Hei09a]. (c) Photoluminescence spectra recorded at different positions on the wafer [Hei09a]. Besides the increase in PL intensity towards the flat of the wafer as also observable in (a), a shift towards lower emission energies is found.*

for the growth of epitaxial layers this effect is compensated for by rotating the wafer during growth. During formation of the quantum dots, the rotation is stopped leading to spatially varying growth conditions across the wafer. This results in the realization of QD growth under different conditions in a single growth run and replaces a longsome growth series to explore different combinations of growth parameters. However, this method comes at the cost of only a small fraction of the wafer of typically several mm^2 exhibiting QDs growth with the desired characteristics. To determine this region on the wafer, a combination of spectroscopic and microscopic measurements are employed as presented in figure 2.4.

In figure 2.4(a), the spatially resolved emission of capped QDs after non-resonant optical excitation is presented in a color coded image plot. For this wafer mapping, PL spectra were recorded at every point of a square mesh with 2 mm lattice constant across the whole wafer and integrated over the whole spectral QD emission range. A clear increase in quantum dot PL signal intensity towards the flat of the wafer facing the indium effusion cell as illustrated in figure 2.2 is observed, indicating a higher dot density in the region of higher material coverage. This is confirmed by AFM imaging of uncapped QDs grown on the surface detected at different distances from the flat as shown in figure 2.4(b) performed on an uncapped sample grown under similar conditions. The areal QD density varies from $\sim$ 100 dots per μm^2 to practically zero at the opposite end of the wafer. Figure 2.4(c) presents a waterfall plot of PL spectra recorded on a sample of capped dots at different positions along a line perpendicular to the flat. The figure also shows emission from the quasi continuum wetting layer states and bound excitons in bulk GaAs. Wetting layer and bulk emission are not observed in the high dot density area since relaxation of charge carriers into the dot occurs within picoseconds [Hei97], much faster than radiative recombination [Kre05d]. The linewidth of the QD emission is given by inhomogeneous broadening due to the statistical fluctuations in size, shape, and material composition within the probed ensemble. Besides the change in total QD PL intensity as demonstrated in figure 2.4(a), a red shift of the emission towards the flat is observed. This is caused by a decrease in width and height of dots that is observed for decreasing material coverage. The smaller dimensions lead to a stronger confinement potential resulting in a higher emission energy as will be discussed in section 2.2. With this information at hand, the wafer can be cleaved and a piece of $\sim$ 3 x 3 mm^2 with a QD density suitable for single dot spectroscopy and desired emission wavelength can be extracted.

2.1.3 Partially capped overgrowth with *indium-flush*

For the self-assembled InGaAs quantum dots investigated in chapter 3 and 4, a partially capped overgrowth technique with an *indium-flush* step was introduced to the growth process. The *In-flush* was first presented by *Fafard et al.* [Faf99] for InAs dots as part of a method to achieve a better reproducibility of growth results and to obtain a higher level

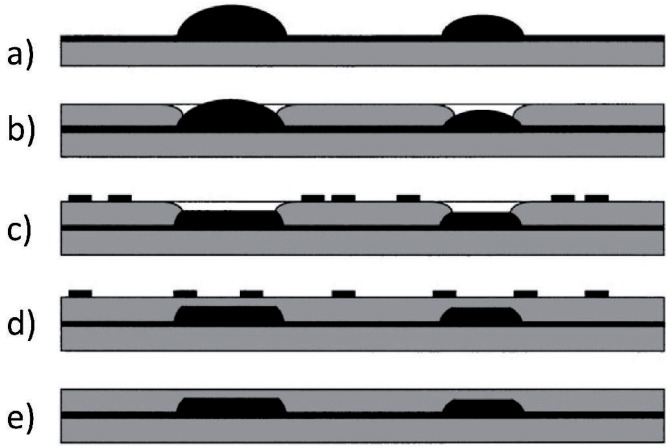

Figure 2.5. *(a)- (e) Stages of the partially capped overgrowth technique including an In-flush step as proposed by Wasilewski et al. [Was99]. GaAs and InAs are represented as gray and black regions, respectively. Figure adapted from [Was99].*

of uniformity in the QD characteristics of a macroscopic ensemble. This was realized by introducing an annealing step after formation of the dots followed by a cycling of the temperature during the overgrowth in combination with very precise control of material deposition [Faf99]. This treatment results in flat, disk-shaped dots [Was99] with a height tunable by the thickness of the partial capping layer [Kei10].

An explanation for the processes taking place during the overgrowth and *In-flush* step was proposed by *Wasilewski et al.* for InAs dots as illustrated in figure 2.5 [Was99]: Starting point is the formation of self-assembled 3D InAs islands from a 2D wetting layer deposited on a GaAs substrate (figure 2.5(a)). Next, a GaAs layer with a sub QD height thickness is grown, partially capping the dots figure 2.5(b). The larger lattice constant of the upper layers of the InAs dots due to elastic relaxation makes the top of the QD an unfavorable site for gallium adsorption and in combination with tetragonal distortion in the lower layers of the InAs dot also prevents wetting of the dot edges to some extend by introducing strain to the GaAs in the immediate vicinity of the InAs island [Xie94]. However, the situation depicted in figure 2.5(b) is not stable since the uncapped top of the dot can be regarded as a QD without a wetting layer, representing an energetically unfavorable configuration as InAs dots form on the GaAs surface via the Stranski-Krastanow mode [Str37; Str38]. Additionally, the GaAs surrounding the dot induces strain to the uncapped upper layers of the InAs island. These effects are expected to result in a migration of the In atoms from the still exposed top region of the dot to the GaAs surface forming a new, partial wetting layer figure 2.5(c). The InAs lattice of the now flat and disk shaped QDs can not release strain towards the new top of the dot as occurring for free-standing dots since there is no space for lateral extension due to the surrounding GaAs of the partial capping layer. As a result, the lateral lattice constant on top of the flattened dots is expected to be nearly identical to unstrained

GaAs. Consequently, growth of GaAs on top of the InAs islands is no longer energetically unfavorable and is presumed to occur even without any further gallium supply since filling of the craters results in a more stable configuration of the system as shown in figure 2.5(d). In a last step, the growth is interrupted and the substrate temperature is increased resulting in desorption of the In from the surface (the *indium-flush* step) while the QDs are protected against evaporation by the GaAs layer, leaving the system in a state as depicted in figure 2.5(e), typically followed by further overgrowth of the structure with GaAs. The degree to which each of the described steps are taking place during the process is determined by the exact growth kinetics and can be tuned via growth parameters, also allowing overgrowth of self-assembled dots without significant modification of the original geometry.

Figure 2.6 presents a set of X-TEM images of self-assembled InGaAs QDs grown using the partially capped overgrowth technique including an *In-flush* step using different thicknesses of the partial capping layer. The depicted dots were grown in consecutive layers with a GaAs spacer in between. The thickness of the spacer layers was chosen such that a coupling of the QD layers strong enough to lead to a stacking of the dots during growth was achieved. In this case, formation of a dot in the strain field of the previous dot is energetically favorable due to reduction of the surface free energy leading to a vertical alignment of the dots of the different layers [Xie95; Led96]. This is an important prerequisite to examine the influence of growth parameters on dot characteristics such

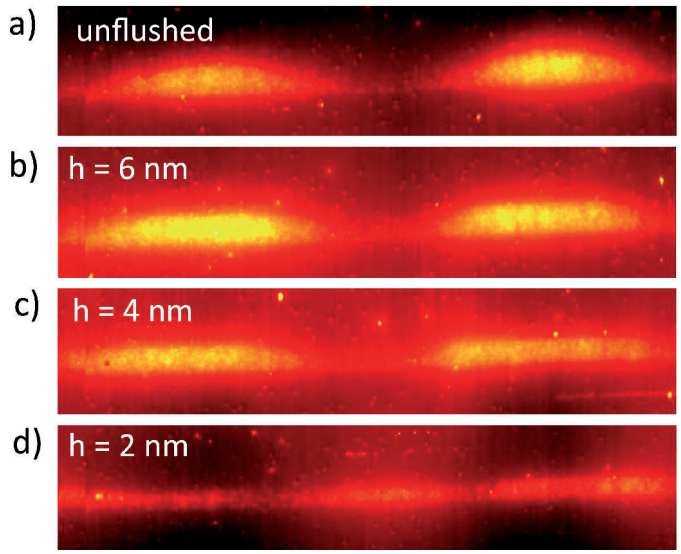

Figure 2.6. *Cross-sectional scanning transmission microscope images [Cla09] of self-assembled InGaAs quantum dots grown with partially capped overgrowth including an In-flush step. Results are shown for different thicknesses of the partial capping layer and without double-capping. The depicted QDs were grown on top of each other using a vertical stacking technique based on preferred formation of dots in the strain field of dots in the subjacent layer. The indium content within the dots is color-coded in yellow.*

as height since X-TEM imaging only provides information of a cross-section of the investigated structures on the cleaved surface and comparisons between different dots can only be made if the dot profile is recorded at the same position of the dot. The results presented in figure 2.6 for thicknesses of the partial capping layer of 2 nm, 4 nm, and 6 nm and without double-capping clearly show, that this technique allows to tailor the height of self-assembled dots with high precision [Cla09; Kei10].

2.2 Basic properties of self assembled quantum dots

The nanoscale confinement of quantum dots results, in analogy to the particle in a box problem, in a discrete, atom like energy spectrum [Haw98]. The precise energy level structure is determined by the exact properties of the confinement potential that depends on the size, shape, materials composition and strain distribution of the semiconductor nanostructure forming the QD [Haw98; Chu99; Shu01; Haw03; Lan04]. In this section, a basic model of the three-dimensional potential of self-assembled InGaAs dots is used to derive their basic electronic structure and the resulting electronic and optical properties. The spectrum arising from the confinement is further modified by interactions of the confined charge carriers with externally applied electric or magnetic fields [Mil84; Wal98; Kut98; Haw98; Fry00b; Fin01a; Bay02b], hyperfine coupling to the mesoscopic nuclear spin ensemble within the dot [Coi09; Urb12], and inter-particle interactions such as Coulomb or exchange interaction [Eto97; War98; Bay98; Bay99a; Fin01d; Haw03]. The most important of these effects will be introduced in this section.

2.2.1 Quantum dot model

Confinement

Based on the size and shape of self-assembled QDs obtained from structural investigations as sketched in section 2.1, a simple model of the confinement potential can be set up. Using a single particle treatment, this model allows to qualitatively understand the basic electronic properties of QDs as will be discussed in this section. However, to quantitatively reproduce the much more complex full electronic spectrum, a detailed simulation has to be performed taking into account relevant interactions such as multi-particle effects [Eto97; War98; Bay98; Bay99a; Fin01d; Haw03] and inter-band mixing [Haw98] as well as a realistic composition and strain distribution within the dot [Pry98; Sti99; Shu01; Haw03; Mai12].

In GaAs-InGaAs heterostructures, the band alignment is of type-I with the band gaps of bulk GaAs and $In_{0.5}Ga_{0.5}As$ being $E_g = 1500$ meV [Lev96] and $E_g = 850$ meV [Goe83] at $T = 2$ K, respectively. However, strain caused by the lattice mismatch of the two materials can result in a significantly modified effective bandgap for the InGaAs material forming the QD. The band structure of the system forms a potential minimum in the

InGaAs quantum dot for electrons in the conduction band as well as for holes in the valence band confining the charge carriers in all three spatial dimensions [Ara82].

The structural investigations presented in section 2.1 revealed that the QD height is a factor of 5 - 7 smaller than its base. This results in a significantly stronger confinement in the z-direction than in the lateral directions. It was found to be practical to model the resulting potential by approximating the confinement in z-direction by a square potential well of height V_0 and the in-plane confinement in x- and y-direction by a rotationally symmetric 2D harmonic oscillator potential as sketched in the center and right part of figure 2.7, respectively. As energies close to the band minima are of interest here, the problem in such a nanostructure can be treated in the effective mass approximation [Din74; Bur92]. The time-dependent Schrödinger equation describing the system is

$$\left[-\frac{\hbar^2}{2m^*} + V(\mathbf{r})\right] \Psi_k(\mathbf{r}) = E_k \Psi_k(\mathbf{r}) \tag{2.1}$$

with the potential $V(\mathbf{r})$ given by

$$V(\mathbf{r}) = \begin{cases} \frac{1}{2} m^* \omega_0^2 (x^2 + y^2) & |z| < d/2 \\ V_0 & |z| > d/2 \end{cases} \tag{2.2}$$

where m^* is the effective mass of the charge carrier, ω_0 its oscillation frequency in the harmonic potential, and d the height of the QD. To solve equation 2.1, a product ansatz

$$\Psi_k(\mathbf{r}) = \Phi_{k_x k_y}(x, y) \cdot \chi_{k_z}(z) \ , \tag{2.3}$$

where $\Phi_{k_x k_y}(x, y)$ and $\chi_{k_z}(z)$ are the wave functions in z- and in the x-y-direction, respectively, can be used to separate the problem allowing to treat the vertical and the lateral part individually. The eigenstates of the well known harmonic oscillator problem are given by the Hermite polynomials H_k [Che59; Her64; Mes61]. Together with the solution for a square potential well [Mes61], the eigenstates of the full system read:

$$\Psi_k \propto H_{k_x}(x) H_{k_y}(y) \exp\left[-\frac{\omega_0 m^*}{2\hbar}\left(x^2 + y^2\right)\right] \cdot \cos\left(\frac{\pi z k_z}{d}\right) \qquad k_i = 0, 1, ... \tag{2.4}$$

with the corresponding eigenvalues for the energies of

$$E_k = \hbar\omega_0(1 + k_x + k_y) + \frac{\pi^2 \hbar^2}{2m^* d^2}(k_z + 1)^2 \qquad k_i = 0, 1, ... \quad . \tag{2.5}$$

For self-assembled InGaAs QDs, $d < 10$ nm is usually found and the resulting vertical confinement energies $E^{\mathrm{e}}_{\mathrm{conf},z} + E^{\mathrm{h}}_{\mathrm{conf},z}$ observed in experiments are several hundred meV [Fin00; Fin01b; Fin01c]. Normally, only one bound state in z-direction is found ($k_z = 0$). As depicted in figure 2.7, the reduced thickness of the InGaAs wetting layer in z-direction as compared to the QD height results in a higher confinement energy $E^{\mathrm{e}}_{\mathrm{WL}} + E^{\mathrm{h}}_{\mathrm{WL}}$. Typically, differences of $\sim 100 - 200$ meV in energy between WL and QD

emission are observed [Hei09a] (cf. figure 2.4c). As a result, charge carriers generated in the wetting layer continuum quickly relax to the QD lower energy QD states whereas escape from the dot to the wetting layer due to thermal activation or via electric fields is strongly suppressed.

The p-like character of the valence band Bloch functions at the Brillouin zone center reduces the rotational symmetry resulting in the formation of valence sub-bands that are described by their different effective masses m^*. The internal angular momentum of the p-type orbitals of $J_\mathrm{p} = 1$ with $J_{\mathrm{p},z} = -1, 0, +1$ couples to the spin of the electron ($J_\mathrm{e} = 1/2, J_{\mathrm{e},z} = \pm 1/2$) filling the valence band state. This results in the formation of the following hole sub-bands with a total angular momentum of $\boldsymbol{J}_\mathrm{h} = \boldsymbol{J}_\mathrm{p} + \boldsymbol{J}_\mathrm{e}$:

- $J_\mathrm{hh} = 3/2, J_{\mathrm{hh},z} = \pm 3/2$ heavy hole sub-band (hh)
- $J_\mathrm{lh} = 3/2, J_{\mathrm{lh},z} = \pm 1/2$ light hole sub-band (lh)
- $J_\mathrm{so} = 1/2, J_{\mathrm{so},z} = \pm 1/2$ spin-orbit split-off sub-band (so).

Since the spin-orbit coupling effectively increases the energy splitting of the split-off sub-band by several hundred meV [Ger89; daS97], it is of no relevance for our considerations and, therefore, will be neglected in the following discussions. As m^* enters the vertical confinement, the degeneracy between heavy holes ($m^*_\mathrm{hh} = 0.46 m_0$ for $In_{0.5}Ga_{0.5}As$, with m_0 = free electron mass) [Gol99] and light holes ($m^*_\mathrm{lh} = 0.054 m_0$ for $In_{0.5}Ga_{0.5}As$) [Gol99] is lifted. Due to the large difference in effective masses between heavy and light hole of about one order of magnitude, the confinement energy is much stronger for light holes than for heavy holes. As a result, confirmed both experimentally [Fry00c; Fry00b] as well as by theoretical calculations [Wan99; Bar00], the highest energy valence band state is predominantly of heavy hole character, an effect that is further enhanced by strain as occurring in self-assembled QDs. Consequently, the term 'hole' is often used synonymously for 'heavy hole' in this work unless stated otherwise.

The confinement in x-y-direction is sketched in the right part of figure 2.7. The bandgap is is modified by the much stronger confinement in z-direction. The lowest energy level is lifted above the bandgap $E_{\mathrm{g,eff}} = E_{\mathrm{g,dot}} + E_{\mathrm{conf},z}$ by the energy of the 2D harmonic potential $\hbar\omega_0$. Usually, several bound excited states ($n = 1, 2, ...$) are observed [Fin00; Koe09] that are commonly labeled s-, p-, d-, ... shell in analogy to atomic states. They are typically split by $E_{\mathrm{s-p}} = \hbar\omega \sim 15 - 60$ μeV for the conduction band and $\sim 10 - 40$ μeV for the valence band states in self-assembled InGaAs QDs [War98; Fin00; Fin01d; Koe09]. Taking the spin degree of freedom into account, each level is of $2\left(k_x + k_y + 1\right)$-fold degeneracy. The illustration of the lateral confinement potential on the right side of figure 2.7 suggests an increase of the band-gap energy at the edge of the QD as predicted to arise from strain effects by calculations based on a realistic QD model [Box07]. The blue (red) arrows represent electrons (holes) populating the QD levels with a spin projection indicated by the arrow orientation.

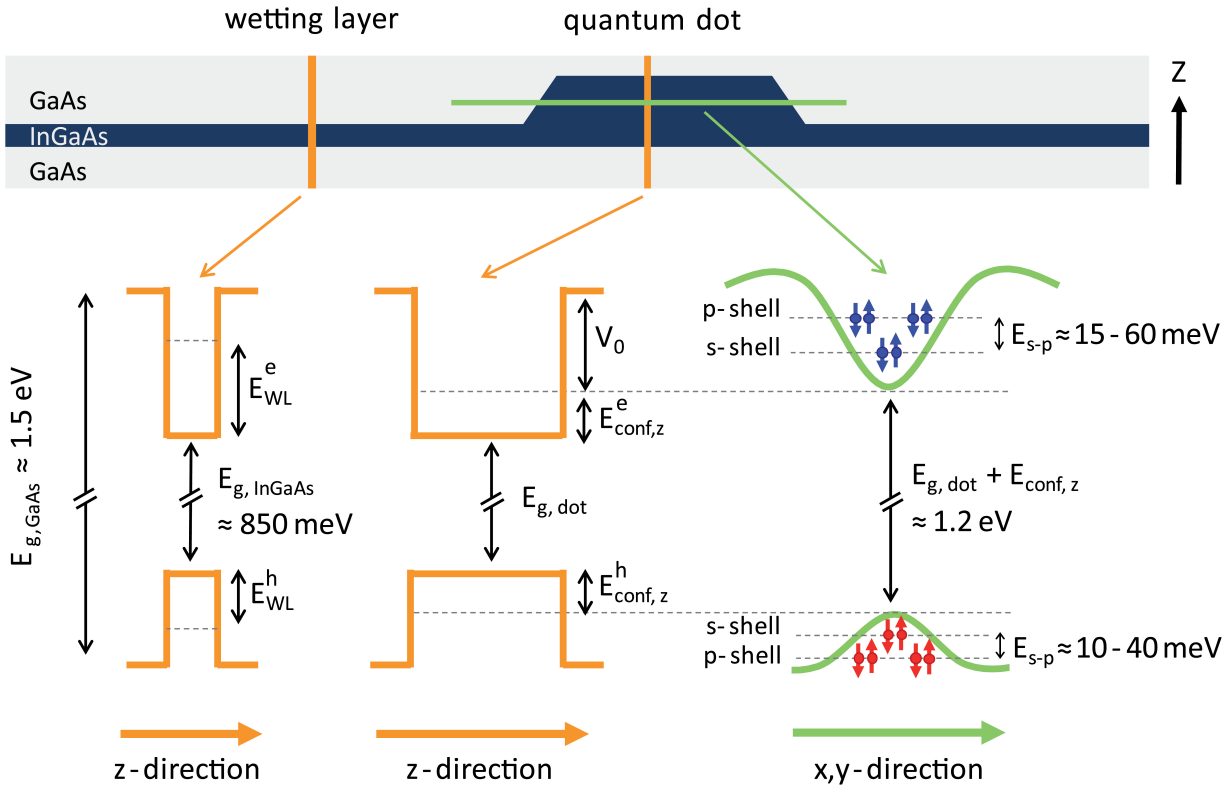

Figure 2.7. *Illustration of the confinement potentials for both electrons (blue arrows) and holes (red arrows) in quantum dots and wetting layer arising from the type I band alignment in GaAs-InGaAs heterostructures. In z-direction, it can be modeled by a square potential well. Typically, only the first level of the resulting discrete energy spectrum is observed to form a bound state in self-assembled InGaAs QDs. Since the QD base is significantly larger than its height, the lateral confinement is much weaker and more appropriately described by a 2D harmonic potential. Diagram adapted from [Hei09a]*

2.2.2 Optical selection rules and fine structure

Optical transitions

At low temperatures ($k_B T \ll E_g$), the valence band in the QD is fully populated while the conduction band is empty. Using light with $\hbar\omega > E_{g,\mathrm{eff}}$, the system can be optically excited whereby an electron is lifted from the valence to the conduction band in the dot. The missing electron in the valence band is most conveniently described as a quasi-particle hole state. In this picture, the process is described as the generation of an electron-hole pair which, due to the direct bandgap, can take place without assistance of a phonon. In quantum dot literature, such a bound electron-hole pair is commonly referred to as an exciton although the binding of the charge carriers is not dominated by the Coulomb attraction but by the QD confinement potential.

As mentioned above, the highest energy valence band state relevant for optical transitions is of predominantly heavy hole character [Fry00c; Fry00b; Wan99; Bar00]. This

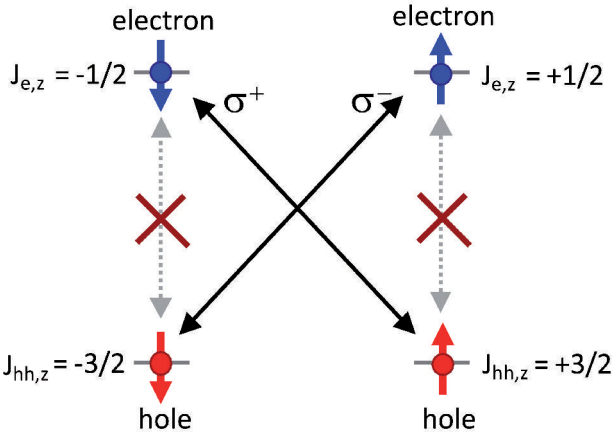

Figure 2.8. *Schematic representation of optical selection rules. Transitions with $\Delta J_z = \pm 1$ couple to σ^+ and σ^- polarized light while transitions with $\Delta J_z = \pm 2$ can not be optically excited via a one-photon process. Hence, the corresponding excitons with an angular momentum projection of $J_{ex,z} = +1$ ($|\downarrow\Uparrow\rangle$) and $J_{ex,z} = -1$ ($|\uparrow\Downarrow\rangle$) are denoted 'bright' and excitons with $J_{ex,z} = +2$ ($|\uparrow\Uparrow\rangle$) and $J_{ex,z} = -2$ ($|\downarrow\Downarrow\rangle$) are accordingly named 'dark'. $\uparrow,\downarrow$ ($\Uparrow,\Downarrow$) represent the electron (hole) spin orientation*

gives rise to optical selection rules as illustrated in figure 2.8. The two electron and two heavy hole states with $J_{e,z} = \pm 1/2$ and $J_{hh,z} = \pm 3/2$, respectively, can form four excitons with ($\Delta J_{ex,z} = +1$ ($|\downarrow\Uparrow\rangle$), -1 ($|\uparrow\Downarrow\rangle$), $+2$($|\uparrow\Uparrow\rangle$) and -2 ($|\downarrow\Downarrow\rangle$), where $\uparrow,\downarrow$ ($\Uparrow,\Downarrow$) denote the electron (heavy hole) spin orientation. Since photons carry an angular momentum of $M = \pm 1$, depending on the helicity of the circular polarization, only transitions with a difference of the angular momentum z-projection of $\Delta J_z = \pm 1$ between the initial and final state can be optically excited in a one-photon process due to conservation of spin (diagonal black arrows in figure 2.8). Thus, excitons with $J_{ex,z} = \pm 1$ are termed 'bright'. Excitons with $J_{ex,z} = \pm 2$ are optically inactive as they only couple to light fields via two-photon processes [GM31] that are of second-order making them orders of magnitude weaker than single photon absorption (vertical gray dashed arrows in figure 2.8). Accordingly, they are referred to as 'dark'.

The polarization selection rules for optical transitions can be exploited in experiment as they grant access to the spin degree of freedom of excitons by using light of appropriate circular polarization. A photon of σ^+ (σ^-) polarization generates an exciton with spin projection of $J_{ex,z} = +1$ ($J_{ex,z} = -1$) relative to the propagation direction of the light, consisting of a spin down $\downarrow$ (up $\uparrow$) electron and a spin up $\Uparrow$ (down $\Downarrow$) hole. In return, detection of the polarization of emitted light in photoluminescence measurements allows to draw conclusions regarding the spin configuration of the recombining charge carriers.

Fine structure

The energy spectrum presented in section 2.2.1 derived from an idealized model of the confinement in lateral and growth direction allows to qualitatively understand several

QD properties. However, this simplified picture cannot reproduce all features observed in experiment. This is not surprising since it does not take into account inter-particle effects, interactions with the environment, coupling to externally applied electric fields, or the influence of asymmetry in the confinement potential which all together cause a rich fine structure in the energy spectrum [Gam96a; Haw98; Bay99a; Bay02b; War05; Bra08; Coi09]. Here, a brief overview of the most relevant interactions modifying the energy level scheme in self-assembled QDs is given. In this section, inter-particle interactions and effects of reduced symmetry in the confinement potential will be discussed while the influence of external fields and hyperfine coupling to the crystal environment will be covered in sections 2.2.3 and 2.2.4, respectively.

A schematic overview of the modifications to the exciton energy spectrum occurring in a realistic QD is presented in figure 2.9. The electrostatic attraction between the electron and the hole in the dot lowers the transition energy by 10-20 meV [Bay98]. This Coulomb energy is larger than for bulk electron-hole pairs due to the vicinity of both charge carriers resulting from the localization caused by the QD confinement potential [Bay98].

Due to the fermionic nature of electrons and holes, their overlap in the dot requires the formation of antisymmetric wavefunctions. This gives rise to an exchange interaction, a purely quantum mechanical effect stemming from the Pauli exclusion principle [Pj25]. In its general form, the exchange interaction (with the quantization axis chosen in z-direction along the growth direction) is given by [Kes90; Bay99a]

$$H_{\text{exchange}} = a_z \, J_{\text{hh},z} \times J_{\text{e},z} \;\; + \sum_{i=x,y,z} b_i \, \boldsymbol{J}^3_{\text{hh},i} \times \boldsymbol{J}_{\text{e},i} \, . \tag{2.6}$$

The exchange interaction causes a splitting separating the bright from the dark excitons by an energy $\delta_0 = 1.5a_z + 3.375b_z$ which is typically found to be $100 - 200$ μeV [Kes90; Bay99a; Bay02b]. Furthermore, it results in a splitting of the two dark states from each other by $\delta_1^{\text{d}} = 0.75(b_y + b_x)$ and of the two bright states by $\delta_1^{\text{b}} = 0.75(b_y - b_x)$ [Kes90; Bay99a; Bay02b]. Consequently, for QDs with perfect rotational symmetry (D_{2d}: $b_y = b_x$), the anisotropic exchange splitting of the bright exciton levels vanishes and the states are pure spin states $|\uparrow\Downarrow\rangle$ and $|\downarrow\Uparrow\rangle$. The dark states always hybridize, irregardless of the QD symmetry. In reality, self-assembled dots tend to grow in an elliptical shape ($b_y \neq b_x$) resulting in $\delta_1^{\text{b}} \neq 0$ [Bay02b]. In this case, the angular momentum is not a good quantum number anymore as the eigenstates of such a system are not pure spin states but symmetric and antisymmetric linear combinations of those. An overview of the eigenstates formed in structures with D_{2d} and less than D_{2d} ($<\text{D}_{2d}$) symmetry is given in table 2.1. The mixed character of the states at $B_{\text{ext}} = 0$ T also leads to a lifting of the polarization selection rules and linearly polarized optical transitions (π^x and π^y) are possible as indicated in figure 2.9.

Table 2.1. *Excitonic eigenstates and corresponding energies of rotationally symmetric (D_{2d}) and elliptical ($<D_{2d}$) QDs in a magnetic field B_{ext} applied in Faraday geometry ($B_{\text{ext}} \| z$) [Bay02b]. δ_0 is the exchange splitting between bright and dark states, $\delta_1^{\text{b(d)}}$ the splitting of the bright (dark) excitons from another. The Zeeman energy $E_{\text{ex,Z}}$ of the bright (dark) states is given by $E_{\text{ex,Z}}^{\text{b(d)}} = \mu_{\text{B}}\, g_{\text{ex}}^{\text{b(d)}}\, B_{\text{ext}}$, where $g_{\text{ex}}^{\text{b(d)}} = g_{\text{e}} \overset{+}{(-)} g_{\text{hh}}$ is the bright (dark) exciton g-factor and $g_{\text{e,(hh)}}$ the electron (heavy hole) g-factor. N_i, $i = 1, ..., 4$ are magnetic field-dependent normalization constants. In this work, the higher energy Zeeman branch of the bright (dark) neutral exciton that is determined by the magnitude and sign of g_{e} and g_{hh} is always denoted $|E_1\rangle$ ($|E_3\rangle$) irregardless of the spin configuration.*

sym.	energy	eigenstate
D_{2d}	$-\frac{1}{2}\delta_0 - \frac{1}{2}E_{\text{Z}}^{\text{b}}$	$\lvert E_1\rangle = \lvert\downarrow\Uparrow\rangle$
	$-\frac{1}{2}\delta_0 + \frac{1}{2}E_{\text{Z}}^{\text{b}}$	$\lvert E_2\rangle = \lvert\uparrow\Downarrow\rangle$
	$-\frac{1}{2}\delta_0 - \frac{1}{2}\sqrt{(\delta_1^{\text{d}})^2 + (E_{\text{Z}}^{\text{d}})^2}$	$\lvert E_3\rangle = N_3 \left[\lvert\uparrow\Uparrow\rangle + \left(\frac{E_{\text{Z}}^{\text{d}}}{\delta_1^{\text{d}}} - \sqrt{1 + \left(\frac{E_{\text{Z}}\text{d}}{\delta_1^{\text{d}}} \right)^2} \right) \lvert\downarrow\Downarrow\rangle \right]$
	$-\frac{1}{2}\delta_0 + \frac{1}{2}\sqrt{(\delta_1^{\text{d}})^2 + (E_{\text{Z}}^{\text{d}})^2}$	$\lvert E_4\rangle = N_4 \left[\lvert\uparrow\Uparrow\rangle + \left(\frac{E_{\text{Z}}^{\text{d}}}{\delta_1^{\text{d}}} + \sqrt{1 + \left(\frac{E_{\text{Z}}^{\text{d}}}{\delta_1^{\text{d}}} \right)^2} \right) \lvert\downarrow\Downarrow\rangle \right]$
$<D_{2d}$	$-\frac{1}{2}\delta_0 - \frac{1}{2}\sqrt{(\delta_1^{\text{b}})^2 + (E_{\text{Z}}^{\text{b}})^2}$	$\lvert E_1\rangle = N_1 \left[\lvert\downarrow\Uparrow\rangle + \left(\frac{E_{\text{Z}}^{\text{b}}}{\delta_1^{\text{b}}} - \sqrt{1 + \left(\frac{E_{\text{Z}}^{\text{b}}}{\delta_1^{\text{b}}} \right)^2} \right) \lvert\uparrow\Downarrow\rangle \right]$
	$-\frac{1}{2}\delta_0 + \frac{1}{2}\sqrt{(\delta_1^{\text{b}})^2 + (E_{\text{Z}}^{\text{b}})^2}$	$\lvert E_2\rangle = N_2 \left[\lvert\downarrow\Uparrow\rangle + \left(\frac{E_{\text{Z}}^{\text{b}}}{\delta_1^{\text{b}}} + \sqrt{1 + \left(\frac{E_{\text{Z}}^{\text{b}}}{\delta_1^{\text{b}}} \right)^2} \right) \lvert\uparrow\Downarrow\rangle \right]$
	$-\frac{1}{2}\delta_0 - \frac{1}{2}\sqrt{(\delta_1^{\text{d}})^2 + (E_{\text{Z}}^{\text{d}})^2}$	$\lvert E_3\rangle = N_3 \left[\lvert\uparrow\Uparrow\rangle + \left(\frac{E_{\text{Z}}^{\text{d}}}{\delta_1^{\text{d}}} - \sqrt{1 + \left(\frac{E_{\text{Z}}^{\text{d}}}{\delta_1^{\text{d}}} \right)^2} \right) \lvert\downarrow\Downarrow\rangle \right]$
	$-\frac{1}{2}\delta_0 + \frac{1}{2}\sqrt{(\delta_1^{\text{d}})^2 + (E_{\text{Z}}^{\text{d}})^2}$	$\lvert E_4\rangle = N_4 \left[\lvert\uparrow\Uparrow\rangle + \left(\frac{E_{\text{Z}}^{\text{d}}}{\delta_1^{\text{d}}} + \sqrt{1 + \left(\frac{E_{\text{Z}}^{\text{d}}}{\delta_1^{\text{d}}} \right)^2} \right) \lvert\downarrow\Downarrow\rangle \right]$

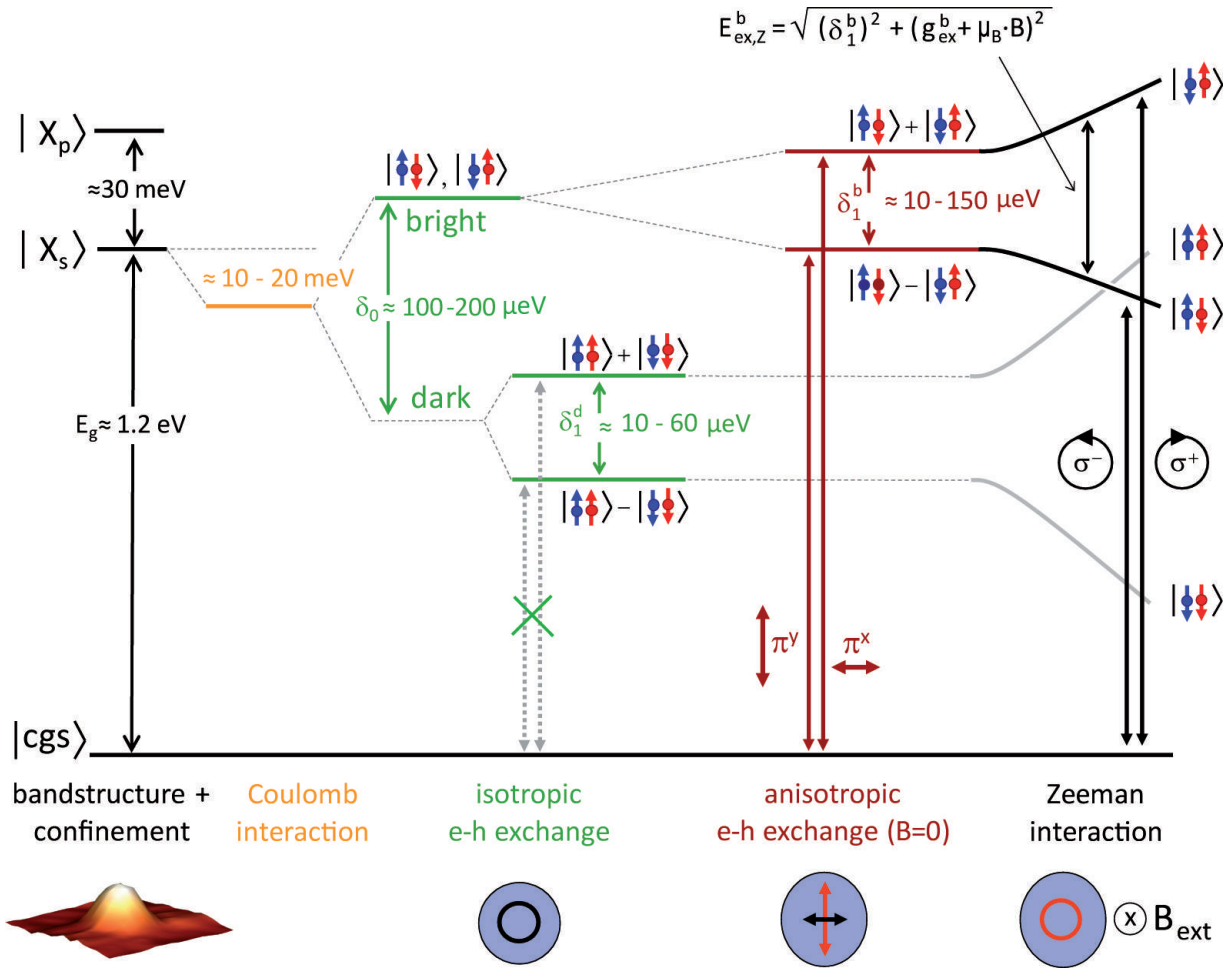

Figure 2.9. *Schematic overview of the exciton fine structure and related optical transitions of an elliptical self-assembled QDs with a magnetic field B_{ext} applied in Faraday configuration. The modification of the energy spectrum arises from inter-particle interactions and the reduced rotational symmetry of the confinement potential. Blue (red) arrows represent electrons (holes) with a spin projection indicated by the arrow orientation.*

2.2.3 Quantum dots in magnetic and electric fields

Quantum dots in magnetic fields

If a magnetic field $\boldsymbol{B}_{ext} \neq 0$ T is applied, electrons and holes couple to it via the Zeeman interaction [Mes61]. For $\boldsymbol{B}_{ext}$ applied in Faraday geometry, i.e. along growth direction of the QD ($B_{ext} \| z$), it is given by [Haw98; Bay02b; Gyw09]

$$H_{ex,Z} = -\mu_B \left(g_e J_{e,z} - g_{hh} J_{hh,z}\right) B_{ext,z}\,, \tag{2.7}$$

where $\mu_B = e\hbar/2m_0 = 5.788 \cdot 10^{-5}$ eV/T is the Bohr magneton and $g_{e(hh)}$ the electron (heavy hole) g-factor. Unless stated otherwise, in this work $g_{e(hh)}$ always refers to the z-component of the g-factor tensor. In semiconductors, spin-orbit coupling

in the valence bands changes the g-factor from the free electron value [Rot59] of $g_e \approx 2.0023$ [Moh00]. Interband mixing also influences the electron g-factor and values of $g_e \approx -14.8$ and $g_h \approx -46$ are found for bulk InAs [Mad87]. In QDs, both the spin-orbit coupling as well as the interband mixing are significantly modified by the geometry, strain, and confinement potential [And09a]. Additionally, the strong spatial localization leads to an orbital angular momentum quenching [Pry06] resulting in a further modification of g_e and g_{hh}. Particularly the hole g-factor can vary strongly as a function of dot parameters such as height, width, strain, composition and distribution [Sne92; Pry06; She07; Kim09; And09a] or external parameters like applied electric and magnetic fields [Jov11; Pin11; Jov12b; Eis12b] as will be discussed in chapter 3. In contrast, g_e is found to be less sensitive to these influences [Sne92; She07; She08; Jov11; Jov12b]. As a result, a wide range of exciton g-factors g_{ex} is observed experimentally [Bay99a; Bay99b; Bay02b; Nak04; Klo10b; Jov11; Jov12b] and calculated theoretically [She07; She10; And09a; Eis12b]. The Zeeman energy $E_{ex,Z}$ of the bright (dark) states is given by $E_{ex,Z}^{b,(d)} = \mu_B \, g_{ex}^{b(d)} \, B_{ext}$, where $g_{ex}^{b(d)} = g_e \, {}^{+}_{(-)} g_h$ is the bright (dark) exciton g-factor. The effect of a magnetic field applied in Faraday geometry on the excitonic states can be seen from table 2.1. The Zeeman interaction reduces the mixing of the states and for sufficiently high applied magnetic fields (i.e. $E_{ex,Z}^{b(d)} \gg \delta_1^{b(d)}$), the pure spin states and the optical polarization selection rules can be recovered as graphically indicated on the right side of figure 2.9. Whether the $|\downarrow\Uparrow\rangle$ or $|\uparrow\Downarrow\rangle$ state is higher in energy at large B_{ext} depends on the magnitude and sign of g_e and g_{hh} and can vary for different QDs. In this work, the higher energy Zeeman branch of the bright and dark neutral exciton is always denoted $|E_1\rangle$ and $|E_3\rangle$, respectively (accordingly, the lower energy state of the bright and dark doublet is referred to as $|E_2\rangle$ and $|E_4\rangle$, respectively), regardless of its spin configuration.

Other than by the Zeeman interaction, the energy of the exciton states in a magnetic field is additionally shifted by the diamagnetic response of the system. The diamagnetic shift ΔE_{dia} leads to an increase in transition energy with increasing applied magnetic field. For rotationally symmetric dots, ΔE_{dia} can be described by [Wal98; Kut98]

$$\Delta E_{dia} = \gamma_2 \cdot B_{ext}^2 \, . \tag{2.8}$$

The diamagnetic coefficient γ_2 can in the case of strong 3D confinement be approximated by

$$\gamma_2 = \frac{e^2}{8} \left[\frac{\langle r_e^2 \rangle}{m_e} + \frac{\langle r_h^2 \rangle}{m_h} \right] , \tag{2.9}$$

with the mean square of the lateral extension of the electron and hole wavefunctions $\langle r_e^2 \rangle$ and $\langle r_h^2 \rangle$, respectively. Due to the dependence of γ_2 on the horizontal extension of the charge carrier wave functions the diamagnetic shift can be used as a measure of the lateral size of the QD [Bay98].

Quantum dots in electric fields

Since excitons carry an electric dipole moment $\boldsymbol{p} = e\boldsymbol{d}$, where $\boldsymbol{d}$ is the vector pointing from the center of the electron wave function to the center of the hole wavefunction and e is the elementary charge, they couple to externally applied electric fields $\boldsymbol{F}$ [Fry00b; Fin01a]. The resulting energy shift $\Delta E = \boldsymbol{p} \cdot \boldsymbol{F}$ provides an experimentally convenient method to accurately tune the energy of QD states. This working principle is extensively used for the measurements presented in chapters 3 and 4 where exciton transitions are either tuned into resonance with an excitation laser of wavelength λ_{exc} or kept at a well defined detuning from the laser energy.

There are two contributions to the exciton dipole moment: (i) The intrinsic dipole $\boldsymbol{p}_{int}$ exists independently of applied electric fields. It arises from displacement of electron and hole wavefunctions due to the asymmetric confinement potential in growth direction with the electron located at the base of the dot and the hole at its In-rich apex [Fry00b] and strain-induced piezo-electric fields [San00; Pat00]. Hence, a confinement potential which is symmetric along the direction of the electric field direction leads to $\boldsymbol{p}_{int} = 0$ as was demonstrated in quantum wells with an electric field applied along growth direction [Hsu01]. (ii) The electric field-induced contribution is caused by a displacement of the electron and hole wavefunction. It can be described by $\beta\boldsymbol{F}$, where β is the polarizability of the exciton. Ionization of the electron hole pair is suppressed as compared to free excitons by the QD confinement [Mil84]. Put together, the total shift of transition energy is given by

$$\Delta E_{\text{QCSE}} = E_0 + \boldsymbol{p}_{int} \cdot \boldsymbol{F} + \beta \boldsymbol{F}^2 \,, \tag{2.10}$$

where E_0 is the transition energy in the absence of electric fields. The effect of a shifting of the exciton energy as a function of electric fields in charge carrier confining nanostructures is referred to as quantum confined Stark effect (QCSE) [Mil84; Fry00b; Fin01a].

Besides a shifting of the QD states via the QCSE, an application of electric fields to the structure also alters the tunnel escape rate of trapped charge carriers out of the dot by effectively modifying the confinement barrier. In the regime of high electric fields where exciton lifetime and decay mechanism are governed by tunneling and not by radiative recombination, this allows to tune the dwell time of electrons and holes in the dot.

The electric field dependence of the tunneling rate Γ_{t} can be determined by applying a one-dimensional Wentzel-Kramers-Brillouin (WKB) calculation [Wen26; Kra26; Bri26] to a tunneling process from a square well potential of width h_{well} and energy barrier E_{barrier} with an electric field F_z applied perpendicular to the well. Using this approximation, Γ_{t} is found to be [Vin79; Kuo00; Fry00a]

$$\Gamma_{\text{t}} = \frac{\hbar\pi}{2m^* h_{\text{well}}^2} \exp\left(-\frac{4}{3\hbar e F_z} \sqrt{2m^* E_{\text{barrier}}^3} \right) \,, \tag{2.11}$$

where m^* is the effective mass of the tunneling charge carrier. The exponential de-

pendence on F_z allows electric field tuning of the tunneling time over several orders of magnitude [Fry00a; Beh02; Hei08a; Hei09b] with an upper limit given by the radiative recombination time of ~ 1 ns [Kre05d]. Since both the effective mass m^* as well as the tunneling barrier E_{barrier} are different for conduction and valence band, the same is true for the dwell time of electrons and holes generated in the dot in the tunneling regime. The two individual tunneling times can be obtained from separate measurements:

(i) The lifetime of the faster tunneling particle $\tau_{\text{fast}} = 1/\Gamma_{\text{t,fast}}$ limits the lifetime of the exciton state and can, thus, be determined from the natural linewidth Δ_0 of the exciton transition. The two quantities are correlated by the Heisenberg uncertainty principle by [Hei27]

$$\Delta E \cdot \Delta t \geq h\,, \tag{2.12}$$

with $\Delta_0 = \Delta E$ and $\tau_{\text{fast}} = \Delta t$. This relation gives direct access to τ_{fast} provided that the experiment allows to determine the natural linewidth of the transition.

(ii) The tunneling time of the slower particle $\tau_{\text{slow}} = 1/\Gamma_{\text{t,slow}}$ can be found from the saturation behavior of the signal in resonant photocurrent experiments [Beh01; Beh02]. In this type of measurement, optical excitation of the QD is only possible if the dot is empty as the laser wavelength is matched to the neutral exciton transition energy. Charge carriers in the dot lead to a renormalization of the energy spectrum, shifting the QD levels by much more than the linewidth of the transition [War00; Fin01c; Fin01d]. As a result, the system is detuned from the laser energy and can not be optically excited until both charge carriers have left the dot and the initial resonant situation is restored. Consequently, the maximum possible optical excitation rate of the QD is limited by the decay rate of the charge carrier population in the dot. The population of the two configurations N_0 (dot empty) and N_1 (dot occupied with one exciton) can be treated using a simple rate equation model. After generation of an exciton at a rate which is proportional to the excitation power $\Gamma_{\text{gen}} = \alpha_{\text{g}} P_{\text{exc}}$, the system can return to an empty dot state via three ways: (a) Tunnel escape of both charge carriers. This process is limited by τ_{slow} [Beh01; Beh02]. (b) Radiative recombination of the electron hole pair which takes place at a rate $\Gamma_{\text{rad}} \sim 1$ ns [Kre05d]. (c) Stimulated radiative decay of the exciton taking place at a rate $\Gamma_{\text{stim}} = \Gamma_{\text{rad}}$ in a quantum mechanical two-level system [Lou73]. Considering all three paths, the rate equations read [Beh01; Beh02]

$$\begin{aligned} dN_0/dt &= -N_0 \cdot \Gamma_{\text{stim}} + N_1 \cdot (\Gamma_{\text{rad}} + \Gamma_{\text{stim}} + \Gamma_{\text{t,slow}})\,, \\ dN_1/dt &= N_0 \cdot \Gamma_{\text{stim}} - N_1 \cdot (\Gamma_{\text{rad}} + \Gamma_{\text{stim}} + \Gamma_{\text{t,slow}})\,, \\ N_0 + N_1 &= 1. \end{aligned} \tag{2.13}$$

The recorded photocurrent signal in steady state ($dN_0/dt = dN_1/dt = 0$) is then given by

$$I = e \cdot N_1 \cdot \Gamma_{\mathrm{t,slow}} = e \cdot \frac{1}{2} \frac{\alpha_{\mathrm{g}} P_{\mathrm{exc}} \cdot \Gamma_{\mathrm{t,slow}}}{\alpha_{\mathrm{g}} P_{\mathrm{exc}} + \Gamma_{\mathrm{rad}} + \Gamma_{\mathrm{t,slow}}}\,, \tag{2.14}$$

converging towards

$$I_{\mathrm{sat}} = \frac{1}{2} \cdot e \cdot \Gamma_{\mathrm{t,slow}} \tag{2.15}$$

in the limit of large powers P_{exc}. The factor $\frac{1}{2}$ stems from the stimulated emission.

2.2.4 Influence of the nuclear spin system

Since all atoms forming self-assembled InGaAs quantum dots carry a non-zero nuclear spin (cf. table 2.2), the interaction of confined electrons and holes with the nuclei of the atoms forming the dot has to be taken into account for a realistic description of the energy level structure and related effects. Particularly for the spin dynamics of confined charge carriers, the coupling to the nuclear spin system plays a major role that was studied intensively both in experiment [Pet05; Kop05; Bru09] and theory [Bur99a; Erl01; Kha02; Mer02; Coi04; Fis08; Tes09]. A detailed overview of relevant nuclear interactions in solids in general and for semiconductor nanostructures in particular can be found e.g. in [Abr61; Sli80] and [Sch03; DE08; Coi09; Mal08], respectively. The summary presented in this section is mainly based on Refs. [Sch03; Coi09; Mal08].

Hyperfine interaction

Hyperfine-mediated processes and associated effects in QDs are one of the main issues addressed in this thesis and are discussed in detail in chapter 4. The hyperfine (hf) interaction couples the spin of a confined charge carrier and the $10^4 - 10^5$ nuclear spins within a self-assembled QD [Sch03; Coi09]. For reasons discussed below in this section, in III-V semiconductor QDs, this effect is one order of magnitude stronger for s-type conduction band electrons than for p-like valence band hole states [Fis08; Tes09; Ebl09; Fal10; Che11b; Che11c].

Hyperfine coupling may provide optoelectronic access to the mesoscopic nuclear spin system with strong potential for future applications in quantum information technologies. On the other hand, hf interaction was also shown to be the dominant source of electron spin decoherence, leading to a dephasing of the electron spin on a nanosecond timescale. This effect limits the time for potential logical quantum operations [Pet05; Kop05; Joh05; Han08; Bur99a; Erl01; Kha02; Mer02; Coi04]. For holes that are coupled much weaker to the nuclear spin system, significantly longer decoherence and relaxation times up to 1 μs [Bru09] and 1 ms [Hei08b; Ger08], respectively, have been observed. However, as predicted by theory [Fis08; Tes09], hole-nuclear hyperfine interaction [Ebl09; Fal10; Che11b; Che11c] was identified still to be the dominating mechanism for the spin dephasing of holes in many cases [Ebl09].

Table 2.2. *Nuclear properties of all isotopes present in self-assembled InGaAs quantum dots. Values are taken from [Gra72].*

Isotope	natural abundance	nuclear spin J_n
^{115}In	95.3 %	9/2
^{113}In	4.7 %	9/2
^{71}Ga	39.6 %	3/2
^{69}Ga	60.4 %	3/2
^{75}As	100 %	3/2

First, an overview of the relevant interactions involved in the case of an electron spin $\boldsymbol{J}_\mathrm{e}$ coupling to an ensemble of nuclear spins $\boldsymbol{I}$ in a magnetic field $\boldsymbol{B}_\mathrm{ext}$ is presented. The Hamiltonian describing such a system is given by [Coi09]

$$H_\mathrm{e-n} = H_\mathrm{e,Z} + H_\mathrm{n,Z} + H_\mathrm{dd} + H_\mathrm{hf}\,, \tag{2.16}$$

taking into account the Zeeman interaction of electron and nuclear spins with the magnetic field ($H_\mathrm{e,Z}$ and $H_\mathrm{n,Z}$, respectively), as well as the nuclear dipole-dipole (H_dd) and electron-nuclear hyperfine coupling (H_hf).

Coupling of the electron and ith nuclear spin to a magnetic field $\boldsymbol{B}_\mathrm{ext}$ is given by the Zeeman Hamiltonians [Abr61]

$$H_\mathrm{e,Z} = \mu_\mathrm{B} g_\mathrm{e} \boldsymbol{J}_\mathrm{e} \boldsymbol{B}_\mathrm{ext} \qquad \text{and} \qquad H_{\mathrm{n,Z},i} = -\mu_\mathrm{n} g_{\mathrm{n},i} \boldsymbol{I}_i \boldsymbol{B}_\mathrm{ext}\,, \tag{2.17}$$

where $g_{\mathrm{n},i}$ is the nuclear g-factor of the ith nucleus, $\boldsymbol{I}_i$ the spin operator of the ith nucleus with the total spin quantum number I and μ_n the nuclear magneton. The Zeeman Hamiltonian of the whole nuclear spin ensemble is given by the sum over all spins: $H_\mathrm{n,Z} = \sum_i H_{\mathrm{n,Z},i}$.

The dipole-dipole coupling between two nuclear spins i and j is often the dominant nuclear spin-spin interaction and can be written as [Abr61]:

$$H_{\mathrm{dd},ij} = \frac{\mu_0 \mu_\mathrm{n}^2 g_{\mathrm{n}_i} g_{\mathrm{n}_j}}{4\pi r_{ij}^3} \left(\boldsymbol{I}_i \boldsymbol{I}_j - 3 \frac{\left(\boldsymbol{I}_i \boldsymbol{r}_{ij}\right)\left(\boldsymbol{I}_j \boldsymbol{r}_{ij}\right)}{r_{ij}^2} \right)\,, \tag{2.18}$$

where μ_0 is the permeability of free space and r_{ij} the vector connecting the two spins. To obtain the dipole Hamiltonian of the full system, the sum over all spin pairs has to be worked out: $H_\mathrm{dd} = \sum_{i<j} H_{\mathrm{dd},ij}$. The strength of the nuclear dipole-dipole coupling is usually expressed in terms of an effective magnetic field, the local field $\boldsymbol{B}_\mathrm{loc}$, that is generated at the site of a nucleus by the surrounding nuclear spins [Abr61]. In bulk GaAs, it is of the order of $B_\mathrm{loc} \sim 0.1$ mT [Pag77]. Commonly, H_dd is separated into a secular part which commutes with $H_\mathrm{n,Z}$ and a non-secular part which does not [Abr61].

The secular terms are spin conserving while the non-secular contribution leads to spin flip-flop processes between nuclei at different sites. These nuclear flip-flop processes can cause a spatial redistribution of nuclear polarization via spin diffusion [Ram08]. For bulk GaAs, the nuclear spin diffusion constant $D_{\mathrm{n,diff}}$ was experimental determined to $D_{\mathrm{n,diff}} = 10^{-13}\ \mathrm{cm^2 s^{-1}}$ [Pag82]. However, this value is expected to be significantly lower for QDs due to the varying distribution of different nuclear species within the dot and between the dot and the surrounding crystal matrix as well as by the existence of strain. This effect was studied measuring nuclear spin diffusion between quantum wells where the nuclear spin diffusion constant was found to be reduced by one order of magnitude [Mal01]. In combination with hyperfine coupling the nuclear flip-flops can also lead to electron spin decoherence through spectral diffusion [deS03].

The contact hyperfine interaction is the predominant coupling mechanism between s-type conduction band electrons and nuclear spins in III-V semiconductors and the most important source of electron spin decoherence. It was first described by Fermi in 1930 to explain the hyperfine splitting observed in alkali metals and can in its most general form be written as [Fer30; Mei84]

$$H_{\mathrm{c-hf}} = \frac{2}{3}\mu_0\mu_{\mathrm{B}}\mu_{\mathrm{n}}\mathrm{g}_0\mathrm{g}_{\mathrm{n}} \left|\Psi\left(r_I\right)\right|^2 \boldsymbol{J}_{\mathrm{e}}\boldsymbol{I}\,, \tag{2.19}$$

where $\Psi\left(r_I\right)$ is the electron wave function at the site r_I of the nucleus with spin $\boldsymbol{I}$. Due to the periodic potential of the crystal lattice, the electron wave function Ψ in a semiconductor is given by $\Psi = \Theta(r)u(r)$, comprised of a Bloch function $u(r)$ and a modulating envelope function $\Theta(r)$ [Win03; Coi09]. For a conduction band electron confined in a quantum dot in the corresponding orbital ground state, the Hamiltonian describing the coupling of the electron spin to i nuclear spins can be written as [Sch03]

$$H_{\mathrm{c-hf}} = \sum_i A_i \boldsymbol{J}_{\mathrm{e}}\boldsymbol{I}_i\,, \tag{2.20}$$

where $A_i = \frac{2}{3}\nu_0\mu_0\mu_{\mathrm{B}}\mu_{\mathrm{n}}g_0g_{\mathrm{n}_i}n_0\eta\left|\Theta\left(r_i\right)\right|^2$ is the hyperfine coupling constant of the ith nuclei. Here, ν_0 is the unit cell volume, $n_0 = \frac{1}{\nu_0}$ is the density of nuclei, $\left|\Theta\left(r_i\right)\right|^2$ gives the probability to find the electron at the site r_i of the ith nucleus and $\eta = \left|u(r_i)\right|^2$ can be estimated from electron spin resonance experiments [Mei84].

In contrast to s-type conduction band electrons, the valence band states in III-V semiconductors are composed of predominantly p-type orbitals. As a result of this, the wave function becomes zero at the site of the nucleus and the contact hyperfine interaction vanishes [Coi09]. In this case, hyperfine coupling to nuclear spins is weaker by one order of magnitude and only taking place via anisotropic hyperfine interaction and coupling to orbital angular momenta [Yaf61; Fis08; Ebl09; Coi09]. The anisotropic hyperfine interaction is of dipole-dipole nature. For an electron interacting with an

ensemble of i nuclear spins I, it can be written as [Coi09]:

$$H_{\mathrm{a-hf}} = \sum_i \frac{\mu_0 \mu_\mathrm{B} \mu_{\mathrm{n}_i} g_0 g_{\mathrm{n}_i}}{4\pi r_{\mathrm{I}_i\mathrm{e}}^3} \left(\boldsymbol{J}_\mathrm{e} \boldsymbol{I}_i - 3 \frac{\left(\boldsymbol{J}_\mathrm{e} \boldsymbol{r}_{\mathrm{I}_i\mathrm{e}}\right)\left(\boldsymbol{I}_i \boldsymbol{r}_{\mathrm{I}_i\mathrm{e}}\right)}{r_{\mathrm{I}_i\mathrm{e}}^2} \right) , \tag{2.21}$$

where $\boldsymbol{r}_{\mathrm{I}_i\mathrm{e}}$ is the electron spin position operator relative to the position of the ith nucleus $\boldsymbol{r}_{\mathrm{I}_i}$.

The coupling of nuclear spins to the electron orbital momentum is given by [Coi09]

$$H_{\mathrm{so-hf}} = \sum_i \frac{\mu_0 \mu_\mathrm{B} \mu_\mathrm{n} g_0 g_{\mathrm{n}_i}}{4\pi} \frac{\boldsymbol{L}_i \boldsymbol{I}_i}{\left|r_{\mathrm{I}_i\mathrm{e}}\right|^3} , \tag{2.22}$$

where $\boldsymbol{L}_i$ is the total electron orbital angular momentum at the site $\boldsymbol{r}_{\mathrm{I}_i}$ of the ith nucleus.

If the nuclear spin system is subject to electric field gradients which can caused by crystal strain, defects or dopants, nuclear quadrupolar interactions have to be taken into consideration [Coi09; Urb12]. They arise from deviations of the charge distribution within the nucleus of from spherical symmetry which can be described using a multipol-expansion that can be approximated using the first order quadrupolar term. The inhomogeneous nuclear quadrupolar interaction occurring in a strained semiconductor heterostructure can suppress the nuclear dipole-dipole coupling hindering nuclear flip-flop processes and, thus, significantly reduce nuclear spin diffusion [Mal09; Lat11; Klo12].

Dynamic nuclear polarization

The influence of the nuclear spin ensemble in the QD onto the spin of a confined electron can be described as an effective magnetic field $\boldsymbol{B}_\mathrm{n}$, the so called Overhauser field [Ove53]. Here we only consider the component in z-direction, denoted B_n, given by [Ove53; Coi09]:

$$B_\mathrm{n} = \frac{1}{g_\mathrm{e}\mu_\mathrm{B}} \sum_i A_i I_{i,z} = \frac{1}{g_\mathrm{e}\mu_\mathrm{B}} \sum_i A_i \left\langle I_{z,i} \right\rangle , \tag{2.23}$$

where $\langle I_{z,i} \rangle$ indicates an expectation value for the spin projection of the ith nuclei. Depending on the orientation of $\boldsymbol{B}_\mathrm{n}$ relative to a magnetic field $\boldsymbol{B}_\mathrm{ext}$ applied in z-direction (the z-component of $\boldsymbol{B}_\mathrm{ext}$ is denoted B_ext), the nuclear field either increases or decreases the electron Zeeman splitting which, in the presence of an effective nuclear magnetic Overhauser field, is then given by

$$E_{\mathrm{e,Z}} = \mu_\mathrm{B} g_\mathrm{e} J_{\mathrm{e},z} \left(B_\mathrm{ext} + B_\mathrm{n} \right) . \tag{2.24}$$

Due to the small nuclear magnetic moment ($\mu_\mathrm{n} \approx \frac{1}{2000}\mu_\mathrm{B}$), the nuclear spin ensemble is not significantly polarized in thermal equilibrium since $k_\mathrm{B}T \gg E_{\mathrm{n,Z}}$ is always given even at liquid He temperatures and in applied magnetic fields of several Tesla [Sim51].

Consequently, the mean nuclear polarization is a random variable with a Gaussian distribution proportional to the square root of the total number of nuclear spins N. As a result, in the absence of measures to polarize the nuclear spin system, the electron is subject to a randomly oriented, fluctuating magnetic field of $\Delta B_\mathrm{n} \approx (2\widetilde{A}I) \,/\, (g_\mathrm{e}\mu_\mathrm{B}\sqrt{N})$, where $\widetilde{A}$ is an average over all A_i of the nuclear spin ensemble. For self-assembled InGaAs QDs, typical values found are $\Delta B_\mathrm{n} \sim 20 - 40$ mT [Urb12].

Conversely, the electron spin is generating an effective magnetic field

$$B_\mathrm{e} = \frac{1}{g_{\mathrm{n}_i}\mu_\mathrm{n}} A_i J_{\mathrm{e},z} = \frac{1}{g_{\mathrm{n}_i}\mu_\mathrm{n}} A_i \left\langle J_{\mathrm{e},z} \right\rangle \,, \tag{2.25}$$

called the Knight field [Kni49] at the site of the ith nuclei. Again, B_e denotes the z-component of $\boldsymbol{B}_\mathrm{e}$. The Knight field was first observed in 1949 as a shift in resonance frequency in nuclear magnetic resonance (NMR) experiments on particular metals [Kni49]. While the sum of the interaction of all nuclear spins to the electron can be large in the case of a polarized nuclear spin bath (Overhauser fields up to several Tesla have been observed in self-assembled QDs corresponding to a degree of polarization of $\sim 50 - 60$ % [Bro96; Bra06b; Urb07; Mal09; Che10b; Urb12]) each nuclei is only subject to a much smaller effective magnetic field B_e. For InAs QDs, Knight fields of ± 3 mT have been reported [Lai06]. However, for a fully polarized electron, fields up to $B_\mathrm{e} \pm 20$ mT are expected [Lai06]. Figure 2.10 illustrates this interplay of the nuclear spin ensemble and electron coupled via the hyperfine interaction.

Hyperfine coupling to the fluctuating random nuclear spin system was identified as the main source of spin decoherence for electrons confined in QDs [Bur99a; Erl01; Kha02; Mer02; Coi04; Pet05; Kop05; Joh05]. On the other hand, the hf interaction can be exploited to manipulate the nuclear spin system, e.g. by repeated optical or electrical generation of spin-polarized charge carriers in the dot followed by hf-mediated transfer of angular momentum between an electron and nuclear spin. This effect, called dynamical nuclear polarization (DNP), allows to prepare the nuclear spin bath in a QD in a highly polarized, non-thermal equilibrium state which was shown to result in a narrowing of the B_n-variance by suppressing fluctuations of the Overhauser field [Gre07; Oul07; Rei08; Lat09; Vin09; Xu09]. It was shown to have a stabilizing effect on the electron spin polarization significantly extending its relaxation time [Oul07; Rei08; Xu09] and even allows to lock QD transitions to the energy of an excitation laser [Lat09]. DNP was predicted by Overhauser [Ove53] and first observed in 1953 by Carver and Slichter [Car53] in metals. Using photoluminescence measurements, DNP was first detected in a single self-assembled quantum dot in 1996 [Bro96]. Nuclear spin polarization in QDs can occur via electron-nuclear spin flip-flop processes, simultaneously exchanging the orientation of the electron spin and the spin of a nucleus. These processes are described by the contact hyperfine interaction (cf. equation 2.19). Using $\boldsymbol{J}_\mathrm{e}\boldsymbol{I} = J_{\mathrm{e},z}I_z + \frac{1}{2}\left(I^+J_\mathrm{e}^- + J_\mathrm{e}^+I^-\right)$,

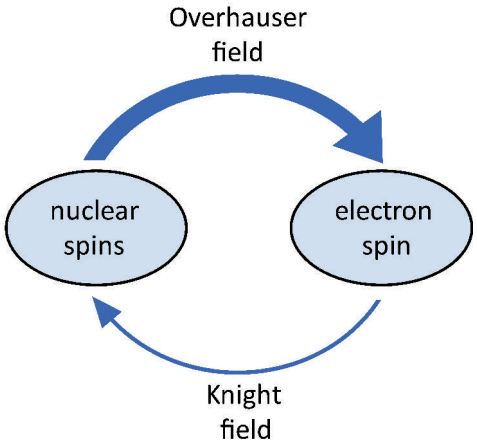

Figure 2.10. *Illustration of the hyperfine coupling in a quantum dot between a confined electron and the nuclear spins of the resident crystal atoms. The effect of the nuclear spin bath on the electron can be described as an effective magnetic field B_n, the Overhauser field. Conversely, the electron spin generates an effective magnetic field $B_\mathrm{e} \ll B_\mathrm{n}$, denoted Knight field, at the site of the nuclei.*

equation 2.20 can be rewritten as

$$H_{\mathrm{c-hf}} = \sum_i A_i \left[J_{\mathrm{e},z} I_{z,i} + \frac{1}{2} \left(I_i^+ J_\mathrm{e}^- + J_\mathrm{e}^+ I_i^- \right) \right] , \tag{2.26}$$

where $I^+ (J_\mathrm{e}^+)$ and $I^- (J_\mathrm{e}^-)$ are the nuclear (electron) spin rising and lowering operators, respectively. The dynamical part ($\propto I_i^+ J_\mathrm{e}^- + J_\mathrm{e}^+ I_i^-$) describes the electron-nuclear flip-flop processes allowing transfer of angular momentum between the electron and nuclear spin. The static part ($\propto J_{\mathrm{e},z} I_z$) accounts for the influence of the effective magnetic fields B_n and B_e on the energy of the electron and nuclear spin states, respectively.

If these hf-mediated electron-nuclear fli flop processes take place into one direction with a higher probability than into the other, repetitive occurrence leads to a non-equilibrium configuration of the nuclear spin system with more nuclear spins oriented along one particular direction generating an Overhauser field B_n significantly larger than ΔB_n. This can be achieved either by repeatedly generating spin-polarized electrons of the same polarization in the dot [Bro96; Ebl06; Tar07; Bel09] or employing intrinsic properties of the system favoring one of the two processes [Klo10a; Che11d]. The latter effect is one of the main issues addressed this thesis, investigated and discussed in detail in chapter 4.

2.3 Experimental setup and characterization of single quantum dot devices

2.3.1 Single quantum dot device design

To investigate the physical properties of a single quantum dot and the interactions of charge carriers confined in it, it is expedient to integrate the dots in a photodiode device [Dre94; Beh00; Fin01a; Zre02]. For the single QD samples investigated in this thesis, a single layer of QDs was embedded in the intrinsic region of a *n-i* Schottky photodiode formed by a heavily *n*-doped back contact and a metallic top gate as described below that form the two plates of a capacitor. This sample design allows the precise application of homogeneous electric fields along the growth direction of the dots [Sze06] enabling tuning of the QD transition energies via the quantum confined Stark effect [Fry00b; Fin01a] (cf. section 2.2.3) by applying a voltage to the sample gates . Via the applied electric fields, it is also possible to manipulate the coupling of the states to the charge carrier reservoir of the back contact enabling control of the charge state of the dot [Dre94; War00] or to manipulate the spin configuration via co-tunneling effects [McF09]. Furthermore, the tunneling time of electrons and holes from the dot to the contacts depends exponentially on the applied electric field (cf. section 2.2.3) which can be used to vary the tunnel rates over a large range, usually several orders of magnitude [Fry00a; Beh02]. Detection of the current generated by the optically created charge carriers that tunnel out of the dot and drift into the gates of the photodiode allows to perform photocurrent spectroscopy of single quantum dots [Sch98a; Beh00; Fry00c].

Figure 2.11 illustrates the device design used for the samples investigated in chapters 3, 4 and in section 5.5. The layer structure in growth direction is schematically depicted

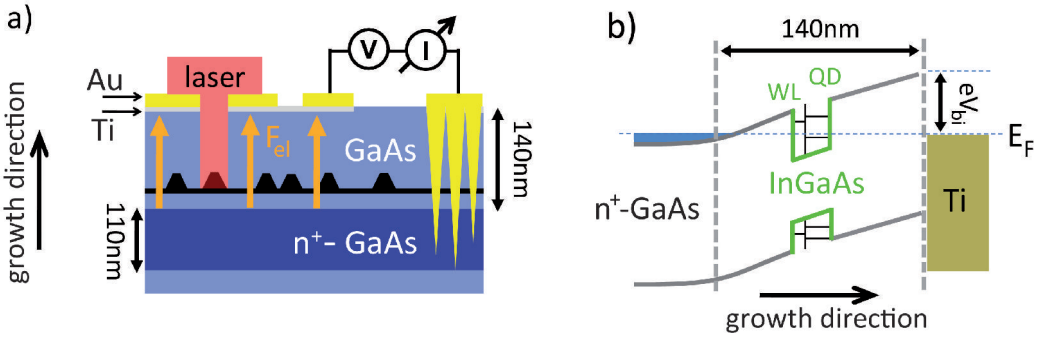

Figure 2.11. *(a) Schematic of the sample structure. A single layer of self-assembled InGaAs is embedded in the intrinsic region of a Schottky photodiode formed by a highly n-doped back contact and a metal top contact. Application of a voltage between the gates allows generation of a homogeneous electric field along the growth direction of the QDs. (b) Corresponding band diagram in growth direction in thermal equilibrium without application of electric fields.*

in figure 2.11(a) and was grown by molecular beam epitaxy as follows: First, to ensure a smooth surface for the sample growth, 300 nm of undoped GaAs were grown as a buffer layer on an intrinsic GaAs substrate of a 2 inch wafer that was rotated and kept at a nominal temperature of 670 °C. Next, a 250 nm thick superlattice consisting of 25 alternating layers of AlAs/GaAs was added (not shown in figure 2.11(a)) to prevent excess current flow in the sample. On top of this, a 100 nm thick layer of highly *n*-doped GaAs followed by a 35 nm buffer layer of undoped GaAs were deposited. In the next step, the QDs were grown via the Stranski-Krastanow mode by depositing 7 monolayers of $In_xGa_{1-x}As$ with nominally $x = 0.5$ at 600 °C without rotation. Omittance of wafer rotation in this step leads to a gradient in material coverage across the wafer resulting in a gradual variation of the quantum dot density from several hundred dots to less than one dot per μm^2 as discussed in section 2.1.2. Hence, a sample with a desired dot density suitable for single dot spectroscopy can be obtained by selecting a piece from the appropriate region of the wafer. After formation of the QDs and wetting layer, an *In-flush* technique was employed to adjust the dot height as desired. For this purpose, a thin layer of undoped GaAs partially capping the QDs was deposited onto the surface at 600 °C. The thickness of this capping layer defines the height of the dots which was chosen to be 5 nm for our samples and leads to the formation of disk-shaped QDs [Was99] as discussed in section 2.1.3. To remove the excess indium that remains on the sample surface after the QD height adjustment process, the substrate temperature was increased to 650 °C, sufficiently high to desorb the surface resident indium. After 30 s, the temperature was lowered to the initial value of 600 °C and the structure was overgrown with a 100 nm thick capping layer of intrinsic GaAs. After removal from the MBE system, the wafer was characterized in a standard macro-photoluminescence setup as described in section 2.3.2 to determine the spacial distribution of the quantum dot density. Then, a $\sim$ 3 x 3 mm^2 piece with a density of a few dots per μm^2 was cleaved from the wafer. In the first processing step, an Ohmic contact was established to the buried *n*-doped GaAs layer with a photolithographically defined contact pad of $\sim$ 3 x 0.3 mm^2 size close to one edge on top of the sample followed by thermal annealing as indicated in figure 2.11(a). The metal pad was formed by subsequent electron beam evaporation of germanium (13 nm), gold (33 nm), nickel (10 nm), and gold (200 nm). After lift off, thermal annealing was done at 420 °C for 60 s under vacuum. Next, the top contact was photolithographically defined at the opposite side of the sample surface. After a cleaning procedure consisting of exposure to an oxygen plasma for 180 s followed by a 30 s dip into 37 % HCl solution, a 5 nm thick layer of titanium is evaporated, forming a Schottky contact. The 5 nm Ti layer is thick enough to provide a homogeneous electric field across the sample structure when a voltage is applied between top and back gate (sheet resistance $\sim$ kΩ, measured at $\sim$ 1 cm distance) and thin enough to allow optical access to the quantum dots (transmissibility $\sim$ 50 % at $\lambda \approx 900 - 1000$ nm) as schematically illustrated in figure 2.11(a). The resulting band diagram of the sample structure in growth direction without the application of any electric fields is sketched in figure 2.11(b). When a metal and a semiconductor are brought into contact, the

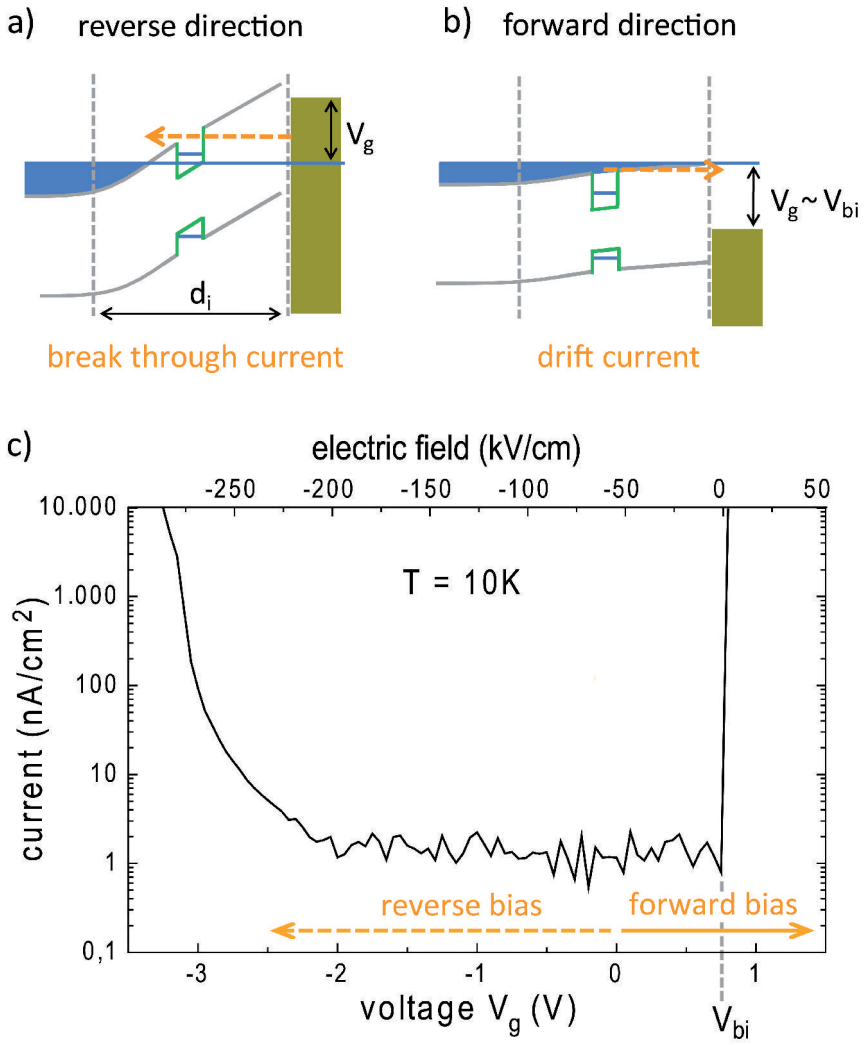

Figure 2.12. *Band diagram of a Schottky diode containing QD illustrating the effect of a voltage applied in (a) reverse and (b) forward direction. (c) Typical current-voltage characteristic of a single quantum dot Schottky photodiode structure as investigated in this thesis. An abrupt onset of the diffusion current in forward direction is observed at V_g =0.75 V when the applied electric field is compensating the build-in field. In reverse bias, the leakage current is ~ 1 nA/cm until $V_g \approx -2.5$ V and increases rapidly for higher negative voltages. The direction of the current is indicated by the dashed arrows.*

difference in their work functions causes a charge flow until thermal equilibrium is established in the system and the Fermi levels are lined up [Sze06]. This leads to a built-in potential across the intrinsic region of the structure even without any externally applied electric fields. Except for a very low leakage current, the band offset $e \cdot V_{\mathrm{bi}}$ at the GaAs/Ti interface, the so-called Schottky barrier, prevents current flow through the device. Application of electric fields across the structure allow to tune the band structure, effectively lowering or raising the potential barrier.

A useful measure for the quality of the Schottky photodiode device is the current-voltage characteristic of the structure as presented in figure 2.12(c). To record this curve, the current through the device was measured as a function of the applied voltage to the gates V_g while the device is kept in the dark at $T \approx 10$ K. Over a range of applied bias from $V_g \approx -2.5$ V to 0.75 V, only a small leakage of $I_{leak} \approx 1$ nA/cm^2 stemming from electrons tunneling from the Ti to the n-doped back contact is found. This low leakage current is very crucial for the experiments performed as a high current flowing through the sample might influence the results of the measurements, e.g. by changing the charge state of the dot. At $V_g \approx 0.75$ V, a current onset is observed as the diode becomes highly conductive and a diffusion current starts to flow. This situation, where the applied electric field is compensating the built-in field at $V_g = V_{bi}$ is illustrated in figure 2.12(b). When the diode is operated in reverse bias, current flow should be strongly blocked and only a small leakage current is expected. However, for very high applied negative voltages $V_g < -2.5$ V, tunneling of the charge carriers through the barrier becomes possible and a steep increase of a break-through current is observed as illustrated in figure 2.12(a).

Assuming that the voltage drop across the intrinsic region is linear, the electric field between the top and the back gate and, hence, at the site of the QD is given by

$$F = \frac{V_g - V_{bi}}{d_i}, \tag{2.27}$$

where d_i denotes the thickness of the intrinsic region. This relation was used to calculate the electric field values on the upper scale of figure 2.12(c) corresponding to the applied voltages at $d_i = 140$ nm. The interested reader can find a more detailed discussion of the properties of Schottky diodes in [Sze06].

To facilitate optical access to single QDs, the semi-transparent Ti layer is covered with an 200 nm thick, opaque gold film in which apertures with a diameter of 1 μm are opened as illustrated in figure 2.11(a). The fabrication process of these apertures is illustrated in figure 2.13(a): First, a droplet of an aqueous suspension containing polystyrene balls with a diameter of 1 μm (Polybead 1 Micron Microspheres 07310-15, Polysciences, Inc.) is deposited on the sample surface where the area that is not part of the titanium top gate is still protected by photoresist. Then, the liquid was dried off by nitrogen gas flow resulting in a randomly distributed ensemble of polystyrene balls on the surface. Next, a 20 nm Ti adhesion layer followed by the 200 nm opaque Au film were evaporated. After metalization, the microspheres were mechanically removed with a paintbrush leaving behind perfectly round apertures as demonstrated in figure 2.13(d). As can be seen in figures 2.13(a) and (b), these apertures are then randomly distributed over the gold shadow mask. The density of the apertures can be varied by changing the dilution of the aqueous suspension prior to the procedure. The characteristic U-shaped layout of the top gate that can be seen in figure 2.13(b) will be addressed in detail in chapter 5. The image shows the terminated end of a coplanar stripline that is designed

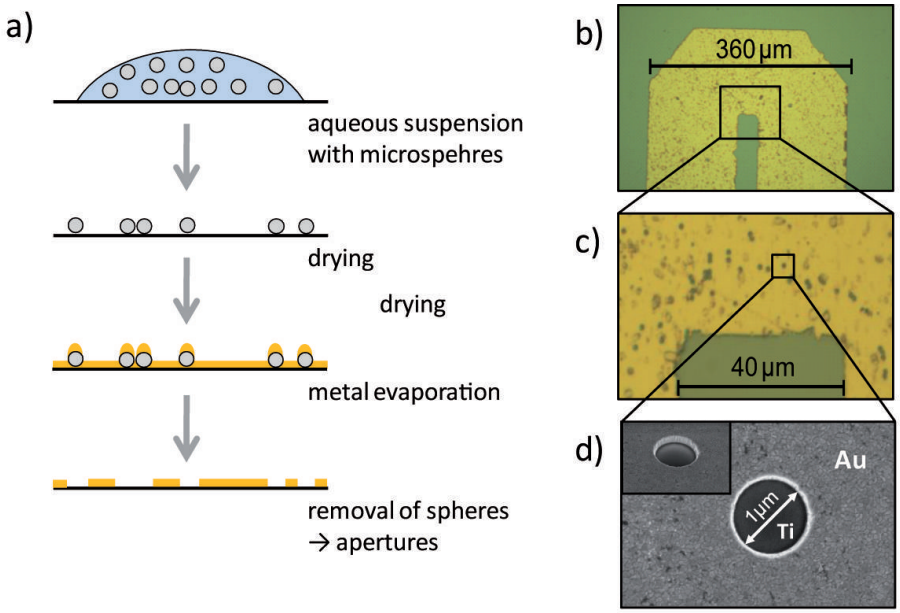

Figure 2.13. *(a) Illustration of the individual steps in the fabrication process to generate round apertures in the opaque gold film covering the semi-transparent titanium top gate. (b) and (c) Optical microscope images of the sample surface with different magnification factors. In (c), the randomly distributed apertures are clearly visible. (d) Scanning electron microscope image of a single aperture showing the high quality of the edge and the roundness of the aperture [Mue10].*

to serve as a microwave delivery system in addition to its function as an electrical gate and a shadow mask and enables generation of an ac magnetic field in the vicinity of the short for potential future spin manipulation experiments (see chapter 5). The data presented in chapter 3 and 4 were obtained using top gate structures as presented in figure 2.13(b) albeit without the application of microwaves. The effects of microwave application to the stripline on the photodiode device and the photoluminescence spectra are presented in section 5.5.

2.3.2 Experimental methods

Two experimental techniques were used predominantly in this thesis to examine the physical properties of single quantum dots embedded in a Schottky photodiode and investigate interactions of charge carriers confined in the dot with each other and the environment: Photoluminescence (PL) and photocurrent (PC) spectroscopy. The working principle of both methods is schematically illustrated in figure 2.14.

To perform photoluminescence measurements, the band structure of the device is tuned to or close to flatband by applying an electric field across the sample structure

via the top and back gate that compensates for the built-in field of the device. In this bias regime, charge carriers that are generated optically via excitation above the bulk band-gap or within the wetting layer continuum states relax into the dot on a picosecond timescale [Hei97], populating the lowest unoccupied states. Holes and electrons confined in the QD recombine radiatively within $\sim$ 1 ns [Kre05d], emitting a photon that is red-shifted from the excitation allowing to spectrally separate it from the excitation laser reflected from the sample surface and to detect it. Measuring the polarization of the emitted light reveals information about the spin polarization of the recombined electrons and holes [Bay02b; Kro04] whereas the photon energy is determined by the size, shape, and composition of the QD that define the confinement potential as well as by the interactions between the charge carriers within the dot, the bulk material and the externally applied electric or magnetic fields [Woj97; Haw98; Sch98b; Was99; Bay00; Dek00; War00; Har00; Fin01c]. Detecting the emitted light over the whole relevant energy range – recording a PL spectrum – under variation of parameters like applied electric or magnetic fields or excitation power allows to reconstruct the energy level structure of the QD and to obtain detailed information about its physical properties as well as interactions of the confined charge carriers (cf. section 2.4). Recombination and interaction times can be determined from time-resolved detection of the PL signal [Dek00; Kre05d].

The excited states of the QD shell structure can be examined by photoluminescence excitation (PLE) measurements where resonant pumping of the excited QD levels is employed [Hei97; Lem01; Hei09a]. In this case, photoluminescence is only generated if the energy of the excitation laser matches the transition energy of the QD state making it possible to map out the excited QD level manifold. When ground states are resonantly excited, the wavelength of the exciting and emitted light are identical and can not be spectrally separated anymore. To perform this type of measurements (called resonant fluorescence), the excitation laser is usually suppressed by using polarizers with an orthogonal orientation in the detection path [Fla09; Nic09; Fal10].

For photocurrent spectroscopy, the bandstructure of the sample structure is tuned such that the radiative lifetime of confined charge carriers is longer than the tunneling time out of the dot to the corresponding contacts. Electrons and holes of optically created excitons in the QD are rapidly separated by the high applied electric field and tunnel through the bulk GaAs barrier into the electric gates generating a detectable photocurrent suitable for single quantum dot PC spectroscopy [Sch98a; Beh00; Fry00c; Fry00a]. In PC measurements, resonant excitation of the QD states is used, where the current signal is monitored as a function of the excitation energy as the laser is tuned in and out of resonance with the QD transitions. Alternatively, the laser can be kept at a fixed wavelength and the QD levels are shifted instead, e.g. using electric fields exploiting the quantum confined Stark effect [Fry00b; Fin01a] (cf. section 2.2.3). As the voltage applied to the sample can be controlled very precisely, this latter technique allows tuning in very fine steps and was almost exclusively used for the PC measurements presented

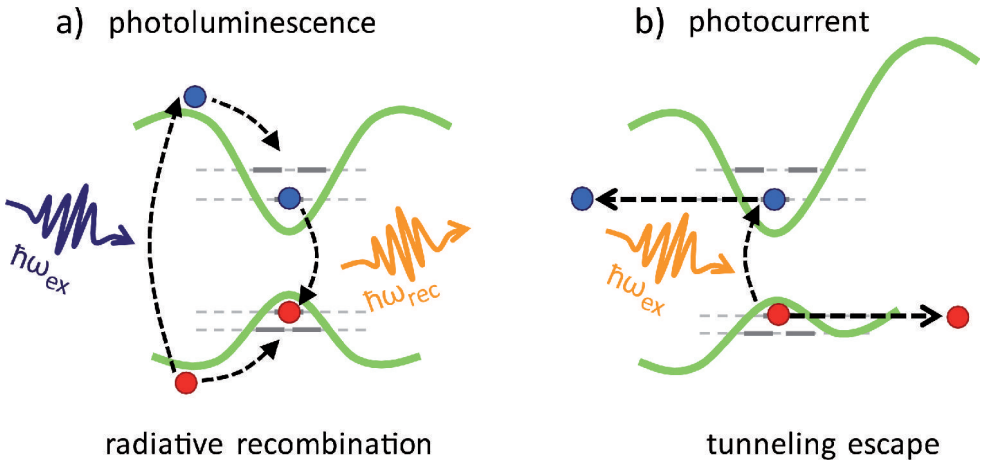

Figure 2.14. *Basic principle for two spectroscopy techniques to investigate the properties of quantum dots: photoluminescence and photocurrent. For photoluminescence (a), the device is tuned to flatband and charge carriers generated in the bulk or wetting layer states first relax into the dot and then recombine radiatively generating a luminescence signal. For photocurrent (b), the band structure is tuned such that the tunneling time of charge carriers from the dot to the corresponding electrodes is shorter than the radiative lifetime. In this case, optical generation of excitons in the QD results in a current which can be detected.*

in this thesis. While photoluminescence is probing the *emission* of the quantum dot, photocurrent is a measurement of its *absorption* spectrum.

Typically, experiments on QDs are performed at temperatures below 50 K where the thermal energy is significantly smaller than the energy splitting between the QD levels. Moreover, a high spatial resolution is needed to carry out measurements on single dots. A typical setup to perform such PL and PC measurements that also allows the application of magnetic fields is sketched in figure 2.15. Light from the excitation laser is coupled into a single mode optical fiber and guided to an optical setup that is mounted on top of a bath cryostat cooled with liquid helium and equipped with a superconducting solenoid magnet system. Since helium has a boiling point of 4.2 K, such a bath cryostat is very suitable and widely used to provide the low temperatures needed for single QD spectroscopy. On top of the cryostat, the light is coupled out of the fiber, passes a set of polarization optics and is sent down free-space to the bottom of the cryostat through an optical window via a beamsplitter into the sample space that is kept under vacuum. At the bottom, the sample is mounted on top of a x, y, z-piezo-positioner stack placed under an objective. The positioners are operable at low temperatures and high magnetic fields allowing to precisely focus the laser beam on the sample and scan the excitation spot across the surface. Together with the objective, the positioners form a cryo-microscope. The emitted light is collected via the same objective and sent back to the optical setup on top of the cryostat where it is coupled into a multimode optical fiber through the orthogonal path of the beamsplitter and guided to a spectrometer.

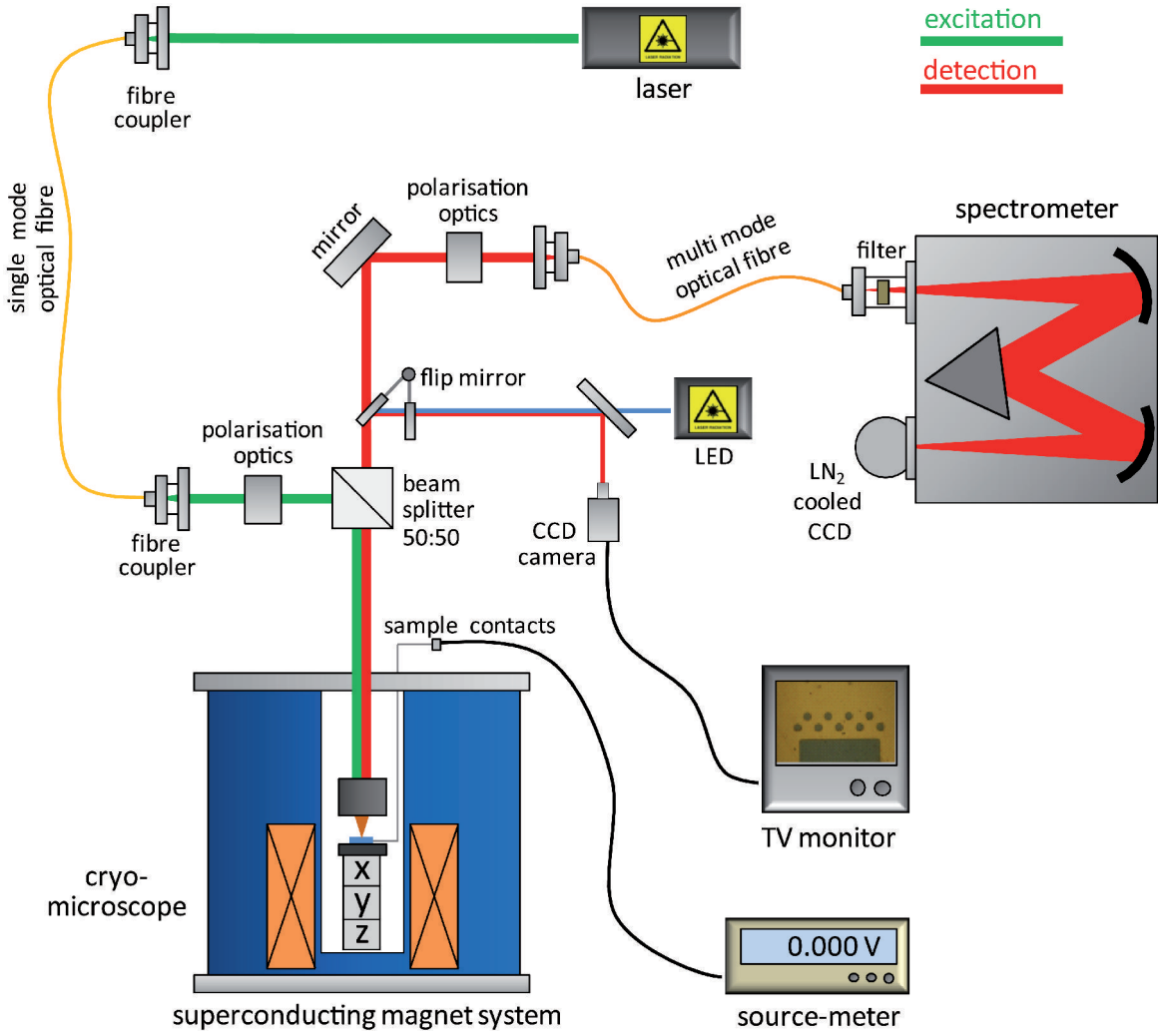

Figure 2.15. *Schematic diagramm of a typical magneto-photoluminescence setup. The sample is placed in a cryo-microscope formed by an objective and a set of low-temperature piezo positioners which is inserted into a liquid helium bath cryostat with a superconducting magnet system. The excitation beam is guided down to the sample free-space via a 50:50 beamsplitter and focused on the surface. The emitted light is collected with the same objective used for excitation and guided to a spectrometer through the orthogonal path of the beamsplitter. Parallel to the light path, a set of cables is guided down the cryostat to contact the electrical gates of the sample and control the positioners. Graphic design adapted from [Hei09a].*

Parallel to the light path, a set of wires is going down into the sample space entering the cryostat at the top via a vacuum feedthrough next to the optical window. They are used to electrically contact the sample, control the piezo-positioners as well as to read out a temperature sensor and operate a resistive heater that are both integrated into the microscope. To image the surface of the sample for alignment purposes, a mirror can be flipped into the detection path after the beamsplitter as indicated in figure 2.15. A 855 nm diode is used to illuminate the sample. The image, which is recorded with and a CCD camera and displayed on a TV monitor, allows to identify individual apertures and focus the spot of the excitation beam on a specific one with high precision.

For photocurrent measurements, excitation of the sample is identical to PL experiments while no detection of luminescence is needed. On the room temperature side of the electric sample circuit, a current meter is added to the voltage source. Since the photocurrent signal to detect is quite small (typically $\sim$ 10 pA, see chapters 3 and 4), shielded cables are used inside and outside the cryostat wherever possible to reduce noise.

Details on the equipment and specifications of the setup actually used in this thesis will be presented in section 3.1.

2.4 Basic characterization of single quantum dots

2.4.1 Single Quantum Dots

In this section, the terminology of optical transitions in a quantum dot is introduced. Typical spectra obtained from single QD spectroscopy experiments are presented and optical characterization as initially performed for every sample is demonstrated exemplarily. The corresponding measurements on the actual samples investigated in this thesis are given in the respective chapters.

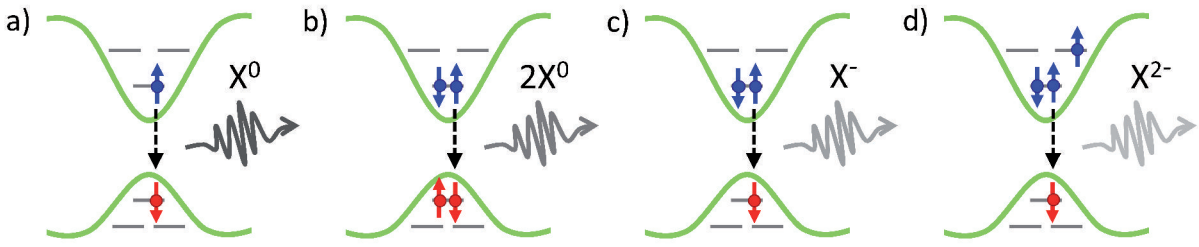

Figure 2.16. *Schematic overview of different exciton complexes $mX^{\pm n}$ in a single QD. In this terminology m denotes the number of excitons and $\pm n$ the net charge present in the dot: (a) neutral exciton X^0, (b) neutral bi-exciton $2X^0$, (c) singly negatively charged exciton X^-, (d) doubly negatively charged exciton X^{2-}, and so on.*

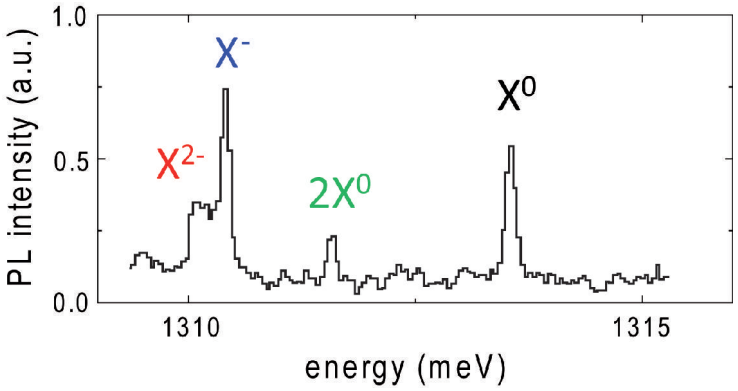

Figure 2.17. *Typical photoluminescence spectrum of a single self-assembled QD after non-resonant optical excitation. Interaction between the charge carriers of the different exciton complexes leads to a characteristic renormalization of the transition energy allowing to spectrally resolve the individual states. Adapted from [Hei09a].*

Figure 2.16 shows a selection of exciton complexes formed by different configurations of charge carriers confined in the dot. The different states are denoted $mX^{\pm n}$ where m indicates the number of excitons and $|\pm n|$ the number of excess electrons $(-)$ or holes $(+)$ in the dot. Different exciton states generally have different transition energies due to inter-particle interactions such as exchange coupling and Coulomb interaction (cf. section 2.2) and can be spectrally resolved [Bay00; Dek00; War00; Fin01c; Fin01d] as can be seen in figure 2.17. The energy shift with respect to the neutral exciton state X^0 is referred to as renormalization energy. The characteristic dependence on excitation power and applied electric field can be employed to identify the individual resonances.

Figure 2.18 presents the photoluminescence response of a single QD following non-resonant optical excitation in the wetting layer detected in an energy window of $1321 - 1331$ meV as a function of applied electric field from $8 - 32$ kV/cm. The results are depicted in a color-coded image plot yielding a characteristic energetic fingerprint for each dot. For electric fields > 30 kVcm, no PL signal is detected as tunneling of the charge carriers from the dot to the electric contacts takes place on a timescale much shorter than the excitonic radiative lifetime, thus, quenching photoemission. Towards flatband condition, for electric fields < 8 kV/cm the drift current in forward direction through the device sets in (cf. section 2.3.1) disturbing the PL signal. In between, emission from different excitonic states is observed. Each state emits only within a characteristic electric field range and exhibits a pronounced Stark shift for all lines that leads to an increase in transition energy for decreasing electric field as discussed in section 2.2.3 [Fry00b; Fin01a].

The observed spectrum can be interpreted as follows: As the electric field is lowered below 30 kV/cm, the tunneling times of the charge carriers from the dot becomes comparable to the radiative recombination time of ~ 1 ns [Kre05d] and luminescence sets in at 1328 meV. In this field regime, the QD is strongly decoupled from the back contact. Optically generated charge carriers relax into the ground state of the dot and

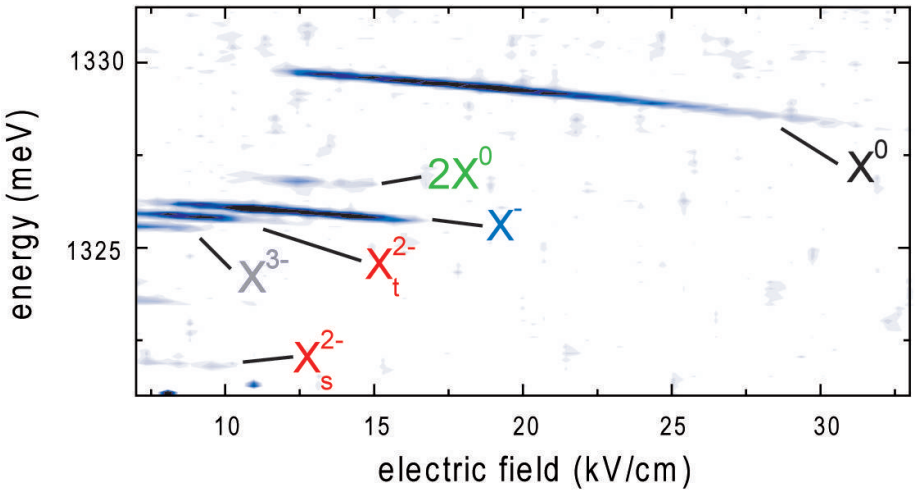

Figure 2.18. *Photoluminescence signal of a single self-assembled QD under wetting layer excitation. The color-coded image plot presents the spectrally resolved PL intensity as a function of the applied electric field. The characteristic electric field dependence allows to identify the individual charged exciton complexes. The quantum confined Stark effect [Fry00b; Fin01a] can clearly be observed. Adapted from [Hei09a].*

recombine radiatively giving rise to emission from the X^0 state. As the electric field is lowered to 16 kV/cm, the lowest orbital states of the QD approach the Fermi level of the back contact and an electron can tunnel into the dot and luminescence from the negatively charged exciton X^- emerges at 1326 meV while simultaneously X^0 emission decreases. Coulomb repulsion prevents the addition of a second electron until further reduction of the applied electric field overcompensates for this effect at 12 kV/cm. At this point, a second electron can enter the dot from the Fermi sea of the *n*-doped back contact and X^{2-} emission sets in at 1326 meV. In the same way, individual electrons can subsequently be added to the dot. This working principle allows for full control of the QD charge state via the application of the electric field. The relatively wide regions of co-existence of different charge states are a result of the comparatively thick tunnel barrier of 40 nm between the QD and the back contact and the statistical nature of the tunneling process as can also be seen in [Fin01b]. Much sharper transitions have been observed for thinner barriers (25 nm: [War00]).

Closer examination of the spectra in figure 2.18 reveals a resonance at 1322 meV with the same electric field behavior as the X^{2-} state discussed above at 1326 meV, however, emitting at much lower intensity. Both emission lines at 1326 meV and 1322 meV can be attributed to the doubly negatively charged exciton state X^{2-}. The splitting into two states with different PL intensities can be understood taking into account spin effects. X^{2-} consists of one hole, two paired electrons in the *s*-shell and one electron in the *p*-shell. In the final state after radiative recombination of the hole with the *s*-shell electron of opposite spin orientation the two remaining electrons can have either parallel or anti-parallel spin configuration, i.e. form a singlet and a triplet. Since the emission

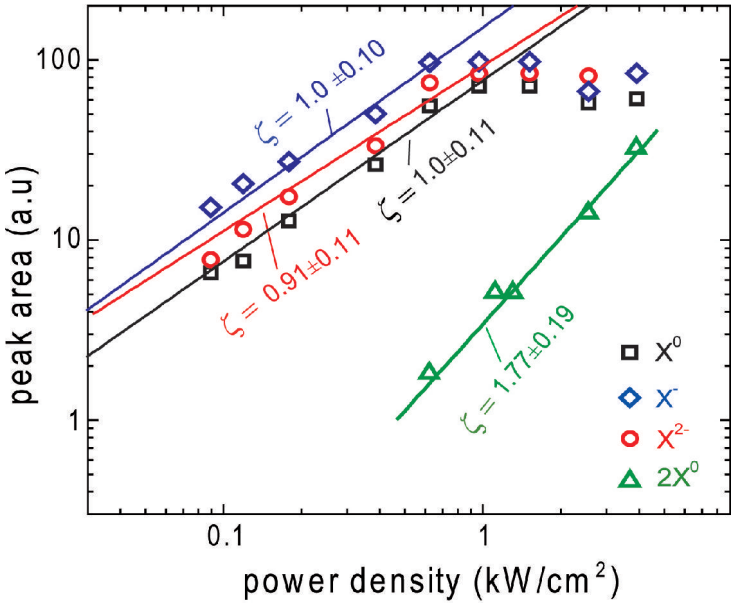

Figure 2.19. *Dependence of the PL emission intensity of the individual states presented in figure 2.16 on the optical excitation power. Plotted is the peak area of the PL resonances as a function of the power density on a log-log scale. The emission from excitonic states increases linearly with power until saturating for high powers. For the bi-exciton, a characteristic quadratic power dependence is observed. Adapted from [Hei09a].*

energy is given by the energy difference between initial and final state, this leads to two distinct emission lines labeled X_s^{2-} (singlet) and X_t^{2-} (triplet) split by twice the exchange interaction of the *s*- and *p*-shell electron, the energy difference between the two possible final states [Woj97]. The difference in intensity arises from the threefold degeneracy of the triplet state in contrast to the onefold degeneracy of the singlet state.

Additional information allowing further interpretation of the PL spectra observed can be obtained from excitation power-dependent measurements. Figure 2.19 presents the photoluminescence intensity of different exciton states expressed by the integrated peak area of the emission lines as a function of the power density used to excite the QD. For single exciton states, a linear increase of the PL signal with increasing power is expected due to the random nature of the carrier capture process [Fin01c; Fin01d]. However, for multi-exciton complexes, several electron hole pairs have to be captured within their radiative lifetime in the dot. As a result, a quadratic power dependence is expected for the bi-excitonic states. For very high excitation powers, when the repopulation rate of a state becomes comparable to the its lifetime, a further increase in power does not lead to a higher PL intensity and the signal saturates. The power dependencies presented in figure 2.19 are fitted (solid lines) using

$$I_{\mathrm{PL}} = b \cdot P_{\mathrm{exc}}^{\zeta}\,, \tag{2.28}$$

where I_{PL} is the peak area and b a scaling constant. As predicted, a linear dependence is

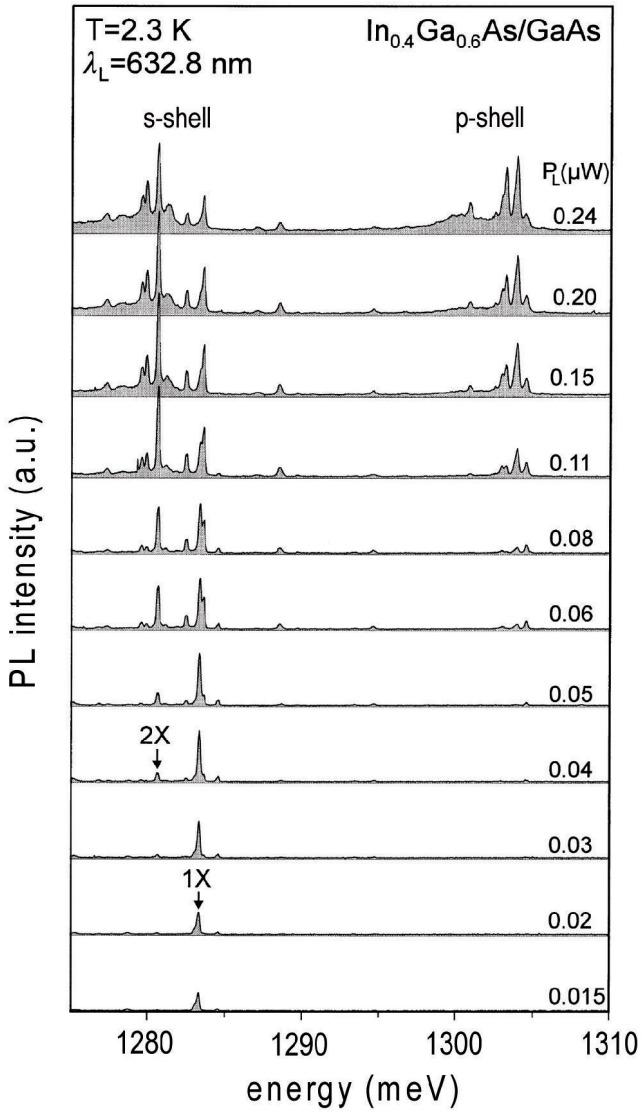

Figure 2.20. *Emission spectrum of a single QD recorded at different excitation powers. With increasing power, more resonances appear as carrier capture takes place faster than radiative recombination in the dot. For very high powers even emission from the p-shell, occurring* ≈ 25 *meV above the s-shell transitions, can be observed. Adapted from [Fin00].*

found for X^0, X^-, and X^{2-} and an exponent of $\xi = 1.77 \pm 0.19$ for the neutral bi-exciton $2X^0$.

For sufficiently high excitation powers, emission from *p*-shell recombination can be observed as presented in figure 2.20. As for the *s*-shell spectrum, recombination from *p*-shell states also results in a manifold of lines within an energy band of about 5 meV yielding a rich fine structure stemming from different multi-particle complexes.

2.5 Single quantum dot molecules

If two quantum dots are positioned at a close distance, interactions between the individual dots take place and, in case these effects are strong enough, a coupled system is formed [Bay01; Ort03; Ort04; Kre05c; Kre05b; Bra06a; Sti06; Sch08]. Following the practice of referring to QDs as 'artificial atoms', such a system formed by a pair of coupled QDs is commonly called 'artificial molecule' or 'quantum dot molecule' (QDM). Besides providing the opportunity to study coupling effects in low-dimensional system, QDMs represent a first step towards scalability of quantum information processing architectures based on QDs as the fundamental building blocks. Coupled low-dimensional nanostructures with tunable interaction strength were already realized in the late 1980's from double quantum well heterostructures [Via87; Gol88; Zre90; Sou99]. The first coupled system composed of QDs was achieved in 1997 using dots fabricated via the cleaved edge overgrowth (CEO) method [Sch97]. This technique [Pfe90] allows for sub-nanometer precision in the positioning of the QDs. The molecules were fabricated using a twofold application of CEO [Sch97]. However, due to its inherent complexity and the difficulty to implement schemes for tuning of the coupling, until now, CEO has not been established as a widely used method for fabrication of QDMs. A more practical way is offered by strain-driven self-organization of QDMs that takes place when two layers of QDs are grown sequentially separated by a thin barrier. Formation of the dots in the upper layer occurs preferentially on top of the islands underneath due to their strain field that is still present on the surface [Gol85; Xie95; Sol96]. If the growth parameters (separation between the dot layers, substrate temperature, ...) are chosen accordingly, a very high efficiency of this process with near unity stacking probability can be achieved allowing to generate a large number of QDMs at once [Xie95; Kre05a; Bru03]. Furthermore, they can easily be embedded in an electrically active structure analogously to the single QD samples discussed in section 2.3. The QDMs examined in this work were fabricated by molecular beam epitaxy growth of double QDs layer structure at the Walter Schottky Institut in the framework of the PhD thesis of *H. Krenner* [Kre05a] where details on the growth parameters as well as a comprehensive overview of the properties of quantum dot molecules and related effects can be found.

2.5.1 Basic properties of self-assembled quantum dot molecules

The QDMs examined in this work were composed of two layers of self-assembled InGaAs quantum dots grown by molecular beam epitaxy in the Stranski-Krastanow mode [Str37; Str38] as discussed in section 2.1. First, a single layer of InGaAs was grown on a GaAs substrate. Next, the structures were overgrown with a GaAs capping layer thin enough for the strain field caused by the InGaAs QD underneath not to be fully relaxed and still present at the surface. As a result, self-assembly of the QDs in the following layer takes place preferentially on top of the dots in the first layer underneath since the surface potential for indium adatoms is modified by strain field

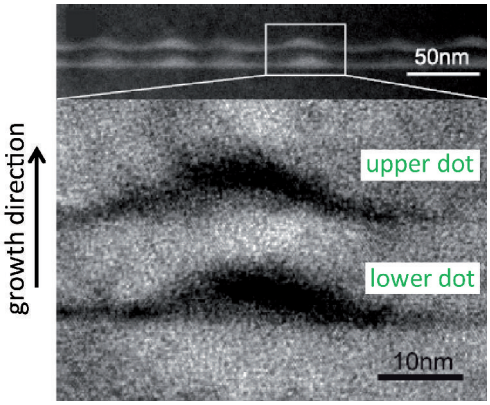

Figure 2.21. *Cross-sectional transmission electron microscopy image of a double QD layer. Upper panel: Two sequentially grown layers of quantum dots. If the separation layer is thin enough, self-assembly of the QDs in the second layer takes place preferentially directly on top of the dots in the layer underneath due to their strain field. Lower panel: Enlarged view of a single quantum dot molecule formed by a pair of vertically stacked self assembled QDs. The dot grown first is referred to as lower dot, the one grown second on top of the first one as upper dot. The separation layer for the QDMs examined in this thesis was 7 nm. Adapted from [Kre05a].*

preservation, forming a minimum directly above the overgrown QDs [Gol85; Xie95; Sol96]. An overview of this effect of strain driven self-alignment can be found e.g. in Refs. [Sta04; Kre05a]. The high efficiency of this process can be seen in the upper panel of figure 2.21 where a cross-sectional transmission electron microscopy image of such a double QD layer structure is presented. More detailed investigations on the growth of self-aligned multilayer structures showed that for separation layers < 15 nm, a close to unity stacking probability can be achieved [Xie95; Kre05a; Bru03]. To obtain such high stacking efficiencies, the diffusion length of the In adatoms of the surface which can be controlled by the substrate temperature has to be equal to or greater than the inter-dot distance in the seed layer to allow for sufficient material transport to the nucleation sites. [Kre05a]. Repeated application of this technique can be used to generate vertically aligned columns of QDs [Bru03]. The lower panel of figure 2.21 shows an enlarged image of a single pair of vertically stacked QDs forming a quantum dot molecule. The QD belonging to the first layer is referred to as 'lower dot' and the one being part of the second layer 'upper dot'. The $In_xGa_{1-x}As$ QDMs investigated in this thesis were grown with a GaAs separation layer thickness of 7 nm and an In content of nominally $x = 0.5$.

Figure 2.22(a) presents the cross section of the sample structure used for the investigation of single QDMs in this work. The device features the same basic design as the single QD sample shown in figure 2.11: The QDM layer is embedded in the intrinsic region of a Schottky photodiode formed by a highly n-doped back contact and a metal top contact. Application of a voltage between the gates allows the generation of homogeneous electric fields along the growth direction that can again be used to control the charge state of the QDs, the tunneling behavior of electrons and holes as well as the interaction

between the dots within the molecule. The corresponding band diagram is depicted in figure 2.22(b).

Figure 2.23 presents a selection of different excitonic states that can be populated in a QDM illustrating the increased complexity of a coupled QD system as compared to a single dot. For the case of a neutral exciton in a QDM, electron and hole can either be both confined in the same dot forming a direct exciton (X^0_{dir}) equivalent to the neutral exciton in a single QD or they can be spatially separated and located in different dots of the molecule forming a so-called indirect exciton (X^0_{ind}) as depicted in the upper panel of figure 2.23. The center of the electron and hole wave function in indirect excitons are separated by a distance d mostly determined by the GaAs layer between the dots which is much larger than the displacement for direct excitons caused by the asymmetric confinement potential in growth direction with the electron located at the base of the dot and the hole at its In-rich apex [Fry00b] and strain-induced piezo-electric fields [San00; Pat00]. Consequently, indirect excitons carry a much larger intrinsic dipole moment $\boldsymbol{p}_{int} = e\boldsymbol{d}$. As a a result, they couple much stronger to electric fields and exhibit a stronger Stark shift $\Delta E_{\text{QCSE}} = E_0 + \boldsymbol{p}_{int} \cdot \boldsymbol{F} + \beta \boldsymbol{F}^2$ than direct excitonic states [Mil84; Fry00b; Fin01a; Kre05b]. The different magnitude of the quantum confined Stark effect for direct and indirect excitons allows to distinguish them in experiment and also to control the detuning between them making it possible to tune them in and out of resonance simply by application of electric fields. The lower panel of Figure 2.23 shows three different configurations of the singly negatively charged exciton X^-. The number of states is larger than for the X^0 due to the multiple possible combinations of charge distribution and spin orientation. However, as only effects related to the neural exciton states in QDMs are investigated in this thesis, no further details on charged states are presented here. A comprehensive overview on that topic can be found in Ref. [Kre05a].

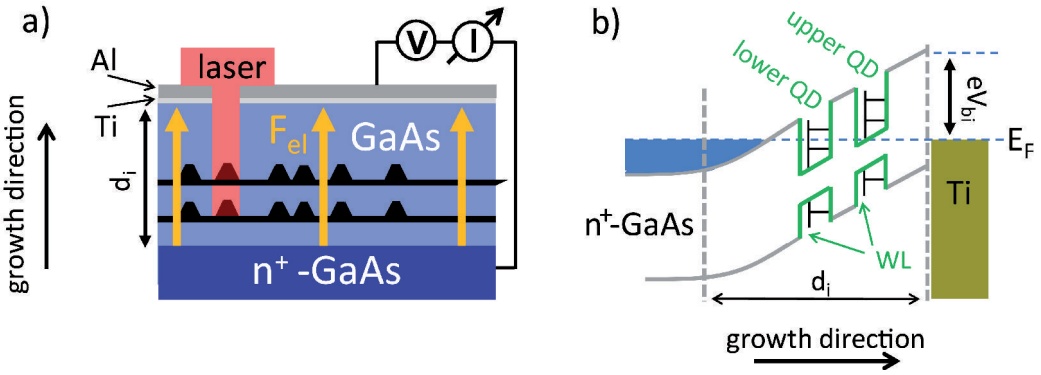

Figure 2.22. *(a) Schematic cross section of the sample structure. A double layer of self-assembled InGaAs QDs grown close enough to form quantum dot molecules via strain-driven vertical stacking is embedded in the intrinsic region of a Schottky photodiode made of a highly n-doped back contact and a metal top contact. (b) Corresponding band diagram in growth direction without application of electric fields illustrating the confinement potential for excitons generated by the quantum dots.*

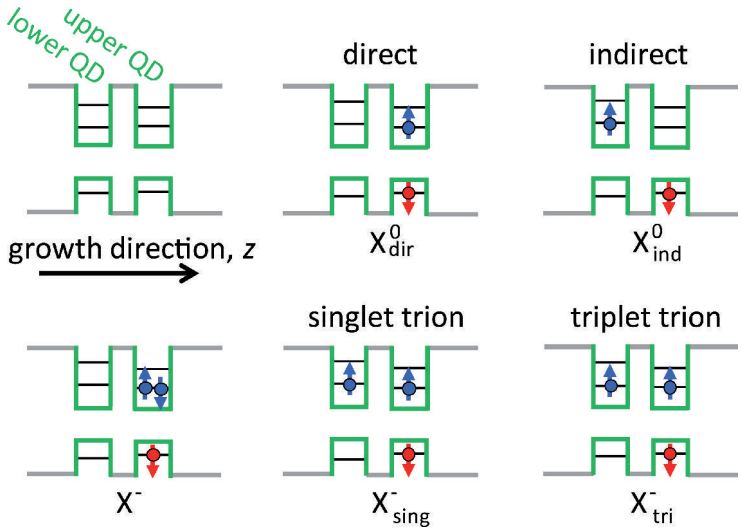

Figure 2.23. *Illustration of different excitonic states in a quantum dot molecule. The arrows indicate the spin orientation of electrons (blue) and holes (red). For the neutral exciton state X^0, electron and hole can either both be located in one of the two dots (direct) or spatially separated, confined in different dots of the molecule (indirect). For the singly negatively charged trion state X^-, different configurations of the charge distribution and spin orientation are possible.*

Coupled states

As the two dots in a quantum dot molecule are only separated by a thin barrier, in our case 7 nm of GaAs between the InGaAs dots, interactions between states of the individual dots can become of significant strength depending on their relative energy detuning resulting in the formation of a coupled system. This effect leads to an avoided crossing behavior, commonly referred to as 'anticrossing', as two interacting states are tuned in and out of resonance. Here, it is discussed exemplarily for the case of tunnel-coupling between the direct and the indirect neutral exciton state of a QDM. This coupling mechanism results from quantum mechanical tunneling of electrons from one dot to the other through the barrier. If the levels are aligned, resonant tunneling can take place, strongly coupling the two states and leading to a coupled system with new eigenstates [Kre05b]. Experimentally, the detuning between the two states $\Delta_{\mathrm{dir-ind}}$ can be tuned via the application of electric fields due to the strongly different Stark shift of direct and indirect excitons.
In the absence of coupling, the eigenstates of the direct and indirect neutral exciton, Ψ_{di} and Ψ_{ind}, respectively, satisfy the Schrödinger equation

$$H^0\,\Psi_{\mathrm{m}} = E_{\mathrm{m}}\,\Psi_{\mathrm{m}} \quad , \qquad \mathrm{m} = \mathrm{direct}, \mathrm{indirect} \tag{2.29}$$

with the uncoupled Hamiltonian H^0 and the corresponding eigenenergies E_{dir} and E_{ind}, respectively. If the two states are interacting via a coupling κ, the new eigenstates of the system Φ_i can be written as linear combinations of Ψ_{dir} and Ψ_{ind}

$$\Phi_i = \alpha\Psi_{\mathrm{dir}} + \beta\Psi_{\mathrm{ind}} \quad \text{with} \quad |\alpha|^2 + |\beta|^2 = 1\,. \tag{2.30}$$

Using first order perturbation theory, the coupled Hamiltonian $H_\mathrm{c} = H^0 + \kappa$ can be written as [Kre05a]

$$H_\mathrm{c} = \begin{pmatrix} E_{\mathrm{dir}} & \kappa_{dir-ind}/2 \\ \kappa^*_{ind-dir}/2 & E_{\mathrm{ind}} \end{pmatrix}\,. \tag{2.31}$$

Here, $\kappa_{\mathrm{dir-ind}}$ and $\kappa^*_{\mathrm{ind-dir}}$ are the coupling matrix elements given by $\kappa_{\mathrm{dir-ind}} = \kappa^*_{\mathrm{ind-dir}} = \langle\Psi_{\mathrm{dir}}\,|\kappa|\,\Psi_{\mathrm{ind}}\rangle$. The eigenvalues $E_\pm$ of the coupled system H_c can be expressed in terms of the detuning between the uncoupled states $\Delta_{\mathrm{dir-ind}} = E_{\mathrm{dir}} - E_{\mathrm{ind}}$. They read

$$E_\pm = E_{\mathrm{dir}} + \frac{1}{2}\left(\Delta_{\mathrm{dir-ind}} \pm \sqrt{\Delta^2_{\mathrm{dir-ind}} + \kappa^2_{\mathrm{dir-ind}}}\right)\,. \tag{2.32}$$

The eigenstates $\Phi_\pm$ are symmetric and antisymmetric linear combinations of the uncoupled states Ψ_{dir} and Ψ_{ind} forming bonding (Φ_+) and antibonding (Φ_-) molecular states

$$\Phi_+ = \frac{1}{\sqrt{2}}\left(\Psi_{\mathrm{dir}} + \Psi_{\mathrm{ind}}\right) \tag{2.33}$$

$$\Phi_- = \frac{1}{\sqrt{2}}\left(\Psi_{\mathrm{dir}} - \Psi_{\mathrm{ind}}\right)\,. \tag{2.34}$$

Figure 2.24 presents a schematic diagram of such a tunnel anticrossing between the direct and indirect neutral exciton states X^0_{dir} and X^0_{ind} (cf. figure 2.23). For simplicity, the energy of the direct neutral exciton X^0_{dir} is set to zero. Also depicted in the graph is the electron localization within the molecule at different detunings $\Delta_{\mathrm{dir-ind}}$. For large $\Delta_{\mathrm{dir-ind}}$, the energies of the coupled states $E_\pm$ coincide with the ones of the uncoupled states $E_{\mathrm{dir,ind}}$. As the detuning is reduced, the coupling via tunneling processes increases and hybridized states are forming. At $\Delta_{\mathrm{dir-ind}} = 0$, the degeneracy of the system is fully lifted and the electron is delocalized equally over both QDs. The energy splitting between the bonding and antibonding state at the anticrossing is $2\kappa_{\mathrm{dir-ind}}$ and mainly determined by the thickness of the GaAs layer separating the dots [Kre05b] as well as the effective mass of the particles. In this idealized model, the states are maximally entangled. In reality, a reduction of coupling strength and degree of entanglement is expected due to effects such as strain, broken geometry along the growth axis or asymmetries in the system [Kre05a]. This assumption was supported by more complex calculations taking into account a more realistic QDM model [Bes04; Bes05; Zhu05].

2.5.2 Basic charactertisation of single quantum dot molecules

As for the single QDs, a series of photoluminescence spectra recorded at different electric fields applied yields information allowing to determine basic properties of the system.

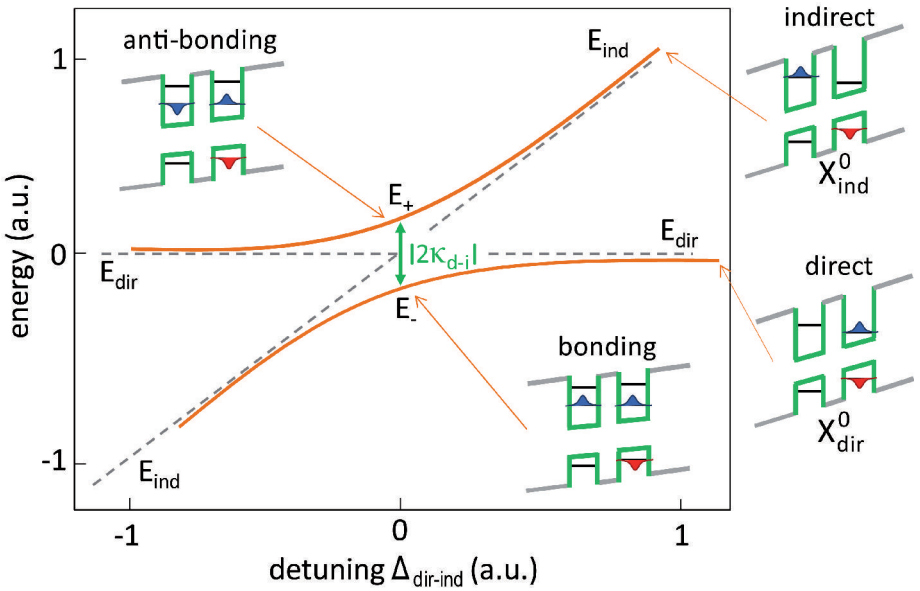

Figure 2.24. *Schematic diagram of an avoided crossing, a so-called anticrossing, occurring as the direct and indirect neutral exciton states X^0_{dir} and X^0_{ind} are tuned in and out of resonance. At zero detuning ($\Delta_{\mathrm{dir-ind}} = 0$) between the states when the electron energy levels of both dots are aligned, resonant tunneling processes between the upper and lower QD take place forming a coupled system with eigenenergies E_+ and E_-. As a result, the eigenstates of the system are hybridized bonding and antibonding molecular states split by an energy determined by the coupling strength κ. Also indicated are the electron positions in the regions of different detunings $\Delta_{\mathrm{dir-ind}}$.*

Figure 2.25 presents emission spectra of a single QDM after non-resonant optical wetting layer excitation as a function of electric field in a greyscale image plot [Mue11]. The signal was recorded in a detection window of $1304 - 1314$ meV and for electric fields from 18 kV/cm to 30 kV/cm. Clearly observable is an anticrossing behavior at $F = 23.02$ kV/cm providing direct proof for coupling in the system probed. The red and blue trace are calculated energy levels for a tunnel anticrossing between X^0_{dir} and X^0_{ind} according to equation 2.32. The straight dashed lines indicate the states in the absence of coupling towards which the eigenstates converge for large detunings $\Delta_{\mathrm{dir-ind}}$. The observed avoided crossing shown in figure 2.25 is a typical signature for an X^0 electron-electron anticrossing stemming from spatially direct and indirect excitons in the QDM that can be used to identify the lines [Kre05b; Mue11]. The strongly different Stark shift of the direct and indirect exciton is clearly visible. Furthermore, it can be seen from the graph that the PL emission in the indirect X^0 branch gradually fades for increasing detuning and becomes optically more active the closer it is to the anticrossing. This is an effect caused by the changing mixing ratio of the levels that depends on the detuning. As indirect excitons are optically inactive due to the weak electron-hole overlap, they can only be seen due to coupling effects and the coupled states appears brighter the larger the contribution of the direct exciton is.

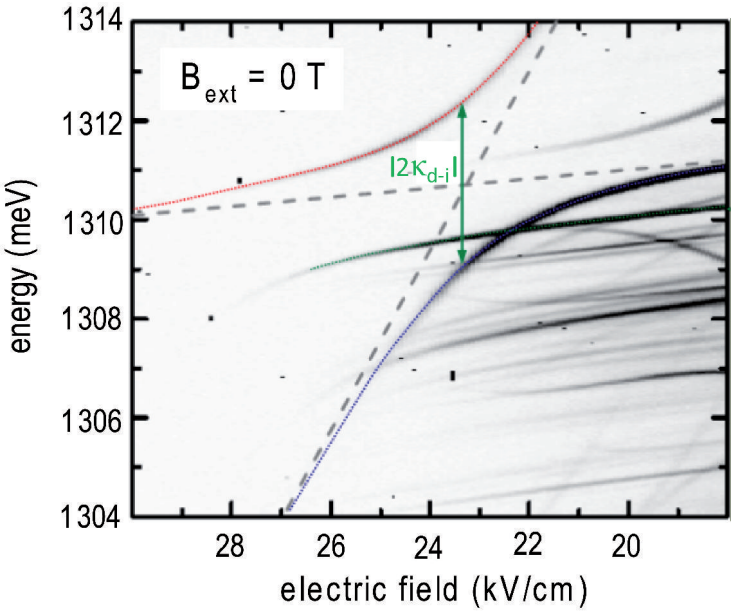

Figure 2.25. *Emission signal of a single quantum dot molecule after wetting layer excitation as a function of applied electric field presented in a greyscale image plot. Clearly visible is the X^0 electron-electron with a coupling strength indicated by the vertical green arrow. The blue and red trace are calculations of the energy levels according to equation 2.32. The straight dashed lines indicate the uncoupled states of the direct and indirect neutral excitons. Adapted from [Mue11].*

2.6 Summary

In this chapter, InGaAs quantum dots, semiconductor nanostructures that are grown by molecular beam epitaxy employing a self-assembly mechanism, were introduced. After a brief overview of the growth and microscopic structure, a simple model based on the confinement potential was presented to qualitatively explain the basic properties of these structures that are often referred to as 'artificial atoms'. In a second step, the model was developed further including interactions with electric and magnetic fields as well as coupling to the solid-state environment. Next, the experimental setup, design and fabrication of the sample as well as the measurement techniques used for characterization of the system was discussed. Experimental methods employed for the measurements carried out in this thesis, namely photoluminescence and photocurrent spectroscopy, were introduced and a series of measurements as typically performed to characterize a single QD structure was presented. Finally, a system composed of a pair of vertically stacked coupled quantum dots, often called 'quantum dot molecules', was introduced and its basic properties as well as a set of characterization measurements presented.

3

Electrical tuning of the exciton g-factor

The quantum mechanical two-level system formed by the spin of a charge carrier trapped in a semiconductor quantum dot is a promising candidate for future quantum information applications [Los98] due to the long spin lifetime and decoherence time [Tar04; Kro04; Kop08]. One of the key quantities characterizing a magnetic moment is the Landé g-factor – generally a tensor for electrons and holes localized in such nanostructures [Kat03; Ale06; Pry06; Wit11; Dea11] – quantitatively accounting for the Zeeman interaction of the spin with the magnetic field. Therefore, a detailed understanding of the electron, hole and exciton g-factors in QDs and the development of methods to control and manipulate these quantities currently attract much attention [Nak04; Nak07; Bjo05; Tes08; Rie08; She07; She09; And09b; Pry06; Klo10b; Jov11; Jov12b].

A high excitonic g-factor would in general be advantageous in experiments where a large splitting of the spin states is required, for example to reduce off-resonant laser coupling [Ata06]. To build a quantum receiver, an electron g-factor close to zero in combination with a comparatively large hole g-factor is needed [Vri01]. In these respects, the ability to tune the single particle and exciton g-factors would be of significant benefit, for example to tailor the hyperfine interaction of the electron spin with the nuclear spins in the QD (cf. chapter 4) which represents the dominant decoherence mechanism in GaAs QDs, limiting the time for coherent operations [Kha02; Kop08]. An electric field-tunable g-factor could also provide a route toward electrical spin manipulation without the need to create a local oscillating magnetic field [Kat03; Pin08]. Generation of localized high frequency oscillating magnetic fields, a task discussed in chapter 5, is experimentally much more challenging than local electric fields that can routinely be generated using mesoscopic metallic gates. Furthermore, to perform logical quantum operations, it is necessary to selectively manipulate a specific spin qubit within a quantum register. This task of selective addressing individual spins could be performed by applying

time-dependent highly local ($\sim$ 100 nm) electric fields as has been demonstrated using parabolically composition-graded AlGaAs quantum wells [Sal01].

To date, control of the g-factor via changes of the QD structure has been investigated theoretically [Sti99; Pry06; Nak04] and has recently been achieved experimentally [Nak05; Kim09; Kle09; Rud09; Jov12a]. Electrical control of the g-factor has been demonstrated in stacked QDs by inducing hybridization of the single particle wavefunctions over the two dots forming the molecule which requires vertically coupled QDs with close energy levels [Dot06]. In single QDs, weak electrical g-factor tuning was achieved with in-plane electric fields where a maximum g-factor change by 8 % was demonstrated [Nak07]. By tuning the vertical built-in fields a change of 15 % was shown [Rie08].

In this chapter, the tuning of the exciton g-factor in self-assembled InGaAs QDs by electric fields applied in growth direction and a non-linear behavior of the Zeeman splitting is demonstrated. Both experimental data as well as a theoretical investigation of this effect based on eight band $\mathbf{k}\cdot\mathbf{p}$ simulations are presented. For the single QDs investigated in this thesis with regard to dynamical nuclear polarization (DNP, cf. chapter 4), a strong electrical tunability of the exciton g-factor of $|(g_{max} - g_{min})\,/\,g_{min}| = 250$ % was observed [Klo10b]. Furthermore, the Zeeman splitting was found to depend on the applied magnetic field in a non-linear way. However, these effects were not the focus of this thesis and no further experiments to examine them were pursued. A detailed experimental investigation was carried out by *Jovanov et al.* [Jov11; Jov12b; Jov12a]. A theoretical model reproducing and explaining the experimental data was developed and simulations were performed by *Eisfelller et al.* [Jov11; Jov12b; Eis12b]. The results of these works are also incorporated in this chapter. Unless stated otherwise, the data presented here were measured in the framework of this thesis on the same single QD samples as examined in chapter 4.

In section 3.1, the setup and the experimental technique of photocurrent bias sweeps performed in this thesis are introduced. In section 3.2, the basic characterization of two individual quantum dots (QD_{A1} and QD_{A2}) investigated regarding DNP in chapter 4 and electrical g-factor tuning as well as non-linear Zeeman splitting in this chapter is carried out. Section 3.3 presents results on the electrical tunability of the fine structure splitting found for QD_{A1} at $B_{\text{ext}} = 0$ T. In section 3.4, the observation of electric field-dependent exciton g-factors and Zeeman interactions depending non-linearly on B_{ext} for both QD_{A1} and QD_{A2} as well as for another type of self-assembled dots, QD_{C1}, which is also examined regarding DNP effects in chapter 4, is presented. In the following two sections 3.6 and 3.5, an explanation for the observed effects based on experimental and theoretical investigations by *Jovanov et al.* and *Eisfeller et al.*, respectively, is given.
The main findings presented in this chapter are published in [Klo10b; Jov11; Jov12b; Jov12a; Eis12b]. Sections 3.3 and 3.4 are based on [Klo10b]. Sections 3.5 and 3.6 are based on [Jov12b] and [Jov11], respectively.

3.1 Experimental setup and method

Before the empirical data are presented and discussed, the measurement setup and experimental technique is introduced. A general overview of the working principle of photocurrent and photoluminescence experiments as well as a basic description of the according spectroscopy setup was given in 2.3.2. Here, the actual design used for the experiments carried out in this thesis is presented and discussed.

An overview of the setup including all relevant components is given in figure 3.1. The sample is placed in a cryo-microscope formed by an objective (Melles Griot, Collimating and Focusing Lense Package, GLC-6.5-8.0-830, NA=0.62) and a stack of x-, y-,and z-piezo slip stick motors (Attocube Systems, ANPxyz50/LT attocube nanopositioners) that can be operated at low temperatures and in high magnetic fields allowing to focus the excitation beam onto the sample and scan it across the surface (for details see below and figure 3.2). The microscope is attached to the lower end of a sample stick that can be inserted into the sample space of a liquid helium cooled top loading bath cryostat (Oxford Instruments Limited) providing the low temperatures needed for single QD spectroscopy. The cryostat is equipped with a superconducting solenoid magnet system (Magnabond Super 13) able to generate magnetic fields up to $B = 12$ T at an operating temperature of $T = 4.2$ K. The sample stick is dimensioned such that the sample is positioned on the symmetry axis as close as possible to the center of the magnet´s bore where the magnetic field is oriented in z-direction and the field strength is maximal. The bore diameter of 30 mm limits the size of the microscope leading to a very compact design of the focusing optics which, despite the spatial restrictions, still allows positioning of the sample in the focus of the objective with sub-micrometer accuracy. The sample can be excited either via a tunable external cavity Littman-Metcalf diode laser (Sacher Lasertechnik TEC-520, tuning range 914 to 978 nm, or TEC-530, tuning range 878 to 948 nm) or a 855 nm laser diode. The wide combined tuning range of 100 nm provided by the Littman-Metcalf lasers is needed to be able to achieve resonant excitation of the QD levels investigated in photocurrent measurements since the transition energies of the QD states can vary widely from one dot to the next. Furthermore, it allows for resonant experiments over a wide range of external parameters such as electric or magnetic fields which cause a shift in energy of the QD states, an effect the excitation wavelength needs to be adjusted for in order to maintain the resonant condition. The 855 nm laser diode is used to excite the QDs in the wetting layer for characterization of single dots via PL measurements and also to perform a so-called randomization procedure to prevent the built up of nuclear spin polarization during the course of PC voltage sweeps as will be described in more detail later in this section. The light from each source is coupled into one of the ends of a 90:10 fused optical single mode fiber and the merged signal is guided to an optical setup that is installed on the room temperature end of the sample stick, the optical head. Mechanical shutters providing a very high signal suppression allow

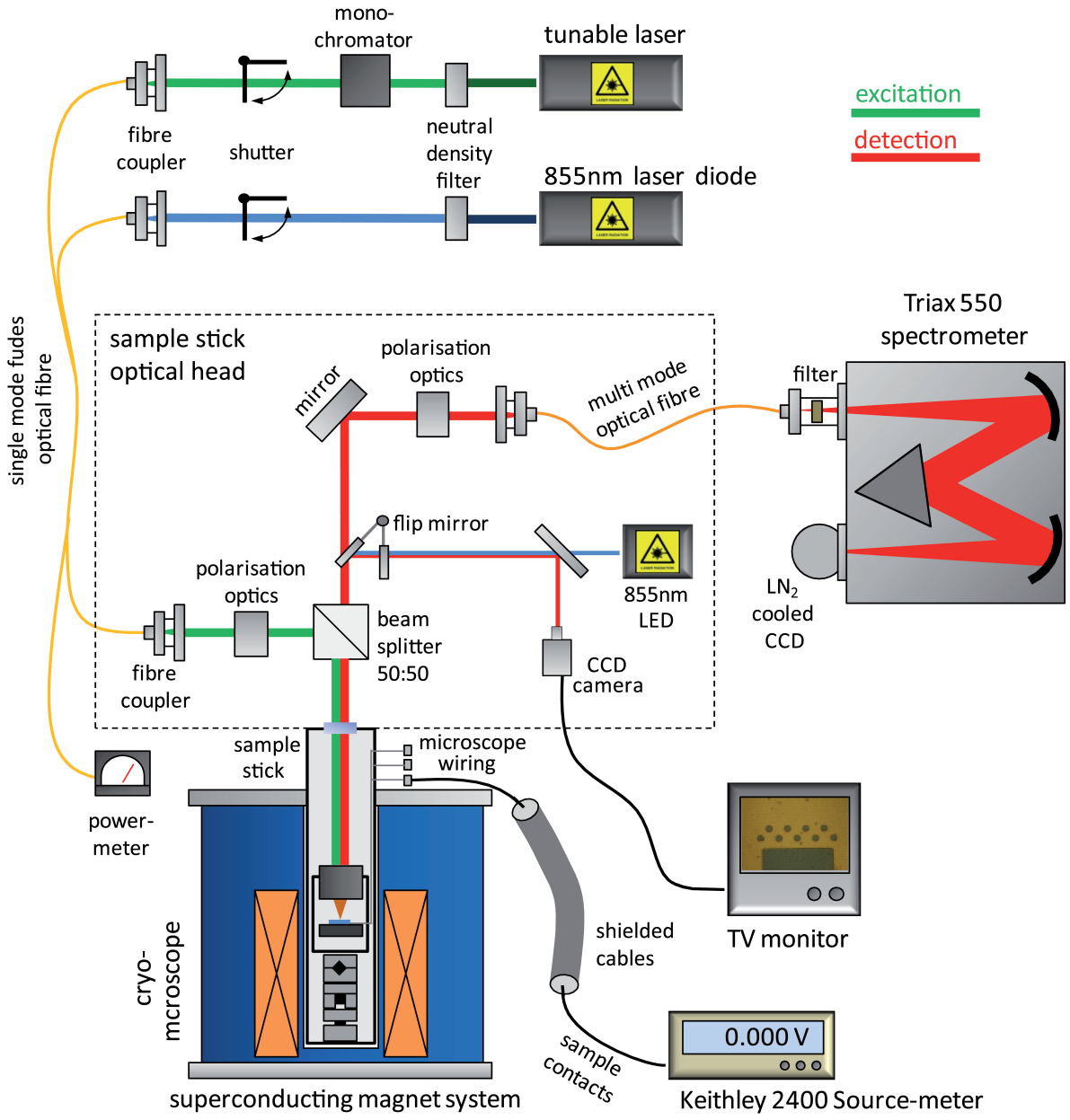

Figure 3.1. *Schematic diagram of the experimental setup used for the PL and PC measurements carried out in this thesis. The sample is placed in a cryo-microscope formed by an objective and a set of low temperature attocube piezo-positioners. The microscope is attached to the end of a sample stick which is inserted in a liquid helium bath cryostat with a superconducting magnet system. The light of a tunable laser and a 855 nm laser diode is merged in a fused optical fiber and the beam is guided down the sample stick to the sample free-space via a 50:50 beamsplitter and focused on the surface with the microscope objective. The same objective is also used to collect the emitted light which is guided to a 0.55 m spectrometer through the orthogonal path of the beamsplitter. Graphic design adapted from [Hei09a].*

to separately switch on and off emission of the 855 nm diode and the Littman-Metcalf laser. In addition to the single mode emission at the wavelength desired with a very small bandwidth < 300 kHz, strong sideband emission with intensities much higher than the single QD photoluminescence signal to be detected is observed for the tunable diode lasers. To circumvent this problem, a prism-based monochromator with a half width of ~ 4 nm (Photophysics Laser Filter Monochromator) is installed in front of the mechanical shutter providing a sufficiently high suppression of the laser sidebands, enabling single dot PL measurements. The other exit of the fused fiber is used to monitor the power applied to the sample. In the optical head, the light is coupled out of the fiber, passes a set of polarization and alignment optics and is, via a 50:50 beamsplitter, sent down the sample stick that allows free-space access to the sample via a vacuum tight optical window. At the low temperature end of the sample stick, the excitation beam is focused on the sample with the cryo-microscope where the use of a single mode fiber provides a small excitation spot of several micrometer diameter. The PL signal emitted from the QD investigated is collected using the same microscope, guided up the sample stick to the optical head, and coupled into a 200 μm optical multimode fiber via the orthogonal path of the beam splitter. The collected PL signal is spectrally analyzed using a 0.55 m single grating (1200 lines/mm) spectrometer (Horiba Jobin Yvon Triax 550) with an attached liquid nitrogen cooled silicon charge-coupled device (CCD) detector. A set of electrical leads enters the sample space at the top of the cryostat via a vacuum feedthrough next to the optical window and is guided down the sample stick to the microscope to contact the sample, control the attocube positioners, read out the temperature sensor (LakeShore Cernox Resistor, CX-1050-SD-1.4D) and operate a heater formed by four 100 Ω resistors. To perform PC measurements, a source meter (Keithley 2400 SourceMeter) is used to both apply the voltage to the sample as well as detect the photocurrent signal. To reduce noise, shielded cables are used to contact the sample wherever possible inside and outside the cryostat. To align and position the excitation beam on the sample, the surface can be imaged via a mirror that can be flipped into the detection bath after the beamsplitter as indicated in figure 3.1. The sample can be illuminated with a 855 nm diode through a semi-transparent mirror. The image is recorded with a CCD camera via the other path of the semi-transparent mirror and displayed on a TV monitor. The achieved resolution allows to identify individual apertures and focus the spot of the excitation beam on a specific one with high precision.

Figure 3.2 shows a picture of the cryo-microscope used to carry out the experiments performed in this thesis. The casing is fabricated from German silver, a non-magnetic alloy of copper, nickel and zinc, that is suitable for use in high magnetic fields. The wiring of the piezo-positioners, resistive heaters, and the temperature sensor is connected to a set of pins on top of the device, allowing to conveniently unplug the whole microscope from the sample stick. In figure 3.2(a), the positioners and the objective are shown without sample holder and sample installed. A close-up image, demonstrating how the sample is integrated into the microscope is presented in figure 3.2(b). The sample holder

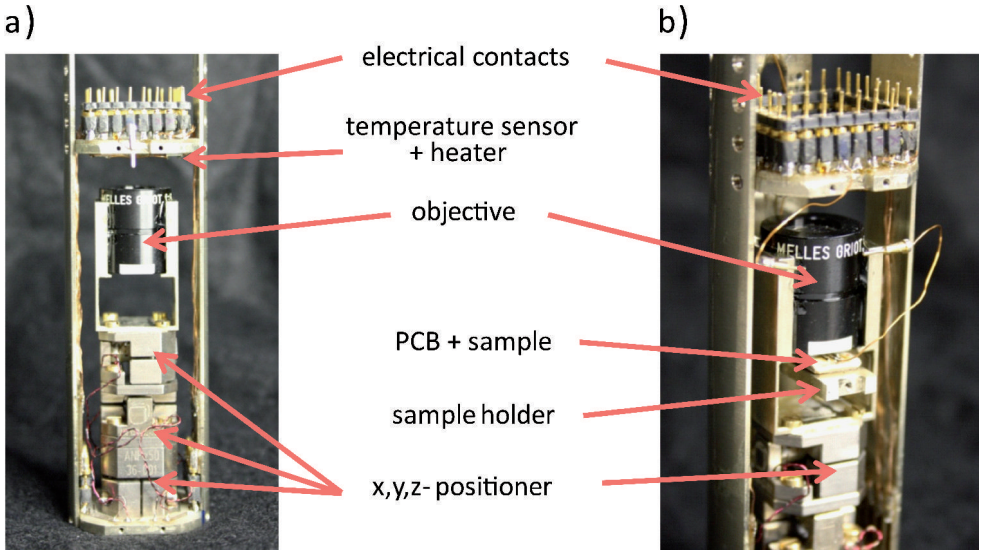

Figure 3.2. *Images of the cryo-microscope used for the single QD spectroscopy. (a) The whole system without sample holder and sample and (b) close-up with sample holder and sample. The x-, y-, and z-positioners are not moving the sample but the objective used to focus the laser beam onto the sample and to collect the emitted photoluminescence signal. The sample holder is fixed on both ends to the side walls of the microscope casing. This arrangement allows to contact the sample e.g. with semirigid coax cables for microwave supply that could not be moved by the positioners.*

is fixed to the side walls of the microscope casing on both ends (the front side walls was removed for the picture for better illustration). This forms a rigid bridge onto which the sample and the printed circuit board is glued (cf. chapter 5), placing them directly under the objective. In contrast to commonly used microscope designs where the sample is moved and the objective is fixed as presented in section 2.3.2, here, the objective is moved to focus the excitation beam on the sample and scan it across the surface. This type of construction allows to contact the sample e.g. with semirigid coax cables for microwave supply as discussed in detail in chapter 5. Otherwise, this would not be possible since the piezo-positioners fail to move the sample if a stable connection to a semirigid coax cable as needed for low loss transmission of GHz frequencies is established, a problem disabling the operation of the microscope. The measurements carried out in this thesis showed no reduced mechanical stability or any other experimental disadvantages of the microscope design presented here with respect to single QD spectroscopy.

Figure 3.3 presents a schematic illustration of a photocurrent bias sweep, the experimental technique mainly used to investigate the orbital ground state of uncharged QDs in this thesis. To perform such a measurement, the laser is kept at a fixed wavelength and the electric field applied to the sample is swept tuning the QD states in and out-of resonance with the laser via the quantum confined Stark effect [Fry00b; Fin01a]. The Stark shift can be determined from PL measurements which enables a direct conversion

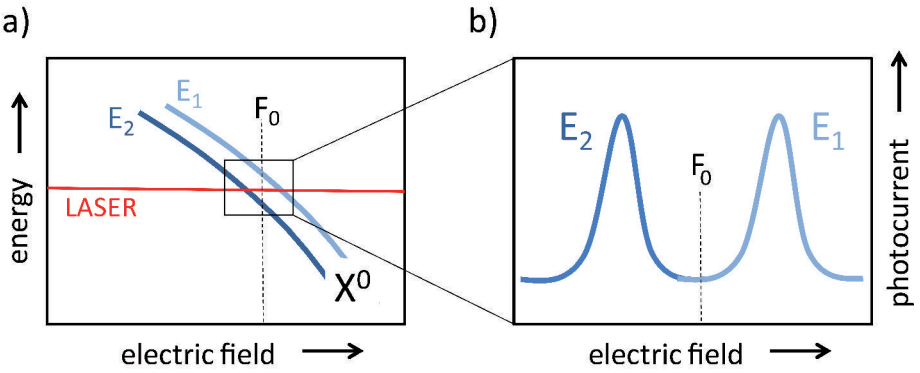

Figure 3.3. *Schematic representation of a photocurrent bias sweep, the experimental technique mainly used to investigate the orbital ground state of uncharged QDs in this thesis. (a) While the laser is kept at a fixed wavelength, the applied electric field is swept and the quantum confined Stark effect is used to tune the X^0 levels in and out-of resonance with the excitation energy. (b) Sketch of a typical PC spectra recorded in a bias sweep measurement. F_0 denotes the electric field in the center between the two resonances.*

of applied electric field to transition energy. This technique allows to record PC spectra with a very high resolution of several μeV since the voltage applied to the sample can be controlled with high precision. A typical result of such a bias sweep is sketched in figure 3.3(b) where the photocurrent amplitude is plotted as a function of the applied electrical field. When the QD transition matches the laser energy, charge carriers are resonantly generated. Since the device is operated in the PC regime, electrons and holes tunnel out of the dot and drift to the corresponding electrical contacts giving rise to a PC signal. Typically, even for $B_{\text{ext}} = 0$ T, two resonances are observed for X^0 due to the anisotropic electron hole exchange interaction giving rise to a fine structure splitting [Gam96a; Bay99a; Bay02b] as discussed in section 2.2.2. In a non-zero magnetic field, the two states exhibit an additional splitting given by the Zeeman interaction as described in section 2.2.3. The resonance observed at higher electric fields is denoted E_1 and the one at lower fields E_2. The electric field in the center between the two resonances is denoted F_0. This terminology is used throughout the whole thesis.

As will be discussed in detail in chapter 4, resonant excitation of the X^0 states as done in a PC bias sweep can lead to pumping of the nuclear spins in the QD leading to a partial polarization of the nuclear spin bath [Mak08b; Klo10a; Coi09; Hoe12; Urb12]. The resulting effective magnetic field $\boldsymbol{B}_{\text{n}}$ leads to an additional Zeeman interaction that shifts the transition energy of the QD states (cf. section 2.2.4). To investigate this effect of dynamical nuclear polarization or the electric and magnetic field-dependence of the g-factor, it is indispensable to obtain reference measurements where buildup of nuclear polarization is suppressed. The procedure employed to achieve DNP suppression is presented in figure 3.4. Prior to every PC data point measured during a bias sweep, a scheme is employed to randomize the nuclear spin bath deleting any nuclear polarization

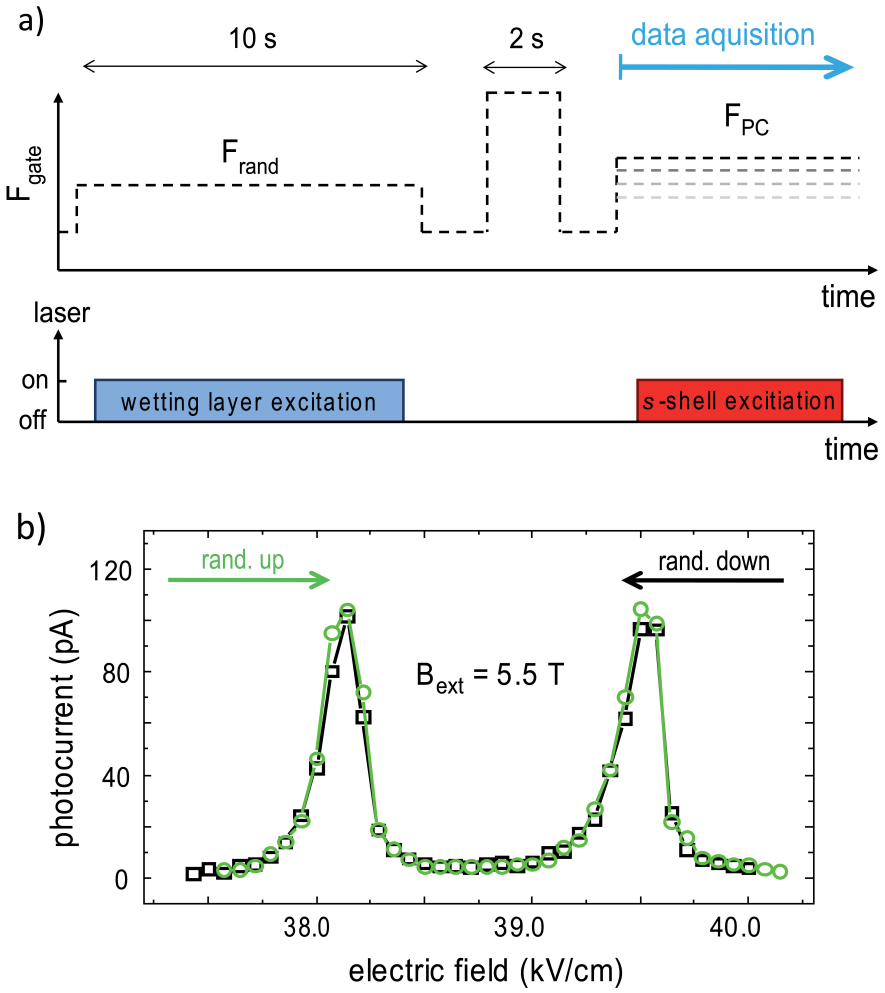

Figure 3.4. *(a) Laser excitation and electric field sequence applied to the sample in order to record one data point during a bias sweep measurement. The procedure prior to PC detection is introduced to remove any polarization of the nuclear spin bath in the QD that can build up during resonant pumping of the X^0 state during the PC sweep. (b) Comparison of two photocurrent measurements carried out at $B_{\mathrm{ext}} = 5.5$ T using opposite sweeping directions of the applied electric field. For both sweeps, the randomization procedure was performed before every PC data point.*

that might have been built up during the recording of the previous data point. To achieve this, the sample is tuned close to flatband and excited non-resonantly in the wetting layer for 10 s with linearly polarized light at $\lambda_{\mathrm{exc}} = 855$ nm. This procedure pumps randomly oriented electron spins through the QD in the photoluminescence regime, whereupon hyperfine interactions efficiently depolarize the nuclear spin system leading to a thermal nuclear spin configuration. Next, a high electric field of ≈ 250 kV/cm is applied to the sample for 2 s while the dot is kept in the dark to remove all charge carriers that might have accumulated. After this, the electric field value for the bias sweep is set, the resonant laser switched on, the PC signal detected, and the laser switched of again. The

timing for the electric field and laser excitation sequence is illustrated in figure 3.4(a). To record the next step of the sweep, the whole procedure is repeated.

To test the effectiveness of the randomization procedure, PC measurements with opposite sweeping directions of the applied electric field (denoted 'up' and 'down' in figure 3.4(b)) including the randomization procedure have been carried out at $B_{\text{ext}} = 5.5$ T. As can be seen in figure 3.4(b), identical spectra are recorded for both sweeping directions. This result is in strong contrast to observations made when performing the same experiment without the randomization procedure where optically pumped nuclear polarization leads to a shifting of the PC resonances during the course of the measurement, an effect most pronounced at $B_{\text{ext}} \approx 5.5$ T (cf. chapter 4). The fact that the sweeping direction has no influence on the recorded PC spectra when applying the randomization procedure allows to conclude that DNP is efficiently suppressed. A more detailed discussion and quantitative examination of the randomization procedure can be found in section 4.3.2.

3.2 Sample characterization

In the framework of this thesis, the effect of g-factor tuning was investigated on two individual quantum dots from the same wafer denoted QD_{A1} and QD_{A2}. Before the effect can be studied, a basic characterization of the dots is necessary. This procedure is done here exemplarily for QD_{A1}. For this purpose, photoluminescence and photocurrent measurements have been carried out using the setup described above. The results are summarized in figure 3.5. For low electric fields < 35 kV/cm, PL measurements were

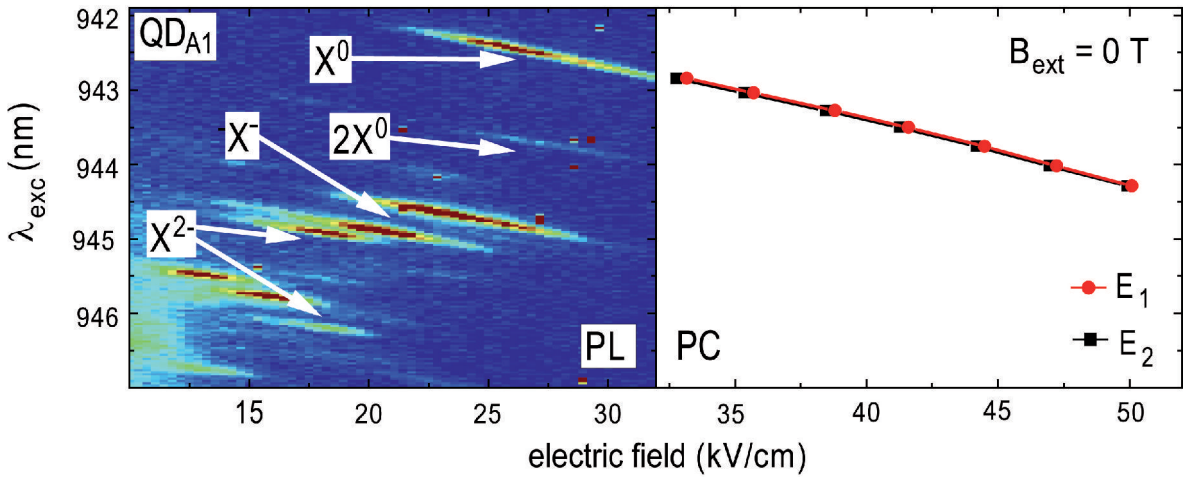

Figure 3.5. *Characterization measurements of QD_{A1} at $B_{\text{ext}} = 0$ T and $T = 10$ K showing the Stark shift of the QD states. Comparison of the photoluminescence and photocurrent measurements allows to unambiguously identify the resonances probed in the PC bias sweeps as the lowest orbital state of the uncharged QD X^0.*

performed at $B_{\text{ext}} = 0$ T and $T = 10$ K exciting the QD non-resonantly in the wetting layer using linearly polarized light at $\lambda_{\text{exc}} = 855$ nm. The detected PL signal is presented on the left side of figure 3.5 as a function of the applied electric field in a color-coded image plot and shows all the typical features of a single quantum dot spectrum [Fin01b] as discussed in section 2.4. Emission from a set of lines is observed in the wavelength range from $942 - 947$ nm and for electric fields from 12 to 35 kV/cm. For electric fields < 12 kV/cm, the drift current of the photodiode in forward direction sets on and the flow of charge carriers through the device causes a disturbance of the PL signal. On the high electric field side > 35 kV/cm, the tunneling time of the confined charge carriers becomes shorter than the radiative lifetime and photoluminescence quenches due to electric field-induced carrier escape. Emission from each state is only found in a characteristic electric field range. The set-on field decreases with increasing emission wavelength and a shift in PL intensity from higher to lower emission energies is observed as the electric field is reduced. This behavior originates from subsequent charging of the QD via the back gate. For electric fields > 30 kV/cm, the dot is strongly decoupled from the back contact and optically created charge carriers relax into the QD ground state where they recombine radiatively on a timescale of ~ 1 ns [Kre05d] and luminescence from the neutral X^0 state is observed. When the electric field is lowered, the lowest orbital states of the QD approach the Fermi level of the back contact and an electron can tunnel into the dot. In this situation, emission from the negatively charged X^- sets in. The emergence of the X^- line coincides with a decrease in X^0 intensity. Coulomb repulsion prevents the addition of a second electron from the Fermi reservoir. When the field is further reduced, the Coulomb interaction is compensated and emission from the doubly charged excitonic state emerges as a second electron can enter the dot from the back contact. The increase in intensity is accompanied by a decrease of the X^- signal. The relatively wide regions of co-existence of different charge states are a result of the comparatively thick tunnel barrier of 35 nm between the QD and the back contact and the statistical nature of the tunneling process as can also be seen in [Fin01b]. Due to the quantum confined Stark effect, all emission lines exhibit a shift towards higher energy for decreasing electric field [Fry00b; Fin01a]. The observed Stark shift can be well described using equation 2.10: $\Delta E_{\text{QCSE}} = E_0 + \boldsymbol{p}_{\text{int}}\boldsymbol{F} + \beta\boldsymbol{F}^2$. From the fit, the intrinsic dipole moment $\boldsymbol{p}_{\text{int}}$ and exciton polarizability β of QD_{A1} are found to be $|\boldsymbol{p}_{\text{int}}| = 4 \pm 1 \times 10^{-29}$ Cm and $\beta = 1.8 \pm 0.2 \times 10^{-35}$ Cm^2/V. A corresponding analysis on QD_{A2} gives $|\boldsymbol{p}_{\text{int}}| = 1.2 \pm 0.1 \times 10^{-29}$ Cm and $\beta = 3.2 \pm 0.1 \times 10^{-35}$ Cm^2/V.

With the PL spectrum at hand, photocurrent measurements can be performed. For this resonant technique it is necessary to know the transition energies of the dot, particularly the X^0 state, to be able to match the excitation laser accordingly. The fit to the Stark shift obtained from the PL measurements allows to extrapolate the X^0 line into the PC regime. The results of a series of PC bias sweeps at different excitation energies performed as described above is summarized on the right side of figure 3.5. Photocurrent detection was only possible for electric fields > 35 kV/cm where tunneling times of the charge carriers to the gates are shorter than the radiative lifetime. The higher resolution PC

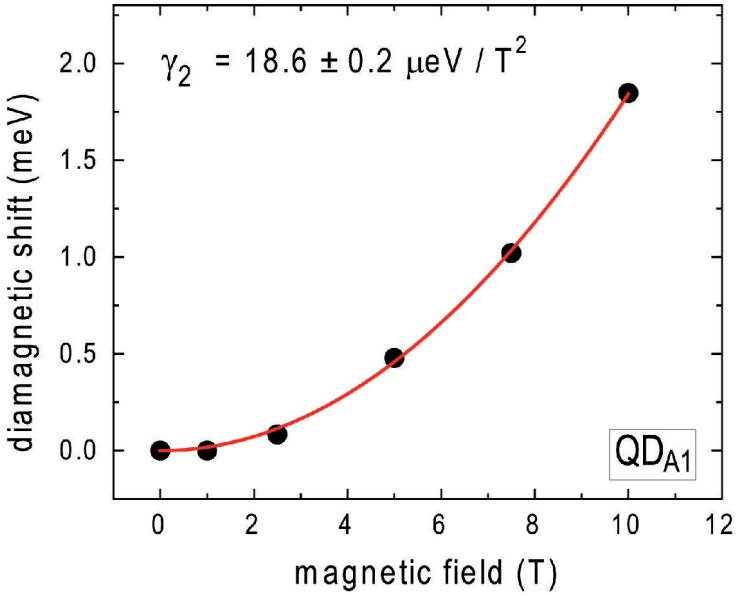

Figure 3.6. *Diamagnetic shift of QD_{A1} at $T = 10$ K. Plotted is the shift of the X^0 transition energy determined from PL bias sweeps as presented in figure 3.5 at a fixed electric field of ≈ 26 kV/cm for different B_{ext}. The diamagnetic coefficient γ_2 was obtained from a fit using equation 2.8 (solid red line).*

scans from which the data points on the right side of figure 3.5 are extracted are depicted in figure 3.7 in the following section and reveal that the X^0 emission consists of two resonances that can not be resolved in the PL measurements. This splitting of the neutral exciton state at $B_{\text{ext}} = 0$ T is caused by the anisotropic electron hole exchange interaction as discussed in section 2.2.2. The black squares and red circles in figure 3.5 mark the position of the two resonances for each λ_{exc} used which coincide well with the electric field values expected from extrapolation of the PL data. Therefore, it is possible to unambiguously identify the resonances probed in the PC bias sweeps as the X^0 states of the QD.

Further information about the QD investigated can be obtained from the diamagnetic shift introduced in section 2.2.3. Figure 3.6 presents the shift of transition energy of the neutral exciton state X^0 at a fixed electric field as a function of applied magnetic field B_{ext}. The data can be well described with a fit using equation 2.8 (solid red line) from which a diamagnetic coefficient of $\gamma_2 = 18.6 \pm 0.2\ \mu\text{eV/T}^2$ can be extracted for QD_{A1}. With the effective masses of electrons and heavy holes in $\text{In}_x\text{Ga}_{1-x}\text{As}$ given by $m_e^* = 0.023 + 0.037(1-x)$ and $m_{hh}^* = 0.46 + 0.1(1-x)$ in units of the free electron mass m_0 [NSM], the lateral dimension of the charge carrier wavefunction can be estimated from equation 2.9.

Under the assumption of equal lateral extension of electron and hole wave functions, the observed diamagnetic shift corresponds to a wavefunction diameter of 11.5 nm for QD_{A1} which is in good agreement with typical lateral sizes of self-assembled InGaAs

QDs of $10 - 30$ nm [Leo93; Pet94]. However, comparison with experimental results suggests that this approximation underestimates the dot size by about a factor of $\sim$1.5 since a diamagnetic coefficient of $\gamma_2 = 19\ \mu\mathrm{eV/T^2}$ was measured to correspond to a lateral dot size of ≈ 20 nm [Bay98] in $In_{0.1}Ga_{0.9}As$ while the relation given in equation 2.9 under the assumption of equal lateral wavefunction extension results in 13.2 nm. For QD_{A2}, a value of $\gamma_2 = 14.9 \pm 0.1\ \mu\mathrm{eV/T^2}$ is found.

3.3 Tuning of the fine structure splitting

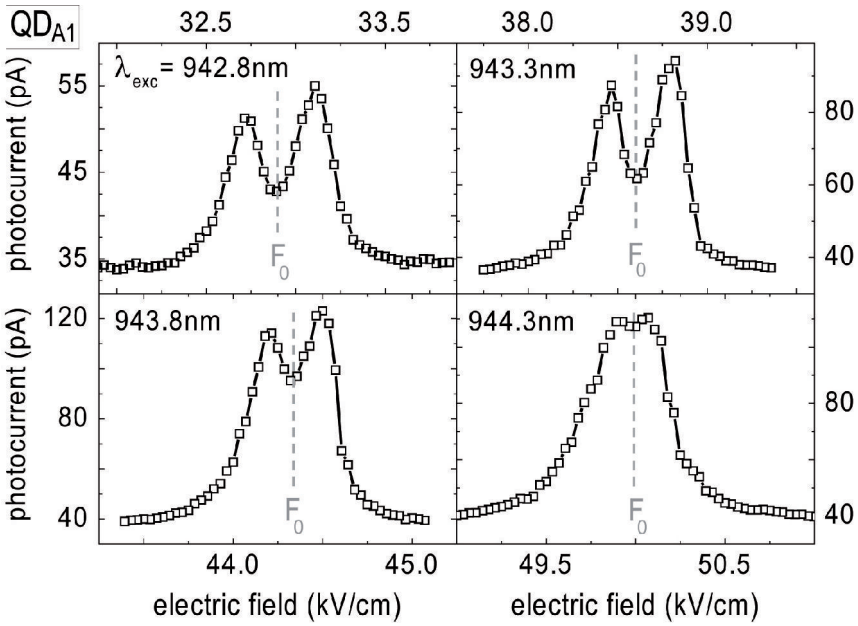

Figure 3.7. *Photocurrent bias sweeps at $B_{\mathrm{ext}} = 0$ T for different excitation wavelengths λ_{exc} resonantly pumping the X^0 state of the QD with linearly polarized light. The observed fine structure splitting in the absence of an external magnetic field is a result of the anisotropic electron hole exchange interaction and is found to vary as a function of the applied electric field. Before every data point, a randomization procedure as described in the text was applied.*

As discussed in section 2.2, in quantum dots with a non-perfectly round shape the anisotropy leads to a fine structure splitting (FSS) caused by the electron hole exchange interaction [Gam96a; Bay99a; Kul99; Bes00; Bay02b]. Typically, the fine structure splitting (denoted δ_1) for self assembled InGaAs is of the order of several tens of μeV [Bay99a; Bay02b; Kow06] which is significantly larger than the homogeneous linewidth of the transition at temperatures $T < 20$ K [Bay02a]. This represents a fundamental obstacle e.g. for the generation of polarization-entangled photon pairs via the biexciton-exciton cascade in a single quantum dot as proposed by *Benson et al.* [Ben00] since it lifts the degeneracy of the two states and leads to distinguishable decay paths in the cascade. For this reason, no quantum entanglement could be achieved in this system until cancellation of the FSS was accomplished by a special growth technique in combination with

an in-plane magnetic field [Ste06]. Therefore, it is of great interest to investigate and develop techniques to control the FSS of individual QDs. An experimentally convenient technique is the application of electric fields that was successfully employed for FSS tuning [Kow06; Kow07].

The high resolution of PC bias sweeps allowed to examine the possibility of electrical FSS tuning for the dots investigated in this thesis. Figure 3.7 shows the PC spectra of QD_{A1} recorded at four different excitation wavelengths and $B_{\text{ext}} = 0$ T. Again, F_0 denotes the electric field value in the center between the two resonances. A clear trend of FSS decreasing for an increasing electric field is observable demonstrating electrical FSS tuning. To exclude any effects of nuclear polarization, the randomization procedure was applied prior to every data point recorded. The fact that the FSS can be altered by applying electric fields in growth direction of the QD suggests that its anisotropy changes along the growth axis since the wave functions of the charge carriers are dislocated parallel to it by the electric field with a shift depending on the field amplitude.

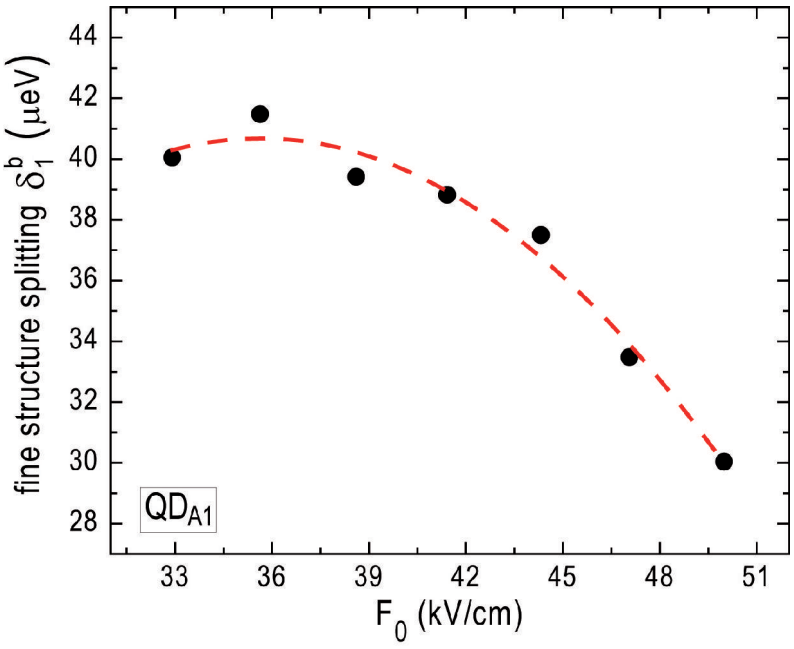

Figure 3.8. *Electric field dependence of the X^0 fine structure splitting obtained from fitting two Lorentzians to the measured data depicted in figure 3.7. F_0 denotes the electric field in the center between the two resonances. The dashed line is a guide to the eye obtained from a quadratic fit.*

To evaluate the PC bias sweeps, the position of the resonances were located by fitting two Lorentzians to the PC spectra. The quadratic fit to the Stark shift was used to convert the electric field values of the peak positions into transition energies allowing to determine the FSS. The results of this procedure are presented in figure 3.8. A tunability of > 10 μeV from $\delta_1 = 43$ μeV to 30 μeV was found by varying the electric field applied to the dot in growth direction over ≈ 20 kV/cm from 33 to 50 kV/cm. The red dashed

line is a guide to the eye obtained from a quadratic fit to the data. This result is in good agreement with polarization resolved photoluminescence experiments reported in literature also using electrical fields in growth direction carried out on similar, non *In-flushed* QDs [Kow06].

3.4 Observation of electrical g-factor tuning and non-linear Zeeman splitting

In this section, observations on electric field-dependent exciton g-factors (reported in Ref. [Klo10b]) and Zeeman interactions exhibiting a non-linear B_{ext} dependence made in the framework of this thesis are presented. All single QDs discussed in this section were also examined regarding nuclear spin pumping. These investigations are presented in chapter 4 using the same labeling for the individual dots.

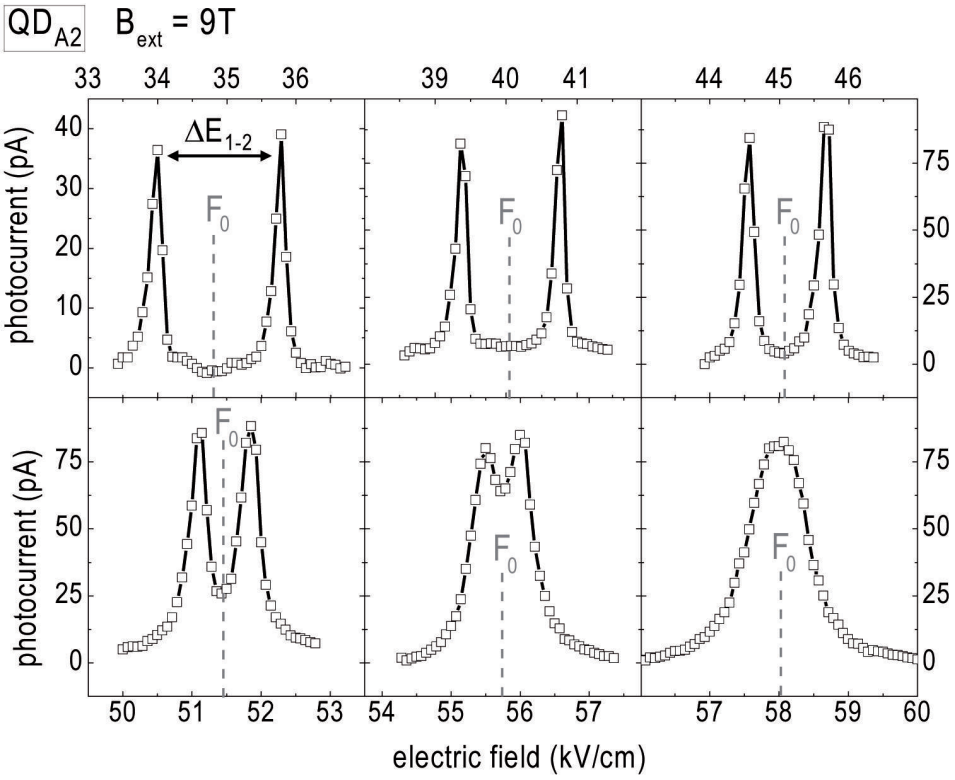

Figure 3.9. *Photocurrent bias sweeps performed on QD_{A2} at $B_{\text{ext}} = 9$ T for different excitation wavelengths λ_{exc} resonantly pumping the two bright neutral exciton states of the dot with linearly polarized light. Before every data point, a randomization procedure as described in the text was applied in order to suppress nuclear spin pumping and the buildup of Overhauser magnetic fields during the sweep. As the electric field range is changed, a strong variation of ΔE_{1-2}, the energy splitting between the two bright X^0 states $|E_1\rangle$ and $|E_2\rangle$, is found.*

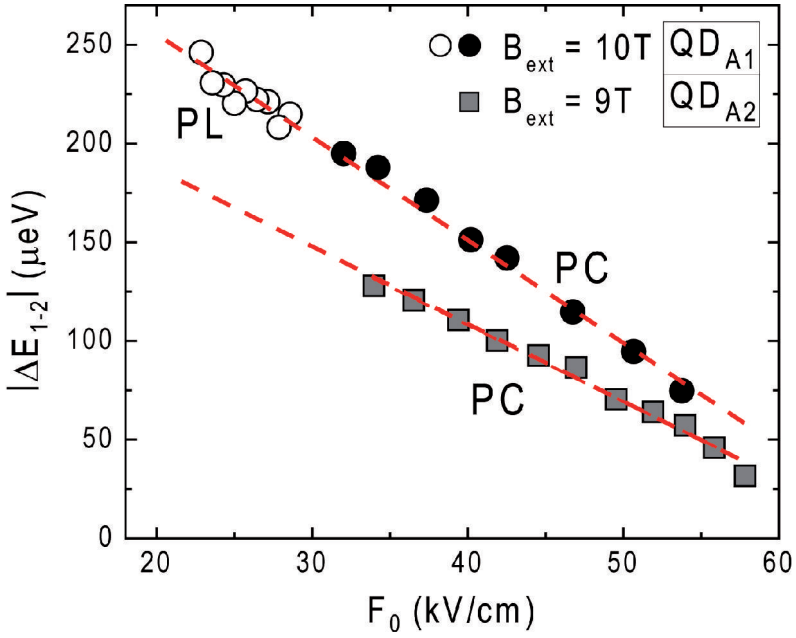

Figure 3.10. *Dependence of ΔE_{1-2}, the energy splitting between the two bright X^0 states $|E_1\rangle$ and $|E_2\rangle$, on the electric field applied. The splitting for QD_{A1} and QD_{A2} was determined from PC bias sweeps as presented in figure 3.9. Additionally, PL spectra were recorded for QD_{A1} to extend the experimentally accessible electric field range. A clear trend of ΔE_{1-2} decreasing monotonically for increasing electric field is observed for both dots.*

3.4.1 Electrical field dependent exciton g-factors

Figure 3.9 presents PC bias sweeps performed on QD_{A2} for different excitation wavelengths λ_{exc} at $B_{\text{ext}} = 9$ T and with application of the randomization procedure before every data point to suppress DNP effects. Due to the Stark shift of the transition energies [Mil84; Fry00b; Fin01a], the use of different excitation laser wavelengths corresponds to different electric field ranges for the bias sweeps in order to achieve resonant pumping of the QD states. Here, this effect is expressed in terms of F_0, the electric field value in the center between the two X^0 resonances $|E_1\rangle$ and $|E_2\rangle$ that are split by an energy ΔE_{1-2}. Displayed in the six graphs of figure 3.9 are measurements for different F_0 varying from 34.8 kV/cm to 60.0 kV/cm. For increasing electric fields, a clear trend of decreasing X^0 splitting ΔE_{1-2} is observed. For the highest electric field of $F_0 = 60$ kV/cm, the two individual resonances can barely be resolved.

To obtain a more quantitative picture of this effect, the resonances were fitted using two Lorentzians and the energy separation between $|E_1\rangle$ and $|E_2\rangle$ was calculated. The result of this analysis is presented in Figure 3.10 where ΔE_{1-2} is plotted as a function of F_0 for QD_{A1} and QD_{A2} at $B_{\text{ext}} = 10$ T and 9 T, respectively. For QD_{A1}, the experimentally accessible electric field range investigated was extended beyond the photocurrent regime down to $F_0 = 23$ kV/cm by employing photoluminescence measurements. For both QDs, a clear trend of decreasing ΔE_{1-2} for increasing F_0 is observed that can be well

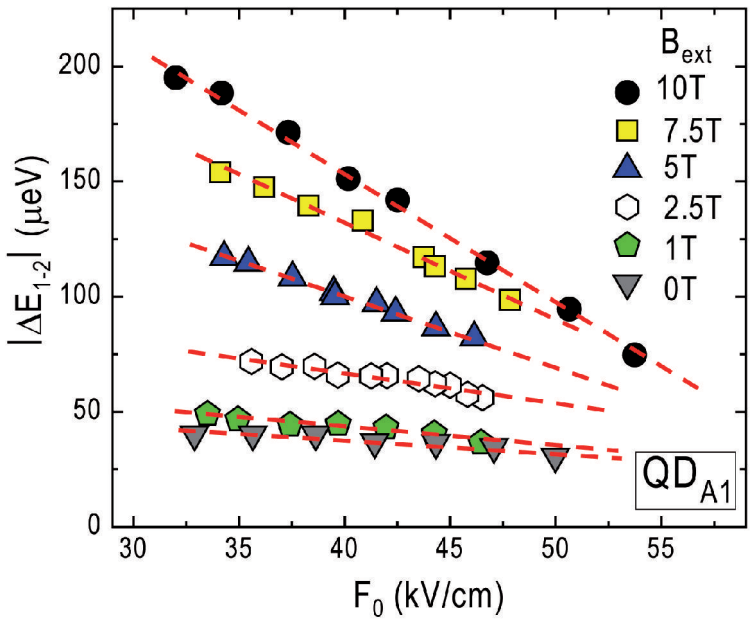

Figure 3.11. *Dependence of ΔE_{1-2}, the energy splitting between the two bright X^0 states $|E_1\rangle$ and $|E_2\rangle$, on the electric field applied for QD_{A1} at different external magnetic fields B_{ext}.*

described using a linear function (dashed red lines in figure 3.10) [Klo10b; Jov11]. For QD_{A1}, the energy splitting reduces from 245 μeV at 23 kV/cm to 75 μeV at 53 kV/cm. For QD_{A2}, a reduction of ΔE_{1-2} from 130 μeV at 34 kV/cm to 33 μeV at 58 kV/cm is found.

The dependence of this effect on the externally applied magnetic field is summarized in figure 3.11 where ΔE_{1-2} is presented as a function of F_0 for magnetic fields from $B_{\text{ext}} = 0$ T to 10 T covering an electric field range from 32 kV/cm to 53 kV/cm. For all B_{ext} examined, ΔE_{1-2} decreases monotonically for increasing electric fields. In all cases, the observed behavior can be approximated with a linear fit, however, using different slopes for the individual data sets (dashed red lines in figure 3.11). A clear trend of increasing slopes for increasing B_{ext} is apparent. At $B_{\text{ext}} = 0$ T, the variation of ΔE_{1-2} is given entirely by the electric field tuning of the fine structure splitting δ_1^{b} presented in figures 3.7 and 3.8.

With the electric field dependence of δ_1^{b} known, the absolute g-factor value $\left|g_{\text{ex}}^{\text{b}}\right|$ can be determined for all F_0 from ΔE_{1-2} using the relations listed in table 2.1. The sign of g_{ex}^{b} and its components g_{e} and g_{h} cannot be obtained from the data presented here. For the former, polarization resolved measurements [Bay99a; Bay02b; Nak04; War05; Jov11], for the latter, experiments that allow to detect the dark exciton states have to be performed [Bay99a; Bay99c; Bay02b; Che11d; Wit11]. The variation of $\left|g_{\text{ex}}^{\text{b}}\right|$ with magnetic field obtained is presented in figure 3.12 for QD_{A1} and QD_{A2} at $B_{\text{ext}} = 10$ T and 9 T, respectively. As expected, the electric field dependence of $\left|g_{\text{ex}}^{\text{b}}\right|$ qualitatively

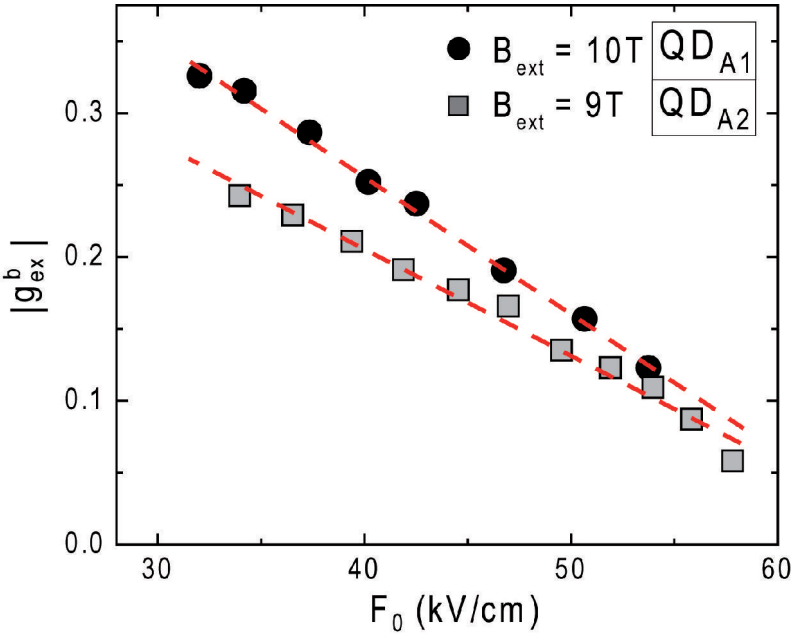

Figure 3.12. *Dependence of $|g_{\mathrm{ex}}^{\mathrm{b}}|$ on the applied electric field for QD_{A1} and QD_{A2} determined at 10 T and 9 T, respectively. The bright exciton g-factor $|g_{\mathrm{ex}}^{\mathrm{b}}|$ was obtained from the PC data presented in figure 3.10 using the equation given in table 2.1 for dots with $< \mathrm{D}_{2d}$ symmetry also taking into account the electric field dependence of the fine structure splitting δ_1^{b} (cf. figure 3.7 and figure 3.8). A clear trend of $|g_{\mathrm{ex}}^{\mathrm{b}}|$ monotonically decreasing for increasing electric field is observed for both dots.*

follows the one of ΔE_{1-2} since the energy splitting at high magnetic fields is dominated by the Zeeman interaction (cf. section 2.2.2). From the PC bias sweeps, a variation of the exciton g-factor from 0.33 to 0.12 is found for QD_{A1} at $B_{\mathrm{ext}} = 10$ T over an electric field range of 32 - 53 kV/cm. Including the PL measurements (cf. figure 3.10), a change from 0.42 to 0.12 is found corresponding to a tunability $\left(|g_{\mathrm{ex}}^{max}| - |g_{\mathrm{ex}}^{min}|\right) / |g_{\mathrm{ex}}^{min}|$ of 250 % [Klo10b]. For QD_{A2}, a change in $|g_{\mathrm{ex}}|$ from 0.34 to 0.07 is observed over an F_0 range from 34 kV/cm to 58 kV/cm. The cause of this strong electric tunability of $g_{\mathrm{ex}}^{\mathrm{b}}$ is discussed in section 3.6.

3.4.2 Non-linear Zeeman splittings

In figure 3.13, the energy splitting between $|E_1\rangle$ and $|E_2\rangle$ is presented as a function of the applied magnetic field for three quantum dots, QD_{A1}, QD_{A2} and QD_{C1}. The splitting ΔE_{1-2} was determined from PC bias sweeps with the randomization procedure applied prior to every measurement point. For each dot, the data was recorded at a fixed F_0 of 38.9 kV/cm at all magnetic fields. This was achieved by adjusting λ_{exc} for every B_{ext} accordingly to compensate for the diamagnetic shift of the system (cf. sections 2.2.3 and 3.2). All three QDs show a finite fine structure splitting δ_1^{b} at zero magnetic field. For $B_{\mathrm{ext}} \neq 0$ T, the energy splitting ΔE_{1-2} is given by a combination of δ_1^{b} and

the Zeeman energy $E_{ex,Z}$ according to the relations given in table 2.1 which were used to fit the experimental data (solid red lines in figure 3.13). For all QDs, a deviation from the expected behavior is observed whereby two cases, labeled *Type-A* and *Type-B*, can be distinguished: For *Type-A* quantum dots (QD_{A1}, QD_{A2}), the splitting for high $B_{ext} > 6$ T stays below the values predicted by the model presented in section 2.2.2. Here, the measured ΔE_{1-2} can be described with a quadratic dependence on the magnetic field [Jov12b], a trend that is particularly apparent for QD_{A2}. For *Type-C* quantum dots (QD_{C1}), the deviation from the expected linear magnetic field dependence in the $\delta_1^b \ll E_{ex,Z}$ - regime is less pronounced than for the *Type-A* dots with splittings ΔE_{1-2} that are found to be larger than predicted by the model for $B_{ext} > 8$ T. This surprising effect is discussed in detail in the following section 3.5.

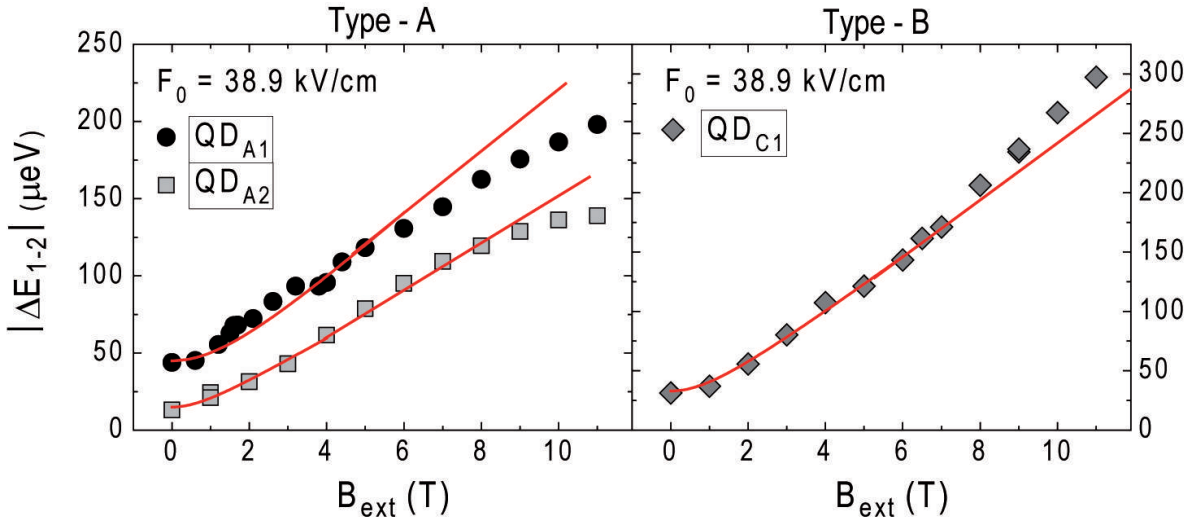

Figure 3.13. *Dependence of ΔE_{1-2} on the applied magnetic field B_{ext} determined for three individual QDs, QD_{A1}, QD_{A2} and QD_{C1}, at the same fixed F_0 of 38.9 kV/cm for all magnetic fields. For all QDs probed, the energy splitting ΔE_{1-2} between the two bright X^0 states $|E_1\rangle$ and $|E_2\rangle$ deviates from the expected behavior (solid red lines) given by a combination of the fine structure splitting δ_1^b and the Zeeman interaction according to the equations listed in table 2.1.*

3.5 Explanation of non-linear Zeeman splitting

In this section, an explanation for the non-linear Zeeman splitting of the neutral exciton states observed in self-assembled InGaAs quantum dots (cf. section 3.4.2) that were investigated with regard to DNP in this thesis is given. The explanation for the effect was developed based on detailed experimental and theoretical investigations by *Jovanov et al.* and *Eisfeller et al.*, respectively. These works allowed to attribute the observed effect to a magnetic field induced hh-lh mixing that leads to a quadratic contribution in the

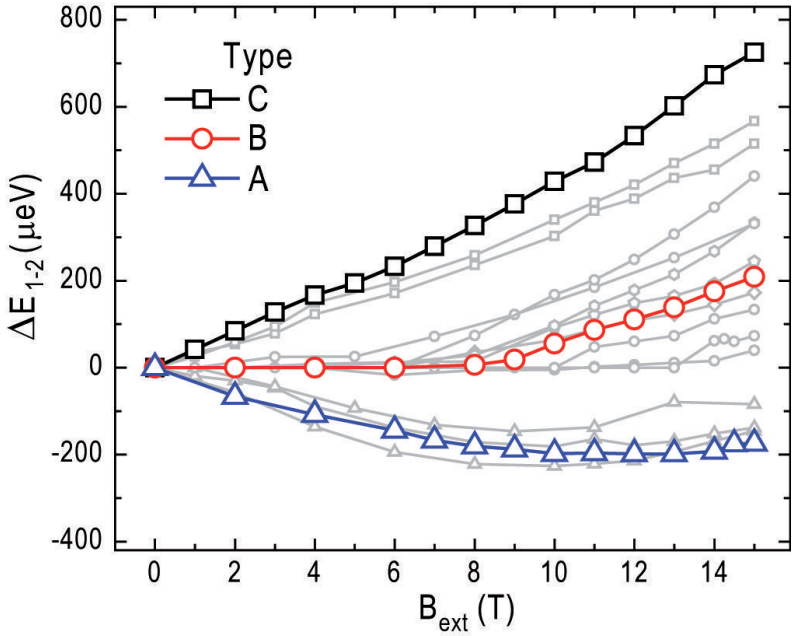

Figure 3.14. *Energy splitting ΔE_{1-2} as a function of the applied magnetic field B_{ext} for a set of single self-assembled InGaAs QDs. The dots show different behaviors that can be arranged into three different groups labeled Type-A (triangles), Type-B (circles) and Type-C (squares). Since no significant fine structure splitting δ_1^{b} was observed for the dots examined, ΔE_{1-2} corresponds to the Zeeman splitting $E_{\text{ex,Z}}^{\text{b}}$. For each category, one QD is highlighted exemplarily. Adapted from [Jov12b].*

B_{ext} dependence of the hole Zeeman interaction. This section is based on Ref. [Jov12b].

The study on non-linear Zeeman splitting presented here was conducted on single, self-assembled $\text{In}_x\text{Ga}_{1-x}\text{As}$ quantum dots with a nominal In-content of $x = 0.5$ grown via molecular beam epitaxy using typical growth parameters listed in Ref. [Jov12b]. Two types of samples were probed, one without and one with the application of the partially capped overgrowth technique including an *In-flush* step (cf. section 2.1.3) where the height of the QD was set to $h_{\text{QD}} = 6$ nm. X-STM measurements in combination with the theoretical model describing the experimental observations of non-linear Zeeman splittings suggest an inverted trumpet like In-profile in the QDs with an indium concentration that decreases from the apex to the base [Bru02; Mig02; Off05; Jov12b]. Furthermore, they revealed that the *In-flush* step effectively reduces the indium content at the apex due to increased desorption during to the flushing process.

A set of > 20 individual QDs from the same sample was probed in photoluminescence experiments with regard to the energy splitting ΔE_{1-2} between the two bright neutral exciton states $|E_1\rangle$ and $|E_2\rangle$ as a function of the magnetic field B_{ext} applied in Faraday geometry. The results of this investigation are summarized in figure 3.14. As no fine structure splitting δ_1^{b} is observed, ΔE_{1-2} is equivalent to the Zeeman splitting $E_{\text{ex,Z}}^{\text{b}}$. Unlike for the measurements on the electric and magnetic field dependence of ΔE_{1-2}

presented above in sections 3.4.2 and 3.4.1, respectively, the experiments discussed in this section allowed not only to determine the magnitude of ΔE_{1-2} but also to assign a sign to the g-factor and, hence, the Zeeman splitting. This was made possible by the application of polarization-resolved techniques in the measurements. As can be seen from figure 3.14, the QDs investigated show qualitatively different behaviors that can be categorized into three different groups labeled *Type-A* (triangles), *-B* (circles) and *-C* (squares). While *Type-C* dot exhibit a positive Zeeman splitting, *Type-A* dots show a negative ΔE_{1-2} and in the *Type-B* group even dots with zero Zeeman splitting are found. The magnetic field dependence of $E^{\mathrm{b}}_{\mathrm{ex,Z}} = g^{\mathrm{b}}_{\mathrm{ex}} \mu_{\mathrm{B}} B_{\mathrm{ext}}$ can be described best using a quadratic fit (solid black, red and blue lines). This corresponds to introducing a magnetic field dependent term to the exciton g-factor: [1] $g^{\mathrm{b}}_{\mathrm{ex}} = g_{\mathrm{e}} + g_{\mathrm{h}} = g^0_{\mathrm{ex}} + g^1_{\mathrm{ex}} B_{\mathrm{ext}}$. For sample grown with the partially capped overgrowth and *In-flush* technique, no *Type-C* and only few *Type-B* dots were observed while most QDs shows *Type-A* behavior [Jov12b].

The labeling of the QDs introduced above in this chapter (QD_{A1}, QD_{A2} and QD_{C1} - cf. figure 3.13) is based on the magnetic field dependence of the energy splitting ΔE_{1-2} observed in the study presented in this section.

To identify the origin of the observed effect on a microscopic basis, eight-band $\mathbf{k}\cdot\mathbf{p}$ calculations in the envelope function approximation based on a realistic QD geometry obtained from X-STM measurements were used to determine the 3D electronic structure of the QD system. The model includes the influence of magnetic fields [Eis11] and effects of strain via deformation potentials and piezoelectric effects [Sti99]. The QDs were modeled to have a truncated lens shape of diameter d_{QD} and height h_{QD} and an inverse trumpet like In-profile with the indium content η_{In} being highest at the apex ($\eta^{\mathrm{apex}}_{\mathrm{In}}$) decreasing towards the base.

The results obtained from the model are presented in figure 3.15 where the Zeeman splitting calculated for three different sets of QD parameters is plotted as a function of the applied magnetic field: (i) $d_{\mathrm{QD}} = 50$ nm, $\eta^{\mathrm{apex}}_{\mathrm{In}} = 0.4$ (blue line); (ii) $d_{\mathrm{QD}} = 45$ nm, $\eta^{\mathrm{apex}}_{\mathrm{In}} = 45$ (red line); (iii) $d_{\mathrm{QD}} = 25$ nm, $\eta^{\mathrm{apex}}_{\mathrm{In}} = 50$ (black line). The calculated B_{ext} dependencies reproduce the three empirically found cases of *Type-A*, *-B* and *-C* dots. As indicated by the schematics of the QD geometry used to calculate each curve, the QD diameter and In-profile play a major role for the magnetic field-dependence of ΔE_{1-2}. The energy splitting reduces with increasing dot size and decreasing indium content, even changing sign over the parameter range examined. Simultaneously, the non-linear component becomes more and more pronounced leading to a stronger deviation from the linear behavior. The variation of the QD parameters used to describe the full range of observations made in experiment are consistent with the fluctuation of the size and material composition of the QDs determined by X-STM measurements [Jov12b]. This

[1] Note that for the model in this and the following section (3.5 and 3.6), the following convention was used: $g_{\mathrm{e}} = -g^m$, $g_{\mathrm{h}} = g^m$ and $g_{\mathrm{ex}} = g_{\mathrm{e}} + g_{\mathrm{h}}$, where $g^m = E^{m\uparrow} - E^{m\downarrow}$ is the g-factor of the m^{th} electronic state with the positive $[001]$ axis as the quantization axis. This choice of quantization direction is natural in multi-band calculations but leads to inverted signs as compared to many other theoretical and experimental works.

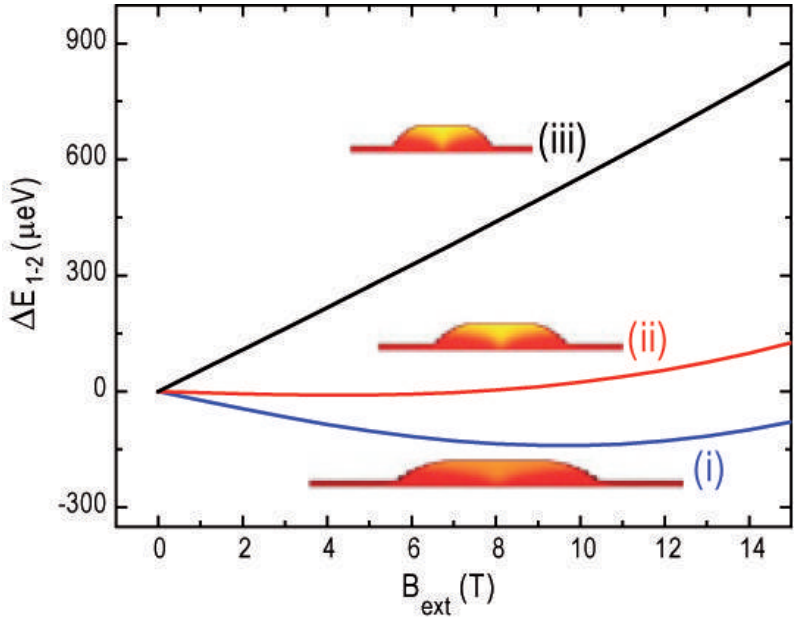

Figure 3.15. *Energy splitting of the bright neutral exciton states as a function of the magnetic field calculated for three different structures, reproducing the behavior of Type-A, -B and -C dots. The dots were modeled using the same height of $h_{QD} = 6$ nm but different diameters d_{QD} and indium contents η_{In} at the apex: (i) Type-A: $d_{QD} = 50$ nm, $\eta_{In}^{apex} = 0.4$; (ii) Type-B: $d_{QD} = 45$ nm, $\eta_{In}^{apex} = 45$; (iii) Type-C: $d_{QD} = 25$ nm, $\eta_{In}^{apex} = 50$. Adapted from [Jov12b].*

makes the observation that for the sample grown with the *In-flush* technique mainly one type of QDs (*Type-A*) are found plausible since this process leads to a homogenization of the QD height and also alters the In-profile, effectively reducing fluctuations in QD characteristics across a sample (cf. section 2.1.3).

The effect of non-linear Zeeman splittings in semiconductor nanostructures has first been reported for electrons [Dob88] in GaAs-AlGaAs and holes [War93; Tra95; Kot01] in GaAs-InGaAs quantum wells and superlattices. For the latter, the effect could be attributed to magnetic field induced mixing of hh-$\Uparrow$ states and light hole bands that was shown to lead to a heavy hole g-factor varying linearly with the magnetic field [Kot01]. As mentioned above (cf. figure 3.15), the quadratic character of the Zeeman splitting becomes more and more prominent for increasing dot diameter. The comparatively weak lateral confinement due to the low In-content in combination with the large diameter of the QD leads to the formation of states that somewhat resemble quantum well states and, therefore, result in a similar behavior that becomes more pronounced the larger the dot is. This intuitive interpretation is supported by the calculations which confirm that the quadratic component of the magnetic field dependence of ΔE_{1-2} stems exclusively from hh-like lowest energy valence band state due to coupling of the hh state to light hole bands adding a magnetic field term $g_{ex}^{1} B_{ext}$ to the bright exciton g-factor g_{ex} [Jov12b].

3.6 Explanation of electrical g-factor tuning

In this section, an explanation for the observed strong electrical tunability of the exciton g-factor demonstrated in section 3.4.1 is given. Based on work by *Jovanov et al.* and *Eisfeller et al.*, respectively, the effect could be attributed to a strong electric field dependence of the hole g-factor caused by angular momentum quenching with the electron contributing only weakly [Jov11]. This section is based on Ref. [Jov11].

The investigations regarding electrical g-factor tuning were carried out on single, self-assembled $In_xGa_{1-x}As$ QDs with a nominal In-content of $x = 0.5$ grown via molecular beam epitaxy using typical growth parameters listed in Ref. [Jov11]. All QDs used for this study showed *Type-C* behavior. However, the results are transferable to *Type-A* dots albeit with different amplitudes of the observed effects due to the different QD parameters [Eis12a].

Figure 3.16 shows the dependence of the exciton g-factor on the applied electric field. The graph depicts experimental data obtained from two individual QDs, QD_{C2} and QD_{C3} at $B_{\text{ext}} = 10$ T (red circles) and 15 T (blue squares) as well as results deduced from eight-band $\mathbf{k}\cdot\mathbf{p}$ calculations (dashed red line). By performing both PC (closed symbols) and PL (open symbols) measurements, a range from 5 kV/cm to 75 kV/cm was covered. The exciton g-factor g_{ex}^{b} was determined by fitting the $|E_1\rangle$ and $|E_2\rangle$ resonances in the recorded PL and PC spectra and using the relation given in table 2.1. In contrast to the results discussed above in section 3.4.1 which are summarized in figure 3.12, not only the magnitude of g_{ex}^{b} but also its sign could be measured due to the application of polarization resolved experimental techniques. As for the observations on QD_{A1} and QD_{A2} (cf. 3.4.1), a monotonic, almost linear variation of g_{ex} as a function of the applied electric field is observed. For both, QD_{C2} and QD_{C3}, an increase of g_{ex}^{b} with increasing electric field is observed. The same outcome was found for all other dots examined in this study and is also reproduced by the calculations. This indicates that the sign of g_{ex}^{b} for QD_{A1} and QD_{A2} is negative. In this case, the reduction of $|g_{\text{ex}}|$ with increasing electric field found in experiment corresponds to an increase of g_{ex}^{b}. This is also consistent with conclusions drawn from the observation of non-linear Zeeman splittings presented in the previous section 3.5 where generally a negative Zeeman splitting is observed for *Type-A* dots.

As for the study presented in the previous section, eight-band $\mathbf{k}\cdot\mathbf{p}$ simulations based on the same dot geometry and composition (cf. section 3.5) were employed to investigate the underlying mechanisms and the microscopic origin of the effect. For the calculation of the electronic structure, strain fields [Sti99], the applied magnetic field [And08; Bur99b] and Coulomb interactions are taken into account as described in Ref. [Jov11]. The results are shown in figure 3.16 (dashed red line). Using a QD structure with $d_{\text{QD}} = 25$ nm, $h_{\text{QD}} = 6$ nm and $\eta_{\text{In}}^{\text{apex}} = 35$ %, the model not only reproduces the observed dependence of g_{ex} on electric fields but also simultaneously yields the dc Stark

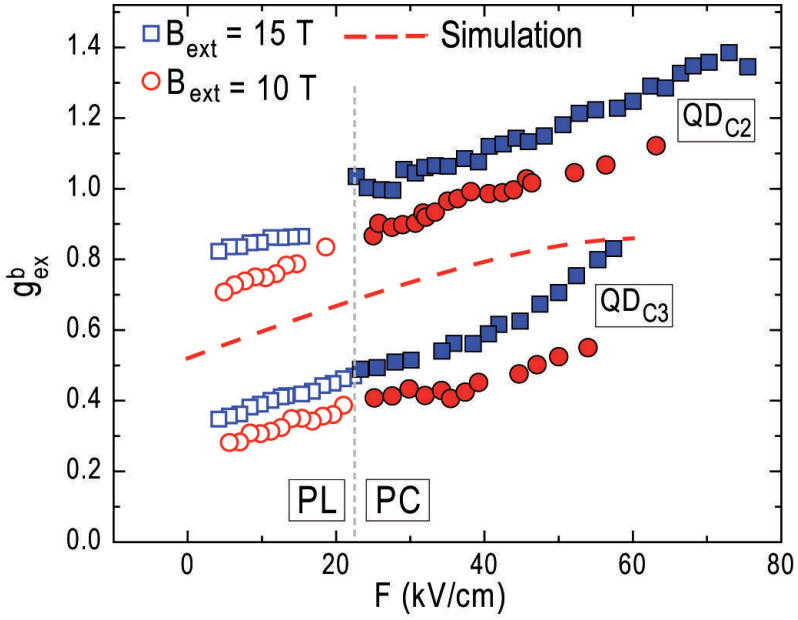

Figure 3.16. *Bright exciton g-factor $g_{\mathrm{ex}}^{\mathrm{b}}$ as a function of the applied electric field obtained from theory (dashed line) and experiments carried out on two individual QDs (symbols). To to be able to probe the neutral exciton Zeeman splitting over an electric field range of $\approx$ 70 kV/cm, photocurrent (closed symbols) as well as photoluminescence (open symbols) measurements were performed on the X^0 states. The experimental data as well as the theoretical results obtained from eight-band $\boldsymbol{k}\cdot\boldsymbol{p}$ calculations reveal a clear trend of increasing $g_{\mathrm{ex}}^{\mathrm{b}}$ for increasing electric fields. Adapted from [Jov11].*

shift, diamagnetic shift and transition energy observed for the QDs in experiment.

The bright exciton g-factor $g_{\mathrm{ex}}^{\mathrm{b}}$ calculated for this particular set of QD parameters is plotted as a function of the applied electric field in the left panel of figure 3.17 (black line). Also depicted are the individual contributions of the electron (orange line) and hole (green line) ($g_{\mathrm{ex}}^{\mathrm{b}} = g_{\mathrm{e}} + g_{\mathrm{h}}$, cf. table 2.1). The graph clearly reveals that the variation of $g_{\mathrm{ex}}^{\mathrm{b}}$ is dominated by the contribution of the hole as g_{h} shows a pronounced electric field-dependence changing from $g_{\mathrm{h}} = -0.45$ at $F = 0$ kV/cm to -0.01 at $F = 60$ kV/cm. In contrast to that, the electron g-factor g_{e} is only weakly affected undergoing a shift from $g_{\mathrm{e}} = 0.98$ to 0.87 by ramping the electric field over the same range of 60 kV/cm.

In numerous theoretical works, several contributions to the g-factors in self-assembled QDs such as strain-induced band mixing [Nak05] or orbital angular momentum quenching [Lom85; Pry06; Kis98] have been identified and investigated. The model used here allows to unambiguously identify quenching of the orbital angular momentum to be primarily responsible for the strong electric field-dependence of the hole g-factor. The contribution of any electronic state with orbital index m to the g-factor can be written as [Kis98]

$$g_m = g_0 + g_{\mathrm{L},m} + g_{\mathrm{R},m}\,. \tag{3.1}$$

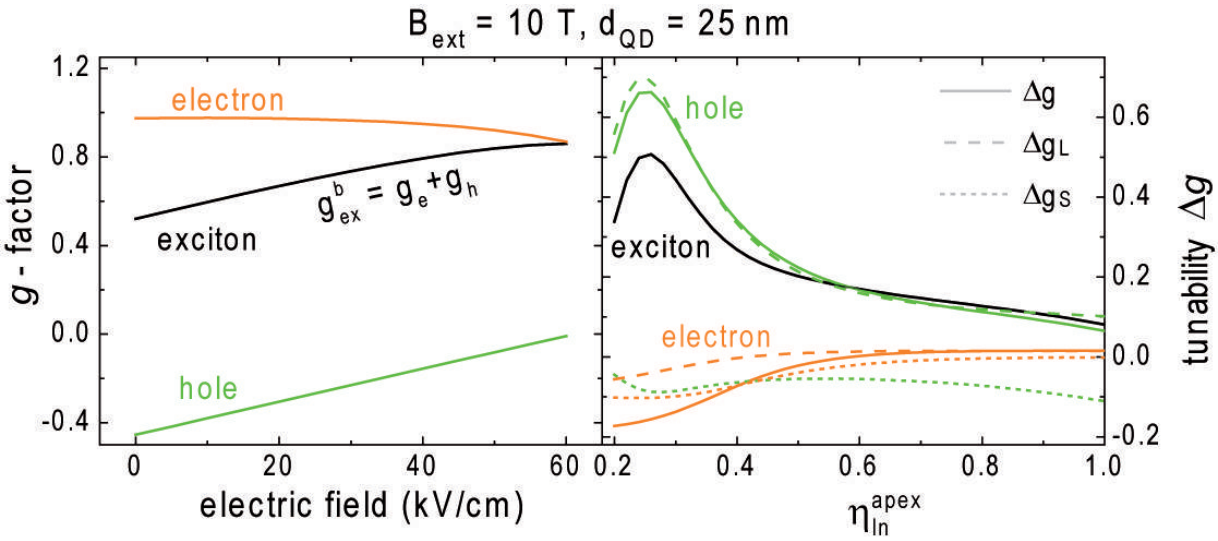

Figure 3.17. *Left: Calculated g-factor of the exciton, electron and hole as a function of the applied electric field at $B_{\text{ext}} = 10$ T for a dot with $d_{\text{QD}} = 25$ nm, $h_{\text{QD}} = 6$ nm and $\eta_{\text{In}}^{\text{apex}} = 35$ %. Right: Electric field tunability of the exciton, electron and hole g-factor (solid lines). The tunability Δg is defined as the difference of the g-factor at $F = 0$ kV/cm and $F = 60$ kV/cm. Also depicted are the contributions of the individual components, remote bands (g_R; dotted line) and angular momentum (g_L; dashed line), to the tunability. Adapted from [Jov11].*

Here, g_0 is the free electron g-factor; $g_{\text{R},m}$ is the contribution of remote bands which is a function of the indium content within the envelope function and is treated perturbatively in the model; $g_{\text{L},m}$ is the contribution of the angular momentum of the electron and can be expressed using first oder perturbation theory. It reads [Kis98]

$$g_{\text{L},m} = -\left(\langle m\uparrow|\boldsymbol{L}_z|m\uparrow\rangle - \langle m\downarrow|\boldsymbol{L}_z|m\downarrow\rangle\right), \tag{3.2}$$

where $\boldsymbol{L}_z$ is the angular momentum operator given by $\boldsymbol{L}_z = (\boldsymbol{r}\times\boldsymbol{P})_z$ and $\boldsymbol{P}$ the eight-band momentum operator [For00]. From equation 3.2, the electric field-dependence of $g_{\text{L},m}$ can be determined. The result is depicted in the right panel of figure 3.17 where the tunability (defined as $\Delta g = g$ (60kV/cm) $-g$ (0kV/cm)) of g_{L} (dashed lines), g_{R} (dotted lines) and the resulting g-factors (solid lines) are plotted for the electron and hole states as a function of the indium content at the apex $\eta_{\text{In}}^{\text{apex}}$. Also plotted is the resulting tunability of the exciton g-factor. The graph clearly shows that the g_{ex} tunability is dominated by $\Delta g_{\text{L,h}}$, the angular momentum contribution of the hole, whereas the electronic contribution has only a weak effect on Δg_{ex}. It can also be seen that the influence of the individual contributions g_{L} and g_{R} is different for the electron and the hole. Δg_{h} is almost entirely determined by the angular momentum part while Δg_{L} plays a less dominant role for the electron. Furthermore, a characteristic dependence of the tunabilities on $\eta_{\text{In}}^{\text{apex}}$ is observed with a maximum of $\Delta g_{\text{L,h}}$ (and, consequently, also of Δg_{h} and Δg_{ex}) for an indium concentration at the apex of 25 %- 35 %. The fact that the

electrical field g-factor tunability observed for the QD invesitgated here and in section 3.4.1 is so large in comaprison to similar effects reported in literature for $In_{0.5}Ga_{0.5}As$ dots suggests that the actual In content incorporated into the dots is lower than the nominal value of 0.5.

Calculations performed for a *Type-A* dot using the parameters given in the previous section ($d_{QD} = 50$ nm, $\eta_{In}^{apex} = 0.4$) show a g_{ex}^{b} tunability of $\Delta g_{ex}^{b} = 0.3$ [Eis12a]. Besides the dependence of Δg_{ex}^{b} on the indium content at the apex as presented in the left panel of figure 3.17, a general trend of decreasing g-factor tunability for increasing diameter and decreasing height of the quantum dot is found [Eis12a].

The calculations show that Δg_R only plays a minor role for the g-factor tunability. This disagrees with the idea that a change in alloy overlap due to wavefunction displacement caused by the electric field might be responsible for g-factor tunability as was speculated in previous works [Klo10b]. In fact, the model reveals that this effect, that was shown to lead to appreciable g-factor modulation in semiconductor quantum wells [Ivc97; Jia01; Sal01] and coupled quantum dot systems [Dot06], is only of minor importance here. From the simulations, a change of the In-alloy overlap of only ≈ 0.14 % and ≈ -2.2 % for the electron and hole, respectively, is found for a change of the electric field from $F = 0$ kV/cm to 60 kV/cm using the QD paramenters given on the left side of figure 3.17. This small variation only leads to a very small contribution of Δg_R to the overall g-factor tuning.

To gain a qualitative understanding of the results presented on the right side of figure 3.17, it is useful to express g_L employing second-order perturbation theory which is equivalent to the expression given in equation 3.2 [Kis98]. Using this approach, it reads

$$g_{L,m} = -\frac{2m_0}{\hbar^2} \sum_{m' \neq m,\, r'} \frac{|\langle m \uparrow | \boldsymbol{P}_+ | m' r' \uparrow \rangle|^2 - |\langle m \uparrow | \boldsymbol{P}_- | m' r' \uparrow \rangle|^2}{E_m - E_{m'}}, \tag{3.3}$$

where $|\langle m \uparrow | \boldsymbol{P}_\pm | m' r' \uparrow \rangle|$ are the momentum matrix elements that exhibit an electric field dependence. Application of an electric field potentially reduces the momentum matrix elements between particular pairs of bound conduction and valence band states. As a consequence of the completeness of the eigenstates, this reduction is compensated by an increase of the momentum matrix elements between other orbital states [Jov12b; Eis12b]. The different impact of this effect on the angular momentum part of g_e and g_h stems from the different number of bound states and energy spacings between them. For the QD parameters used here, > 24 bound hole states but only 3 bound electron states are predicted. This means, that for the electron state, there are many bound hole states available to compensate for the electric field induced modification of the momentum matrix element. As the energy spacing between these hole states is small, the energy difference in the denominator of equation 3.3 is similar for all pairs of conduction and valence band states involved. As a result, $\Delta g_{L,e}$ does not exhibit a strong dependence on electric fields. For the hole state on the other hand, only a small number of electron

states is available to compensate for the change of the momentum matrix element. The fact that the energy spacing between the electron states is much larger as compared to the hole states due to the lower effective mass results in an increase of the energy term in the denominator of equation 3.3. This corresponds to a reduction of $g_{\mathrm{L,h}}$ - i.e. a quenching of the angular momentum.

3.7 Summary

In this chapter, tuning of the bright exciton g-factor g_{ex} in single self-assembled QDs via applied electric and magnetic fields was demonstrated. To gain a deeper insight into these effects, eight-band $\mathbf{k}\cdot\mathbf{p}$ calculations based on a realistic QD geometry and composition obtained from structural investigations were performed. The simulations reproduce the experimental results and allow to identify the microscopic origin of the g-factor tunability. In both cases, the effect is dominated by variation of the hole g-factor with the electron contributing only weakly. The electrical tunability stems from electric field induced quenching of the angular momentum of the hole g-factor [Jov11; Jov12a; Eis12b]. The magnetic tunability, found particularly in large QDs, arises from magnetic field induced hh-lh mixing of the valence band ground state that introduces a magnetic field dependent contribution to g_{ex} [Jov12b; Jov12a; Eis12b].

4

Dynamic nuclear polarization in neutral quantum dots

The exceptionally well isolated nuclear spin system in semiconductor quantum dot nanostructures has attracted considerable attention in recent years [Coi09; Tay03; Kha02; Oul07; Xu09; Mal07; Ebl06; Bra05; Gam01; Tar07; Yok05; Mos09; Mal09; Mak08a; Mak08b; Che11d; Blu11]. Experimental and theoretical studies of optical nuclear spin orientation in bulk material date back to the 1950s [Car53; Car56; Abr78; Mei84]. Lately, optically active quantum dots opened up new ways to gain insights into nuclear spin physics in semiconductors [Coi09; Sch03; Urb12]. The hyperfine interaction couples confined electrons and the $10^4 - 10^5$ nuclear spins within the QD [Sch03; Coi09] and opens the possibility to address the nuclear spin environment.

Consequently, a single electron confined in a semiconductor quantum dot provides a model system to study the central spin problem where one central spin is coupled to an ensemble of spins that are not interacting with each other.

For the potential use of QDs as fundamental building blocks in quantum computation, the coupling between confined charge carriers and the solid state environment can be both a bane and a boon. On the one hand, the potential opto-electronic access to the mesoscopic nuclear spin system yields strong potential for future applications in quantum information technology such as the use of nuclear spins as a long-lived memory for mesoscopic quantum bits [Tay03]. On the other hand, hyperfine coupling to the fluctuating random nuclear spin system was identified as the main source of spin decoherence for electrons confined in QDs limiting the time for logical operations in a spin-based quantum dot qubit [Bur99a; Erl01; Kha02; Mer02; Coi04; Pet05; Kop05; Joh05; Han08; Blu11]. Since almost all advances in the use of QDs for quantum information processing have been made in III-V semiconductors where all nuclei carry a non-zero

angular momentum [Gra72], reliable strategies to control the nuclear field are highly desirable. Particularly for self-assembled InGaAs quantum dots, all atoms carry a non-zero nuclear spin (cf. table 2.2). As a result, the coupling of confined charge carriers to the nuclear spin system and the resulting effects on the spin dynamics were studied intensively both in experiment [Pet05; Kop05; Bru09; Urb12] and theory [Bur99a; Erl01; Kha02; Mer02; Coi04; Fis08; Tes09]. A comprehensive overview of nuclear spin physics in quantum dots can be found in Refs. [Sch03; Coi09; Urb12]. In fundamental experiments, it was shown that fluctuations of the nuclear spin polarization can be suppressed via repeated optical or electrical generation of spin polarized charge carriers [Gre07; Oul07; Rei08; Lat09; Vin09; Xu09]. Hyperfine-mediated transfer of angular momentum between an electron and a nuclear spin via electron-nuclear spin flip-flop processes allows to manipulate the nuclear spin ensemble and prepare it in a highly polarized, non-thermal equilibrium state [Bro96; Urb12]. It was demonstrated that this effect, called dynamical nuclear polarization (DNP), can have a stabilizing effect on the electron spin polarization significantly extending its relaxation time [Oul07] and can even be used to lock QD transitions to the energy of an excitation laser [Lat09]. Very recently, coherent control of the nuclear spin ensemble has been demonstrated in NMR experiments on natural strain free GaAs/AlGaAs QDs opening the way to a new class of experiments based on DNP and nuclear spin effects [Mak11].

To date, the vast majority of experiments on dynamical nuclear polarization have been carried out on charged QDs containing a resident electron [Mal07; Ebl06; Bra05a]. However, this system is subject to fast depolarization effects that are typically mediated by the residual electron in the dot [Mal07]. Comparatively few studies of DNP in neutral QDs have been reported [Gam01; Tar07; Yok05; Mos09; Mal09; Mak08b; Kor99; Hoe12] for which a stable polarization of the nuclear spin system over timescales exceeding 1 h has been demonstrated [Mal09] making it a system of particular interest.

In this chapter, a comprehensive investigation of a new nuclear spin pumping cycle generating DNP in an uncharged InGaAs quantum dot is presented. The nuclear spin environment is addressed via resonant optical excitation of the lowest orbital state of the neutral QD. In contrast to other resonant excitation experiments on DNP [Che10a; Gre07; Klo11a], the measurements in this work were performed in the photocurrent (PC) regime were optically generated electrons and holes tunnel out of the dot into the corresponding contacts on a timescale much faster than the radiative recombination time due to the application of large electric fields. The measurements reveal a large maximum polarization of the nuclear spin ensemble of 54% and, most surprisingly, DNP predominantly occurs upon pumping of the higher energy Zeeman level of the two bright X^0 states. Furthermore, the associated Overhauser magnetic field B_n is found to be always generated with the same relative orientation with respect to the externally applied magnetic field B_ext irregardless of the state used to pump it.

To gain a better understanding of the observed effects and the underlying processes, a detailed theoretical model of the driven neutral QD was developed that allows to

perform numerical calculations simulating the actual experimental procedure used in the measurements. Solving the master equation of the system, the simulations of the steady-state population in the excitonic subspace qualitatively reproduce the experimental results.

Further insights into the system are given by measuring the time evolution of the nuclear spin polarization both under resonant optical pumping and when kept in the dark. As the detected photocurrent signal is a quantitative measurement, the total number of charge carriers generated in the dot per time can be deduced which, in combination with the time-resolved buildup of B_n, allows to monitor the buildup of the Overhauser field in real-time and determine the efficiency of the hyperfine-mediated nuclear spin pumping giving an estimate of the coupling strength. Probing the depolarization rate of the nuclear spin polarization reveals that even after 1.5 h, 80 % of the generated polarization is still present. Only after more than 2.5 h, the Overhauser field has decreased to 50 % of its initial value.

In section 4.1, the method of steady-state PC bias sweeps employed in this thesis is introduced. The dependence of the Overhauser field-generated during these measurements on the electric and magnetic field applied as well as the optical excitation power used is presented. In section 4.2, the model developed to describe the observations in order to identify and quantify the relevant processes involved is discussed. Furthermore, the results of numerical simulations based on the model are compared with the experimental data showing the achievements and chances but also the limitations of the model. In section 4.3, investigations on the buildup dynamics of nuclear spin polarization under resonant pumping as well as the decay of the Overhauser field are presented. In section 4.4, first results on DNP in a a quantum dot molecule consisting of two strongly coupled QDs are shown and the potential of that system for further investigations is discussed. The main findings presented here are published in [Klo10a; Kie10] and can also be found in [Klo12]. This chapter is based on [Klo10a; Klo12].

4.1 Steady-state photocurrent bias sweeps

In this section, the investigation of dynamical nuclear spin pumping in neutral quantum dots is presented. The experimental technique employed for this purpose was photocurrent spectroscopy carried out as electric field sweeps under illumination at a fixed wavelength λ_exc. In this technique, the quantum confined Stark effect [Mil84; Fry00b; Fin01a] is used to tune the transition energies of the QD levels in and out-of resonance with the laser as described in detail in section 3.1. Resonant pumping of the states can lead to a buildup of nuclear spin polarization via hyperfine-mediated electron-nuclear spin flip-flop processes [Bro96; Mak08b; Lat09]. The generated polarization of the nuclear spin bath acts back on the charge carriers confined in the dot in the form of an effective magnetic field, the so-called Overhauser field B_n. As a result, the QD levels

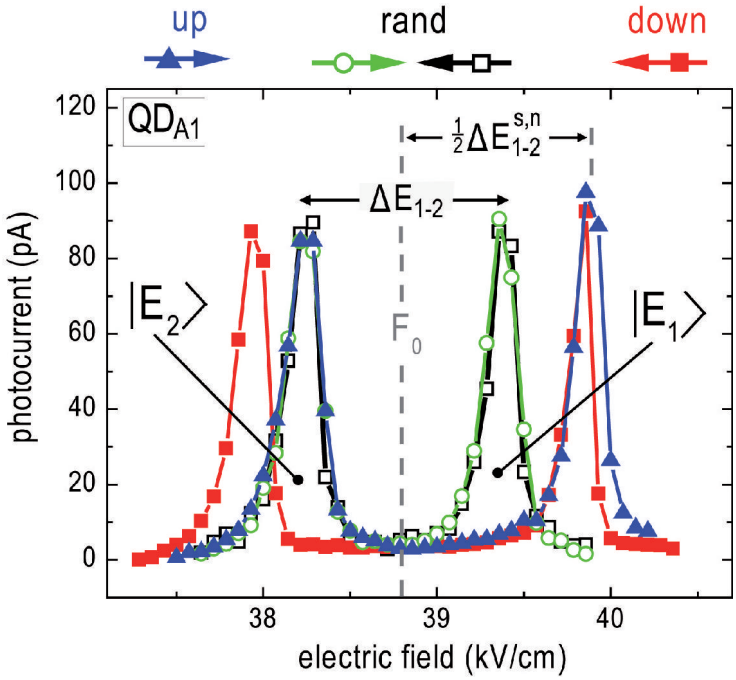

Figure 4.1. *Photocurrent bias sweeps performed on QD_{A1} at $B_{ext} = 5.5$ T, $T \approx 10$ K, $P_{exc} = 30$ µW with and without application of the randomization procedure (denoted 'rand') prior to the measurement of every data point. Clearly observable are the two resonances of the bright X^0 states $|E_1\rangle$ and $|E_2\rangle$. The color and symbol coding for the different types of electric field sweeps will be used throughout the whole chapter. The position of the peaks depends on the direction of the electric field sweep and on whether the randomization procedure is employed or not. The energetic shift is caused by DNP generated during the optical excitation of the QD during the measurement. F_0 denotes the electric field value in the center between the two resonances. A constant offset of 100 pA was subtracted from all traces for the sake of clarity.*

exhibit a shift in energy, the Overhauser shift δ_n, that can be used as a probe for the nuclear polarization. To study this phenomena, it is necessary to obtain reference data for an unpolarized state of the nuclear spin system in the dot. This was achieved by application of a randomization procedure (introduced in figure 3.4) which effectively depolarizes the nuclear spin environment prior to the recording of every data point in the sweep and allows to record PC spectra in the absence of any nuclear spin polarization. The setup used to perform the measurements is the same as introduced in section 3.1 and depicted in figure 3.1.

Figure 4.1 exemplarily presents a set of bias sweeps at $B_{ext} = 5$ T carried out on QD_{A1} with (open light and closed dark green circles) and without (red squares and blue triangles) application of the randomization procedure (cf. figure 3.4) and for different sweeping directions of the electric field, i.e. from low to high ('sweep up' – blue triangles and empty light green circles) and from high to low ('sweep down' – red squares and

closed dark green circles) values. The color and symbol coding for the different types of electric field sweeps will be used throughout the whole chapter. The recorded PC spectra clearly reveal the two optically active ('bright') *s*-shell states of the neutral exciton X^0, $|E_1\rangle$ and $|E_2\rangle$, which are tuned in and out of resonance with the laser energy by the QCSE. As before, the electric field value in the center between the two resonances is again referred to as F_0.

From the bias sweeps presented in figure 4.1, several general observations can be made:

(i) In strong contrast to the bias sweeps performed without the randomization scheme prior to every data point, an insensitivity to the sweep direction is found when the procedure is applied. As discussed in section 3.1, the fact that the PC resonances coincide perfectly for both up and down-sweeps allows to conclude that the randomization routine indeed prevents the buildup of nuclear polarization during a bias sweep. Moreover, it can be deduced that DNP during the measurement of each data point between these depolarization procedures is negligible for the powers and illumination times used. Consequently, this technique allows to probe the exciton levels in the absence of nuclear spin polarization.

(ii) A clear difference exists between the up- and down-sweep performed without the randomization procedure during the bias sweep. These differences are shown to be caused by DNP and the resulting Overhauser field B_n [Ove53] introduced in section 2.2.4 which is generated by the partially polarized nuclear spin ensemble within the QD. As will be discussed in detail later in this chapter, the nuclear polarization is built up due to hyperfine-assisted flip-flops between the nuclei and the electrons pumped through the dot during the measurement. These processes simultaneously exchange one unit of spin orientation of an electron and a nuclear spin [Ove53; Bro96; Coi09]. The effective magnetic field B_n leads to an additional Zeeman interaction and introduces an Overhauser shift of $\delta_\mathrm{n} = g_\mathrm{e}\mu_\mathrm{B}B_\mathrm{n}$ to the states [Bro96; Gam01]. To avoid any accumulative effects and to ensure a well defined initial state for every measurement, the randomization procedure was applied once before every bias sweep to delete any residual nuclear polarization.

(iii) The effect of DNP is qualitatively different for excitation of the two Zeeman split states $|E_1\rangle$ and $|E_2\rangle$ of the neutral exciton as the Overhauser shift of the states induced during the up- and down-sweeps without the randomization procedure are not symmetric with respect to the reference curves. The observed *asymmetric* nuclear spin pumping mechanism is shown below to arise from the characteristic level structure of the neutral exciton manifold and the mixed character of the bright as well as the dark states [Klo10a]. For all measurements without randomization, the electric field was swept at most at 0.011 kV/cm per second, slow in comparison to the time needed to reach the steady state of the nuclear spin polarization. This ensures that the system is in a steady-state configuration throughout the whole measurement and the maximum achievable steady-state Overhauser shift $\delta_\mathrm{n}^\mathrm{s}$ is obtained as confirmed below by the time-resolved experiments in

section 4.3.1. As indicated in the graph, the energy splitting between $|E_1\rangle$ and $|E_2\rangle$ in the presence of a Overhauser field in steady-state configuration is denoted $\Delta E^{s,n}_{1-2}$.

To demonstrate the *asymmetry* observed for pumping the two bright exciton states and illustrate the interpretation and evaluation of the PC traces recorded, we discuss the PC bias sweeps presented in figure 4.1. For the up-sweep, first $|E_2\rangle$ is tuned into resonance with the laser energy by the QCSE [Mil84; Fry00b; Fin01a]. Although the QD is optically excited as can be deduced from the detected PC signal of ≈ 90 pA, corresponding to $\approx 6 \cdot 10^8$ electrons per second pumped through the dot assuming a near unity detection efficiency [Beh01; Fin01a; Beh02], no significant polarization of the nuclear spin bath is observed since the recorded curve exactly retraces the reference measurement obtained without any DNP effects. However, as $|E_1\rangle$ approaches the laser energy, the system is obviously subject to nuclear spin pumping since a pronounced shift of the state towards higher electric fields is observed. This shift towards higher transition energies indicates an increase in the Zeeman splitting of the bright X^0 states. It occurs as a 'pushing' of the resonance as for this sweeping direction of the electric field both the QCSE as well as the built-up Overhauser field shift $|E_1\rangle$ into the same direction. When the electric field is swept in the opposite direction, first the energetically higher $|E_1\rangle$ is tuned towards the laser energy. Again, buildup of an Overhauser field is observed. However, in a down-sweep, the $|E_1\rangle$ resonance is 'pulled' towards the laser energy by the Overhauser shift. This leads to a different buildup dynamics of the nuclear spin polarization as shown below in the time-resolved measurements. As a result, not the full steady-state polarization is reached in the down-sweep for the experimental parameters used in this measurements. As the electric field is swept further down, the energetically lower $|E_2\rangle$ state is found to be red shifted as compared to the reference measurement. In combination with the information obtained by the up-sweep this clearly shows that the nuclear polarization generated by optical pumping of the higher energy Zeeman branch ≈ 170 s earlier in the bias sweep is still present. As will be demonstrated later in this chapter, the *asymmetry* in DNP observed for pumping the two, energetically distinct Zeeman levels $|E_1\rangle$ and $|E_2\rangle$ is shown to persist over the whole range of static magnetic fields B_{ext} and excitation energies λ_{exc} investigated for which DNP occurs. Moreover, it follows a characteristic magnetic field dependence that is well described by our model as will be discussed in sections 4.1.1 and 4.2, respectively.

In figure 4.2, steady-state PC bias sweeps are compared for four individual QDs from the same sample and performed over the same electric field region. For *Type-A* and *Type-C* dots as introduced in section 3.4.2, qualitatively different responses to resonant excitation during the sweeps are found. Three out of four examined QDs (QD_{A1}, QD_{A2}, QD_{A3}) exhibit a *Type-A* magnetic field-dependence of the bright X^0 energy splitting ΔE_{1-2} as presented in figure 3.13. As can be seen in the upper panel of figure 4.2, all of them show the same behavior in terms of DNP, identical to the one presented in figure 4.1 and discussed directly above. Only one dot (QD_{C1}, cf. figure 3.13) was found to be

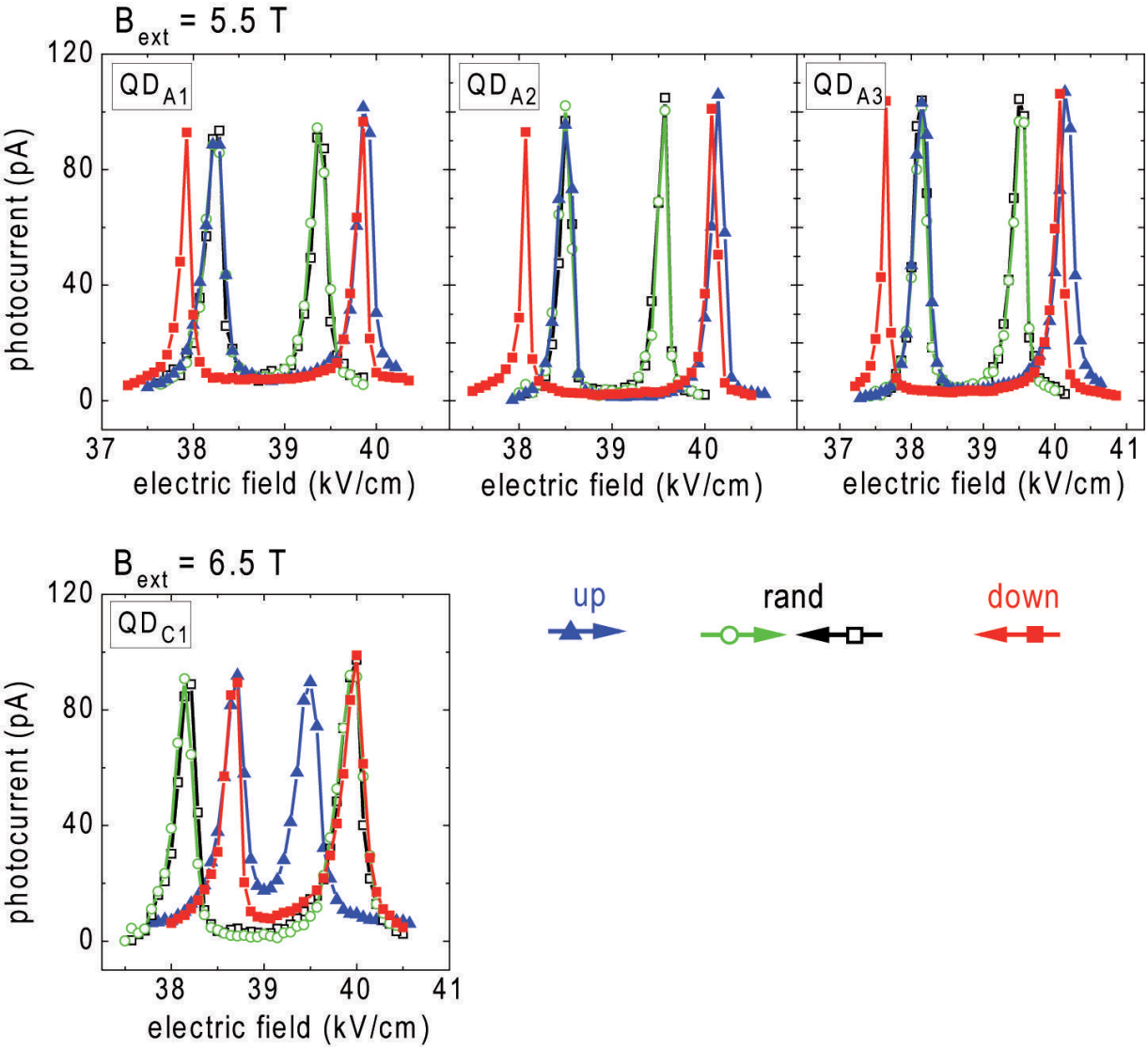

Figure 4.2. *Steady-state PC bias sweeps on four individual quantum dots probed on the same sample. Two different types of responses, Type-A (upper panel) and Type-C (lower panel), are found. Type-A dots correspond to the case presented and discussed in figure 4.1 whereas Type-C dots show a behavior that can, in comparison, be described as 'inverted'.*

of type *C* according to the definition given in section 3.4.2. The PC traces recorded in steady-state bias sweeps on QD_{C1} are depicted in the lower panel of figure 4.2. It shares several characteristic features with *Type-A* dots regarding occurrence of Overhauser shifts in electric field sweeps such as the *asymmetry* for pumping of the two Zeeman branches of the neutral exciton states. However, some qualitative differences are found based on which the behavior of *Type-C* can be described as 'inverted' as compared to *Type-A* dots: Instead of $|E_1\rangle$, polarization of the nuclear spin bath occurs upon resonant optical excitation of the energetically lower X^0 state $|E_2\rangle$. Furthermore, the Overhauser shift does not result in an increase but a reduction of the energy splitting ΔE_{1-2} between

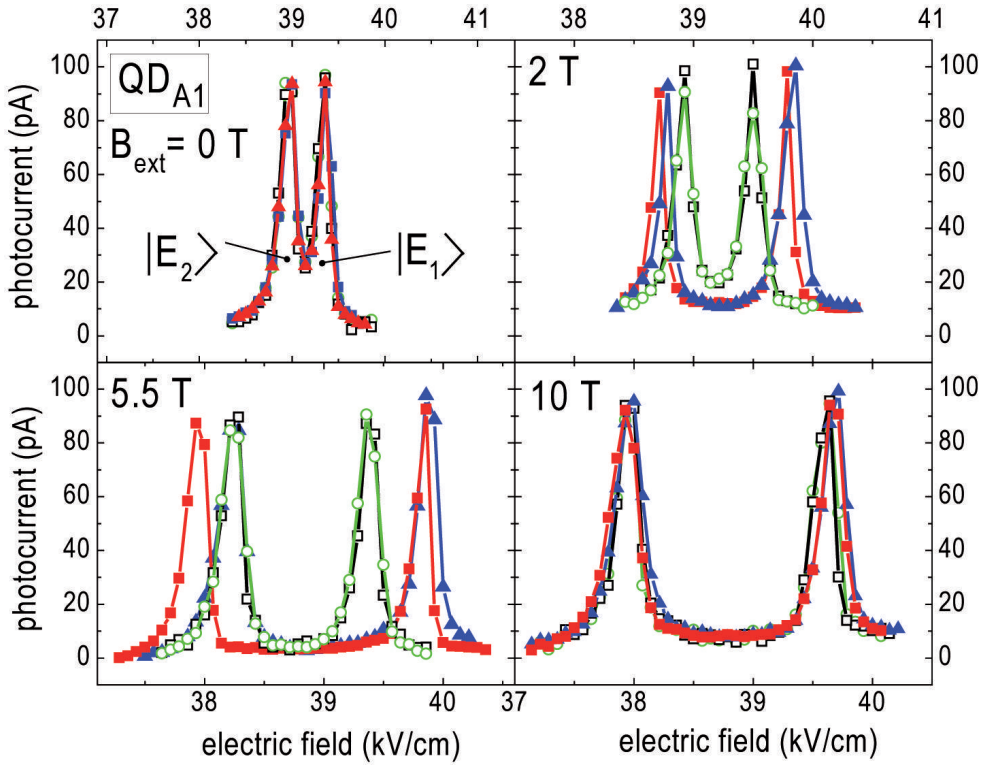

Figure 4.3. *Steady-state PC bias sweeps performed on QD_{A1} at different B_{ext} over the same electric field region and at constant excitation rate. A strong magnetic field dependence of the Overhauser shift generated upon resonant excitation of the bright X^0 states $|E_1\rangle$ and $|E_2\rangle$ during the sweep is be observed.*

the two levels. As for *Type-A* dots, the Overhauser field generated at one point during the sweep is still present when the other, in terms of DNP inactive resonance (here $|E_1\rangle$), is reached. The mechanisms leading to the observed properties of DNP effects will be discussed in detail later in this chapter.

4.1.1 Magnetic field dependence

Figures 4.3 and 4.4 present steady-state PC bias sweeps on QD_{A1} and QD_{C1}, respectively, performed at different B_{ext} between 0 T and 10 T. The color and symbol coding are the same as introduced in figure 4.1. The measurements were all carried out at a excitation power P_{exc} resulting in the same PC peak height and over the same electric field region. In order to meet the latter criteria, the excitation wavelength λ_{exc} had to be adjusted in order to compensate for the diamagnetic shift of the system [Wal98]. Although the Overhauser shift generated during the resonant excitation of the two bright X^0 states during the bias sweep is qualitatively different for *Type-A* and *Type-C* dots, the efficiency of the nuclear spin pumping exhibits the same B_{ext} dependence for both types of QDs: At $B_{\text{ext}} = 0$ T, no significant Overhauser shift is observed for pumping either of the two X^0

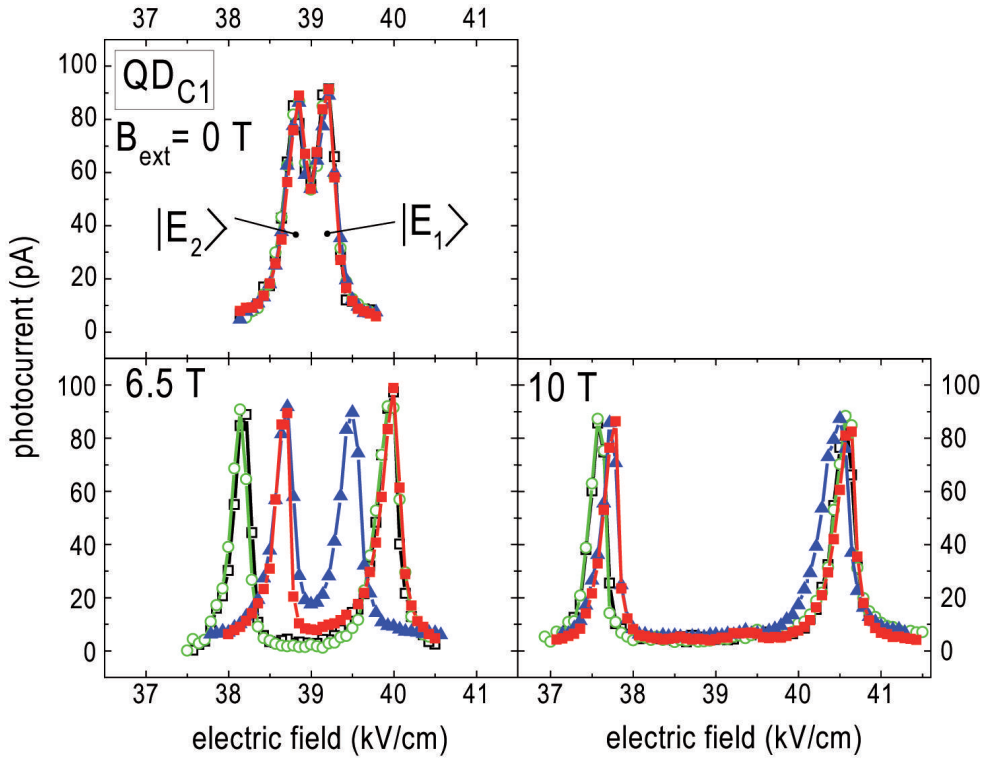

Figure 4.4. *Steady-state PC bias sweeps performed on QD_{C1} at different B_{ext} over the same electric field region and at constant excitation rate. A strong magnetic field dependence of the Overhauser shift generated upon resonant excitation of the bright X^0 states $|E_1\rangle$ and $|E_2\rangle$ during the sweep is be observed.*

states. For intermediate magnetic fields of $B_{ext} = 5.5 - 6.5$ T, DNP is most pronounced with an *asymmetric* behavior for $|E_1\rangle$ and $|E_2\rangle$ where pumping of the nuclear spin system occurs only upon excitation of one of the two states ($|E_1\rangle$ for *Type-A* and $|E_2\rangle$ for *Type-C* dots). In the low magnetic field range of $B_{ext} \sim 2$ T, the *asymmetry* is still present. However, a small Overhauser shift is also found for excitation of the other Zeeman branch ($|E_2\rangle$ for *Type-A* and $|E_1\rangle$ for *Type-C* dots). For both types of QDs, the effect of DNP on the energy splitting between the two states ΔE_{1-2} is identical for the pumping of both resonances, i.e. *unidirectional* (an increase of ΔE_{1-2} for *Type-A* and a decrease of ΔE_{1-2} for *Type-C* dots). This implies that the generated nuclear spin polarization is oriented in the same direction irregardless of the Zeeman branch pumped[1]. At high fields of $B_{ext} = 10$ T, the effect is quenched and no effects of DNP are observed. Furthermore, we find that application of the randomization procedure leads to independence of the recorded curves on the bias sweeping direction for all magnetic fields examined, demonstrating the effectiveness of the randomization scheme for all B_{ext} and types of QDs. In this work, an Overhauser shift leading to an increase in the energy splitting between

[1] In this B_{ext} region, no spectra on QD_{C1} were recorded for the specific set of parameter presented in figure 4.4. However, the characteristic *asymmetric* and *unidirectional* behavior can be seen in the lower panel of figure 4.5 where a quantitative analysis of the Overhauser shift in QD_{C1} is presented.

$|E_1\rangle$ and $|E_2\rangle$ is defined as positive and vice versa a shift reducing ΔE_{1-2} as negative. Hence, for QD_{A1}, all shifts δ_n observed in figure 4.3 are positive for resonant pumping of both bright X^0 resonances. For QD_{C1}, the Overhauser shifts observable in figure 4.4 are always negative. As will be shown below in this section, the *unidirectionality* of DNP, i.e. the insensitivity of the direction of the nuclear spin polarization on whether it was generated via resonant pumping of $|E_1\rangle$ or $|E_2\rangle$, is found to be true for all magnetic and electric fields as well as all optical pumping powers investigated. The same holds true for the sign of $\delta_\mathrm{n}^\mathrm{s}$ being always positive for *Type-A* dots and negative for *Type-C* QDs.

A quantitative analysis of the magnetic field dependence of nuclear spin pumping is presented in figure 4.5 for QD_{A1}, QD_{A2} and QD_{C1} at $F_0 \approx 39.2$ kV/cm. Plotted is the steady-state Overhauser shift $\delta_\mathrm{n}^\mathrm{s}$ of both bright X^0 states $|E_1\rangle$ (orange circles) and $|E_2\rangle$ (gray squares) which can be extracted from the experimental quantities δ_1, $\Delta E_{1-2}^{\mathrm{s,n}}$ and ΔE_{1-2} according to

$$\delta_\mathrm{n}^\mathrm{s} = \sqrt{\Delta E_{1-2}^{\mathrm{s,n}} - \delta_1^\mathrm{b}} - \sqrt{\Delta E_{1-2} - \delta_1^\mathrm{b}} \tag{4.1}$$

derived from the relations given in table 2.1. The quantitative evaluation underpins the first observations made on figures 4.3 and 4.4. For QD_{A2}, the Overhauser shift δ_n^s observed upon pumping of $|E_1\rangle$ increases monotonically from 0 μeV to $\approx$ 120 μeV for increasing B_ext in the range $B_\mathrm{ext} = 0 - 6$ T and then decreases again for larger magnetic fields approaching a value of $\delta_\mathrm{n}^s \approx 15$ μeV for $B_\mathrm{ext} > 9$ T. The largest Overhauser shift observed for a dot on this sample was $\delta_\mathrm{n}^s \approx 135$ μeV at $B_\mathrm{ext} \approx 6$ T [Klo10a] corresponding to a degree of polarization of the nuclear spin bath of 54 %[t1] [Ebl06] and an Overhauser field of $B_\mathrm{n} = 3.8$ T (using g_e = -0.6 as calculated for our dots [And09b] in good agreement with values reported in literature [Kro08b; Bay99a]). For resonant excitation of $|E_2\rangle$, δ_n^s increases with increasing magnetic field for $B_\mathrm{ext} < 3$ T up to $\delta_\mathrm{n}^s \approx 25$ μeV and then decreases again, reaching $\delta_\mathrm{n}^s = 0$ μeV at $B_\mathrm{ext} \approx 4$ T. For higher applied magnetic fields, no DNP is observed for pumping of $|E_2\rangle$. The DNP magnetic field dependence of QD_{A1} depicted on the right side of the upper panel in figure 4.5 qualitatively coincides with the one found for QD_{A2}. In contrast to QD_{A2}, a pronounced dip appears simultaneously in both curves around $B_\mathrm{ext} = 3.7$ T. However, since this discontinuity is also found for the splitting ΔE_{1-2} that was recorded in the absence of DNP by employing the randomization procedure (cf. left part of figure 3.13), we do not attribute it to nuclear spin pumping but rather to a peculiarity of the level structure of this particular QD. All these main features observed in experiment, in particular the *unidirectional* nuclear polarization, the *asymmetry* upon pumping of the two X^0 Zeeman levels, and the characteristic magnetic field dependences are reproduced by the numerical simulations presented below in section 4.2.2. For QD_{C1} presented in the lower panel of figure 4.5, a dependence of DNP on the applied magnetic field similar to QD_{A1} and QD_{A2} is found. However, as mentioned above, the behavior can be described as 'inverted' with respect to the role of $|E_1\rangle$ and $|E_2\rangle$ as well as the direction of the Overhauser shift. Note that for QD_{C1} in the lower panel of figure 4.5, it is $(-\delta_\mathrm{n}^\mathrm{s})$ instead of $\delta_\mathrm{n}^\mathrm{s}$ that is plotted on the positive y-axis.

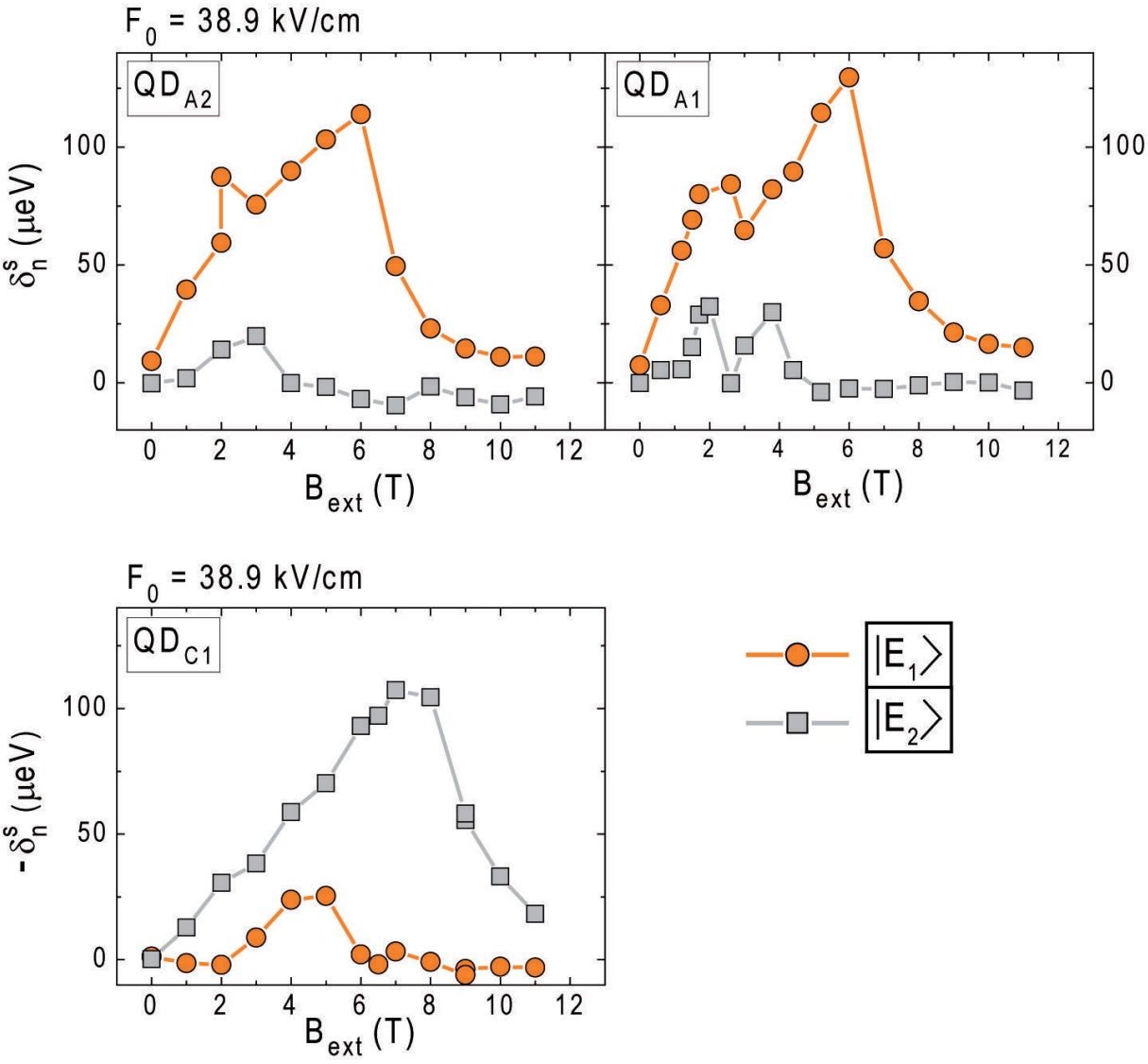

Figure 4.5. *Quantitative analysis of the steady-state Overhauser shift δ^s_n generated upon resonant optical excitation of $|E_1\rangle$ and $|E_2\rangle$ as a function of the magnetic field applied. All measurements on QD_{A1}, QD_{A2} and QD_{C1} were carried out at a constant excitation rate of the dots and over the same electric field range of the sweep. For QD_{A1} and QD_{A2} (upper panel), generation of DNP qualitatively yields the same effects. QD_{C1} (lower panel) shows a similar behavior as that can be described as 'inverted' as compared to QD_{A1} and QD_{A2} with respect to the role of $|E_1\rangle$ and $|E_2\rangle$ as well as the direction of the Overhauser shift.*

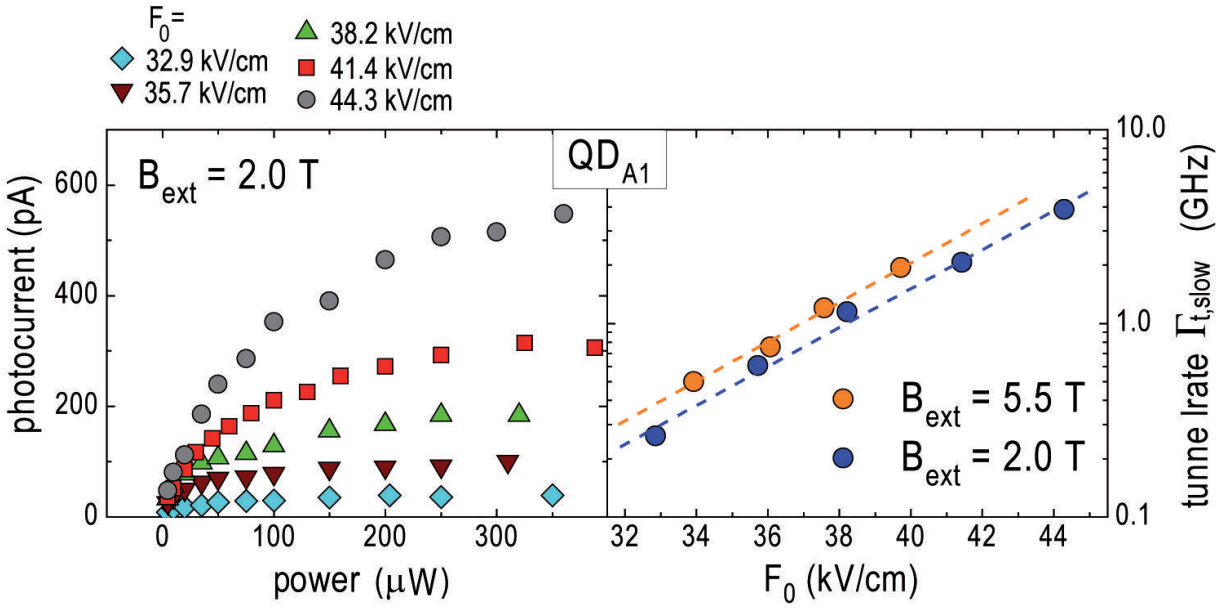

Figure 4.6. *Dependence of the PC signal on the optical excitation power. Left: Amplitude of the $|E_1\rangle$ PC peak as a function of laser power measured in steady-state bias sweeps at $B_{\text{ext}} = 2$ T for different electric field regions indicated by the corresponding F_0 values. For each F_0 the PC signal saturates at a characteristic value determined by the tunnel escape rate of the slower charge carrier Γ_{exc}. Right: Tunnel rates as a function of F_0 for two different magnetic fields. Γ_{exc} increases exponentially with the electric field (the dashed lines are guides to the eye) with the same exponent for the two data sets at $B_{\text{ext}} = 2$ T and 5.5 T.*

The maximum Overhauser shift observed is $\delta_{\text{n}}^{\text{s}} \approx$ -115 μeV and occurs upon pumping of $|E_2\rangle$ at $B_{\text{ext}} = 7$ T. For resonant excitation of $|E_1\rangle$, a maximum $\delta_{\text{n}}^{\text{s}}$ of ≈ -25 μeV is achieved at $B_{\text{ext}} = 4.5$ T.

4.1.2 Pumping power dependence

In this section, the effect of the optical pumping rate on the steady-state Overhauser shift generated in PC bias sweeps is presented. In the case of resonant excitation of neutral exciton states, optical generation of charge carriers can only occur if the dot is empty because Coulomb interaction of electrons and holes in the dot detune the QD state from the laser energy. Consequently, after optical generation of an exciton in the dot the system can only be excited again after all charge carriers have left the dot and the initial resonant situation is restored. As a result, the photocurrent amplitude exhibits a saturation behavior as the optical generation rate of charge carriers becomes comparable to the tunneling escape rate (cf. section 2.2.3) which represents the dominant decay mechanism for excitons in the PC regime [Beh01; Beh02]. In the left part of figure 4.6, the PC amplitude of the $|E_1\rangle$ resonance obtained from electric field sweeps at $B_{\text{ext}} = 2$ T is plotted as a function of the optical excitation power applied to the QD for different F_0.

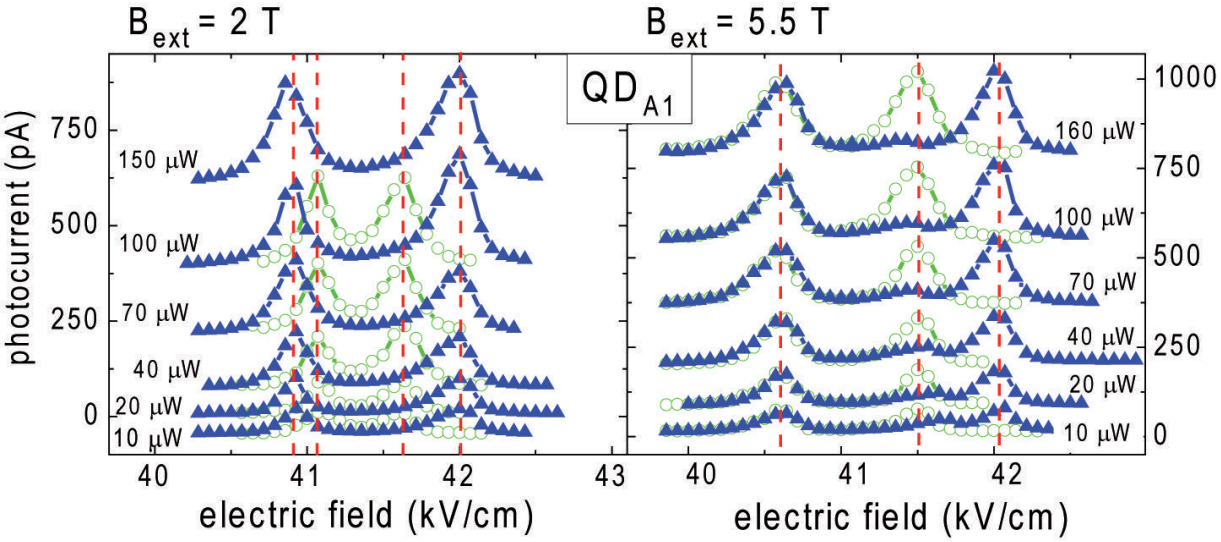

Figure 4.7. *Steady-state PC bias sweeps performed at $B_{ext} = 2$ T (left side) and 5.5 T (right side) on QD_{A1} for different laser intensities. For both types of up-sweeps, with (open green circles) and without (closed blue triangles) randomization, no dependence of the resonance positions on the optical pumping rate is found. For the sake of clarity, an offset was introduced to every set of PC curves.*

The effect of signal saturation is clearly observable with a saturation value characteristic for each F_0 that is given by the electric field-dependent tunnel rate of the slower particle $\Gamma_{t,slow}$. Determining the saturation PC signal from a power series allows to calculate the tunnel rate $\Gamma_{t,slow}$ according to equation 2.15. The result of this evaluation is given on the right side of figure 4.6 for different F_0 at $B_{ext} = 2$ T and 5.5 T. For the electric fields examined in this thesis between 32 kV/cm and 45 kV/cm the exciton tunnel decay rate increases from 0.25 GHz and 4 GHz for increasing F_0 following an exponential field dependence as expected [Beh01; Beh02] with an identical exponent for $B_{ext} = 2$ T and 5.5 T. However, the tunnel escape of the electron takes place even faster than $\Gamma_{t,slow}$ due the smaller effective mass as compared to the hole that determines the saturation level of the PC signal. Consequently, the coupling of the electron to the leads is expected to be noticeably stronger than suggested by $\Gamma_{t,slow}$.

To account for the effect of PC saturation, in this work mostly the excitation rate of the quantum dot Γ_{exc} is used as a figure of merit for pumping intensity instead of the laser power P_{exc}. For this, Γ_{exc} is given in terms of the PC signal amplitude generated which is directly proportional to the number of excitons optically generated in the dot per time. Unless stated otherwise, Γ_{exc} always refers to the excitation rate generated at full resonance between laser and QD state, i.e. the PC signal of the maximum peak height ($\Gamma_{exc} = \frac{1}{e} \cdot PC\ peak\ height\ [A/e]$).

Figure 4.7 presents steady-state PC bias sweeps performed at $B_{ext} = 2$ T (left side) and 5.5 T (right side) on QD_{A1} over the same electric field range for different excitation

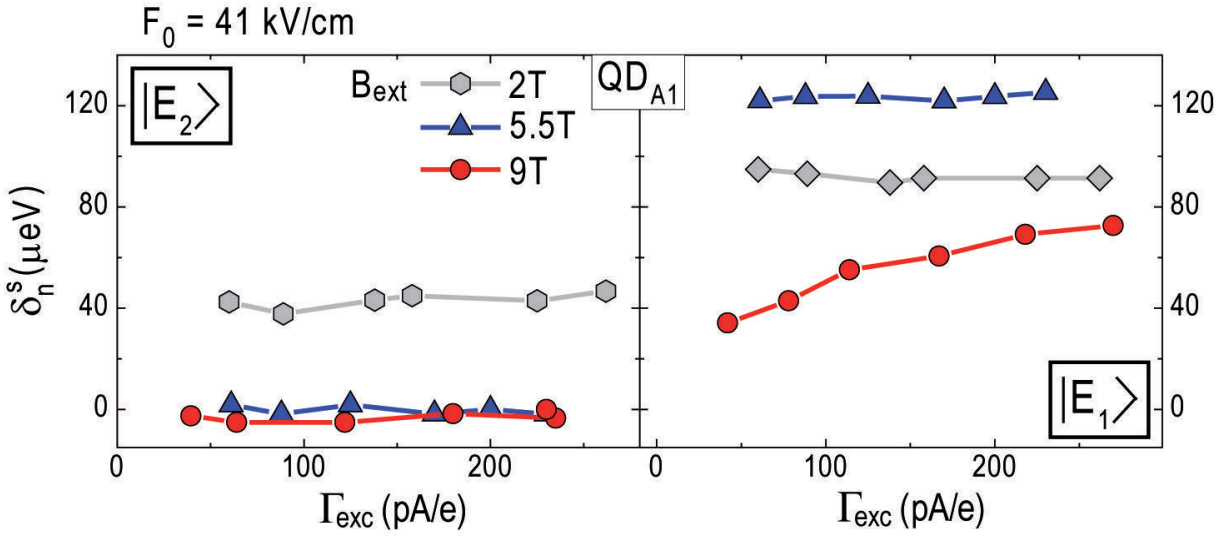

Figure 4.8. *Dependence of the steady-state Overhauser shift δ_n^s generated via resonant pumping of $|E_2\rangle$ (left side) and $|E_1\rangle$ (right side) on the excitation rate of the quantum dot Γ_{exc} which is directly proportional to PC signal amplitude ($\Gamma_{exc} = \frac{1}{e} \cdot$ PC signal amplitude $[A/e]$). For $B_{ext} = 2$ T and 5.5 T, δ_n^s is insensitive to a variation of the excitation rate by a factor of ≈ 6. Only for $B_{ext} = 9$ T, a dependence of DNP on Γ_{exc} is observed.*

powers. At both magnetic fields, the laser intensity was varied by a factor of ≈ 15, changing the excitation rate by a factor of ≈ 5 and 4, respectively. For both types of up-sweeps, with (open green circles) and without (closed blue triangles) randomization, no dependence of the resonance positions on the optical pumping rate is found. This demonstrates that even at excitation rates much larger than commonly used for the measurements in this thesis, the randomization procedure still allows to efficiently suppress buildup of nuclear spin polarization during a bias sweep. Furthermore, it shows that, at least for the parameter range investigated here, the steady-state Overhauser shift generated via resonant pumping of both $|E_1\rangle$ and $|E_2\rangle$ does not depend on the excitation rate of the states at $B_{ext} = 2$ T and 5.5 T.

Figure 4.8 compares the influence of the optical excitation rate on the Overhauser shift generated during steady-state up-sweeps at $F_0 = 41$ kV/cm for different magnetic fields applied. For $B_{ext} = 5.5$ T (blue triangles) and $B_{ext} = 2$ T (gray circles), the steady-state degree of nuclear polarization generated via pumping of either $|E_1\rangle$ and $|E_2\rangle$ is found to be independent on the pumping rate used. The steady-state Overhauser shift δ_n^s is insensitive to a change in excitation rate by a factor of ≈ 6. The highest rates employed are 270 pA and already correspond to the saturation regime of the PC signal. A different behavior is found at $B_{ext} = 9$ T (red circles), where δ_n^s pumped via the higher energy Zeeman branch $|E_1\rangle$ increases from 25 μeV to 75 μeV as the PC signal amplitude is increased from 40 pA to 270 pA. No power dependence is found for DNP generated by $|E_2\rangle$ excitation. However, a detectable nuclear spin polarization upon resonant pumping of $|E_2\rangle$ is only generated for $B_{ext} < 4$ T as can be seen from figure 4.5. Generally, δ_n^s

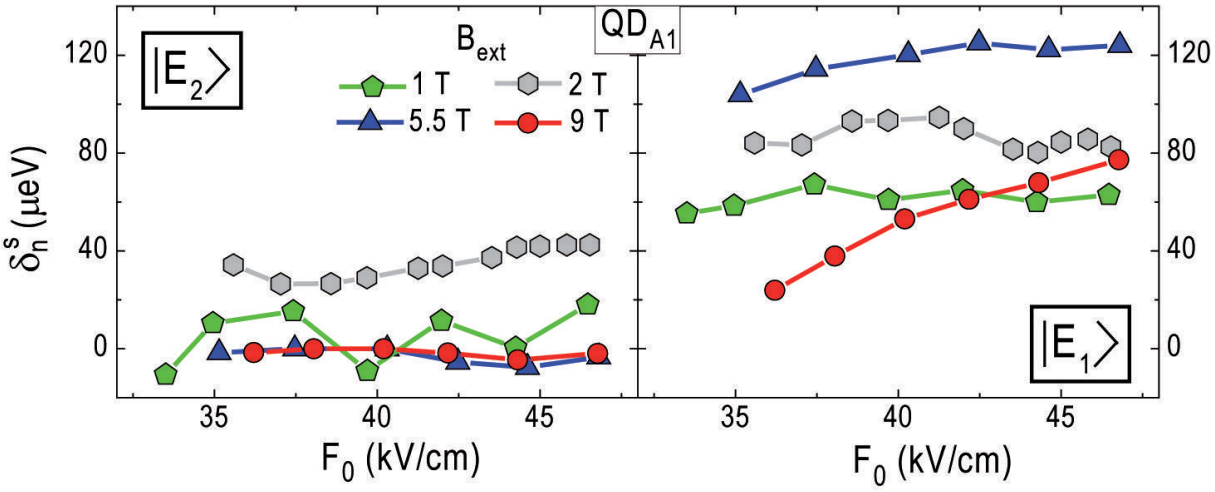

Figure 4.9. *Dependence of the Overhauser shift generated during a steady-state PC bias sweep on the electric field range over which the measurement was performed. The effect was investigated for both bright states of the neutral exciton $|E_1\rangle$ (right side) and $|E_2\rangle$ (left side) at different magnetic fields B_{ext} applied using a constant excitation rate.*

is found to be independent on the excitation power for all $B_{\text{ext}} \leq 6$ T. For all higher magnetic fields, a clear power dependence with a monotonically increasing δ_{n}^{s} for an increasing pumping rate of the QD is observed.

4.1.3 Electric field dependence

In figure 4.9, the influence of the electric field applied on DNP is shown. The graph depicts the steady-state Overhauser shift δ_{n}^{s} for the pumping of each Zeeman branch $|E_1\rangle$ (right side) and $|E_2\rangle$ (left side) for bias sweeps over different electric field ranges. For all measurements, the same excitation rate of the QD states was used. The electric field determines the tunneling rate of the optically generated charge carriers from the dot to the electrical contacts. This effect can be used to tune the dwell time over a wide range with an upper limit given by the radiative exciton lifetime of ~ 1 ns [Kre05d] (cf. section 2.2.3). At $B_{\text{ext}} = 1$ T and 2 T (green pentagons and gray hexagons), δ_{n}^{s} generated via $|E_1\rangle$ excitation is insensitive to the electric field range the measurement is performed at. For $B_{\text{ext}} = 5.5$ T (blue triangles), a small change of δ_{n}^{s} from 100 μeV to 120 μeV for an increasing F_0 from 35 kV/cm to 47 kV/cm, i.e. for stronger tunnel coupling to the contacts, emerges. This trend becomes more pronounced for increasing magnetic fields and at $B_{\text{ext}} = 9$ T (red circles) a clear dependence of δ_{n}^{s} on F_0 is observed with δ_{n}^{s} increasing from 23 μeV to 77 μeV over the same bias range. No electric field dependence is found for nuclear spin polarization generated by $|E_2\rangle$ excitation.

Figure 4.10 directly compares the magnetic field dependence of DNP in QD_{A1} for two different electric field ranges, F_0 =38.9 kV/cm (closed symbols) as depicted in figure 4.5 and 44.3 kV/cm (open symbols) using a constant excitation rate for all measurements.

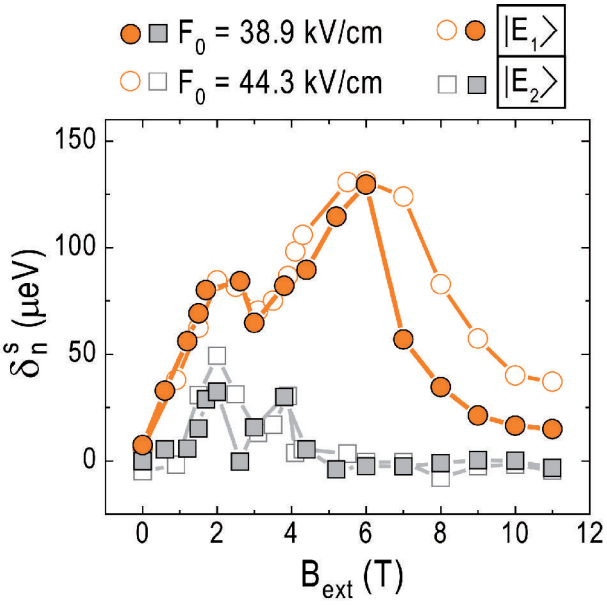

Figure 4.10. *Magnetic field dependence of DNP probed for F_0 =38.9 kV/cm (cf. figure 4.5) and 44.3 kV/cm at a constant excitation rate. In agreement with the data presented in figure 4.9, only for $B_{ext} > 6$ T a difference is found between different electric field ranges whereas the obtained results are identical for $B_{ext} < 6$ T.*

The electric field dependence shows a characteristic behavior similar to the one of the excitation power on DNP. For $B_{ext} < 6$ T, the steady-state Overhauser shifts generated via resonant excitation of either $|E_1\rangle$ (orange circles) or $|E_2\rangle$ (squared) are insensitive to a variation of the experimental parameter, in this case the electric field applied. In contrast, a clear difference in the generated Overhauser shift is found for magnetic fields $B_{ext} > 6$ T with δ_n^s being larger for higher electric fields. The behavior presented in figure 4.10 is in agreement with the results presented in figure 4.9 and suggest more efficient nuclear spin pumping via resonant optical excitation for a stronger tunnel coupling to the leads at high magnetic fields.

4.2 Model and numerical simulation

In this section, a model developed to describe the experimental data in order to gain a deeper understanding of the underlying mechanisms is presented. The general idea and qualitative properties of the model were developed in the framework of this thesis in close collaboration with *Giedke at al.* [Gie12; Klo10a; Klo12]. The derivation of the model from the quantum master equation of the system as presented in the following section 4.2.1 as well as the numerical calculations simulating the actual experimental procedure used in our measurements were mostly performed by *Giedke at al.* [Gie12; Klo10a; Klo12].

4.2.1 Model

Different mechanisms have been identified to potentially be able to cause DNP in an optically excited quantum dot [Ima03; Kor07; Dzh07; Yan10; Hoe12; Urb12]. All of them have in common that they rely on the hyperfine-mediated electron-nuclear spin flip-flop processes. However, they differ with regard to the active quantum dot states, the means by which an imbalance in the up and down polarization rates is achieved, and by which process provides the energy for the typically off-resonant hf flip-flop process. The model presented here focuses on the neutral QD states investigated in the experiments. Many of the characteristic DNP effects observed in measurement emerge naturally within the model and can be understood in terms of hf-mediated spin flip transitions between dark and bright states of the neutral exciton manifold [Klo10a; Klo12].

First, the system and mechanisms considered are sketched: The model describes the experimentally investigated system consisting of an uncharged quantum dot in a magnetic field applied in Faraday geometry strongly coupled to the contacts below and above the dot via tunneling processes induced by electric fields along the growth direction of the structure. As the DNP measurements are carried out in the PC regime, tunneling escape of electrons and holes from the dot represents the major decay mechanism for the QD population and radiative recombination is negligible. Since the hyperfine interaction is much weaker than the tunnel coupling, a clear separation of time scales of the corresponding processes is given: The optically prepared excitonic system quickly reaches a (quasi-)steady state $\rho_\mathrm{s}^\mathrm{e}$. Hyperfine flip-flop processes can then change the nuclear spin polarization and $\rho_\mathrm{s}^\mathrm{e}$ follows adiabatically. As excitation of the QD in the experiment is achieved resonantly, multiple exciton states cannot be generated and only the subspace of a neutral quantum dot populated with either one or no exciton is considered in the model. Effects of singly charged states due to the different tunneling times of electrons and holes are not taken into account for the model as they are expected to have only little influence on nuclear spin pumping. This is the case as in this regime electrons are assumed to tunnel out of the dot faster than holes due their comparatively lighter effective mass [Hei09a]. As a result, mostly single holes states which do not exchange spin with the nuclei are populated during the tunnel decay of an exciton. This allows to employ a master equation that describes the decay process as a direct transition from excitonic states to the empty quantum dot.

The bright exciton states that are optically accessible are coupled to the dark states via the hyperfine interaction. An electron-nuclear spin flip-flop process described by the dynamical part of the contact hyperfine Hamiltonian $H_{\mathrm{c-hf}}^{\mathrm{ff}} \propto J_\mathrm{e}^+ I^- + J_\mathrm{e}^- I^+$ (cf. equation 2.26) simultaneously exchanges one unit of spin orientation of an electron and a nuclear spin transferring the exciton from a bright into an optically inactive dark state (cf. section 2.2.4). The probability for transitions to take place within the neutral exciton manifold scales with the energy splitting $\left(\Delta E_{i-j}\right)^{-2}$ between the bright ($i = 1, 2$) and corresponding dark ($j = 3, 4$) state involved in a flip-flop process. The *asymmetry* in efficiency of nuclear spin pumping upon excitation of the bright X^0 states $|E_1\rangle$ and

$|E_2\rangle$ stems from the difference in ΔE_{i-j} between the individual states in the X^0 energy spectrum. This makes hyperfine flip-flop transitions into one of the dark states more likely than into the other. The resulting imbalance in hyperfine spin flip-flop rates can lead to a net polarization of the nuclei even if the optically excited electrons are not polarized as will be discussed in more detail below. Another factor playing a role for the different efficiencies of the two states with regard to DNP arises from the fact that buildup of the Overhauser field during the process dynamically changes ΔE_{i-j} as well as the mixing ratio of the states modifying the probability for hf-assisted transitions between bright and dark exciton states. In some cases, nuclear polarization alters the level structure such that nuclear spin pumping is reducing, while in other cases the effect is self-enhancing. Based on these principles, all characteristic features of DNP observed upon resonant pumping of the two bright X^0 states can be understood in terms of the properties of the neutral exciton energy level structure as will be demonstrated below in sections 4.2.2 and 4.2.3.

For the model the basis states $|k\rangle, k = 0, \ldots, 4$ are used where $|0\rangle$ denotes the empty QD. The spin eigenstates $|1\rangle = |\uparrow\Downarrow\rangle$ and $|2\rangle = |\downarrow\Uparrow\rangle$ span the bright- and $|3\rangle = |\uparrow\Uparrow\rangle$ and $|4\rangle = |\downarrow\Downarrow\rangle$ the dark-exciton subspace. P_X, P_B, P_D denote the projectors on the exciton, bright-exciton, and dark-exciton subspaces respectively. The electron and hole spin operators in the exciton subspace are given by $J_{\mathrm{e},z} = (|\uparrow\rangle\langle\uparrow| - |\downarrow\rangle\langle\downarrow|)/2$ and $J_{\mathrm{h},z} = (|\Uparrow\rangle\langle\Uparrow| - |\Downarrow\rangle\langle\Downarrow|)/2$.

Hamiltonian master equation

For our model, we assume that the system dynamics is governed by the quantum master equation (Note that for the model, we set $\hbar = 1$)

$$\dot{\rho} = \mathcal{L}\rho \equiv -i[H, \rho] + \mathcal{L}_d\rho\,.$$

The Hamiltonian takes into account several contributions: (i) the levels of the excitonic energy spectrum including Zeeman and exchange interactions ($H_{\mathrm{Z}} + H_{\mathrm{exchange}}$), (ii) the driving laser (H_{l}), and (iii) the hyperfine interaction of electrons with the nuclei (H_{hf}). Written in a frame rotating with the laser frequency ω_{l}, the time-independent QD Hamiltonian reads $H = H_{\mathrm{exchange}} + H_{\mathrm{Z}} + H_{\mathrm{l}} + H_{\mathrm{hf}}$ with

$$\begin{aligned} H_{\mathrm{exchange}} &= \omega_{\mathrm{x}} P_X + \delta_0(P_B - P_D)/2 + \delta_1^{\mathrm{b}}(|1\rangle\langle 2| + |2\rangle\langle 1|)/2 \\ &\quad + \delta_1^{\mathrm{d}}(|3\rangle\langle 4| + |4\rangle\langle 3|)/2\,, \end{aligned} \tag{4.2}$$

$$H_{\mathrm{Z}} = g_{\mathrm{e}}\mu_{\mathrm{B}} B J_{\mathrm{e},z} + g_{\mathrm{h}}\mu_{\mathrm{B}} B J_{\mathrm{h},z}\,, \tag{4.3}$$

$$H_{\mathrm{l}} = \Omega_+ |1\rangle\langle 0| + \Omega_- |2\rangle\langle 0| + \mathrm{h.c.} \tag{4.4}$$

$$H_{\mathrm{hf}} = \vec{A}\cdot\vec{J}_{\mathrm{e}} \equiv J_{\mathrm{e},z} A_z + \frac{1}{2}\left(J_{\mathrm{e}}^+ A^- + J_{\mathrm{e}}^- A^+\right)\,. \tag{4.5}$$

Here, $\vec{A} = \sum_i A_i \vec{I}_i$ is the sum of the individual nuclear spin operators weighted by their respective coupling A_i to the electron spin; $A = \sum_i A_i$ is the total hyperfine interaction; $A^{\pm} = \sum_i A_i I_i^{\pm}$; ω_{x} contains the laser detuning from the bare exciton energy and the dc Stark shift of the excitons which is changed in the experiment to perform the sweeps; $\Omega_{\pm}$ denotes the Rabi frequency of the $\sigma^{\pm}$-circularly polarized laser components; δ_0 is the splitting between dark and bright excitons, $\delta_1^{b(d)}$ the bright (dark) exciton exchange energy as introduced in chapter 2.

Not all parameters describing the system can be determined from experiment. In particular, $\delta_1^{\mathrm{d}}, \delta_0$ and the sign of $g_{\mathrm{ex}}^{\mathrm{b}}$ as well as the individual contributions of its components g_{e} and g_{h} remain unknown. To perform calculations, typical values found for similar systems obtained from other types of experiments were employed. The values used in the simulations are collected in table 4.1. The sign resulting for $g_{\mathrm{ex}}^{\mathrm{b}}$ is in agreement with the findings for *Type-A* dots obtained from the investigations on g-factor tuning presented in sections 3.5 and 3.6.[2] However, the results on DNP obtained from the model are only sensitive to the relative signs of $g_{\mathrm{ex}}^{\mathrm{b}}$ and g_{e}. Therefore, the calculations are invariant under a simultaneous inversion of both the electron and hole g-factor $g_{\mathrm{h}} \to -g_{\mathrm{h}}$, $g_{\mathrm{e}} \to -g_{\mathrm{e}}$ which also leads to $g_{\mathrm{ex}}^{\mathrm{b(d)}} \to -g_{\mathrm{ex}}^{\mathrm{b(d)}}$.

In terms of the excitonic eigenstates, the electron and hole spin operators read

$$J_{\mathrm{e},z} = \frac{1}{2}\left(|1\rangle\langle 1| - |2\rangle\langle 2| + |3\rangle\langle 3| - |4\rangle\langle 4|\right) , \tag{4.6}$$

$$J_{\mathrm{e}}^{+} = |1\rangle\langle 4| + |3\rangle\langle 2| \tag{4.7}$$

$$J_{\mathrm{h},z} = \frac{1}{2}\left(|3\rangle\langle 3| - |1\rangle\langle 1| + |2\rangle\langle 2| - |4\rangle\langle 4|\right) . \tag{4.8}$$

The zz-part of the hyperfine coupling is separated into the (potentially large) Overhauser term $\langle A_z\rangle J_{\mathrm{e},z}$ which is added to H_Z and the rest $(A_z - \langle A_z\rangle)J_{\mathrm{e},z}$.

In order to be consistent with the experiment where linearly polarized light is used, $\Omega_+ = \Omega_-$ is usually considered. However, there is little qualitative dependence on the polarization of the light. Even using σ^- light, the *asymmetric* polarization effect persists (though it will be significantly weaker especially for large magnetic fields).

The decay of the excitons is described by a Lindblad master equation with jump operators $U_k^-, k = 1, \ldots 4$

$$U_k^- = |0\rangle\langle k| \tag{4.9}$$

and associated rates Γ_k. The excitonic-nuclear quantum master equation then reads

$$\frac{d}{dt}\rho = \mathcal{L}\rho \equiv (\mathcal{L}_0 + \mathcal{L}_1)\rho \tag{4.10}$$

[2] Note that the convention for the sign of the g-factor used in the work presented in sections 3.5 and 3.6 is inverted as compared to the one commonly used in literature which was also employed for the work in this chapter.

parameter	value	
δ_0	120 μeV	dark-bright splitting
δ_1^{b}	40 μeV	bright exciton exchange splitting
δ_1^{d}	40 μeV	dark exciton exchange splitting
$g_{\mathrm{ex}}^{\mathrm{b}}$	$g_{\mathrm{e}} + g_{\mathrm{h}}$	bright exciton g factor
$g_{\mathrm{ex}}^{\mathrm{d}}$	$g_{\mathrm{e}} - g_{\mathrm{h}}$	dark exciton g factor
g_{e}	-0.6	electron g factor
g_{h}	1 μeV	heavy hole g factor
$\Omega_{\pm}$	1	Laser Rabi frequencies (linear polarization)
A	150μeV	hyperfine interaction[t1]
N	30 000	number of nuclei
Γ_{nr}	15 μeV	non-radiative decay rate
Γ_{r}	1 μeV	radiative decay rate

[t1] Note that for the model, a comparatively small value for A close to the one given in Ref. [Mal09] (170 μeV) was used, whereas for the determination of the degree of polarization of the nuclear spin system achieved in the experiment, the more common value of 250 μeV [Ebl06; Bra06b; Urb12] was taken. However, this has no qualitative impact on the results of the simulation or the comparisons to the experimental data as far as made here.

Table 4.1. *Typical parameters for self-assembled QDs used in the simulation. Additionally a weak depolarization rate* $f_{\mathrm{depol}} = 1 \cdot 10^{-9}$ *is assumed. For simplification, all nuclear spins are treated as spin-1/2 particles. The values for* δ_1^{b} *and* $\left|g_{\mathrm{ex}}^{\mathrm{b}}\right| = 0.4$ *were directly determined from the experiments. The results of the simulation are invariant under simultaneous inversion of the electron and hole g-factor sign* $g_{\mathrm{h}} \to -g_{\mathrm{h}}$, $g_{\mathrm{e}} \to -g_{\mathrm{e}}$.

with

$$\mathcal{L}_0\rho = \sum_k \Gamma_k \left(2U_k^- \rho U_k^+ - \left\{U_k^+ U_k^-, \rho\right\}_+\right) - i\left[H_0, \rho\right] , \tag{4.11}$$

where $H_0 = H_{\mathrm{exchange}} + H_{\mathrm{Z}} + H_{\mathrm{I}}$ contains all Hamiltonian terms except the hyperfine interaction. The decay rates Γ_k include radiative and non-radiative processes and satisfy the relations $\Gamma_3 \equiv \Gamma_4 = \Gamma_{\mathrm{nrad}}$ and $\Gamma_1 \equiv \Gamma_2 = \Gamma_{\mathrm{nrad}} + \Gamma_{\mathrm{rad}}$.

The time scale of $\mathcal{L}_0$ is set by the decay rates. Thus, as long as $\Gamma_k \gg \|H_{\mathrm{hf}}\|$ holds, the QD decays to its instantaneous steady state $\rho_{\mathrm{s}}^{\mathrm{e}}$ before hyperfine dynamics appreciably changes the nuclear state. Then, the dynamics of the nuclei is determined by $\rho_{\mathrm{s}}^{\mathrm{e}}$ and this steady state, in turn, follows adiabatically the slow evolution of the nuclei (i.e. buildup of nuclear polarization).

Nuclear spin dynamics

This intuition can be formalized by adiabatic elimination of the "fast" non-steady-state subspace of $\mathcal{L}_0$ [Kes12]. For this, let $\rho_{\mathrm{s}}^{\mathrm{e}}$ denote the steady state of the Liouvillian $\mathcal{L}_0(\langle A_z \rangle)$, i.e., the instantaneous steady state of the QD at fixed Overhauser field $\langle A_z \rangle$, and define

the projector on the electronic steady state ("slow subspace") by

$$\mathcal{P} : \rho \mapsto \rho_{\mathrm{s}}^{\mathrm{e}} \otimes \mathrm{tr}_{\mathrm{qd}}(\rho) \equiv \rho_{\mathrm{s}}^{\mathrm{e}} \otimes \mu \,, \tag{4.12}$$

and its complement by $\mathcal{Q} = \mathbb{1} - \mathcal{P}$. Here, $\mathcal{H} = \mathcal{H}_{\mathrm{qd}} \otimes \mathcal{H}_{\mathrm{nuc}}$ is the Hilbert space of the composite system; $\mathrm{tr}_{\mathrm{qd}}$ denotes the trace over the QD degrees of freedom and $\mu = \mathrm{tr}_{\mathrm{qd}}(\rho)$ denotes the reduced state of the nuclear system.

The master equation 4.10 leads to two coupled equations for $\mathcal{P}\rho$ and $\mathcal{Q}\rho$. Setting $\frac{d}{dt}\mathcal{Q}\rho = 0$, as the electronic system quickly reaches $\rho_{\mathrm{s}}^{\mathrm{e}}$, one obtains for $\mathcal{P}\rho$ the equation

$$\frac{d}{dt}\mathcal{P}\rho = \mathcal{P}\mathcal{L}_1\mathcal{P}\rho - \mathcal{P}\mathcal{L}_1\mathcal{Q}\left(\mathcal{Q}\mathcal{L}_0\mathcal{Q}\right)^{-1}\mathcal{Q}\mathcal{L}_1\mathcal{P}\rho \,, \tag{4.13}$$

which describes (to second order in $\|\mathcal{L}_1\|/\|\mathcal{L}_0\|$) the dynamics on the slow subspace, i.e. the evolution of the nuclear spin system. Note that $\mathcal{L}_0$ is invertible on the subspace $\mathcal{Q}$. Inserting $\mathcal{L}_1(\rho) = -i[H_{\mathrm{hf}}, \rho]$ and writing the hyperfine Hamiltonian $H_{\mathrm{hf}} = \sum_{r=\pm,z} h_r J_{\mathrm{e}}^r \left(A^r\right)^\dagger$ as $\sum_{r=\pm,z} h_r(\Delta J_{\mathrm{e}}^r + \langle J_{\mathrm{e}}^r\rangle_{\mathrm{s}})A_{\mathrm{e}}^r$ leads to[3]

$$\begin{aligned}\frac{d}{dt}\mathrm{tr}_{\mathrm{qd}}(\mathcal{P}\rho) = &-i[\sum_{r=\pm,z} h_r\langle J_{\mathrm{e}}^r\rangle_{\mathrm{s}} A^r\mu] + \\ &\sum_{r,m=\pm,z} h_r h_m[c_{rm}^{(1)}A^rA^m\mu - c_{rm}^{(1)}A^r\mu A^m - c_{rm}^{(2)}A^m\mu A^r + c_{rm}^{(2)}\mu A^rA^m] \,,\end{aligned} \tag{4.14}$$

where $c_{rs}^{(1)}$ and $c_{rs}^{(2)}$ are given by

$$\begin{aligned}c_{rs}^{(1)} &= \mathrm{tr}_{\mathrm{qd}}(\Delta J_{\mathrm{e}}^r \mathcal{L}_{0,Q}^{-1}(\Delta J_{\mathrm{e}}^m \rho_{\mathrm{s}}^{\mathrm{e}})) \,, \\ c_{rs}^{(2)} &= \mathrm{tr}_{\mathrm{qd}}(\Delta J_{\mathrm{e}}^r \mathcal{L}_{0,Q}^{-1}(\rho_{\mathrm{s}}^{\mathrm{e}} \Delta J_{\mathrm{e}}^m)) \,,\end{aligned} \tag{4.15}$$

and $\mathcal{L}_{0,Q}$ by

$$\begin{aligned}\mathcal{L}_{0,Q} &= \mathcal{Q}\mathcal{L}_0\mathcal{Q} \,, \\ h_\pm = 1/2 \,&, \; h_z = 1 \,.\end{aligned} \tag{4.16}$$

Amongst others, equation 4.14 contains the terms responsible for nuclear spin pumping. Note that $c_{\pm\mp}^{(2)} = (c_{\mp\pm}^{(1)})^*$, which ensures that the (spin pumping) master equation for the nuclear spins is of Lindblad type. For the polarization rates (prefactors of the

[3] Note that in order to allow for the compact form of expressions 4.14 and 4.15, the following modification of the notation is necessary: $J_{\mathrm{e}}^z \equiv J_{\mathrm{e},z}$ and $A^z \equiv A_z$.

terms $A^+\mu A^-$ and $A^-\mu A^+$) one finds

$$\gamma_+ = -\mathrm{Re}(\mathrm{tr}_{qd}\left[\mathcal{L}_0^{-1}(\Delta J_\mathrm{e}^+\rho_\mathrm{s}^\mathrm{e})J_\mathrm{e}^-\right])/2\,, \tag{4.17}$$

$$\gamma_- = -\mathrm{Re}(\mathrm{tr}_{qd}\left[\mathcal{L}_0^{-1}(\Delta J_\mathrm{e}^-\rho_\mathrm{s}^\mathrm{e})J_\mathrm{e}^+\right])/2\,, \tag{4.18}$$

respectively. All the other terms in equation 4.14 ($\propto A^+A^+, A_zA^+, A_zA_z$ etc.) are either very small or do not contribute to DNP and are, thus, neglected. The imaginary part of $\mathrm{tr}_{qd}\left[\mathcal{L}_0^{-1}(\Delta J_\mathrm{e}^+\rho_\mathrm{s}^\mathrm{e})J_\mathrm{e}^-\right]$ yields the electron-mediated nuclear spin interaction $\propto \{A^+, A^-\}_+$ which is also neglect here.

Even after all these simplifications, solving equation 4.14 is still difficult due to the exponentially large size of the Hilbert space of the N nuclear spins. It can be significantly simplified by neglecting some (or all) correlations between nuclear spins allowing to factorize the problem [And93; Chr07; Kes10]. Since for the case here the long times are of interest on which nuclear coherences are likely to play no role (due to inhomogeneities and dipolar interaction), a semiclassical approximation can be employed in which the nuclear spin state is taken to be separable and diagonal in the z-basis at all times. Using this approach one obtains the equation of motion for the lth nuclear spin reading

$$\frac{d}{dt}\mu_l = \gamma_+A_l^2\left(I_l^+\mu_l I_l^- - \{I_l^-I_l^+,\mu_l\}_+/2\right) + \gamma_-A_l^2\left(I_l^-\mu_l I_l^+ - \{I_l^+I_l^-,\mu_l\}_+/2\right)\,. \tag{4.19}$$

Assuming spin-I nuclei and states that are diagonal in the I_z-basis, equation 4.19 yields a rate equation for the probabilities $p_{l,m}$ of the ith nuclear spin to be in state $|I,m\rangle$ given by

$$\begin{aligned}\frac{d}{dt}p_{l,m} = &-\left[\gamma_{l,+}(I-m)(I+m+1) + \gamma_{l,-}(I+m)(I-m+1)\right]p_{l,m} \\ &+\ \gamma_{l,+}(I-m+1)(I+m)p_{l,m-1} + \gamma_{l,-}(I+m+1)(I-m)p_{l,m+1}\,.\end{aligned} \tag{4.20}$$

From this the steady-state nuclear polarization (for given $\gamma_{l,\pm}$, i.e. given $\rho_\mathrm{s}^\mathrm{e}$) can be easily found as $p_{l,m} = ((1-x)/(1-x^{2I+1}))x^{I+m}$. E.g., for spin-1/2 nuclei the steady-state population in the $I_z = +1/2$ state is $p_{l,+1/2}^\mathrm{s} = (\gamma_{l,+})/(\gamma_{l,+}+\gamma_{l,-})$. Similar expression follow for larger spins. Since the rates $\gamma_{l,\pm}$ depend (nonlinearly) on the nuclear polarization the model has to integrated numerically to find the nuclear steady state at given magnetic field and laser detuning as discussed below. For simplicity, only homogeneously coupled nuclei ($\gamma_{l,\pm} = \gamma_\pm$) are considered in this work and, hence, the index l is omitted from now on.

4.2.2 Numerical simulations

Based on this model, numerical calculations were performed simulating the actual experimental procedure to determine the polarization process during the PC bias sweeps performed. For every magnetic field value, the initial situation of a maximally mixed, i.e. fully depolarized, state is assumed. In the next step, the electronic steady state and the associated coefficients $c_{rs}^{(i)}$ in the nuclear master equation equation 4.19 are numerically determined for a given detuning of the laser energy from the QD state ω_x. This yields the instantaneous DNP rates $\gamma_\pm$ and the associated nuclear steady state. Next, the following two steps are repeated until the nuclear steady state is reached: (i) Determine $\rho_\mathrm{s}^\mathrm{e}$ as steady state of $\mathcal{L}_0$ for given $\langle A_z \rangle = \sum p_m m$ and $\gamma_\pm$. (ii) Evolve p_m according to equation 4.20 until $\langle A_z \rangle$ has changed by some non-negligible amount or the nuclear steady state has been reached. Once it is reached, the nuclear polarization $P(B_\mathrm{ext}, \omega_x) = \langle I_z \rangle_{\mu_s^n}$ and the exciton population $\langle P_X \rangle_{\rho_\mathrm{s}^\mathrm{e}}$ are recorded. The latter is proportional to the steady-state photocurrent, which is the observable from which the Overhauser shift is deduced in the experiment. Now ω_x is changed (without changing μ_s^n) and the same calculation to determine $\langle P_X \rangle_{\rho_\mathrm{s}^\mathrm{e}}$ is performed again. This procedure is repeated until the whole sweep is simulated.

A calculated full PC trace obtained this way is presented on the left side of figure 4.11 for an applied magnetic field of $B_\mathrm{ext} = 5$ T. The vertical green dashed lines mark the position of the two bright X^0 states $|E_1\rangle$ and $|E_2\rangle$ in the absence of any nuclear spin polarization. They correspond to the reference curves in the experiment recorded with the application of the randomization procedure prior to every data point (cf. e.g. figure 4.3, open green circles and open black squares). The solid lines depict the calculated steady-state photocurrent signal. For each detuning of the laser from the QD states, corresponding to the different values of the electric field applied during a bias sweep in the experiment, the steady-state photocurrent signal amplitude was determined from the simulation as described above. The simulated PC spectrum clearly reveals a double-peak structure formed by the two resonances of the bright X^0 states $|E_1\rangle$ and $|E_2\rangle$. Variation of the detuning results in a peak in the calculated photocurrent signal as either of the QD transitions is tuned into resonance with the laser energy and optical excitation sets in. As can be seen from a comparison with the empirical results at a similar B_ext as depicted e.g. in figure 4.1, the PC traces obtained from the numerical simulations qualitatively show the same characteristic features as the ones recorded in experiment: Resonant pumping of $|E_2\rangle$ does not result in any notable nuclear spin pumping whereas excitation of $|E_1\rangle$ leads to a significant shift of the QD resonances due to the buildup of an Overhauser magnetic field with an Overhauser shift that increases the energy splitting ΔE_{1-2}.

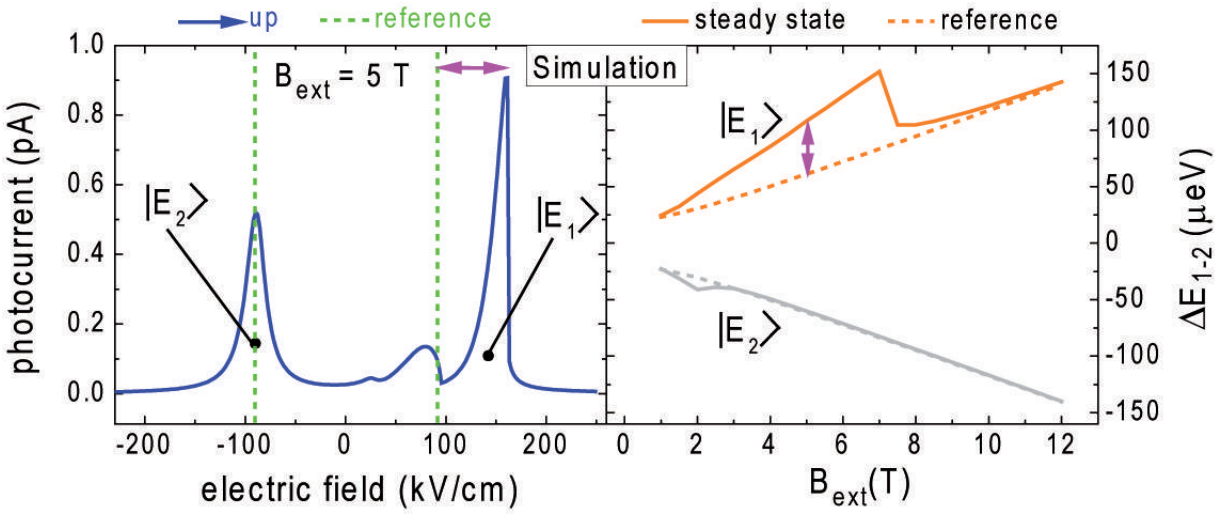

Figure 4.11. *Left: Simulated full steady-state PC bias up-sweep at $B_{\text{ext}} = 5$ T. The vertical dashed lines mark the position of $|E_1\rangle$ and $|E_2\rangle$ in the absence of any nuclear spin polarization corresponding to the reference curves in the experiment. The solid lines depict the calculated steady-state photocurrent signal for each detuning of the laser from the QD states corresponding to the different values of the electric field applied during a bias sweep in the experiment. Right: Energy splitting ΔE_{1-2} of the bright neutral exciton states as a function of the applied magnetic field B_{ext} plotted in a symmetrized Breit-Rabi diagram. The dashed lines depict the situation without any Overhauser field calculated using the relations given in table 2.1. The solid lines mark the position of the PC peaks for the case of steady-state polarization. The energy difference between the dashed line and the peak of the solid line (purple arrows) is caused by the steady-state Overhauser shift at a given B_{ext}.*

After the simulation of the sweep is completed, the positions of the PC resonances are determined numerically from the calculated PC traces.[4] The result of such an analysis on sweeps simulated at different magnetic fields B_{ext} is summarized on the right side of figure 4.11. The graph depicts the position of both states $|E_1\rangle$ and $|E_2\rangle$ (solid lines) after pumping of the nuclear spin system to characteristic steady-state polarization with respect to the reference data (dashed lines) in a Breit-Rabi type diagram. The graph clearly reveals a magnetic field-dependent shift of the QD transitions with strongly differing amplitudes for $|E_1\rangle$ and $|E_2\rangle$. A quantitative analysis of this result is presented in figure 4.12. The fitted positions of the PC resonances at the end of the steady-state sweep can be evaluated in a analog manner to the analysis of the experimental data with

[4]This is done by determining the local maximum and fitting a Lorentzian to it and the two adjacent simulated data points. It should be remarked that the peaks are decidedly non-Lorentzian and that this fitting procedure is only used to smoothen the result and to avoid artifacts arising from the discrete steps in laser detuning when simulating the PC curves.

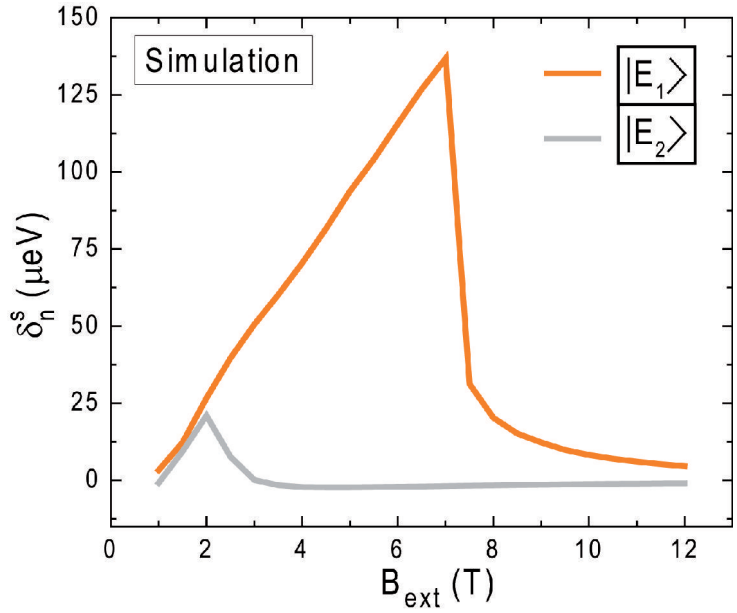

Figure 4.12. *Magnetic field dependence of the steady-state Overhauser shift δ_n^s generated upon resonant pumping of the two bright neutral exciton states $|E_1\rangle$ and $|E_2\rangle$. The results were obtained from numerical calculations of PC bias sweeps simulating the actual experimental procedure. The Overhauser shifts were extracted from the PC traces as described in the text.*

equation 4.1 by solving

$$\Delta\omega_b(B) = \frac{1}{2}\left(\sqrt{(\delta_1^b)^2 + (E_{ex,Z}^b(B) + \delta_n^s(B))^2}\right. \\ \left. - \sqrt{(\delta_1^b)^2 + (E_{ex,Z}^b(B))^2}\right) \tag{4.21}$$

$$\Delta\omega_r(B) = -\frac{1}{2}\left(\sqrt{(\delta_1^b)^2 + (E_{ex,Z}^b(B) + \delta_n^s(B))^2}\right. \\ \left. - \sqrt{(\delta_1^b)^2 + (E_{ex,Z}^b(B))^2}\right) \tag{4.22}$$

for the Overhauser interaction where $E_{ex,Z}^b(B)$ denotes the Zeeman energy. This procedure leads to a characteristic δ_n^s for each pair of parameters B_{ext} and ω_x. Figure 4.12 presents the steady-state Overhauser shift δ_n^s for resonant pumping of $|E_1\rangle$ and $|E_2\rangle$ obtained from a series of simulated steady-state PC bias sweeps at different B_{ext}. Again, the results obtained from the calculations based on the model presented above reproduce the experimentally observed characteristics of resonantly generated DNP in a neutral QD presented in figure 4.5 such as *asymmetric* and *unidirectional* spin polarization upon pumping of $|E_1\rangle$ and $|E_2\rangle$ as well as the magnetic field dependence of the steady-state Overhauser shift generated.

4.2.3 Comparison of simulation and experiment

This section presents a comparison of the results of the investigated DNP effects obtained from experiment and theory as introduced above. Since the data shown were already discussed and analyzed in sections 4.1 and 4.2.2, respectively, this will not be repeated here unless new insights can be gained. The intention of this section is to give a direct comparison of experiment and theory to show the agreements but also the limitations of the model.

Figure 4.13 depicts two photocurrent traces recorded from electric field sweeps both in experiment (left part) and theory (right part). The left part of figure 4.13 shows a set of steady-state bias up-sweeps at $B_{\text{ext}} = 5.5$ T performed with and without the application of the randomization procedure (cf. figure 4.1). The right part of figure 4.13 presents the numerical simulation of a steady-state up-sweep (cf. left part of figure 4.11) where the positions of the PC resonances in the absence of any DNP are marked by the vertical dashed lines. The two curves qualitatively show the same behavior: Resonant pumping of the higher energy Zeeman branch $|E_1\rangle$ results in an Overhauser shift on the QD transition towards higher energies by 2 - 4 linewidths whereas no notable effect of nuclear spin pumping is found for excitation of $|E_2\rangle$. However, the calculated PC curve yields an additional smaller peak on the low energy side of $|E_1\rangle$ that is not observable in the experimental data. In the simulation, this small feature results from hyperfine-assisted optical excitation of the dark exciton state $|E_3\rangle$. This process is weak but efficient as every excitation is accompanied by a nuclear spin flip. Particularly in the beginning of the nuclear spin pumping process when an increase of nuclear polarization quickly blue-detunes $|E_1\rangle$ from the laser, this effect contributes to DNP. In this case, buildup of B_{n} shifts $|E_3\rangle$ to lower energies which reduces the detuning to the excitation laser. Eventually, the energy of $|E_3\rangle$ falls below $\hbar\omega_{\text{exc}}$ and the effect is self-detuning. The reason why this double-peak structure is not seen in experiment is not clear yet. Possible reasons could be an additional broadening of the lines or a lower nuclear polarization which reduces the splitting between the peaks.

Figure 4.14 presents a comparison of experimental (4.14b) and theoretical (4.14c) results on the magnetic field dependence of δ_{n}^{s} upon pumping of $|E_1\rangle$ and $|E_2\rangle$ that were determined as discussed above. Based on the model presented in the previous section, the magnetic field dependence as well as the *asymmetric* and *unidirectional* behavior observed in experiment (cf. section 4.1.1) can be understood in terms of the interplay between two magnetic field-dependent factors: (i) the energy gap ΔE_{i-j} between the bright ($i = 1,2$) and dark ($j = 3,4$) X^0 states involved in a hf-mediated spin flip determining the transition probability and (ii) the mixing ratio of the eigenstates given by the ratio between exchange coupling and Zeeman interaction defining the purity of the spin states according to the relation in table 2.1.

Figure 4.14(a) depicts the energy level spectrum used for the numerical simulations in a symmetrized Breit-Rabi diagram containing both the bright ($|E_1\rangle$, $|E_2\rangle$) and dark ($|E_3\rangle$, $|E_4\rangle$) exciton configurations in the absence of any Overhauser fields for QC_{A2} (dashed

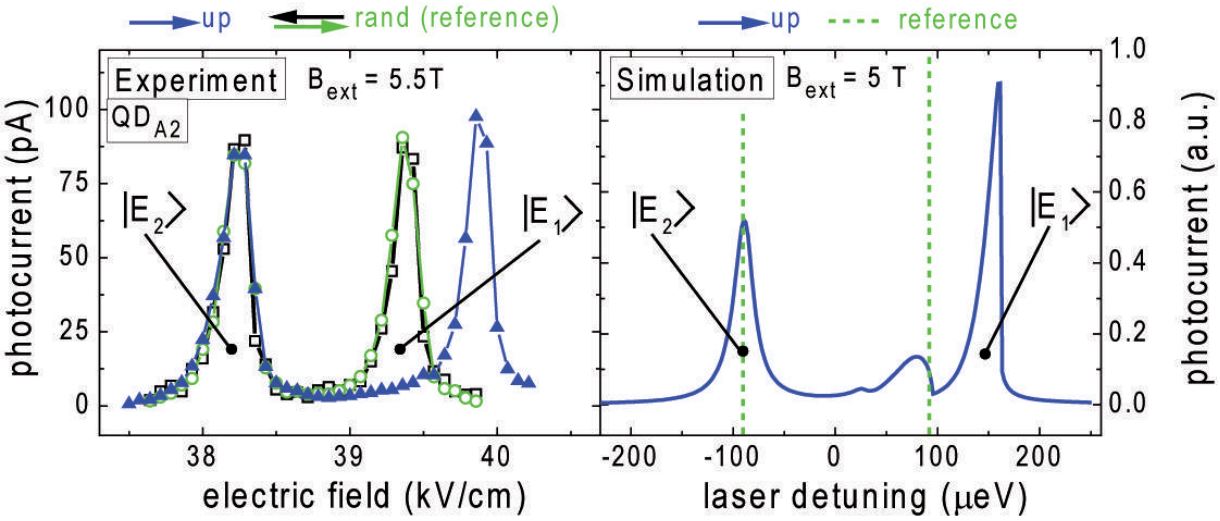

Figure 4.13. *Comparison of steady-state PC bias sweeps obtained from experiment and numerical simulation. Left: Experimental results on steady-state nuclear spin pumping via resonant excitation in photocurrent electric field sweeps as presented and discussed in figure 4.1. Right: PC traces calculated in numerical simulations presented and discussed in the left part of figure 4.11.*

lines). The experimental data points were obtained from the reference bias sweeps (cf. left panel of figure 3.13) and allow to determine the anisotropic exchange splitting and the absolute value of the bright exciton g-factor. Depending on the QD, δ_1^{b} is found to range from $15-40$ μeV. The values used to calculate the full spectrum are given in table 4.1. Although *Type-A* QDs show a non-linear Zeeman splitting (cf. section 3.4.2), a constant value is used here for the exciton g-factor which was obtained from fitting the relation given in table 2.1. As can be seen from the graph, this approximation describes the experimental data sufficiently well for this purpose. The level diagram also shows that the dark exciton state $|E_3\rangle$ ($\approx |\uparrow\Uparrow\rangle$ for large B_{ext}) is energetically closer to both bright states than $|E_4\rangle$ ($\approx |\downarrow\Downarrow\rangle$ for large B_{ext}) for all magnetic fields. Since the probability for hyperfine-assisted electron spin flips transferring the exciton from a bright into a dark state scales with $\left(\Delta E_{i-j}\right)^{-2}$, processes J_{e}^{+} with $|E_3\rangle$ as a final state (green up arrows) are more likely than transitions J_{e}^{-} to $|E_4\rangle$ (green down arrows). After such a flip-flop event took place, the dark states decay non-radiatively via tunneling escape of electron and hole to the corresponding contacts.

Consequently, the peaks in the Overhauser field generated which are observed both in experiment and simulations are related to the crossings of bright and dark exciton states where ΔE_{i-j} is minimal. Due to the spin character of $|E_1\rangle$, $|E_2\rangle$ and $|E_3\rangle$, electron-nuclear spin flip-flop processes are particularly efficient for transitions from $|E_1\rangle$ to $|E_3\rangle$. However, as the $|\downarrow\Uparrow\rangle$ component of $|E_2\rangle$ is small but non-zero due to exchange interaction, a hf-mediated coupling between $|E_2\rangle$ and $|E_3\rangle$ exists which is strong enough to generate detectable nuclear spin pumping upon resonant excitation of $|E_2\rangle$ as long as ΔE_{2-3} is small enough. For large B_{ext}, DNP is suppressed since both bright states are

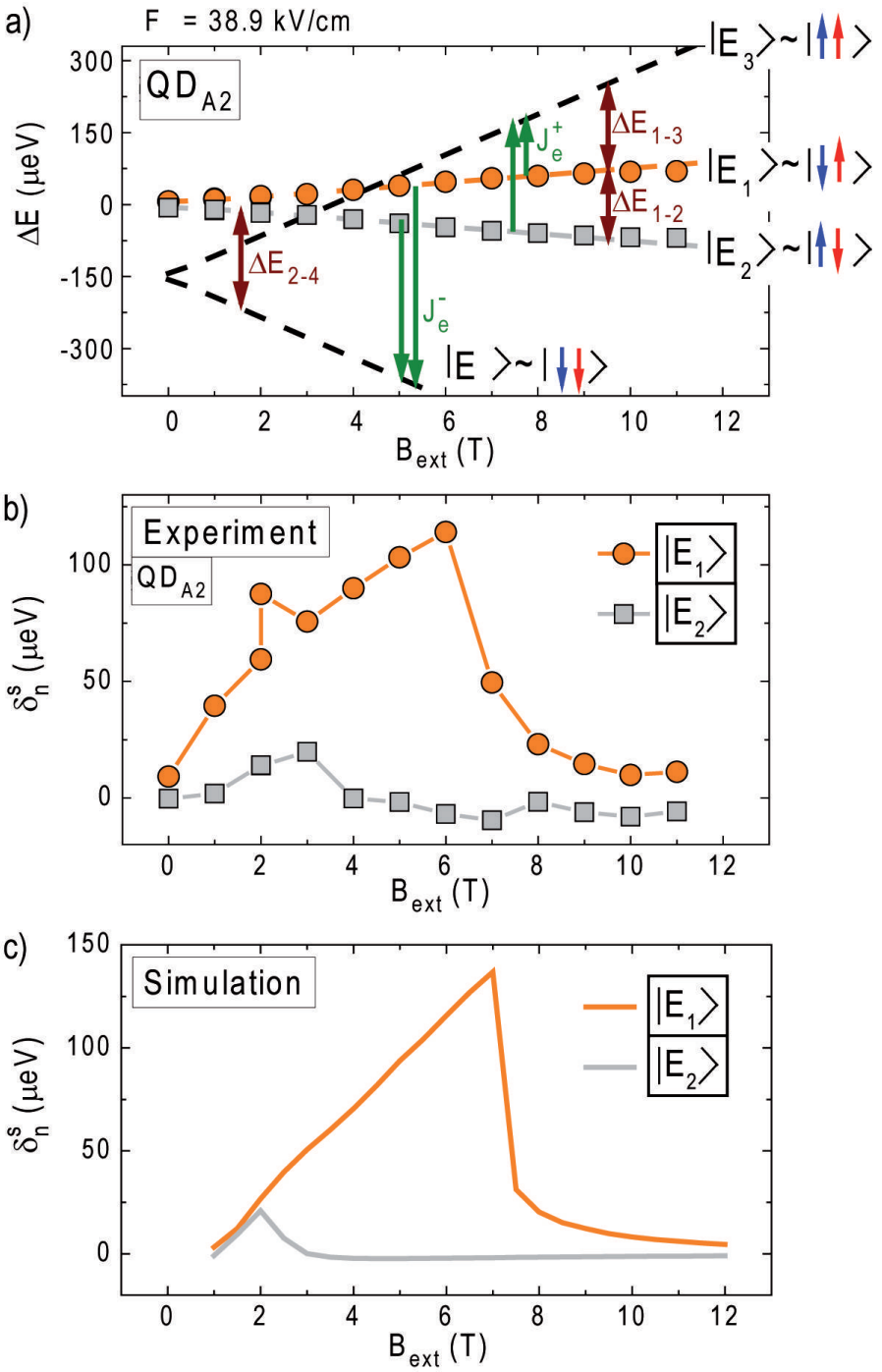

Figure 4.14. *(a) Breit-Rabi diagram of the X^0 energy level spectrum (dashed lines) used for the simulations. The experimental data points are obtained from PC bias sweeps performed with the randomization procedure to suppress DNP (cf. figure 3.13). The green vertical arrows indicate transitions from bright to dark X^0 states as they occur for hyperfine-mediated electron-nuclear spin flip-flop processes. (b) Magnetic field-dependence of DNP found in experiment as presented in figure 4.5. (c) Magnetic field-dependence of DNP obtained from numerically simulated steady-state bias sweeps as presented in figure 4.12. All observed characteristic features of the experimentally investigated resonant nuclear spin pumping are qualitatively reproduced by the simulations.*

strongly detuned from the dark states. For $B_{\mathrm{ext}} \approx 0$ T, no significant net nuclear spin pumping takes place since both doublets are of strongly mixed character in this case and ΔE_{i-j} is almost identical for all types of transitions.

Comparison of the magnetic field dependence of DNP obtained from experiment and numerical simulation, depicted in figure 4.14(b) and (c), respectively, shows that all empirically found features of the resonantly generated DNP effects, in particular the *unidirectional* nuclear polarization, the *asymmetry* upon pumping of the two X^0 Zeeman levels and the characteristic magnetic field dependences are reproduced by the numerical simulations. The fact that the peaks in $\delta_{\mathrm{n}}^{\mathrm{s}}$ do not occur at the B_{ext} values where $|E_3\rangle$ is in resonance with $|E_1\rangle$ and $|E_2\rangle$ according to the diagram in the upper panel of the figure is due to the fact that the energy level scheme given there is only representing the case of an externally applied magnetic field B_{ext} without any additional nuclear effective magnetic field. As nuclear spin pumping and buildup of an Overhauser magnetic field takes place during a PC bias sweep, the states experience an shift in energy and the level diagram changes dynamically throughout the measurement. The peaks of $\delta_{\mathrm{n}}^{\mathrm{s}}$ in the simulation coincide with the crossing points of $|E_3\rangle$ with $|E_1\rangle$ and $|E_2\rangle$ in the presence of the steady-state Overhauser field.

Given how many system parameters have not been measured directly and the stark simplifications (homogeneously coupled, factorizing spin-1/2 nuclei without dipolar or quadrupolar interaction, neglect of singly-charged states of the QD) used, the model is not used to fit the measured data. Its purpose is only to achieve qualitative agreement to corroborate the proposed mechanism as the likely reason for the observed effect. Furthermore, the introduction of a small constant nuclear depolarization rate f_{depol} [Vin09] (given in table 4.1) is necessary to obtain the peaked steady-state Overhauser shift $\delta_{\mathrm{n}}^{\mathrm{s}}$ (as a function of B_{ext}) shown in figure 4.12. If f_{depol} is set to zero, an almost constant Overhauser shift corresponding to maximum nuclear polarization is obtained from the simulation. While there are certainly depolarization processes active, for example dipolar coupling, off-axis quadrupolar terms or singly-charged states, they are not explicitly represented in the model since the identification and individual contribution of the relevant mechanisms is still an open question. Consequently, the assumption of a depolarization rate f_{depol} constant for all magnetic fields, excitation rates and tunneling times as employed in the model can only be a simplification. It allows to perform numerical simulations that can describe many of the observed characteristic properties of DNP generated via resonant pumping of a neutral QD as discussed above. However, it cannot reproduce all observations, particularly the dependence of $\delta_{\mathrm{n}}^{\mathrm{s}}$ on the excitation rate of the QD cannot be understood assuming a constant depolarization rate as will be discussed at the end of section 4.3.2.

To what extent *Type-C* dots can be described within the model is not immediately clear. However, the fact that the observed behavior differs from *Type-A* dots only in the sign of δ_{n} and the roles of $|E_1\rangle$ and $|E_2\rangle$ suggests that it can be understood in terms of a change in sign of one or several quantities such as e.g. g_{ex} or g_{h} [She07; And09a; Jov12b]. In fact, the results presented in chapter 3 even imply that *Type-A* and *Type-C* dots have exciton

g-factors of opposite sign. The most obvious scenario to obtain the observed *Type-C* behavior is a change of sign of δ_0 while all other parameters of the system are kept the same. This would directly result in bias sweeps and a magnetic field dependency as depicted in figures 4.2 and 4.5, respectively. However, this case appears to be unrealistic, since it would result in an anomalous level spectrum which has never been reported for self-assembled InGaAs quantum dots. Hence, the theoretical study of *Type-C* dot based on the model is still an open task and remains subject to future work.

4.3 Dynamics

We will now turn to the buildup dynamics of nuclear spin polarization as well as the decay of the generated Overhauser field. To probe the evolution of nuclear spin polarization under resonant optical pumping of either of the two neutral exciton states, time-resolved PC measurements have been performed. These experiments allow to directly monitor the buildup of B_n in real-time by resolving the temporal variation of the Overhauser shift δ_n the QD states exhibit under excitation. These measurements provide a better understanding of the processes taking place during DNP and allow to determine the experimental parameters to ensure that the PC bias sweeps presented in section 4.1 were indeed performed adiabatically such that the system remains in a steady state during the whole measurement.

The depolarization dynamics of the nuclear spin bath are investigated for two different cases: (i) while the dot is kept in the dark and electrically isolated from the electron reservoir in the back contact as well as (ii) when it is strongly coupled to the back contact via tunneling processes with and without non-resonant wetting layer excitation. The results of (i) give a timescale for the self-depolarization rate of a partially polarized nuclear spin ensemble in a QD while the experiments carried out for case (ii) demonstrate the effectiveness of the randomization procedure applied in the reference PC bias sweeps to suppress DNP.

4.3.1 Polarization dynamics

The experimental technique used to perform the time-resolved experiments is illustrated in figure 4.15. The measurements were performed using the following scheme: First, the randomization procedure was carried out once to delete any residual nuclear polarization. After this, a bias was applied to the sample defining an initial detuning d_i of the QD resonances from the laser energy $\hbar\omega_\mathrm{exc}$. Finally, the laser was switched on and the PC signal was recorded as a function of time keeping the electric field as well as λ_exc and P_exc fixed. In this arrangement, a change in PC signal indicates a change of detuning between QD states and laser energy leading to an change of the optical pumping rate and, consequently, the photocurrent signal recorded. Figure 4.15(a) presents a typical time-resolved PC trace recorded at $B_\mathrm{ext} = 2$ T on QD_{A1}: First, the PC signal varies non-monotonically and eventually remains at a constant level I_PC^s that is reached after

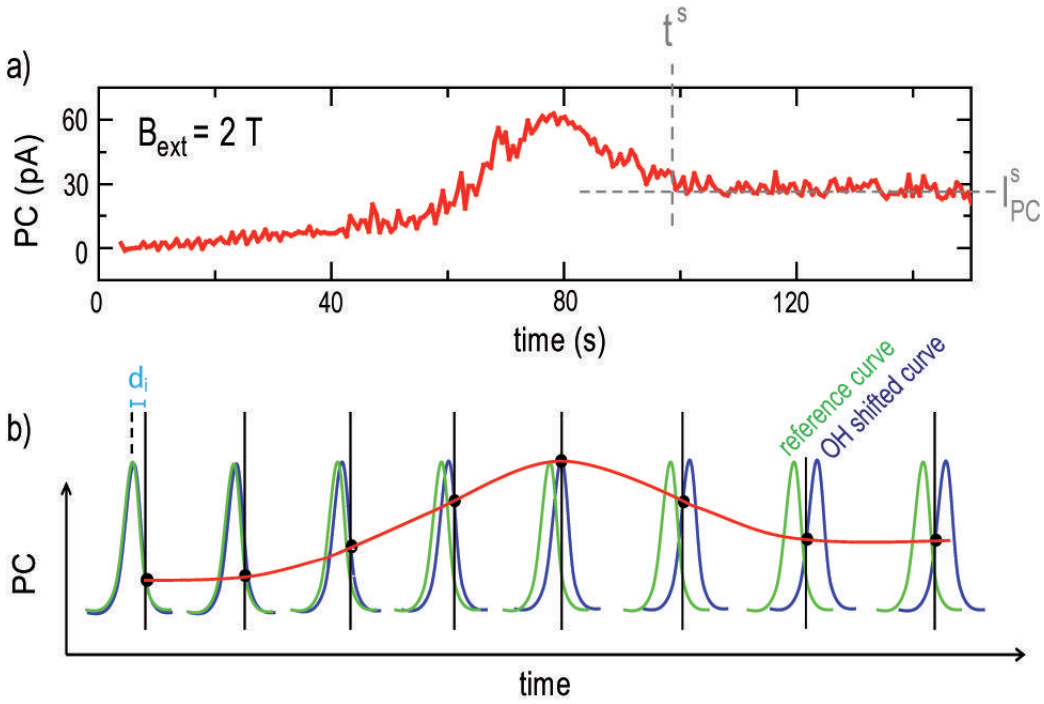

Figure 4.15. *Working principle of the time-resolved PC measurements employed to examine the buildup of nuclear spin polarization under resonant optical excitation of the X^0 states. (a) Photocurrent signal recorded at $B_{ext} = 2$ T as a function of time for a fixed electric field F applied and constant λ_{exc}. An initial increase of the PC signal is followed by a monotonic decrease approaching a constant level I^s_{PC} that is reached after a characteristic time t^s. (b) Schematic illustration of the time evolution of the system under resonant pumping to explain the PC trace presented directly above. The laser energy (vertical black line) and electric field F are kept constant throughout the whole measurement and define the initial detuning d_i between laser and QD state (green peak). Buildup of an Overhauser field during excitation of the QD shifts the transition energy of the energy levels and alters the detuning between laser and QD states. As a result, the optical pumping rate and, consequently, the photocurrent signal are also changed. After a time t^s, the PC signal does not change anymore and remains at a level I^s_{PC} as the system has reached steady state.*

a characteristic time t^s. Figure 4.15(b) shows a schematic diagramm illustrating the time evolution of the system under resonant pumping to allow an interpretation of the recorded PC trace presented directly above. Such an evaluation will be be done exemplarily for the example presented here and in more detail below: The excitation frequency (vertical black line) and electric field F define the initial detuning d_i between laser and QD state (green peak) and are kept constant throughout the whole measurement. During the measurement, buildup of a nuclear spin polarization via excitation of the QD shifts the transition energies of the dot levels and alters the detuning between laser and QD states due to the buildup of an Overhauser magnetic field B_n. As a result, the optical pumping rate and, consequently, the photocurrent signal also change. In the

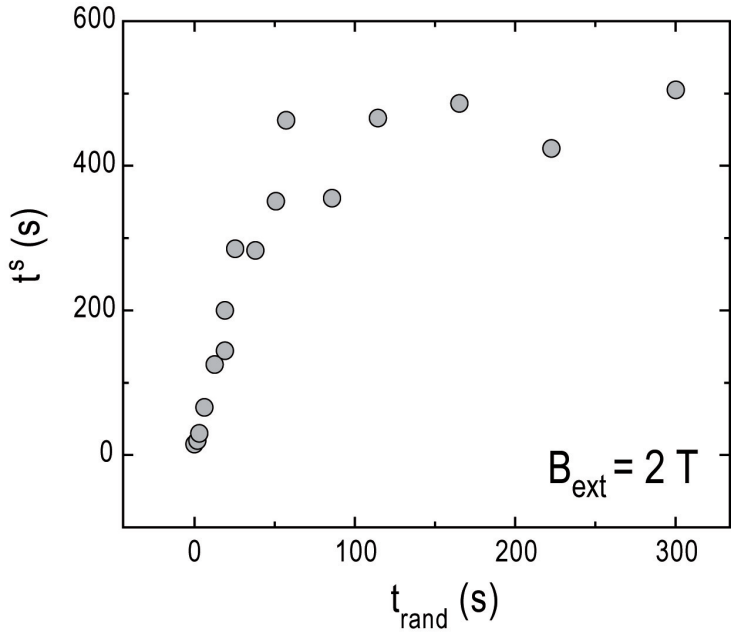

Figure 4.16. *Time t^s until the steady-state nuclear polarization is reached under cw excitation of the QD for a fixed initial detuning d_i as a function of the time t_{rand} the randomization procedure is applied prior to the recording of the PC trace. For $t_{rand} > 100$ s, the influence of nuclear spin pumping during the previous measurement is fully removed. To guarantee an identical, fully depolarized initial situation for all measurements, a randomization time of $t_{rand} = 240$ s was chosen for the time-resolved PC measurements performed in this thesis.*

beginning, for times up to $t = 75$ s, the detuning is reduced and the overlap between laser and dot level (blue peak) is increased resulting in a higher excitation rate. The PC signal is maximal when laser and QD transition are in resonance and the detuning is zero. In the following time between $t = 75$ s and 100 s, the detuning is increased again and the PC signal decreases. Finally, after the time $t^s = 100$ s has passed, a steady state of the nuclear spin polarization is reached and the PC signal remains at a constant level $I^s_{PC} = 25$ pA. Two of the key figures that can be extracted from these measurements are the time t^s until the steady state is reached and the PC amplitude in this state I^s_{PC} for a particular electric field F applied to the structure.

To ensure that the initial situation is identical for all time-resolved measurements and that all effects of nuclear spin pumping during the previous measurement are fully removed, the time t^s until the steady-state nuclear polarization is reached was determined as a function of t_{rand}, the time the randomization procedure is applied prior to recording of the PC trace. The result is plotted in figure 4.16 for QD_{A1} at $B_{ext} = 2$ T. For the time-resolved measurements, the randomization procedure needs to be applied significantly longer in order to fully delete nuclear spin polarization as compared to the PC bias sweeps to obtain reference spectra of the bright exciton resonances. This is understandable as during a PC reference sweep the scheme is performed after recording of every data point corresponding to resonant pumping of $|E_1\rangle$ or $|E_2\rangle$ of less than

one second. This short illumination time does not generate significant nuclear spin polarization as can be seen below, e.g. in figure 4.17 or figure 4.18. The randomization procedure prior to the recording of a time-resolved PC trace, however, has to remove the full steady-state polarization generated in the previous measurement. As can be seen from figure 4.16, t^{s} is constant for times $t_{\mathrm{rand}} > 100$ s indicating that nuclear spin polarization is fully removed. For $t_{\mathrm{rand}} < 100$ s, the time t^{s} decreases with decreasing randomization time as less nuclear spin pumping is necessary to reach the steady state due to an increasing residual polarization from the previous run. To guarantee an identical, fully depolarized initial situation for all measurements, a randomization time of $t_{\mathrm{rand}} = 240$ s was chosen for the time-resolved PC measurements performed in this thesis.

Figure 4.17(a) presents a set of photocurrent traces recorded for different d_{i} at $B_{\mathrm{ext}} = 2$ T, $F_0 = 38.3$ kV/cm and a PC peak height of ≈ 50 pA corresponding to a laser power of $P_{\mathrm{exc}} = 16$ μW showing the temporal dependence of the PC signal. The bias region used in every of the four graphs is marked in figure 4.17(b) which also contains a steady-state PC bias sweep carried out at identical excitation wavelength and excitation rate. For each d_{i}, the time-dependent PC signal follows an individual path eventually reaching a characteristic steady-state value $I^{\mathrm{s}}_{\mathrm{PC}}$ (marked by yellow symbols). In figure 4.17(b), $I^{\mathrm{s}}_{\mathrm{PC}}$ of each time-resolved PC trace is plotted as a function of the electric field the curve was recorded at (yellow symbols). Identical yellow symbols ($\square$, $\diamond$, $\triangle$, ...) in figures 4.17(a) and (b) refer to the same electric field and corresponding d_{i}. A comparison shows that the $I^{\mathrm{s}}_{\mathrm{PC}}$ values are directly mapping out the sweep-up curve. This observation clearly demonstrates that the PC bias up-sweep was indeed performed such that the systems was in a steady state during the whole measurement.

In bias regime (I), both X^0 states are blue detuned from the laser at the beginning of the measurement. All traces recorded in this electric field range are presented in the upper left panel of figure 4.17(a) and first show a monotonic increase of the PC signal approaching a constant current level $I^{\mathrm{s}}_{\mathrm{PC}}$. This increase in photocurrent is caused by the buildup of an Overhauser field that shifts the QD states and reduces the detuning of $|E_2\rangle$ from the laser energy leading to an increase in the optical excitation rate of the dot. The maxium $I^{\mathrm{s}}_{\mathrm{PC}}$ observed corresponds to the electric field where the steady-state Overhauser shift δ^{s}_{n} reached for sufficiently long pumping of the nuclear spin system exactly compensates d_{i} (yellow $\triangledown$ symbol). In this case, the laser and $|E_2\rangle$ are fully tuned into resonance in the final state of the measurement resulting in a maxium optical excitation rate. For the electric field values in regime (II), $|E_2\rangle$ is initially also blue detuned from the excitation energy. Again, buildup of nuclear polarization generates an Overhauser shift that leads to an initial increase in photocurrent up to a maximum value where $\delta_{\mathrm{n}} = d_{\mathrm{i}}$ is met. However, in this regime $\delta^{s}_{\mathrm{n}} > d_{\mathrm{i}}$ is given and as δ_{n} increases further, $|E_2\rangle$ becomes increasingly red detuned from the laser leading to a reduction in PC generated until the steady state is reached as can be seen in the upper right panel of figure 4.17(a). The behavior of the system in the bias regimes (III) and (IV) can be

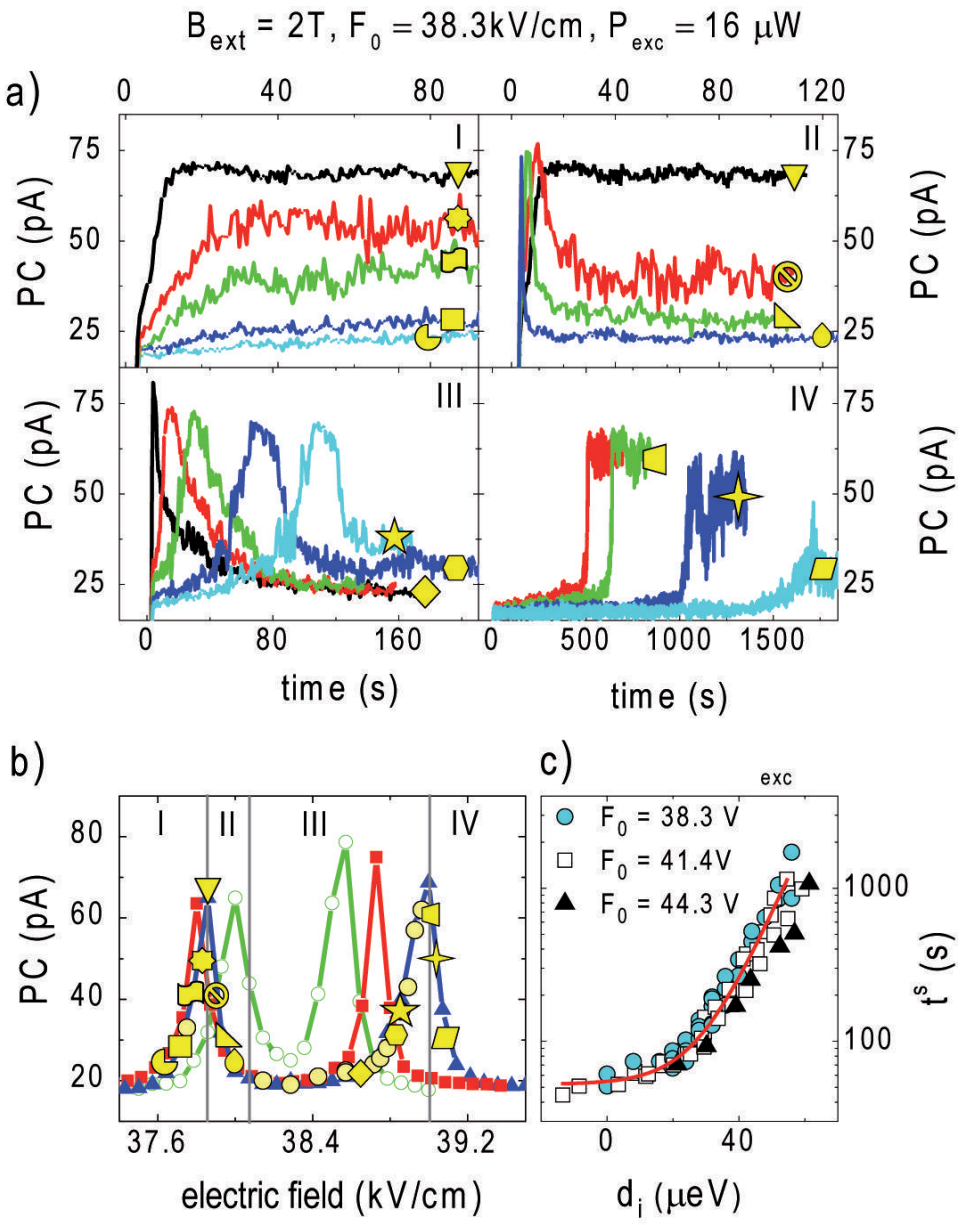

Figure 4.17. *(a) Time-dependent PC traces recorded at different, fixed electric fields F at $B_{ext} = 2$ T. Each field defines a particular initial detuning d_i of $|E_1\rangle$ and $|E_2\rangle$ from the laser energy. Yellow symbols mark the steady-state PC value I^s_{PC} that is approached for each d_i after a characteristic time t^s. (b) Steady-state photocurrent I^s_{PC} as a function of the applied electric field (yellow symbols) in comparison with corresponding steady-state PC bias sweeps performed at the same excitation power and wavelength. Identical yellow symbols (□, ◇, △, ...) in (a) and (b) refer to the same applied electric field and corresponding d_i. (c) Time t^s until the system has reached the steady state as a function of on the initial red detuning d_i of $|E_1\rangle$ from the laser (bias regime (III) and (IV)) for different F_0. The solid red line is a mono-exponential fit with an offset of 50 s.*

understood analogously. For the traces presented in regime (III), $|E_1\rangle$ is initially red detuned from the laser, then shifted into resonance, and subsequently blue detuned by the buildup of an Overhauser field. This results in the initial increase, peaking, and decrease of the PC signal to a steady-state value as observable in the lower left panel of figure 4.17(a). The traces presented in the lower right panel of figure 4.17(a) for the bias regime (IV) only show a monotonic increase to a $I_{\mathrm{PC}}^{\mathrm{s}}$ value since δ_{n}^{s} cannot fully compensate d_{i}. As can be seen from figure 4.17(a), not only $I_{\mathrm{PC}}^{\mathrm{s}}$ but also the time t^{s} until the steady state is reached is characteristic for each d_{i}. The dependence of t^{s} on the initial red detuning d_{i} of $|E_1\rangle$ from the laser (bias regime (III) and (IV)) is summarized in figure 4.17(c) measured for different F_0 at $B_{\mathrm{ext}} = 2$ T. The relation between t^{s} and d_{i} can be well described with an mono-exponential fit with an offset of ≈ 50 s (solid red line). No significant difference is found between the data obtained at $F_0 = 33.5$ kV/cm, 41.4 kV/cm, and 44.3 kV/cm. This means that at $B_{\mathrm{ext}} = 2$ T not only δ_{n}^{s} but also the time until the steady state of B_{n} is reached do not change under variation of the charge carrier tunneling times over the range examined here by the use of different electric fields regions for the measurements. Furthermore, the control experiments at $F_0 =$ 33.5 kV/cm, 41.4 kV/cm, and 44.3 kV/cm also confirmed that the corresponding PC bias sweeps were all performed adiabatically with the system being in steady state throughout the whole measurement as the recorded PC curves coincide with the $I_{\mathrm{PC}}^{\mathrm{s}}$ values determined from the time-resolved measurements identically to the case shown in figure 4.17(b).

The course of the time-resolved PC traces describes the temporal evolution of the Overhauser shift and allows besides the determination of $I_{\mathrm{PC}}^{\mathrm{s}}$ and t^{s} to monitor the buildup of the nuclear spin polarization in real time as demonstrated in figure 4.18 for QD_{A1} at $B_{\mathrm{ext}} = 2.5$ T. This can be achieved by mapping the steady-state PC spectrum recorded with randomization (open green circles left side of figure 4.18(a) onto the time resolved data (given on the right side of figure 4.18a) by shifting it such as to reproduce the instantaneous PC signal measured at a time t. The instantaneous Overhauser shift $\delta_{\mathrm{n}}(t)$ can then be extracted from this shift as plotted in figure 4.18(b) for different values of d_{i}. A characteristic behavior is observed for all curves that becomes more pronounced for larger d_{i}. A first slow linear increase in $\delta_{\mathrm{n}}(t)$ is followed by a faster buildup as the steep slope on the high energy flank of the resonance approaches the laser energy. This direct resonance is accompanied by a strong increase in excitation rate of the QD and, thus, a much higher nuclear spin pumping rate.

Figures 4.19 and 4.20 show measurements equivalent to the investigation presented in figure 4.17 but for magnetic fields of $B_{\mathrm{ext}} = 5.5$ T and 9 T, respectively, using the same excitation power and similar F_0. Interpretation of the time-dependent PC traces, $I_{\mathrm{PC}}^{\mathrm{s}}$ and t^{s} values is analog as to the one carried out for figure 4.17 above. The graphs demonstrate that the Overhauser shifts determined from the bias sweeps are indeed representing the steady-state nuclear polarization for the whole B_{ext} region probed.

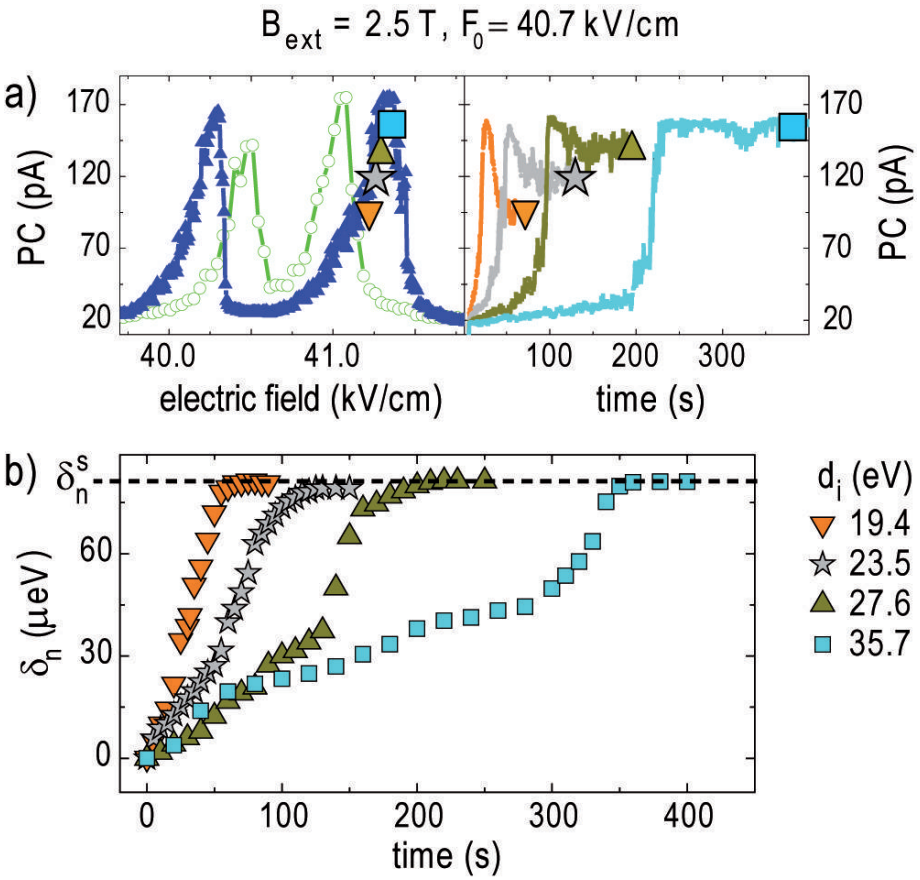

Figure 4.18. *(a)Steady-state PC bias sweeps and I^{s}_{PC} values for the corresponding electric fields F marked by the symbols (□, △, ...) determined from the time-resolved PC traces presented on the right side. (b) Overhauser shift $\delta_n(t)$ as a function of time for different d_i obtained from the data depicted in (a) via a folding of the resonance lineshape with the time-resolved PC signal as explained in the text. Identical yellow symbols (□, △, ...) in (a) and (b) refer to the same applied electric fields and corresponding d_i.*

Figure 4.21 summarizes the d_i dependence of t^s for different B_{ext}. The time t^s until steady-state nuclear polarization is reached under permanent excitation of the QD for a particular d_i is a measure for the efficiency of nuclear spin pumping. As expected from the magnetic field dependence of δ^s_n, nuclear spin pumping is most efficient at $B_{ext} = 5.5$ T and takes place with maximum detunings up to $d_i = 80$ μeV, whereas at $B_{ext} = 9$ T DNP is less pronounced and quenches already for $d_i > 20$ μeV. However, a notable difference is found for the d_i dependence of t^s at $B_{ext} = 5.5$ T. Instead of a monotonic increase of the time taken to reach the steady-state nuclear polarization with increasing initial detuning, a minimum for t^s corresponding to very efficient nuclear spin pumping is observed for $d_i \approx 60$ μeV. This effect can also be seen in the steady-state up-sweep presented in figure 4.19(b) where a side peak is found next to $|E_1\rangle$ at the position of the reference peak. In contrast to the similar-looking feature in the calculated PC curves which arises from hyperfine-assisted excitation of dark excitons

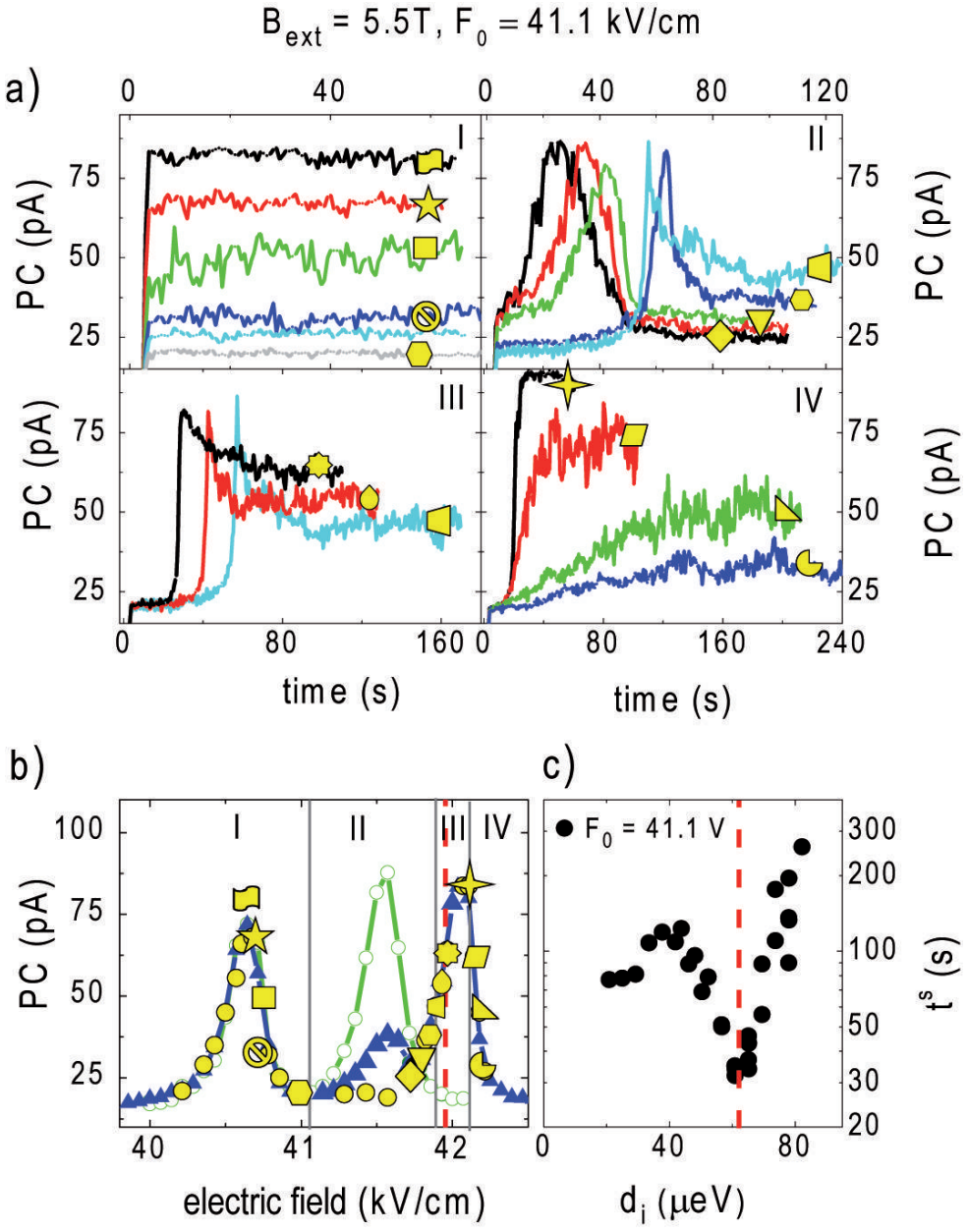

Figure 4.19. *(a) Time-dependent PC traces recorded at different, fixed electric fields F, i.e. initial detunings d_i, and at $B_{ext} = 5.5$ T. Yellow symbols mark the steady-state PC value I^s_{PC} that is approached for each d_i after a characteristic time t^s. (b) Steady-state photocurrent I^s_{PC} as a function of the applied electric field (yellow symbols) in comparison with corresponding steady-state PC bias sweeps performed at the same excitation power and wavelength. Identical yellow symbols (□, ◇, △, ...) in (a) and (b) refer to the same applied electric field and corresponding d_i. (c) Time t^s until the system has reached the steady state as a function of on the initial red detuning d_i of $|E_1\rangle$ from the laser (bias regimes (III) and (IV)).*

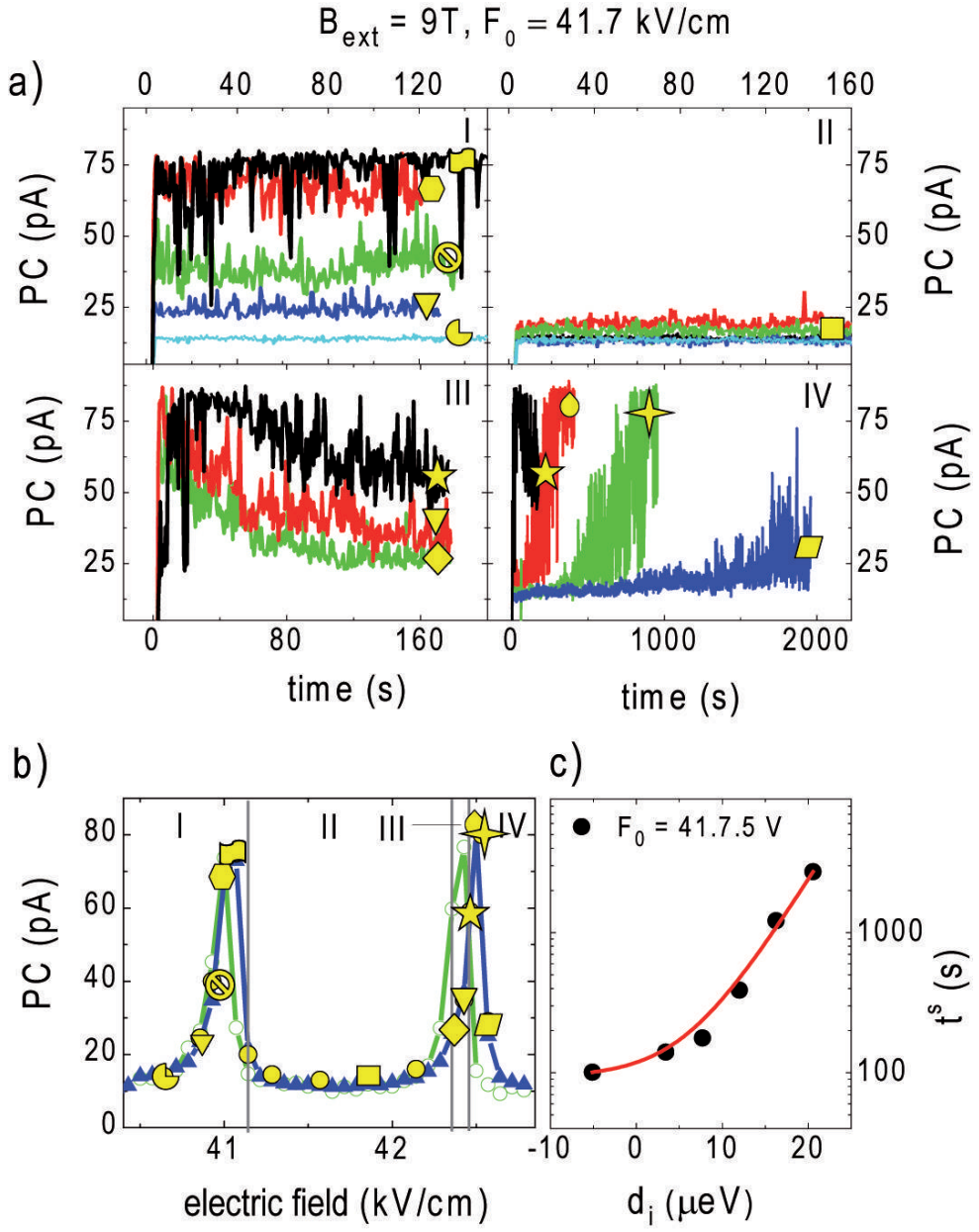

Figure 4.20. *(a) Time-dependent PC traces recorded at different, fixed electric fields F ,i.e. initial detunings d_i, and at $B_{ext} = 9$ T. Yellow symbols mark the steady-state PC value I^s_{PC} that is approached for each d_i after a characteristic time t^s. (b) Steady-state photocurrent I^s_{PC} as a function of the applied electric field (yellow symbols) in comparison with corresponding steady-state PC bias sweeps performed at the same excitation power and wavelength. Identical yellow symbols (□, ◇, △, ...) in (a) and (b) refer to the same applied electric field and corresponding d_i. (c) Time t^s until the system has reached the steady state as a function of on the initial red detuning d_i of $|E_1\rangle$ from the laser (bias regimes (III) and (IV)). The solid red line is a mono-exponential fit with an offset of 90 s.*

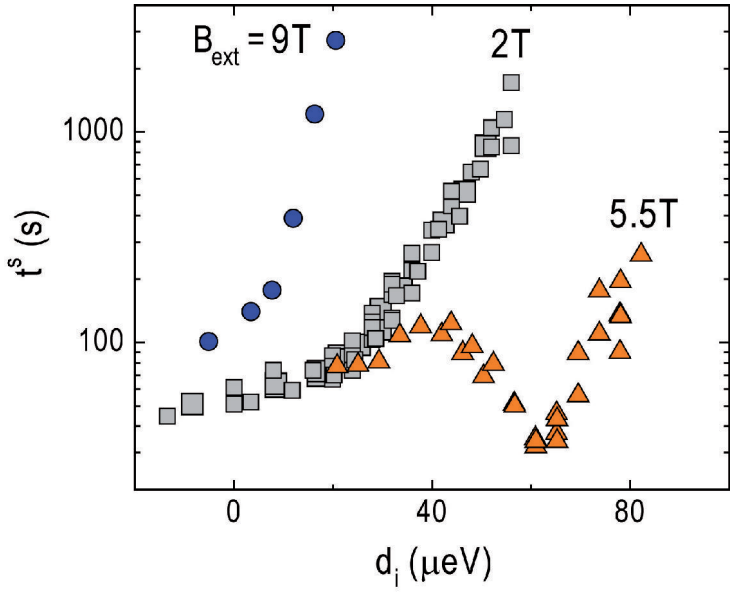

Figure 4.21. *Time t^s until the nuclear spin system has reached steady-state polarization under cw excitation of the QD as a function of the initial detuning between the higher energy X^0 Zeeman branch $|E_1\rangle$ and the laser energy for different external magnetic fields B_{ext}.*

(cf. figure 4.13), the side peak observed here stems from the fact that in this electric field region the bias sweep is not performed in steady state. This conclusion can be deduced from a comparison with the yellow symbols that are obtained from the time-resolved measurements and mark the steady-state PC signal for every electric field value in the region over which the sweep is performed. The same interpretation is found from the excitation power series presented on the right side of figure 4.7, where the side peak is also visible, becoming less and less pronounced for higher and higher pumping powers. Both, a slower sweeping rate as well as higher laser power result in a reduction of the side peak. However, in all cases, the Overhauser shift $\delta_{\text{n}}^{\text{s}}$ generated is not effected by the appearance of the side peak. This is due to the increase in nuclear pumping efficiency at a detuning of 60 μeV ensuring the steady state of the system is reached for detunings larger than this. The cause of the dip in t^{s} at $d_{\text{i}} = 60$ μeV is not clear yet. The efficiency for net nuclear spin flips to occur and further increase the Overhauser field depends on the present degree of polarization and decreases asymptotically to zero as the steady-state polarization is reached. As the electric field is fixed and the buildup of B_{n} changes the detuning between laser and QD state, different initial detunings cause the maximum excitation rate (when the laser and QD state are in resonance) to take place at different degrees of polarization. A possible explanation for the short t^{s} times for an initial detuning of $d_{\text{i}} = 60$ μeV could be a particularly advantageous combination of excitation rate and degree of polarization averaged over the whole time of the measurement. Another possibility is hf-assisted excitation of dark excitons. The parameters for $d_{\text{i}} = 60$ μeV could represent a situation where both the detuning between $|E_3\rangle$ and the laser as well as the dark-bright splitting Δ_{1-3} are appreciably small

throughout the measurement. This could lead to at an excitation rate low enough not the generate a significant PC signal but, due to the high efficiency of the process, large enough to cause noticeable DNP (cf. section 4.2.3).

Figures 4.22(a) and (b) present time-resolved PC traces recorded for varying excitation powers at different magnetic fields and detunings. Figure 4.22(a) shows power series at $B_{\text{ext}} = 2$ T and $F_0 = 41.4$ kV/cm for initial detunings of $|E_1\rangle$ from the laser by $d_{\text{i}} = 24$ meV (left side) and 40 meV (right side). The corresponding electrical fields are marked by the color-coded vertical lines in the inset on the right side showing a steady-state and reference bias sweep for the same F_0 and B_{ext}. The optical excitation power was changed from $P_{\text{exc}} = 3$ μW to 180 μW. Although the steady-state Overhauser shift generated at $B_{\text{ext}} = 2$ T is identical for all powers used as demonstrated in section 4.1.2 (cf. figures 4.7 and 4.8), the time t^{s} to reach this steady state is clearly power-dependent. The qualitatively same result is found for the equivalent measurements performed at $B_{\text{ext}} = 5.5$ T for $d_{\text{i}} = 47$ meV and 64 meV which are presented in figure 4.22(b). Again, the electric fields used are marked in the inset on the right.

Figure 4.22(c) shows the dependence of t^{s} on the optical excitation rate of the dot in a semilogarithmic plot. The data was extracted from the curves presented above in figures 4.22(a) and (b). For all parameters examined, t^{s} exhibits qualitatively the same dependence on the excitation rate. The time until steady state is reached decreases monotonically for increasing excitation rate. A minimal t^{s} characteristic for each series of measurements is found that is approached asymptotically. For $B_{\text{ext}} = 2$ T and $d_{\text{i}} = 40$ meV depicted on the left side of figure 4.22(c), t^{s} drops from 700 s to 40 s for an increase of the excitation rate from $\Gamma_{\text{exc}} = 30$ pA/e to 260 pA/e. For $d_{\text{i}} = 24$ meV, t^{s} varies from 150 s to 15 s for the same change of the excitation rate. Results of the same order are found for $B_{\text{ext}} = 5.5$ T presented on the right side of figure 4.22(c). The minimal t^{s} values observed are in agreement with the detuning dependence of t^{s} depicted in figure 4.21.

The time-resolved recording of the Overhauser shift allows to deduce the electron-nuclear flip-flop rate and to quantitatively determine the probability for such a process to occur. This is possible as the employed PC measurement technique is a quantitative method with near unity detection efficiency [Beh01; Fin01a; Beh02]. Integration of the recorded time-resolved photocurrent signal from $t = 0$ to t^{s} gives access to the total number of charge carriers pumped through the dot until the steady-state polarization of the nuclear spin system is reached. Since both the total number of flip-flops as well as charge carriers pumped through the dot is known, the net electron-nuclear spin flip-flop probability P^{ff} can be extracted.

For example, the steady-state Overhauser shift of $\delta_{\text{n}}^{s} = 77\mu$eV at $B_{\text{ext}} = 2$ T observed for QD_{A1} (cf. figure 4.5) represents a nuclear spin bath polarization of 31%[t1] [Ebl06] corresponding to a total of $\approx 1.5 \cdot 10^4$ polarized spins, i.e. net flip-flops (assuming a dot of typical size with $\sim 5 \cdot 10^4$ atoms). Comparison of this quantity with the total number of electrons pumped through the dot in order to achieve this degree of nuclear polarization allows to extract the probablilty for an optically generated generated to

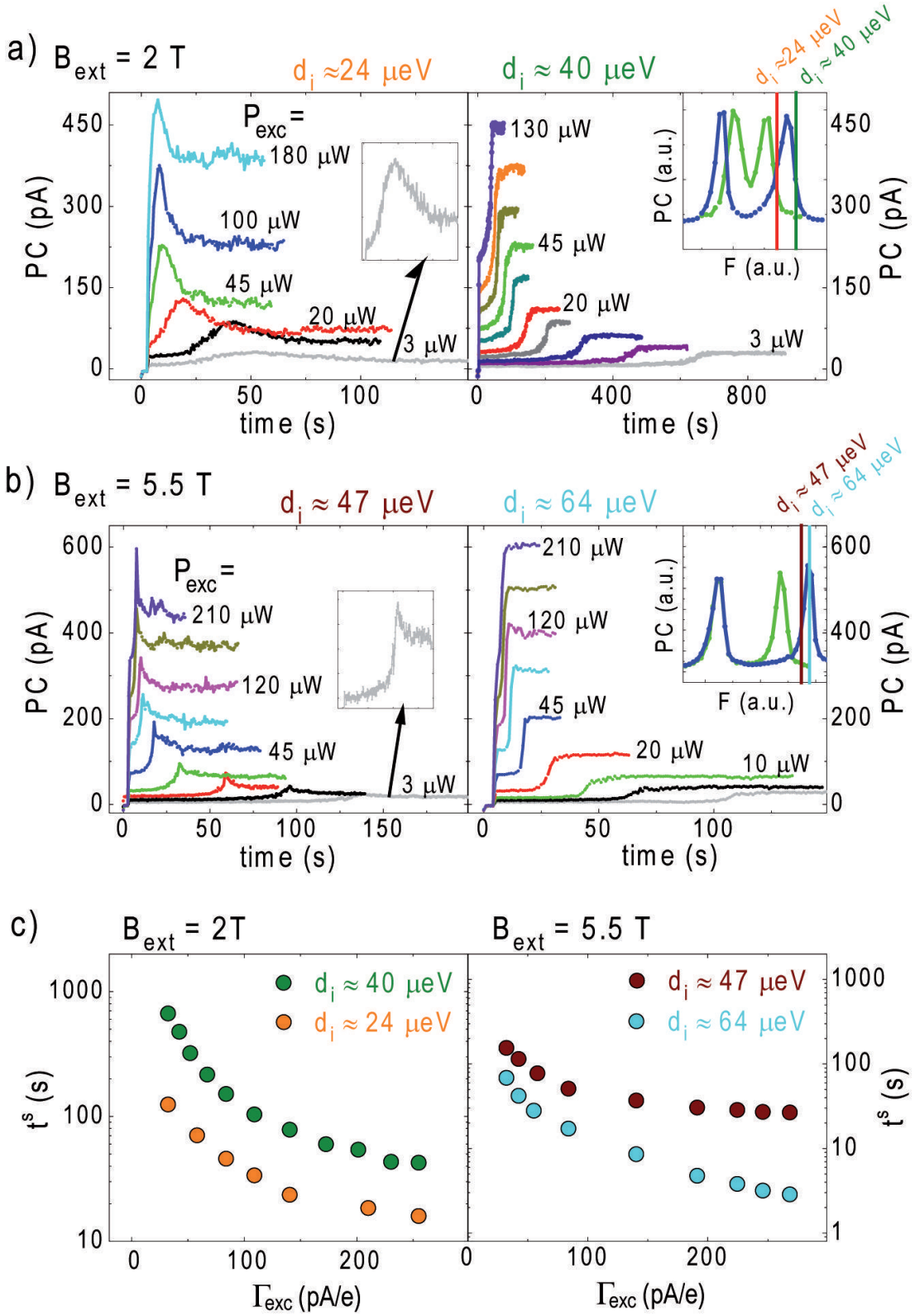

Figure 4.22. *(a) and (b) Time-resolved PC traces recorded at B_{ext} = 2 T and 5.5 T, respectively, for different pumping powers P_{exc}. (c) Time t^s until steady state is reached extracted from the curves depicted in (a) and (b) as a function of the optical pump power expressed in terms of the excitation rate ($\Gamma_{exc} = \frac{1}{e} \cdot$ PC peak height $[A/e]$).*

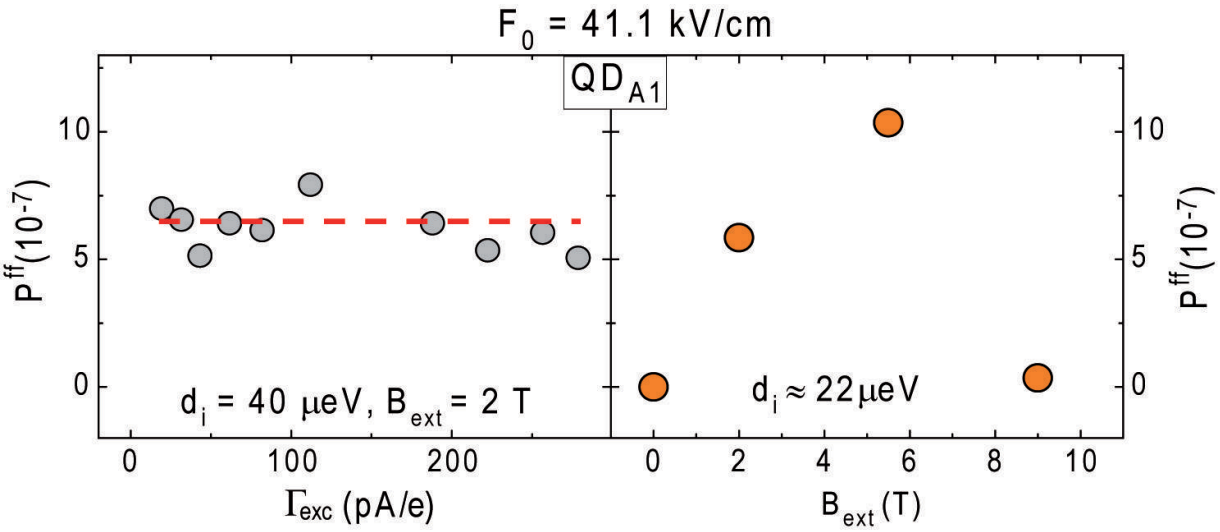

Figure 4.23. *Probability P^{ff} for a hyperfine-mediated net electron-nuclear spin flip-flop process to occur as an optically generated exciton is pumped through the dot. Values for P^{ff} were obtained from the time-resolved PC measurements as described in the text. Left: Dependence of P^{ff} on the optical excitation power used determined from the time-resolved PC traces presented in the right part of figure 4.22(a) at $B_{\mathrm{ext}} = 2$ T and $d_{\mathrm{i}} = 40$ μeV. The dashed red line is a fit to the data using a constant function. Right: Magnetic field-dependence of P^{ff} determined at a constant excitation power corresponding to a PC peak height of ≈ 70 pA and an initial detuning $d_{\mathrm{i}} = 22$ μeV. Hereby, P^{ff} is found to exhibit the same dependence on B_{ext} than $\delta_{\mathrm{n}}^{\mathrm{s}}$ (cf. figure 4.5).*

undergo a flip-flop process with a resident nuclei during its dwell time in the QD. Using this approach, the traces depicted on the right side of figure 4.22(a) were evaluated. The result is presented on the left side of figure 4.23 where P^{ff} is plotted as a function of the optical excitation rate used. As expected, the probability for an electron to exchange its spin orientation with a nuclear spin does not depend on the optical excitation rate used since the exctions are generated successively in the dot without any correlation between them. Fitting a constant function (horizontal red line), we obtain $P^{\mathrm{ff}} = (8 \pm 0.3) \cdot 10^{-7}$. This means that for the parameters used here, only one in $1.25 \cdot 10^6$ electrons actually undergoes a net flip-flop process with a nuclear spin before tunneling out of the dot. The influence of the applied magnetic field B_{ext} on the electron-nuclear spin flip-flop probability is shown in the right panel of figure 4.23 measured for identical d_{i}, F_0, and P_{exc}. The observed behavior is consistent with results obtained from steady-state PC bias sweeps with P^{ff} following the same qualitative magnetic field dependency as δ_{n}^{s} (cf. figure 4.5). The probability for a net flip of a nuclear spin to occur when an electron is pumped through the dot first increases with increasing applied magnetic field reaching a maximum of $1.6 \cdot 10^{-6}$ at $B_{\mathrm{ext}} \approx 6$ T and then drops by more than one order of magnitude to $1.6 \cdot 0.8^{-8}$ at $B_{\mathrm{ext}} = 9$ T.

4.3.2 Depolarization dynamics

To gain further insight into the nature of the depolarization procedure used to obtain the reference data, we quantify the efficiency of the randomization scheme as a function of the electric field F_{rand} at $B_{\text{ext}} = 5$ T. First, the nuclear spin bath was pumped to steady-state polarization. This is followed by a PC bias sweep including the randomization procedure performed for 10 s prior to every PC data point. The upper panel of figure 4.24 presents the observed remaining Overhauser shift measured for different applied fields F_{rand} during randomization for the two cases with (red squares) and without (blue circles) wetting layer excitation. The lower panel shows the PL spectrum of the QD recorded over the same bias range. Without any optically generated charge carriers (blue circles), randomization of the nuclear spin bath sets in when electric field is reduced to $F_{\text{rand}} \approx 28$ kV/cm. This coincides with the emergence of the X^- line in the PL signal as the QD state approaches the Fermi energy of the back contact and a first electron can tunnel onto the dot. This observation is in good agreement with a recently published study on decay mechanisms of the Overhauser field that demonstrated fast decay of the nuclear spin system within seconds when the QD is kept at a bias region of strong cotunneling [Lat11]. The relatively large cotunneling regimes observed for each charge state of the QD in the PL spectrum in figure 4.24 are due to the large spatial separation of the QD from the back contact of 35 nm and the statistical nature of the tunneling process. The depolarization processes remain efficient until $F_{\text{rand}} \approx 16$ kV/cm and then decrease as no strong cotunneling occurs in this bias region. For even smaller electric fields, randomization becomes gradually more effective again as the device is approaching flat band configuration and current flow in forward direction sets in. If unpolarized charge carriers are additionally generated via non-resonant wetting layer excitation (red squares), an efficient depolarization of the nuclear spin system is observed over the whole electric field regime where photoluminescence occurs. To ensure an effective deletion of any Overhauser fields in the measurements whenever desired, optical wetting layer pumping with $\lambda_{\text{exc}} = 855$ nm while applying an electric field of $F_{\text{rand}} = 22$ kV/cm to the QD for the randomization procedure was employed.

The fact that for magnetic fields $B_{\text{ext}} > 5$ T, no observable DNP occurs upon optical pumping of $|E_2\rangle$ allows to probe the self depolarization rate of the nuclear spin system. This was measured using a series of PC bias down-sweeps at $B_{\text{ext}} = 5.5$ T as presented in figure 4.25 to which a waiting period of varying length was introduced. First, the nuclear spin bath was pumped to steady-state polarization by optical excitation of $|E_1\rangle$ while tuning it in and out-of resonance with the laser energy during the bias sweep (open squares). When the applied electric field has reached F_0, the measurement was halted and the excitation laser switched off. While the dot was kept in the dark, a high electric field of $F = 50$ kV/cm was applied to efficiently decouple the dot from the Fermi reservoir of the back contact in order to avoid cotunneling which would quickly depolarize the nuclear spin system [Lat11]. After a waiting time τ_w, the excitation laser was switched on again and the bias sweep was continued to record the position of

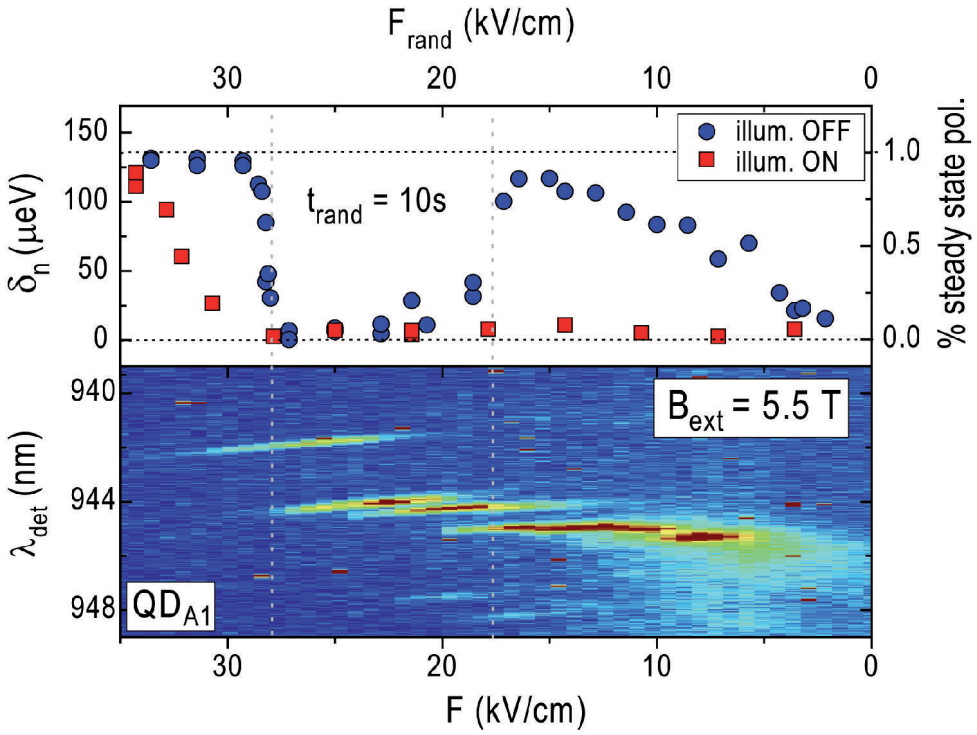

Figure 4.24. *Efficiency of the randomization procedure employed to depolarize the nuclear system as a function of the applied electric field F_{rand}, with (red squares) and without (blue circles) non-resonant wetting layer excitation of the QD. The upper panel shows the remaining Overhauser shift measured as a function of the bias applied during the randomization scheme. The lower panel presents the PL response of the QD over the same electric field regime following wetting layer excitation with $\lambda_{\mathrm{exc}} = 855$ nm.*

the $|E_2\rangle$ PC peak (closed squares). Comparison of the $|E_2\rangle$ position measured in the second half of the bias sweep with the reference curve allows to determine the remaining nuclear spin polarization at the end of the waiting time τ_w (horizontal lines). After the bias sweep was completed, the randomization procedure was applied once to guarantee an identical starting point for all sweeps and the measurement was repeated for another τ_w. This way, only the depolarization of the Overhauser field during the waiting time is probed as any perturbation of the nuclear spin system that might occur during optical excitation of $|E_2\rangle$ by any process is identical for all sweeps performed and, thus, has no influence on the measured depolarization rate of B_{n} but would merely introduce a constant offset to the measured decay curve. The obtained result is presented in figure 4.26 where the Overhauser shift δ_{n} observed in the second part of the electric field sweep is plotted as a function of the waiting time τ_w for $F_0 = 40.0$ kV/cm and 44.6 kV/cm.

In agreement with previous experiments reported in literature performed at 0.2 - 4 K on uncharged QDs [Mal09; Lat09; Lat11], no measurable decay of the nuclear spin polarization is observed during the first 20 min at 10 K. Even after $\tau_w = 90$ min,

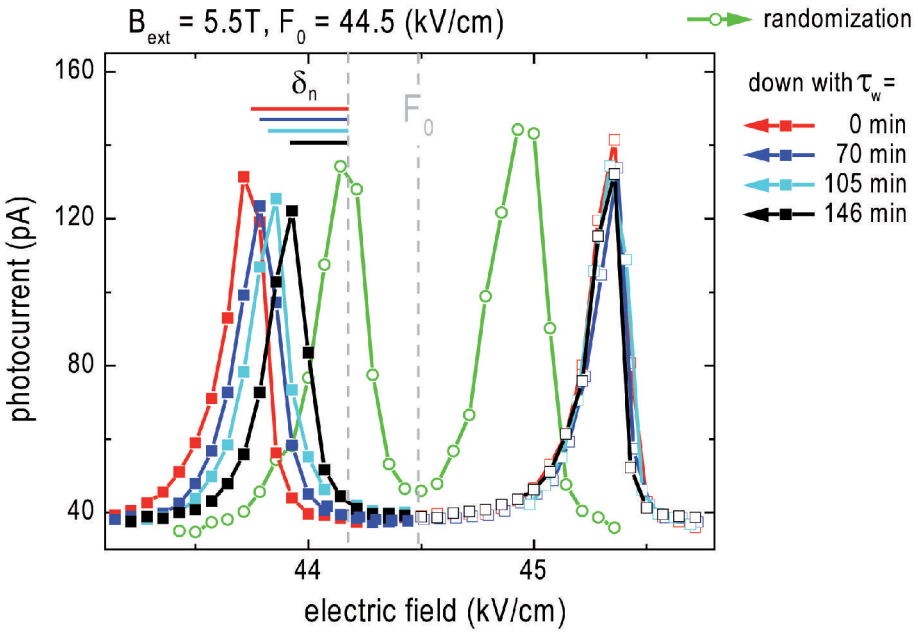

Figure 4.25. *PC bias down-sweeps used to probe the decay of the Overhauser field B_n. First, the nuclear spin bath is pumped to steady state by resonant excitation of $|E_1\rangle$ during the first part of the sweep (open squares). Then a waiting period τ_w is introduced during which the dot is kept in the dark and strongly decoupled from the back contact by a high applied electric field of $F = 50$ kV/cm. Finally, the bias sweep is completed (closed squares) and the remaining Overhauser shift δ_n of $|E_2\rangle$ is determined (horizontal lines).*

80 % of the steady-state polarization is still present and only after more than 2.5 h, B_n has decreases to 50 % of its initial value. Unlike electron-mediated decay processes of the nuclear spin polarization which take place in charged exciton states [Mal07; Che10b; Lat11] and very efficient nuclear spin depolarization by cotunneling effects [Lat11] which can be excluded here as coupling of the dot to the back contact is highly suppressed by the high applied electric field, the decacy of the Overhauser field in uncharged QD is dominated by nuclear spin diffusion [Mak08a]. Only very recently, a microscopic description of the processes leading to the observed slow decay of B_n in uncharged QDs was proposed. It is based on the existence of large and inhomogeneous quadrupolar shifts caused by the biaxial strain within and in the vicinity of ~ 3 nm around self-assembled QDs [Lat11]. As a result, nuclear spin diffusion induced by dipolar-interactions is strongly suppressed, efficiently preventing flux of nuclear spin polarization within and out of the dot into the surrounding material. It should be noted that any modification of strain distribution in the dot as e.g. expected from the *In-flush* technique causing a material redistribution as applied for the samples investigated here, can have an impact on the spin diffusion, altering the B_n lifetime.

The observed free evolution of the polarization after pumping the nuclear spin system into steady state (cf. figure 4.26; the red line is a guide to the eye obtained from a quadratic fit) does at first glance not seem to follow the form expected from a typical

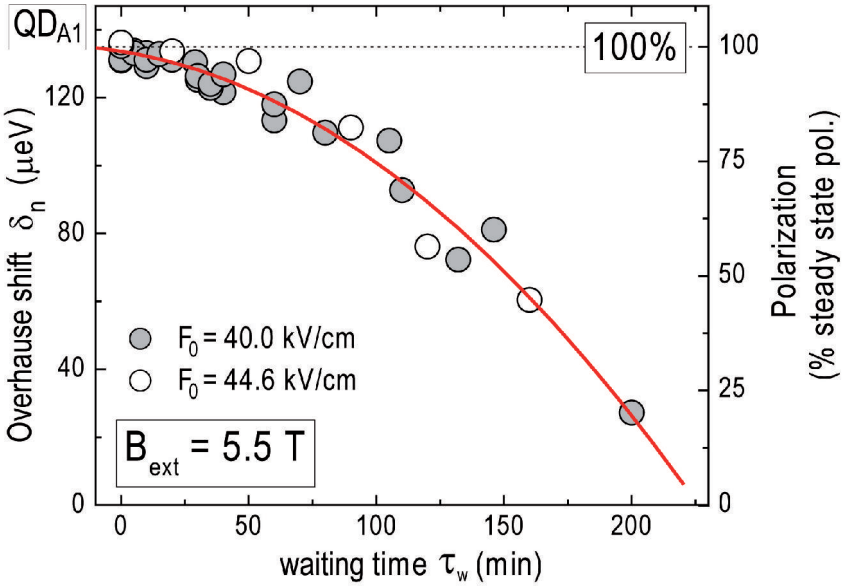

Figure 4.26. *Decay of the Overhauser field B_n recorded at $B_{ext} = 5.5$ T and $T \approx 10$ K for $F_0 = 40.0$ kV/cm and 44.6 kV/cm. The depolarization dynamics were probed in a set of PC bias down-sweeps as presented in figure 4.25 by introducing a waiting period τ_w during which the dot is strongly decoupled from the back contact by a high applied electric field of 50 kV/cm and kept in the dark. After $\approx$ 90 min, 80 % of the steady-state nuclear spin polarization is still present. The solid red line is a guide to the eye obtained from a quadratic fit.*

decay process, however, is very plausible taking into account the way spin polarization is probed in the experiment performed here. Polarization of the nuclear spin system is determined by detecting the Overhauser shift δ_n of the X^0 states arising from a coupling of the electron and hole spin with the spins of the nuclei resident in the QD. The strength of this interaction, i.e. the contribution of each nuclei to the total shift is determined by the overlap with the wave function of the charge carriers confined in the dot. Polarization of the nuclear spin systems within the dot reduces when diffusion across the border of the dot into the surrounding material takes place. This leads to a decay of polarization that is (i) not homogeneous across the whole nuclear spin ensemble but (ii) first occurs in the outer layers of the dot and last in the center where the overlap with the wavefunctions is maximal. Therefore, the decrease of δ_n measured this way is expected to be comparatively slow in the beginning when the outer regions of the dot become depolarized and proceed more quickly as polarization starts to diffuse away from the inner area of the dot, a scenario which is in good agreement with the behavior observed in figure 4.26. As expected, the excitation wavelength used for the experiment, i.e. the electric field range over which the PC bias sweeps were carried out, had no influence on the observed decay of B_n as can clearly be seen in figure 4.26.

As indicated above, the observed slow decay of nuclear spin polarization in a neutral QD electrically decoupled from the back contact and kept in dark presented in figure 4.26

is expected to take place via spin diffusion from the nuclear spin ensemble in the dot into the surrounding bulk material. The diffusion constant $D_{\mathrm{n,diff}}$ in the strained QD material is not precisely known and also not expected to be constant over the whole dot and its direct vicinity. For GaAs bulk material, it was determined experimentally to be $D_{\mathrm{n,diff}} = 10^{-13}$ cm^2 s^{-1} [Pag82]. Assuming a typical self-assembled QD with a lateral size of d_{QD}20 nm, this corresponds to a diffusion of the polarization out of the dot on a timescale of ~ 1 min. However, the diffusion is assumed to be slowed down significantly in a self-assembled InGaAs quantum dot structure due to the presence of different nuclear species and strain within the dot in comparison to the surrounding GaAs matrix. Although this effect has not been not quantified yet for QDs, it was shown experimentally that $D_{\mathrm{n,diff}}$ is reduced by at least one order of magnitude for spin diffusion between two quantum wells [Mal01]. As this trend is expected to continue when going from 2D to 0D structures, the timescale found for the depolarization of the nuclear spin system as presented in figure 4.26 makes nuclear spin diffusion a plausible mechanism for the observed decay of the Overhauser field in a QD in the absence of cotunneling, the presence of charge carriers and laser illumination.

Comparison of the time-resolved experiments and the steady-state bias sweeps allows to draw several conclusions regarding the depolarization mechanisms of the nuclear spin system and to specify some properties of the effects causing decay of the Overhauser field B_{n} as well as limiting the steady-state degree of polarization under resonant pumping.

As discussed directly above, decay of nuclear spin polarization in the absence of external perturbations is expected to occur via nuclear spin diffusion. This is in agreement with the experimentally obtained slow timescale of the depolarization making it a plausible decay mechanism in this case. However, when compared to the time-resolved measurements of the buildup dynamics of B_{n}, the diffusion rate observed without illumination and exciton generation leading to a B_{n} lifetime of hours appears to be far to slow to be the dominant process accounting for the upper limit of steady-state nuclear spin polarization of 54 % achieved in this work and other experiments reported in literature [Bra06b; Urb07; Mal09; Klo10a; Che10b; Urb12]. This intuition is supported by the numerical simulations. As mentioned in section 4.2.3, a depolarization rate f_{depol} has to be assumed in order to reproduce characteristic experimentally observed features of DNP. Although this rate is introduced purely phenomenologically in the model and does not allow to identify particular mechanisms, it provides an estimate for f_{depol}. The values found from the calculation (cf. table 4.1) imply a depolarization rate much larger than observed for the free decay of B_{n} when the dot is empty and kept in the dark.

While the assumption of a constant depolarization rate in the simulation allows to reproduce and understand the observed magnetic field dependence of $\delta_{\mathrm{n}}^{\mathrm{s}}$ (and is in agreement with the B_{ext} dependence of P^{ff}) as well as to describe the photocurrent bias sweeps, it can not simultaneously explain the behavior of $\delta_{\mathrm{n}}^{\mathrm{s}}$ under a variation of the optical excitation rate as presented in section 4.1.2. Since the time-resolved measurements show an increase in the nuclear spin pumping rate with increasing

laser intensity (cf. section 4.3.1), the insensitivity of δ_n^s to a change in excitation power for all $B_{ext} \leq 6$ T proposes a simultaneous increase of depolarization processes for increasing Γ_{exc}. Consequently, laser- and/or exciton-induced processes are likely to play a role. However, although the achievable steady-state nuclear spin polarization for all magnetic fields ≤ 6 T is unaffected by the optical pumping rate (cf. figure 4.8), the temporal evolution of the system towards this δ_n^s value does show a pronounced Γ_{exc} dependence as can be seen from the time-resolved PC measurements (cf. figure 4.22). This observation together with the fact that at larger magnetic fields $B_{ext} > 6$ T a different behavior is found where δ_n^s does depend on the optical pumping rate of the system and increases for increasing Γ_{exc} (cf. figure 4.8) suggests a complex interplay between different depolarization processes and/or the existence of different regimes during the course of pumping the nuclear spin system to the steady-state polarization in this magnetic field regime.

One possible depolarization mechanism which was proposed in a recently published study [Hoe12] are laser-induced nuclear spin flips enabled by the non-collinear terms of the nuclear quadrupolar interactions that arise from the strain within the dot. However, the rates obtained from this approach also turn out to be significantly smaller than found from the numerical simulations [Klo12]. Further potential candidates are for example laser-enabled nuclear dipolar diffusion, electron-mediated nuclear spin diffusion due to the intermediate singly-charged state, spin diffusion enabled by non-collinear terms in the hf Hamiltonian for electron or hole or a combination of several mechanisms. Identification of the relevant processe(s), however, could not be achieved based upon the experimental and theoretical investigations conducted in this thesis and the question of the depolarization mechanism(s) remains open.

4.4 Towards DNP in a single quantum dot molecule

In this section, first results of DNP in a single quantum dot molecule formed by two strongly coupled QDs as introduced in section 2.5 are presented. The investigation of nuclear spin pumping in this system allows to address further questions with regard to nuclear spin effects that cannot be examined in a single dot. For example, generating nuclear spin polarization in one dot of the molecule and detecting the temporal evolution of the Overhauser shift in the other dot would allow to directly measure the nuclear spin diffusion constant since the inter-molecular distance is known with very high precision. Another whole field of experiments is opened when DNP is pumped in the coupling regime of the two dots where the electron wave function is delocalized across the whole molecule.

Figure 4.27 summarizes first results of DNP experiments performed on a QDM. As for the single QDs, nuclear spin pumping was achieved via resonant pumping of the two bright neutral exciton states $|E_1\rangle$ and $|E_2\rangle$ in PC bias sweeps at $B_{ext} \neq 0$ T. Here, the X^0_{dir} resonances of the molecule´s upper X^0_{dir} were probed. Figure 4.27(a) gives an

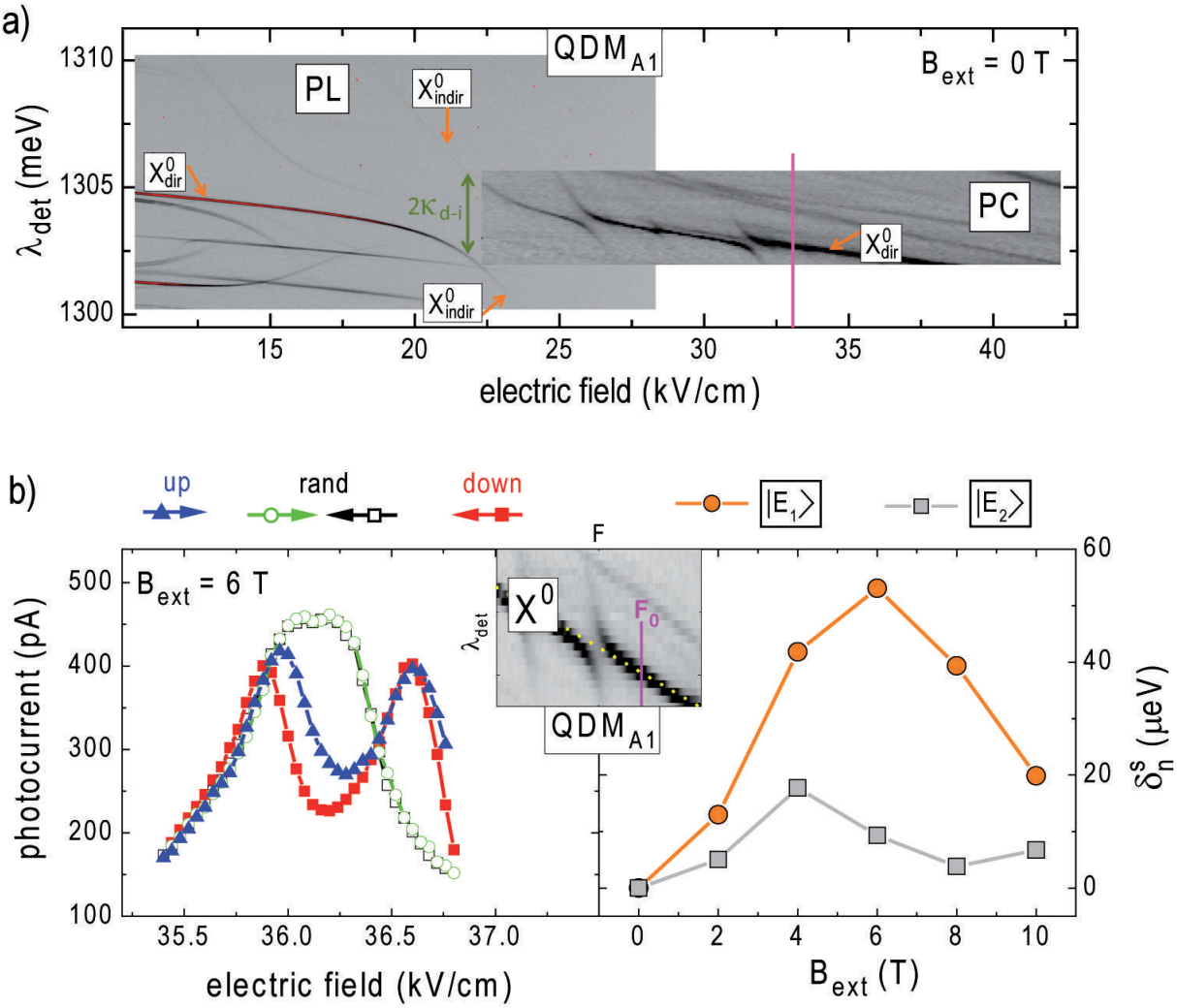

Figure 4.27. *First results on DNP in a quantum dot molecule. (a) PL and PC spectra of QDM_{A1} as a function of the applied electric field in a grayscale image plot at $B_{ext} = 0$ T. The level scheme clearly reveals the typical fingerprint of a single QDM (cf. figure 2.25). (b) Left: Steady-state PC bias sweep performed on the bright neutral exciton X^0_{dir} states $|E_1\rangle$ and $|E_2\rangle$ of the molecules upper dot at $B_{ext} = 6$ T. Right: Magnetic field dependence of δ^s_n upon pumping $|E_1\rangle$ and $|E_2\rangle$. The sweeps at different magnetic fields were performed at a constant position relative to a particular anticrossing marked by the vertical purple line in (a).*

overview of the molecule´s PL and PC response as a function of the electric field applied allowing to characterize the structure and identify the individual states as discussed in section 2.5. Clearly visible is the tunnel coupling between the direct and indirect neutral exciton state in the PL regime that leads to an anticrossing at $F \approx 22$ kV/cm with strength $2\kappa_{\mathrm{dir-ind}}$ indicated in the figure by the green vertical arrow. For $F > 25$ kV/cm where the PL signal quenches due to tunnel escape of the charge carriers from the dot, the X^0_{dir} levels of the upper dot are mapped out via a series of PC bias sweeps depicted in a grayscale image plot. Over the whole electric field range covered, a series of additional anticrossings is observed indicating further coupling effects. The investigation of these avoided crossings that stem from tunnel couplings to excited states and Coulomb couplings between different levels are subject of ongoing studies [Mue12b; Wae12].

Figure 4.27(b) presents DNP probed on QDM_{A1}´s upper dot X^0_{dir} states. The left side of the figure depicts a set of steady-state PC bias sweeps together with the corresponding reference curves at $B_{\mathrm{ext}} = 6$ T and $F_0 = 36.2$ kV/cm. As for the single dots, application of the randomization procedure prior to every data point results in an insensitivity of the recorded curves on the sweeping direction of the electric field. This demonstrates the applicability of the depolarization technique to this system.

The up- and down-sweeps reveal a pattern of the Overhauser shifts generated which is qualitatively the same as found for *Type-A* single dots as presented in figure 4.1. The interpretation of the curves is identical to the one for single QDs as carried out in section 4.1. As the up-sweep performed from low to high electric fields approaches the lower energy Zeeman branch $|E_2\rangle$, no Overhauser shift occurs and the recorded resonance coincides exactly with the reference curves. In contrast, when the higher energy state $|E_1\rangle$ is reached nuclear spin pumping takes place and the resonance is shifted towards higher energies corresponding to an increase of the Zeeman splitting. As the electric field is swept in the opposite direction in a down-sweep measurement, again $|E_1\rangle$ is found to be shifted in the same direction. When $|E_2\rangle$ is reached later in the sweep the nuclear polarization generated is still partially present and $|E_2\rangle$ is shifted towards lower energies as expected for an increased Zeeman splitting. However, in contrast to the single QD experiments presented in figure 4.1, the shift of $|E_2\rangle$ due to the remaining nuclear polarization from spin pumping earlier in the measurement is significantly reduced, a trend that was generally observed in DNP measurements on QDM_{A1}. This hints at a faster decay rate of the Overhauser field or a higher sensitivity of the nuclear spin polarization to the optical excitation without significant DNP and associated potential depolarizing processes taking place while measuring $|E_2\rangle$ in the PC sweep.

On the right side of figure 4.27(b), the magnetic field dependence of the steady-state Overhauser shift $\delta^{\mathrm{s}}_{\mathrm{n}}$ upon pumping of $|E_1\rangle$ (orange circles) and $|E_2\rangle$ (gray squares) is depicted. The individual sweeps at the different B_{ext} values were always performed at the same distance from a particular anticrossing in order so guarantee identical character of the X^0_{dir} states. The corresponding electric field at $B_{\mathrm{ext}} = 0$ T is marked

in figure 4.27(a) by the vertical purple line labeled F_0. However, since the position of the anticrossings varies as a function of the magnetic field applied F_0 hat to adapted accordingly throughout the magnetic field series of the PC bias sweeps. Varying B_{ext} from 0 T to 10 T corresponds to a change of F_0 from 33 to 39 kV/cm. As for the *Type-A* dots, DNP created upon pumping of $|E_1\rangle$ initially increases monotonically for increasing B_{ext}, peaks around $B_{\text{ext}} = 6$ T at a value of $\delta_{\text{n}}^{\text{s}} = 65$ μeV and then decreases for higher magnetic fields reaching $\delta_{\text{n}}^{\text{s}} = 25$ μeV at $B_{\text{ext}} = 10$ T. For resonant excitation of $|E_2\rangle$, a qualitatively similar picture with a maximum $\delta_{\text{n}}^{\text{s}}$ of 25 μeV occurring at $B_{\text{ext}} = 4$ T and a generally lower DNP efficiency across the whole magnetic field range is found.

In summary, both characteristic DNP effects observed in single QDs, namely the *asymmetric* and *unidirectional* effect for pumping of the two bright X^0 states, as well as the characteristic magnetic field dependence are also found for the direct neutral exciton states of the upper dot in a molecule.

The fact that DNP can be generated and probed in an individual dot of a QDM analogously to a single dot is an important prerequisite for further experiments. In a non-coupling regime, i.e. electric fields regions where the probed states have a sufficient energetic distance from an anticrossing, the QDM can be regarded as two QDs with a precisely defined and known distance and relative orientation. This allows to design experiments using one dot to pump the nuclear spin system and the other dot as a sensor. The situation is drastically altered when the electric field is used to tune the states of the two dots into resonance. In the case of tunnel coupling, the electron is delocalized across the molecule. Here, a series of bias sweeps using different F_0 values allows to probe the variation of DNP effects as the character of the state gradually changes from the single dot case to a coupled, hybridized situation. Furthermore, coupling effects in a QDM can be used to tune the tunneling times of the electron from the dot by inducing inter-dot tunneling processes and achieve ultrafast extraction of the electron from the QD on a timescale as fast as 5 ps [Mue12a]. This allows to study the dependence of DNP on the dwell time of the electron for ultra-fast tunneling times.

4.5 Summary

In this chapter, an experimental and theoretical investigation of dynamical nuclear spin pumping in a single, uncharged InGaAs quantum dot was presented. Resonant excitation of the two bright X^0 states in photocurrent bias sweeps revealed an *asymmetry* in the generated degree of polarization upon pumping of $|E_1\rangle$ and $|E_2\rangle$ where nuclear spin polarization is found to be always oriented along the same direction, irregardless of the Zeeman branch used to pump it. This *asymmetric* and *unidirectional* behavior as well as the observed characteristic magnetic field dependence of DNP is reproduced by numerical simulations based on the model developed and can be understood based on hyperfine meditated electron-nuclear flip-flop processes and the associated transitions within the neutral exciton level spectrum. Furthermore, time-resolved PC measurements

were presented that allow to monitor the buildup of the Overhauser magnetic field in real time under resonant excitation as well at its decay when kept in the dark and being electrically decoupled from the contacts. In the end, first results on DNP in a quantum dot molecule are presented and possible future experiments are discussed.

5

Development and testing of an on-chip coplanar stripline antenna structure

One of the key requirements for the use of single electron spins confined in semiconductor nanostructures such as quantum dots for quantum information processing is coherent manipulation of the electron spin over timescales shorter than that over which quantum phase coherence persists as it is an essential prerequisite to perform logical quantum operations [Los98; Lad10]. The most commonly used technique to manipulate electron spins in an external magnetic field B_0 is electron spin resonance (ESR) [Zav45] which employs the oscillating magnetic field component B_1 of a microwave (mw) field to resonantly drive transitions between the two electron spin states split by the Zeeman energy $E_Z = g_e \mu_B B_0$ (cf. section 2.2.3).

Transferring ESR to the single spin level is experimentally challenging and the necessary high sensitivity is e.g. achieved by converting the spin information to a charge information via a spin-dependent charging or transport process [Hei10; Hei08a; Kop06], energy selective readout [Elz04; Mor10] or optical readout [Hei10; Hei08a; Vam10; Jel04]. Until now, coherent control of single electrons in a QD via microwaves has only been demonstrated in electrostatically defined semiconductor QDs [Kop06; Kop08] where the microwaves were supplied via an on-chip antenna formed by a terminated coplanar stripline (CPS) [Kop06]. Transfer of this technique to self-assembled QDs that can be operated at much higher temperatures than gated QDs of up to 70 K or even higher for certain applications [Pol99; Bay02a; Duc04; Hei10] and are optically active [Mar94; Leo95; Gam96b; War00] has not been achieved so far. For these types of dots, only one successful experiment on a single QD involving microwaves has been reported until now [Kro08b]. In this case, a loop antenna placed next to the sample was used, but coherent control of the electron spin was not achieved. Only very recently, this

has been realized for a single, self-assembled QD, however, using an optical method to manipulate the electron spin [Pre10]. A functionally equivalent approach to ESR for spin control is modulation of the g-tensor at the speed of the Larmor frequency, a technique that so far has only been successfully employed in parabolically composition graded AlGaAs quantum wells [Sal01; Kat03] and vertically coupled (Ga)InAs QD molecules [Dot06]. Although notable improvements have been made in experimental realization, modeling, and understanding of electrical control of the exciton g-factor in single, self-assembled quantum dots [And09b; Klo10b; Jov11] as discussed in chapter 3, application of this method for spin manipulation in these systems has not be achieved until now.

In this chapter the development and testing of a coplanar stripline antenna that is designed for integration into a magneto-photoluminescence experiment to allow coherent control of individual electron spins confined in single self-assembled semiconductor quantum dots is described [Klo11b]. The design criteria for such a structure which is multi-functional in the sense that it serves not only as microwave delivery but also as electrical top gate and shadow mask for the single quantum dot spectroscopy are discussed. To test the performance of the CPS antenna, measurements on hydrogenated amorphous silicon (a-Si:H) are performed demonstrating electrically detected magnetic resonance (EDMR) using the in-plane component of the oscillating magnetic field created by the CPS antenna. From reference measurements using a commercial electron spin resonance setup in combination with finite element calculations simulating the field distribution in the structure, at incident microwave power of $P_{\mathrm{mw}} = 120$ mW, an in-plane magnetic field of 0.12 mT is found at the position where the quantum dots would be integrated into the device. This field amplitude corresponds to a π-pulse time of ≈ 0.5 μs.

The in-plane component of the magnetic field and the comparatively large area of the stripline termination (> 800 $\mu\mathrm{m}^2$) that are required here for reasons that will be presented in section 5.3 sets this experiment aside from applications using similar CPS antenna structures for spin manipulation in other systems such as electron spin control in electrostatically defined semiconductors QDs [Kop06], electrically detected magnetic resonance of phosphorus donors in silicon [Bev08; Dre11] or strong driving of single spins in nitrogen vacancy centers in diamond [Fuc09]. When CPS antennas are employed for these experiments, commonly, the out of-plane component of B_1 and significantly smaller termination areas of the stripline (< 50 $\mu\mathrm{m}^2$) resulting in a larger B_1 field are used and, therefore, allow for faster spin manipulation than with the CPS structure presented here. However, these CPS designs are not applicable for the approach developed here since the CPS antenna does not only supply the microwave field but simultaneously also serves as the electrical top contact and the shadow mask both needed for single QD spectroscopy imposing particular demands on the design of structure.

In section 5.1, the technique for initialization, storage, and readout of electron spins in single self-assembled QDs is reviewed and the specific criteria for integration of

the CPS antenna structures into this experiment are introduced. In section 5.2, finite element simulations of the structure performed to obtain information about the spacial distribution of the field generated by the CPS antenna excited by microwaves are presented. Detailed information about design and fabrication of the a-Si:H sample used to test the performance of the CPS antenna, experimental results of the performance tests, and reference EDMR measurements using a commercial resonator are presented in section 5.3. In section 5.4, the experimental data is analyzed, the B_1 field generated by the CPS antenna in the test experiments is determined, and the feasibility of achieving coherent control of electron spins in single QDs is evaluated. Finally, in section 5.5, several experimental challenges attributed to the employment of on-chip CPS antennas are addressed and possible ways to approach them presented.

The main findings presented here are published in [Klo11b]. This chapter is based on [Klo11b]. The a-Si:H films used for the experiments in presented in this chapter were grown by F. Finger and O. Astakhov at the Forschungszentrum Jülich.

5.1 Design criteria for the CPS antenna

Electron spin initialization and readout in single quantum dots

Before introducing the design criteria for the microwave antenna, first, the micro-magnetoluminescence setup used for single spin storage in self-assembled quantum dots presented in figure 5.1(a) including the spin initialization and readout protocol will be reviewed [Hei10; Hei08a]. A brief overview over the experiment the CPS antenna is developed to be integrated into allows to put the different demands to the CPS structure into the experimental context and to motivate the resulting design criteria. A detailed description and analysis of the single spin storage and readout technique can be found e.g. in Refs. [Hei10; Hei08a; Hei09a; Jov12a; Rud09; Kap11]. A schematic of the sample structure and the band diagram in growth direction are presented in figures 5.1(b) and (c), respectively.

Identical to the samples used for the experiments presented in chapter 3 and 4, a single layer of QDs is embedded within the intrinsic region of a Schottky photodiode formed by a heavily n^+-doped back contact and a semitransparent titanium top contact. In order to minimize perturbations of the microwaves propagating along the coplanar stripline by the back contact located 140 nm underneath the CPS structure, an undoped substrate was used and only a 100 nm thin layer was n^+-doped. An ohmic contact to the doped layer was established by evaporation of GeAuNiAu and subsequent annealing for 40 s at 420 °C in vacuum before evaporation of the Ti layer forming top contact. The titanium layer is covered with an opaque Au film in which 1 - 5 μm wide apertures are opened, facilitating optical addressing of individual QDs. However, in contrast to the samples previously presented in this thesis, a layer of AlGaAs with a bandgap larger than that of GaAs is introduced in between the back contact and the QDs as illustrated in figures 5.1(b) and (c). This AlGaAs layer forms a potential barrier between the electron

located in the QD and the corresponding electrical contact but does not so for the hole, leading to an asymmetric tunneling behavior for the two types of charge carriers.

Via the back and top contact, electric fields can be applied along the growth direction of the sample enabling tuning of the bandstructure which allows to switch the device between three different modes of operation: (i) the reset regime, where both electrons and holes are quickly removed from the dot due to application of a strong electric field; (ii) the charging regime, where optically generated excitons are efficiently ionized since holes are removed rapidly from the QD whilst electrons remain trapped over millisecond timescales and beyond [Hei08a; Hei09b]; (iii) the readout regime, where the tunneling time for both types of charge carriers is longer than the radiative recombination time and luminescence is created.

The measurement scheme used for single spin storage and readout combining the different regimes is illustrated in figure 5.2. First, the device is tuned to the reset regime to ensure removal of all resident charge carriers from the dot, preparing an empty QD at the beginning of every measurement cycle (a). Next, the dot is switched to the charging regime and resonantly excited in the lowest orbital state of X^0 (b). Using circularly polarized light for excitation or employing a polarized absorption line allows to create an exciton with predefined spin configuration. After the tunneling of the hole, the spin system is prepared and the coherent manipulation should be performed (c). To probe the

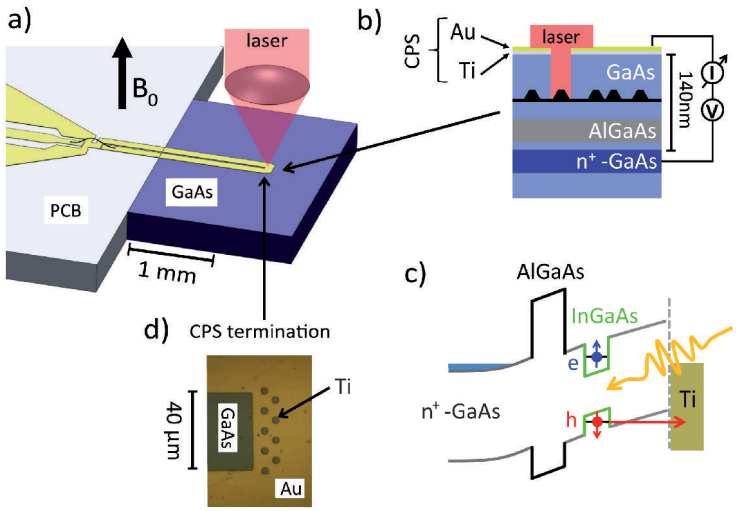

Figure 5.1. *(a) Illustration of the micro-magneto photoluminescence experiment the CPS antenna examined in this work is designed for. The external magnetic field B_0 is perpendicular to the sample surface. (b) Schematic drawing of the electron spin storage sample structure containing an AlGaAs tunneling barrier. (c) Schematic of the band structure in growth direction with. (d) Optical microscope image of a CPS antenna structure for implementation in a single QD micro-photoluminescence experiment. To make single QDs optically addressable, 5 µm wide, lithographically defined apertures are opened to the gold film at the position of the desired oscillating magnetic field created by the antenna.*

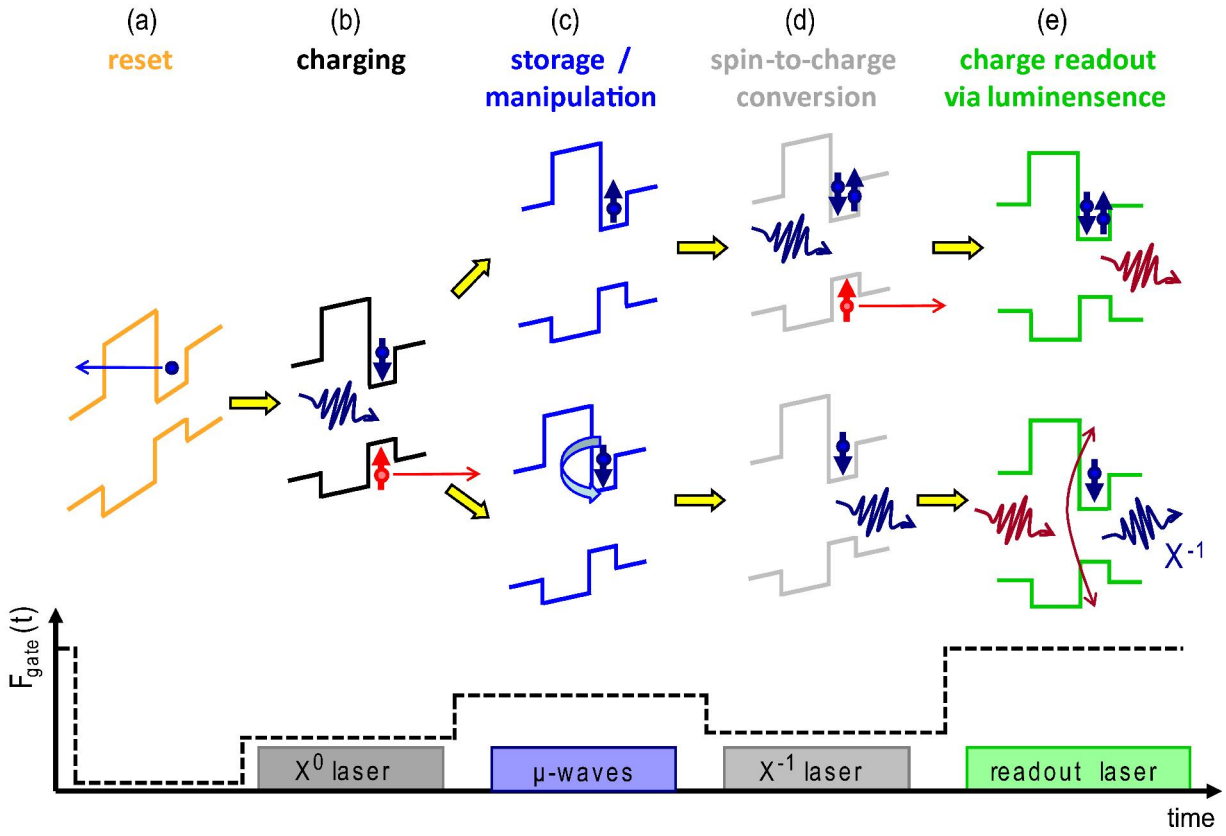

Figure 5.2. *Schematic representation of the pulse sequence used for spin storage and readout experiments. An optically created electron with predefined spin orientation can be stored in the QD over long timescales and probed via a second, spin-dependent optical excitation step, mapping the spin state of the resident electron on the charge occupancy of the dot. In the end, the charge state is detected via a PL measurement.*

spin orientation at the end of the desired storage/manipulation period, a spin-to-charge conversion technique is used. For this, a second charging step with a laser tuned into resonance with the X^- absorption line is employed (d). Absorption of the second laser pulse is spin conditional as it is only possible if the created electron is of opposite spin orientation than the resident electron due to the Pauli exclusion principle, therefore, mapping the spin orientation of the electron onto the charge occupancy of the dot. In a last step, the charge state of the dot is probed in a PL measurement (e). Setting the sample to the readout regime and tuning a third laser into resonance with a *p*-shell state of X^- will only lead to a PL signal if the dot is charged with only one electron allowing to determine the charge state of the dot simply by monitoring the PL signal intensity [Hei10; Hei08a]. The experiment is performed in Faraday configuration and the sample is illuminated under normal incidence. The luminescence signal is collected via the same optical path and is spectrally and temporally separated from the excitation pulse.

Although manipulation of the electron spin during the storage period has not been implemented into the experiment until now, the scheme was successfully used to meas-

ure the spin relaxation time T_1 for electrons in single self-assembled QDs, demonstrating the feasibility of this technique [Hei10].

Demands on the CPS structure

As indicated in figures 5.1(a), (b) and (d), in the design developed in the framework of this thesis, the CPS antenna is not only used to deliver the microwave field to the QD but also forms the electrical top contact and the shadow mask for the single QD spectroscopy which leads to partly contradicting demands for the geometry of the antenna: (i) Since the self-assembled QDs are randomly distributed over the sample, only a small percentage of apertures are placed over exactly one single QD, while others may contain several or no dots. Therefore, a large area of the stripline termination for potential optical measurements containing many apertures is desirable to increase the chance of finding a suitable aperture. (ii) For the application of electric fields, a small area for the whole CPS structure is required to decrease the RC time constant τ_{RC}, allowing fast and accurate voltage switching (with τ_{RC} ideally < 100 ns). Besides a reduction of the stripline termination area, the RC time constant can be further reduced by introducing an electrically insulating layer of e.g. benzocyclobutene (BCB) or SiO_2 between the area of the CPS that does not contain apertures for the QD spectroscopy and the GaAs. For the CPS antenna presented in figure 5.1(d), a RC time constant of $\tau_{RC} \approx 300$ ns was measured. However, this value could be reduced by a factor of three in an advanced version of the structure by shortening the length of the striplines by $\sim 50\%$, an alteration that should not affect the field distribution generated at the short. (iii) A small area for the stripline termination is also wanted since this results in a higher current density leading to a larger amplitude of the oscillating magnetic field B_1 and, therefore, allowing for faster electron spin rotations. However, an increase of the field amplitude comes at the cost of a decrease in the area of the sample available for potential measurements. (iv) The magnetic B_1 field component excited by the CPS antenna has to be perpendicular to B_0 and, therefore, for this particular experimental geometry in the plane of the sample. For a shorted CPS antenna, this B_1 field orientation is found beneath the CPS structure and particularly underneath the short as described by the Biot-Savart law. Advantageously, this allows to use the CPS structure as a shadow mask and electrical contact by positioning it directly on top of the QD. Figure 5.1(d) shows an optical microscope image of a first realization of the termination area of such a structure which satisfies the requirements stated above and which allowed storage of single, electrically injected electrons as observed in standard micro-photoluminescence experiments, albeit without the application of microwaves. The results e.g. presented in [Klo10b] and [Klo10a] were obtained with an CPS antenna structure used as an electrical top gate, the only difference being that the apertures in the gold film were not defined lithographically but created using 1 μm diameter polystyrene balls as described in section 2.3.1.

5.2 Finite element simulation of the structure

To obtain information on the relative field distribution created by the CPS antenna, finite element calculations using the software package COMSOL were performed. The color coded image plots in figure 5.3 show the calculated relative magnetic field distribution generated by the CPS antenna in a plane parallel to and 100 nm beneath the sample surface, the position where the optically active quantum dots are typically located. The absolute values of the magnetic field on the color scale are for an incident microwave power of $P_{\mathrm{mw}} = 120$ mW and were obtained from a comparison to reference experiments as described below. For the simulation, a high frequency AC voltage with $\nu = 9$ GHz was applied to the two ports of the antenna structure. As depicted in figure 5.3, in this geometry an in-plane field is expected underneath the gold antenna structure in the vicinity of the short. Implementation of the apertures to the gold film as presented in figure 5.1(c) into the simulation did not result in any significant change in the field

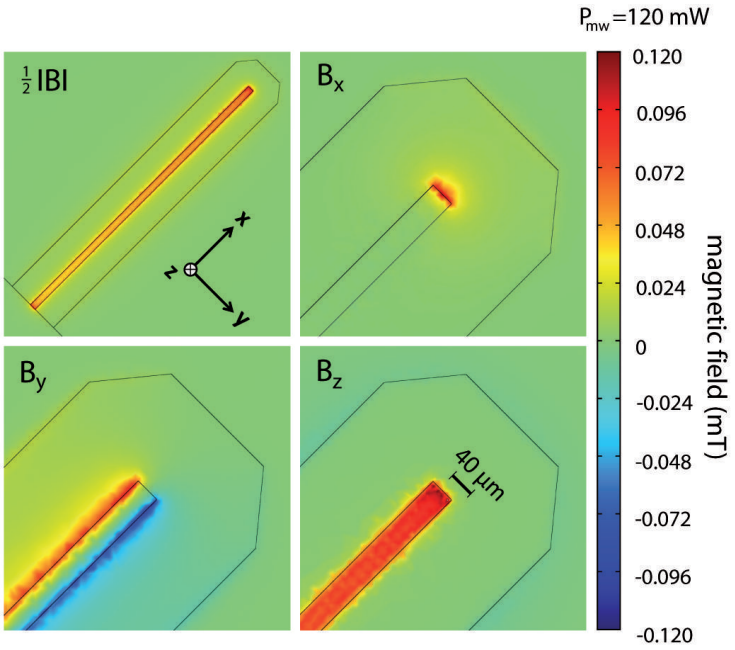

Figure 5.3. *Calculated distribution of the magnetic field in the plane 100 nm below the Au film forming the CPS antenna at the position where the optically active quantum dots are located. $B_{x(y)}$ are the in-plane and B_z the out-of-plane components of B. The relative field distribution is determined from finite element simulations performed with the software package COMSOL for microwave excitation of the CPS antenna structure with $\nu = 9$ GHz. The absolute values of the field amplitudes on the scale are obtained from a comparison to reference experiments as described in the text. For $|B|$ in the upper left panel, the field amplitudes were divided by a factor two to allow the use of the same color code scale for all four graphs. The absolute values on the color scale giving the magnetic field amplitudes were obtained from comparisons of the simulated field distribution with experimental data as described in the text.*

distribution and, thus, are not included in the presented figure for the sake of clarity.

Comparison of the calculated relative field distribution with experimental data from EDMR measurements on a a-Si:H film using the CPS antenna and reference measurements carried out on the same sample in a commercial mw resonator as explained in detail in 5.4 allows to put absolute magnetic field values to the color scale (figure 5.3). The simulations also show that the electric component of the microwave field has a node at the site of the CPS termination, minimizing perturbations of the QD system by electric fields.

5.3 Setup and experimental results

Sample design

To test the antenna design experimentally for spin resonance experiments where the in-plane component is essential, hydrogenated amorphous silicon, a material known to exhibit a strong ESR-induced signal in the electric transport was used. Figure 5.4(a) shows a to-scale model of the experimental setup used in this work. The layer structure of the sample is presented schematically in figure 5.4(b). A 500 nm thick, 1 mm long, and 0.2 mm wide strip of intrinsic hydrogenated amorphous silicon was fabricated from a 500 nm thick layer of plasma-enhanced chemical vapor deposition-grown a-Si:H on a glass substrate by photolithography and reactive ion etching. Subsequently the a-Si:H film was covered with a 400 nm thick, electrically insulating layer of BCB photoresist. On top of this, the CPS antenna structure was defined from a 30 nm titanium adhesion layer and a 200 nm thick gold layer, that were both thermally evaporated using optical lithography.

The lateral geometry of the sample and the microwave delivery system can be seen from the optical microscope image presented in figure 5.4(c). The short of the striplines that defines the region for electron spin resonance measurements was placed directly over the center of the a-Si:H strip that is electrically contacted via two lithographically defined Au contacts with a distance of ≈ 0.7 mm. The microwaves are delivered to the sample via a CPS antenna formed by a 400 nm thick Au film sputtered on a printed circuit board (PCB, Rogers RO3010) where the Cu layer has been fully removed in this area by H_2O_2/HCl etching. The microwaves are fed into the CPS on the PCB via a coplanar waveguide to stripline (CPW-CPS) transition [Kim02; Ana08; But04] which is a slightly modified and scaled-up version of the one presented in Ref. [Kim02].

The CPW itself is contacted via a standard PCB mount-on microwave plug (Rosenberger Mini SMP 18S102-40ML5) which is soldered to a low loss semirigid coax cable as depicted in figure 5.4(a). To improve mechanical stability, the footprint of the Mini SMP plug was protected from the H_2O_2/HCl etching of the PCB Cu layer allowing a solid, soldered connection of the plug to the PCB. The connection between the two CPSs on the PCB and the sample is formed by Au wires that were glued to the striplines on both sides with conducting silver epoxy resin. The whole sample structure was placed in a

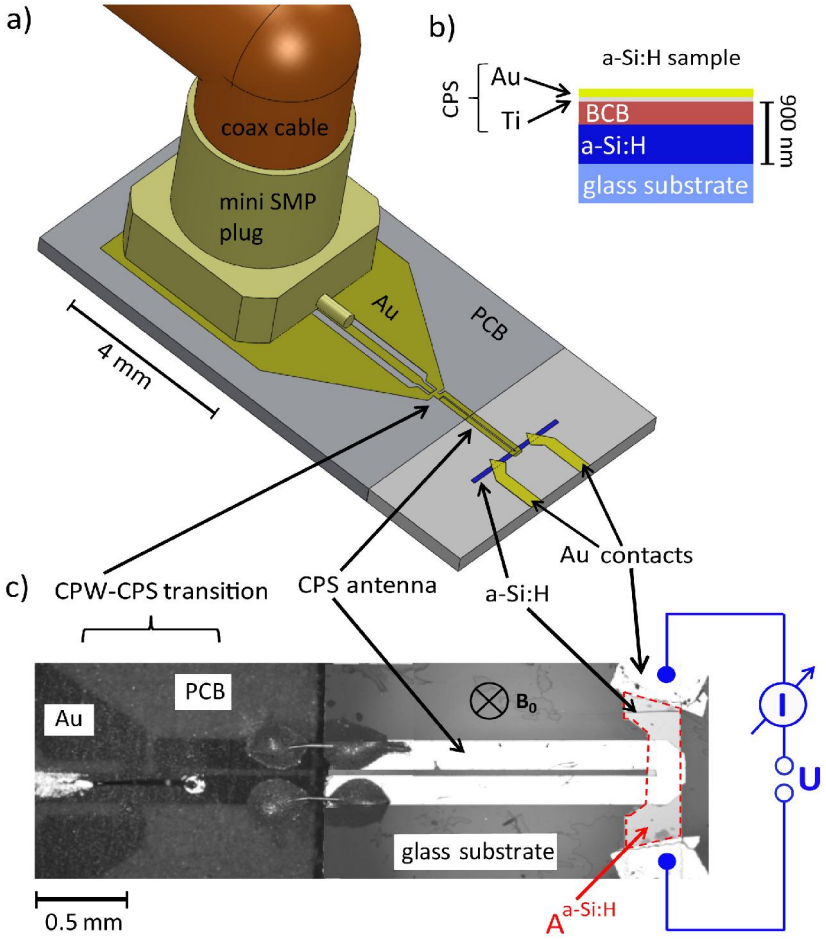

Figure 5.4. *(a) To-scale model of the experimental setup used in this work. (b) Schematic of the sample structure. A 400 nm thick electrically insulating benzocyclobutene (BCB) spacer is placed between the Ti/Au film forming the CPS and the hydrogenated amorphous silicon thin film (a-Si:H). (c) Optical microscope image of the experimental setup used to measure the EDMR spectrum presented here to investigate the performance of the CPS antenna. The CPS is terminated on top of the 500 nm thick a-Si:H strip allowing the creation of oscillating in-plane magnetic fields. The photocurrent signal is detected via two Au contacts on the a-Si:H film with a distance of* $\approx$ *0.7 mm.*

magnetic field of $B_0 \approx 320$ mT applied perpendicularly to the sample surface as in the QD experiment. Illumination of the a-Si:H was achieved from the backside through the glass substrate using the white light of a halogen lamp.

Figure 5.5 presents the results of a performance test of the mw delivery system to the sample carried out at room temperature. An illustration of the test structure used is shown in figure 5.5(a). It consists of a set of two identical mw-delivery structures that are arranged in a symmetric head-to-head configuration. To test the attenuation of the design, microwaves were fed into one port at a constant power of 10 mW and the signal transmitted through the structure was detected with a calibrated mw-diode

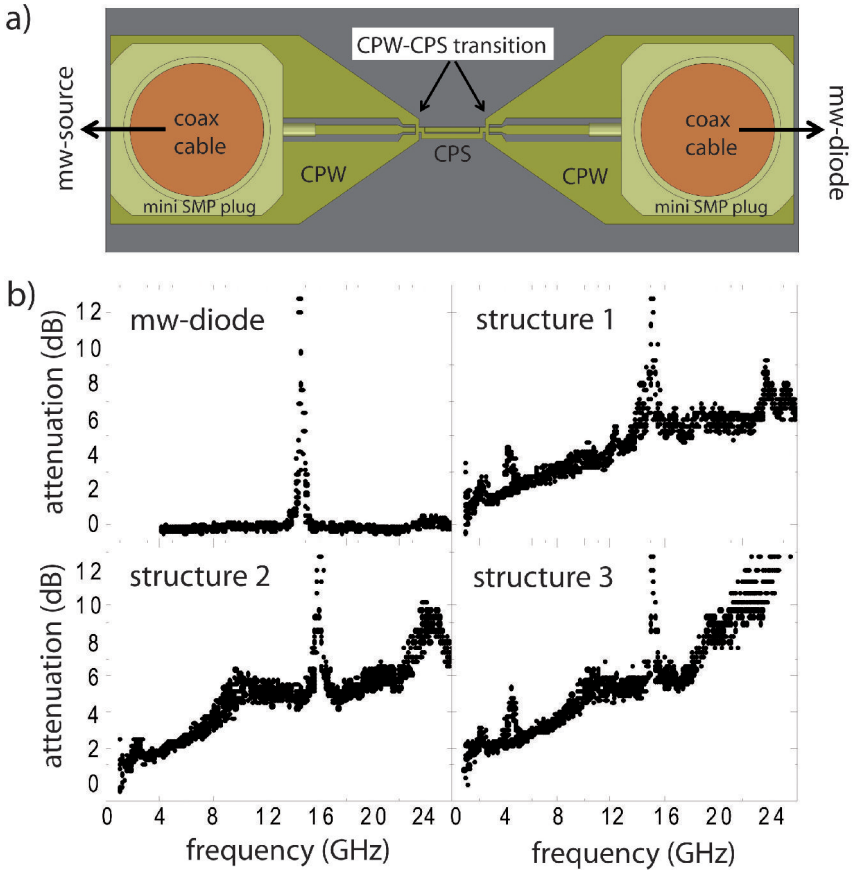

Figure 5.5. *(a) Schematic drawing of the setup to examine the performance of the on-board microwave delivery system consisting of two of such structures in a head-to-head configuration. Microwaves are fed into one port of the structure and the transmitted signal is detected at the other port. (b) Attenuation for three different test structures and the detector diode itself. The attenuation measured here is twice as high as in the actual experiment since there only half of the test structure shown in (a) is used for mw delivery.*

at the other port. The attenuation determined from these measurements is shown in figure 5.5(b) for three different test structures as a function of the mw-frequency ν_{mw} and is given by the whole system including all coax cables, Mini SMP plugs, coplanar waveguides and striplines, CPW-to-CPS transitions, and all connections between these parts. As can be seen from the left graph in the upper panel, the resonant feature around $\nu_{\mathrm{mw}} = 16$ GHz is an artifact of the detector diode. For the experiments presented later in this section, the test-structures were basically cut into half along the vertical symmetry axis and one side was replaced by the a-Si:H sample – i.e. the attenuation measured in figure 5.5 is twice as high as in the actual experiment. The tests show that the on-board mw-delivery system designed and constructed in the framework of this thesis allows to reliably deliver microwaves to the CPS antenna on the sample with an attenuation of less than 5 dB up to frequencies of $\nu_{\mathrm{mw}} \approx 26$ GHz.

EDMR using the CPS antenna

The detection principle of EDMR is based on spin-dependent transport processes in the investigated material [Kap78]. In a-Si:H, a reduction of the photocurrent I by ΔI is observed when flips of the electron spin e.g. of paramagnetic defects are induced by a microwave B_1 field [Sol77]. Figure 5.6(a) presents the result of such a measurement at room temperature. Microwaves at a frequency of $\nu_{\mathrm{mw}} = 9$ GHz were applied via the CPS antenna to the a-Si:H film using amplitude modulation to employ lock-in detection. A clear resonance is observed at 320.61 mT. The resonance position corresponds to a g-factor of 2.0056 ± 0.0001 as expected for dangling bonds in a-Si:H, the dominant signal detected in EDMR of intrinsic a-Si:H thin films with low defect density at room temperature [Str82; Der83]. The applied continuous wave (cw) microwave power in the experiment using the CPS antenna was $P^{\mathrm{CPS}} = 300$ mW, corresponding to only ≈ 120 mW delivered to the CPS antenna taking into account the attenuation of the microwave delivery system at $\nu_{\mathrm{mw}} = 9$ GHz. Low temperature test measurements at $T = 8$ K demonstrated that cw excitation of this power can be applied to the device without causing excessive heating of the sample (cf. section 5.5). The lineshape and linewidth of the dangling bond resonance are governed mostly by the anisotropy of the electron g-factor of dangling bonds as well as the random orientation of these bonds in the amorphous material leading to a so-called powder pattern [Stu89; Feh11]. Since here only the EDMR signal intensity is of interest, a simple Lorentzian is used to describe the resonance. A fit of this lineshape to the spectrum in figure 5.6(a) shows that the relative change in the photocurrent monitored is $\delta^{\mathrm{CPS}} = -\Delta I / I \approx 1.6 \cdot 10^{-5}$ and, after averaging over six measurements, exceeds the noise level by one order of magnitude.

EDMR reference measurements

To obtain a quantitative measure for the magnetic field generated by the CPS antenna B_1^{CPS}, it is compared to the field generated in a $\lambda-$cavity, B_1^{res}, which is more conventionally used for EDMR. For this measurement, the glass sample with the a-Si:H film and the electrical contacts was removed from the PCB sample holder and placed into a commercial TE_{102} resonator with known B_1 field strength. The corresponding EDMR spectrum taken is shown in figure 5.6(b). Since for this experiment magnetic field modulation in combination with lock-in detection was used, the obtained signal is the derivative of the Lorentzian lineshape. Correcting for the modulation amplitude of 0.4 mT used for a FWHM linewidth of 1.4 mT, corresponding to a peak-to-peak linewidth of 0.8 mT (cf. figures 5.6(a) and (b)) [Poo83], the detected signal has an amplitude of $\delta^{\mathrm{res}} = -\Delta I / I \approx 17 \cdot 10^{-5}$ which is about one order of magnitude larger than the signal obtained with the CPS antenna. The observed signal-to-noise ratio is of similar size for both methods.

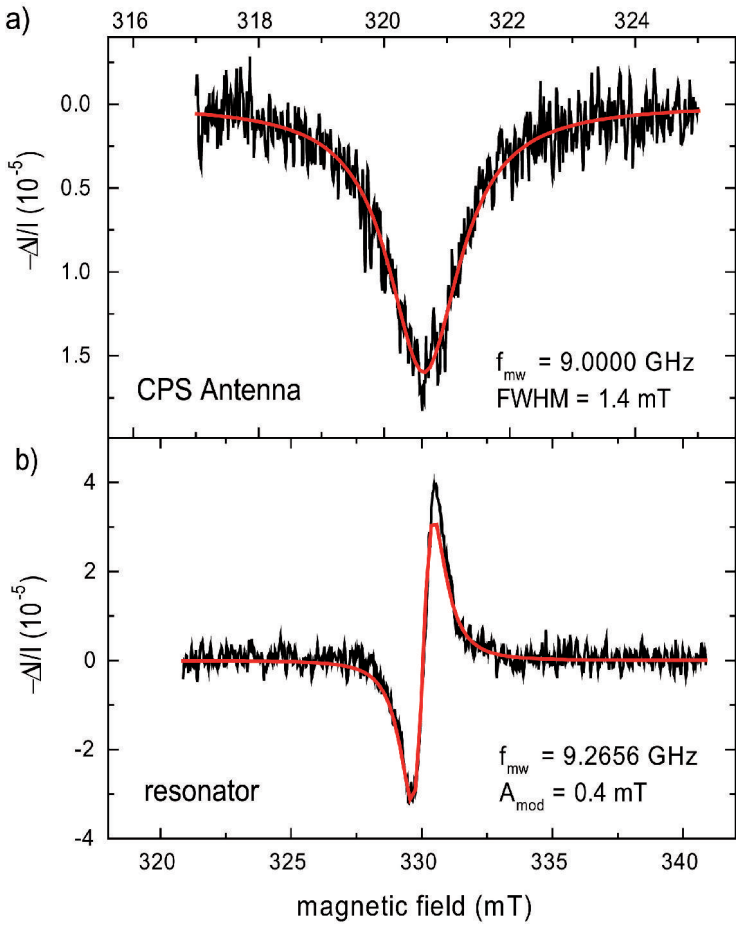

Figure 5.6. *(a) EDMR signal of a-Si:H measured with the CPS antenna structure shown in figure 5.4(c) using mw-amplitude modulation for lock-in detection. (b) EDMR signal of the same sample using the same electrical contacts for photocurrent detection measured in a commercial TE_{102} microwave resonator employing magnetic field modulation for lock-in detection.*

5.4 Applicability for spin control

Determination of B_1

The cw microwave power used for the reference experiment was $P^{\text{res}} = 200$ mW generating a B_1 field amplitude of $B_1^{\text{res}} = 0.066$ mT at the site of the sample in the TE_{102} resonator [Stu86; Kaw97], a regime in which the amplitude of the EDMR signal is proportional to the B_1 field [Kaw97]. For the EDMR experiment in the resonator the whole a-Si:H film in between the Au contacts with an area $A^{\text{a-Si:H}}$ (indicated by the red dashed line in figure 5.4c) was excited by a homogeneous B_1 field and, therefore, all parts contribute to the signal δ equally. This is not true when the mw field is delivered by the CPS antenna due to the spatial inhomogeneous B_1 field distribution as can be seen from figure 5.3. However, the total magnetic flux exciting ESR in the the a-Si:H film generated

by the CPS antenna $\Phi_{\text{exp}}^{\text{CPS}}$ can be deduced by comparing the measured EDMR signal amplitude δ^{CPS} to the one obtained using the TE_{102} resonator δ^{res} as the total area of the a-Si:H stripe is identical in both experiments and the detected signal δ is proportional to Φ_{exp}. The total flux $\Phi_{\text{exp}}^{\text{CPS}}$ is then given by $\Phi_{\text{exp}}^{\text{CPS}} = \left(\delta^{\text{CPS}}/\delta^{\text{res}}\right) \cdot \Phi_{\text{exp}}^{\text{res}} \approx \frac{1}{10}\Phi_{\text{exp}}^{\text{res}}$ where the total flux through the sample in the TE_{102} resonator $\Phi_{\text{exp}}^{\text{res}}$ can be easily determined since both B_1^{res} and $A^{\text{a-Si:H}}$ are known. This allows to calibrate the magnetic field scale obtained from the calculated relative field distribution generated by the CPS antenna. The calculations show that this is possible since there is no significant difference in relative and absolute field distribution between 100 nm and 1 μm beneath the sample surface. Integration of this relative magnetic field over the whole area $A^{\text{a-Si:H}}$ gives the total simulated magnetic flux $\Phi_{\text{sim}}^{\text{CPS}}$. Only the field components B_x and B_y of B_1 have to be taken into account as the sample is positioned such that B_z is parallel to B_0 and, therefore, does not contribute to the EDMR signal. The ratio $\Phi_{\text{exp}}^{\text{CPS}}/\Phi_{\text{sim}}^{\text{CPS}}$ then gives a scaling factor for the magnetic field scale obtained from the simulation and allows to assign absolute field amplitude values to it (figure 5.3). Using this approach we obtain maximum B_1 fields of ≈ 0.12 mT in the vicinity of the short for a cw microwave power of $P^{\text{CPS}} \approx 120$ mW at the beginning of the mw delivery line. At the site of the apertures as depicted in figure 5.1(d), B_1 fields of $\approx 0.1 - 0.07$ mT are expected. However, the maximum field amplitudes of ≈ 0.12 mT should easily be available to be applied to the QD by simply positioning the apertures 2 - 3 μm closer to the edge of the gold film.

Comparison of achievable π-pulse times to T_1 and T_2

To estimate the applicability of this approach to coherent manipulation of electron spins in self-assembled quantum dots via pulsed ESR, the relevant times of the electron spin dynamics in a quantum dot have to be compared with the π-pulse time t_π achievable. For a B_1 field of 0.12 mT, one obtains $t_\pi = h/(2g\mu_{\text{B}}B_1) \approx 0.5$ μs using $|g| = 0.6$ as measured for typical self-assembled InGaAs quantum dots [Kro08b]. The spin-lattice relaxation time T_1 of these types of QDs depends strongly on the applied magnetic field B_0 and ranges between 600 to 50 μs for electron and 400 to 5 μs for hole spins for magnetic fields of 5 T $< B_0 <$ 12 T at a temperature $T = 8$ K [Hei08b; Kro04], a typical temperature for the spectroscopy of single self-assembled QDs. The coherence time T_2 of an electron confined in such a QD also exhibits a magnetic field dependence and was determined from measurements on similar types of QDs to range from $1 - 2.5$ μs for magnetic fields of 2 T $< B_0 <$ 4 T, saturating at 3 μs for higher fields [Pre10; Gre06]. Another important timescale is the storage time t_s, describing the time the electron can be stored in the QD. Tunneling escape of the electron out of the dot strongly depends on the electric field applied to the sample and can be tuned to timescales as long as seconds during the spin manipulation phase [Hei09b], thus, not setting any limitation to the measurement since $T_1, T_2 < t_s$ is always achievable.

A comparison shows that the t_π times accessible by the B_1 fields demonstrated in

this work are significantly shorter than T_1 and t_s and also below T_2. Furthermore, one has to note that the experimental data presented in this work were obtained under cw excitation of the sample and that significantly higher microwave powers can be applied to the sample in pulsed excitation schemes as used for coherent spin control experiments which are typically pursued at low duty cycles [Kop06; Kop08; Fuc09]. This will allow much shorter t_π times as B_1 is proportional to $\sqrt{P^{\mathrm{CPS}}}$, ensuring the conditions $T_1, T_2, t_s \gg t_\pi$ necessary for coherent spin control are fully met. Therefore, our approach should be very suitable for spin control of single electrons confined in self-assembled QDs.

For the frequency of $\nu_{\mathrm{mw}} = 9$ GHz where the operation of the CPS antenna is demonstrated, the corresponding resonance field is $B_0 \approx 1$ T. However, the CPS antenna is a purely non-resonant structure and, therefore, should allow broadband operation. Test measurements showed that the whole microwave delivery system including the CPW to CPS transition and the mount-on devices on the PCB allows operation up to 26 GHz with losses of less than 5 dB as demonstrated in section 5.3. Even up to $\nu_{\mathrm{mw}} = 35$ GHz, losses of less than 10 dB are achievable, offering the possibility to conduct ESR at B_0 fields of 3.5 T. This should allow to investigate the magnetic field dependence of electron spin dynamics via coherent spin manipulation with the CPS antenna over a wide range of several Tesla and could provide valuable information for the identification of decoherence mechanisms in quantum dots.

Performing ESR experiments on self-assembled QDs at higher B_0 fields also has practical benefits since a pair of spectrally resolvable Zeeman states allows to address the two spin configurations via their energy, removing the need for perfectly circularly polarized light for spin initialization and spin-to-charge conversion [Hei10]. Furthermore, the fidelity of the spin initialization, which is achieved by resonant optical excitation of an exciton and subsequent removal of the hole from the dot, potentially increases with increasing B_0. This is due to the anisotropic exchange interaction that excitons experience in self-assembled QDs with imperfect symmetry which leads to a fine-structure splitting of the exciton states at $B_0 = 0$ T, typically in the range of $\sim 30 - 150$ μeV for self assembled InGaAs QDs [Klo10b; Bay02b]. If the exchange coupling is larger than the Zeeman energy and the extraction of the hole does not occur over sufficiently fast timescales, the eigenstates are of strongly mixed spin character in which case spin initialization with a high degree of polarization is not achievable.

5.5 Experimental challenges using on-chip CPS antennas

Although the approach of using a CPS antenna structure not only for mw delivery but also as electrical contact to the sample and shadow mask for the optical spectroscopy yields many benefits, it comes at the cost of some experimental disadvantages and challenges which are summarized in figure 5.7. The presented single QD photoluminescence spectra were measured using a micro-PL setup as described in section 3.1 with a

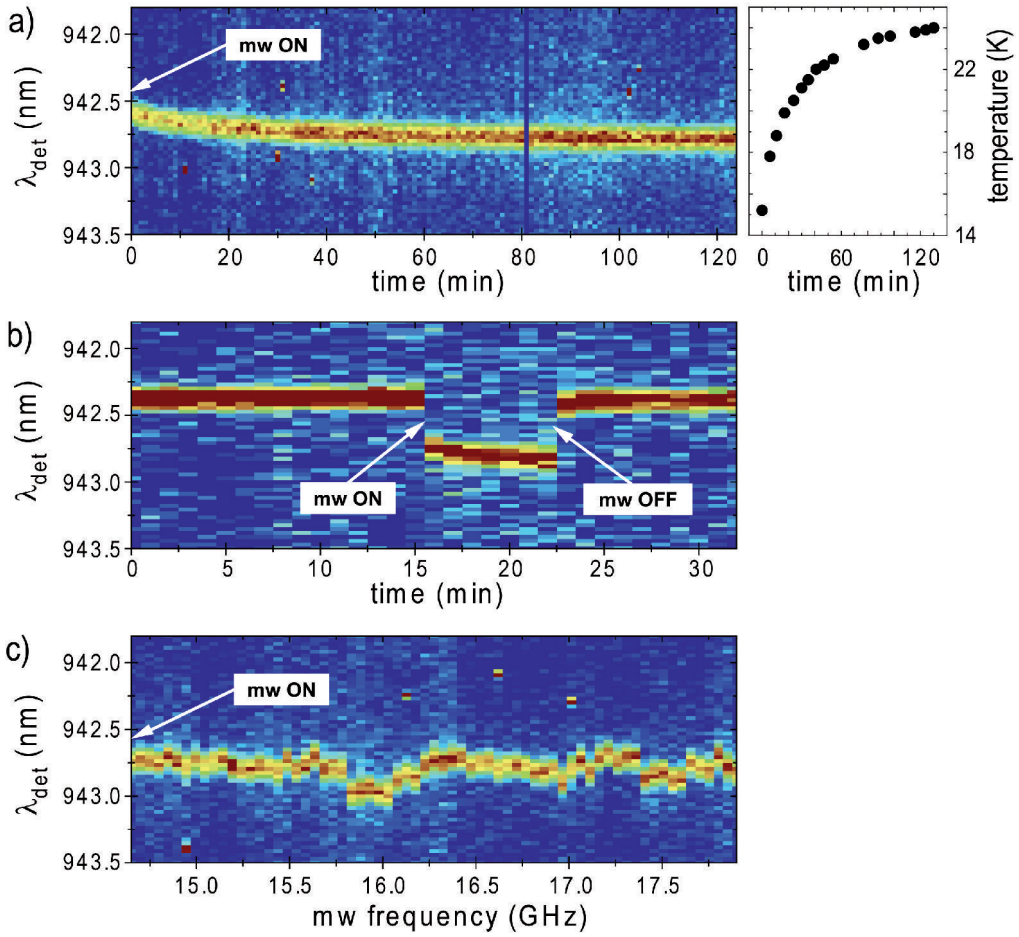

Figure 5.7. *Experimental challenges associated with the use of multi-functionalized on-chip CPS antennas. The power was $P_{\mathrm{CPS}} \approx 200$ mW for all three cases. (a) Temperature shift of the X^0 PL line due to heating of the sample. A stable state of thermal equilibrium is only reached after ≈ 1 hr. (b) Rectification of the oscillating electric field leads to a field offset causing an additional stark shift. (c) Frequency dependent attenuation of the system leads to variations in power delivered to the CPS antenna resulting in a frequency dependent electric field offset.*

multi-functionalized CPS antenna similar to the ones depicted in figures 5.1(a) and (d), only differing in the generation of the apertures in the gold film that were not defined lithographically but created using 1 μm diameter polystyrene balls. The spectra were recorded using wetting layer excitation at $\lambda_{exc} = 855$ nm and show the X^0 emission line. A constant electric dc field was applied to the sample via the contacts throughout the whole measurements to tune the device to the photoluminescence regime and a cw microwave signal of $\nu_{\mathrm{mw}} = 16$ GHz and $P^{\mathrm{CPS}} \approx 200$ mW was additionally switched on as indicated in the graphs.

Figure 5.7(a) shows the effect of a mw constantly applied at fixed frequency and power. A clear shift of the PL line of more than one linewidth occurs over a time of

$\approx$ 30 min. This slow shifting of the resonance can be attributed to heating of the sample by the microwave which was measured to increase the temperature by $\approx$ 8 K during the first 30 min using a resistive temperature sensor (LakeShore Cernox Resistor, CX-1050-SD-1.4D) placed in the vicinity of the sample (cf. section 3.1). After $\approx$ 1 hr, a thermal equilibrium is reached at a total temperature increase of $\approx$ 10 K and no further shifting of the PL line is observed. Although this heating effect is not pronounced enough to perturb the PL quality of the QDs and can even be compensated for by using a setup providing active cooling of the sample, it imposes an unpleasantly long waiting period on the experiment before stable conditions are reached and the measurements can be started since precise resonance conditions of laser and absorption resonances are required for the scheme described in section 5.1.

As can be seen in figure 5.7(b), a sudden jump in the emission wavelength of the X^0 line by several linewidths occurs when the mw excitation of the CPS is switched on. This offset is fully reversed when the microwave is switched off again. Also observable is the slow temperature shift taking place after the mw application was started. The jump could be attributed to an electric field offset arising from the diode properties of the sample. The oscillating electric field component of the microwave is partially rectified by the Schottky contact formed by the TiAu layer of the CPS and the GaAs, generating an electric ac field in addition to the one intentionally applied via the top and back contact and leads to a shift in the emission wavelength due to the quantum confined dc Stark effect as discussed in section 2.2.3. The mw induced electric field offset which strongly depends on the mw power has to be compensated for by carefully determining its amplitude and then taking it into account when applying dc fields to the sample in order to tune absorption lines of the QD in and out of resonance with the laser energies. This can also be done by performing all measurements necessary to characterize the sample and the QD prior to the spin manipulation experiment with the mw switched on at the desired power, thus, incorporating the mw induced offset into the characteristics the sample.

While a constant offset in the electric field across the sample is not a problem as it can be easily corrected for, an offset varying during the course of a measurement presents a harder challenge. This is e.g. the case when the mw frequency is swept as shown in figure 5.7(c). The frequency dependent attenuation of the mw signal by the delivery system leads to a change in power fed into the CPS antenna as ν_{mw} is varied. The resulting shift at $P^{\mathrm{CPS}} = 200$ mW is up to two linewidth for the frequency range presented in figure 5.7(c). Apart from some resonant features, the shift of the QD transitions is small enough to allow frequency sweeps over a range of a few MHz as needed for an ESR experiment on a single quantum dot [Kro08b]. However, due to the variation of the electron g-factor in self-assembled QDs, ranging from $|g| = 0.4$ to 0.8 [Bay99a; Ale06; Kro08b; Pre10; Kro08a], a much larger initial sweep over several GHz is necessary to locate the ESR resonance [Kro08b; Kro08a], a task which is hindered in this case by the fluctuations of the QD state positions. This can be approached by sweeping over a smaller frequency range where the position of the QD states is stable

enough to maintain the resonance condition with the laser throughout the whole scan multiple times, setting the external magnetic field appropriately for each of these short sweep to allow covering of the whole necessary large sweeping range. Alternatively, the magnetic field can be swept at a fixed ν_{mw} as it is usually done in conventional ESR experiments. However, this approach is not very suitable in combination with the spin storage and readout scheme since the QD transitions, particularly the p-shell states used for readout, exhibit a diamagnetic shift (cf. section 2.2.3) that results in a quick detuning from the resonance condition with the laser. In this case, the sweep has to be broken down into a series of smaller scans where the diamagnetic shift of the QD states occurring within each small sweep is small enough not to significantly disturb the measurement technique. The position of the p-shell transitions has to be determined for every magnetic field range and the readout laser must be set accordingly.

Although these challenges require time consuming and cumbersome measures to circumvent the perturbing effects on the measurement, they do not make the use of multi-functionalized on-chip CPS antennas for spin control in single QD experiments unfeasible but rather should still allow their employment for spin manipulation using the techniques discussed in this chapter.

5.6 Summary

In summary, the feasibility of electron spin manipulation using the in-plane component of the oscillating magnetic field created by a coplanar stripline antenna was demonstrated in this chapter. Furthermore, the structure is designed such that it can simultaneously serve as an electrical top contact and opaque shadow mask in a single self-assembled quantum dot spectroscopy experiment.

From cw EDMR reference measurements on amorphous silicon in combination with finite element simulations of the field distribution in the structure, an in-plane B_1 field of ≈ 0.12 mT is obtained for continuous wave excitation at the site of the dots. Even for the cw excitation demonstrated here, the corresponding π-pulse time of ≈ 0.5 μs (for self-assembled InGaAs QDs with $|g| = 0.6$ [Kro08b]) is shorter than required and should, therefore, already make coherent spin manipulation in single self-assembled QDs possible. However, much shorter π-pulse times can be achieved using pulsed excitation schemes that allow for the application of significantly higher microwave powers. In the end, challenges regarding the practical use of this approach for ESR experiments on single QDs are pointed out and strategies to address these issues are discussed.

6
Conclusive remarks and future work

The work conducted in the framework of this thesis addressed several aspects of spin physics in semiconductor nanostructures such as resonant optical nuclear spin pumping (chapter 4), tuning of the exciton *g*-factor by electric and magnetic fields (chapter 3) and the development of integrated on-chip microwave structures for electron spin resonance in single QDs (chapter 5). While several of the effects of interest could be investigated comprehensively in experiment, simulated using theoretical models and understood based on the underlying mechanisms and microscopic origins, other tasks are still open and subject to future work. Furthermore, based on the observations and insights gained in this work, new questions were raised that can be addressed in future experiments. The intention of this chapter is not primarily to discuss general trends in the respective fields of activity this thesis is concerned with but to make concrete suggestions for future experiments, point out the specific challenges and, if possible, propose strategies to circumvent or overcome them.

6.1 Electron spin resonance

6.1.1 Prospects

In chapter 5, the development and testing of an on-chip coplanar stripline microwave antenna that can simultaneously be used as an electrical contact to the sample as well as a shadow mask for optical single QD spectroscopy was presented. The feasibility of the structure for the delivery of adequate microwave fields was successfully demonstrated on an a-Si:H test sample [Klo11b]. In a next step, the method has to be implemented in an experiment to perform the type of measurement it was originally designed for: ESR

on an electron confined in a single quantum dot optically probed in Faraday geometry. To achieve this, the CPS microwave excitation has to be combined with the single spin readout scheme based on spin-to-charge conversion that was developed to detect the orientation of a single electron spin confined in a QD [Hei08a; Hei10].

The possibility to perform spin manipulation of single electrons in individual QDs allows to address a large number of interesting questions.

Coherent spin manipulation would enable performance of echo-type experiments [Hah50; H.Y54] that are necessary to gain further insight into the decoherence processes taking place for an electron spin confined in a QD due to the solid-state matrix [Pre10]. Tasks in this field are the identification of different mechanisms leading to the loss of coherence and their dependence on parameters such as direction and strength of applied magnetic fields, lattice temperature and the nuclear spin system both in thermal equilibrium and prepared in a polarized state.

Another possible application would be the use of the very well defined ESR resonance as a highly sensitive sensor for nuclear fields. A change of the Overhauser field would result in an energy shift of the ESR resonance that can be detected with high accuracy allowing to investigate the dynamics of the nuclear spin ensemble. The temporal resolution of this technique is limited by the time required to detect the ESR resonance and its shift. However, since nuclear spin dynamics are taking place on a comparatively slow timescale (cf. chapter 4), this limit does not seem to represent a major restriction. Spacial shifting of the electron wave function, e.g. by electric fields might allow to probe different sub-ensembles of the nuclear spin system in different areas of the dot. This way, the effect of inhomogeneous strain and material distribution within the dot on nuclear spin polarization could be explored.

Furthermore, there is no obvious reason why on-chip CPS antennas could not be established on quantum dot molecules samples. Since the exact shape and material composition of self-assembled QDs is subject to statistical fluctuations, the g-factors of both electron and hole generally differ from dot to dot. The same is expected for the stacked quantum dots forming a molecule. As a result, the two dots can be addressed separately in ESR experiments by their individual resonance frequency at a given magnetic field. For QDMs, this effect can even by tailored via the growth parameters used during the formation of each of the subsequently grown QD layers. As the CPS antenna is a non-resonant broadband structure, successful implementation of this approach to a QDM would result in a system of two individually manipulatable two level systems with a tunable coupling between them – i.e. the fundamental building block for quantum information processing.

6.1.2 Challenges

Several experimental challenges involved with the use of on-chip CPS antennas were already presented and discussed in section 5.5. However, all these effects such as heating of the sample by the microwave or the occurrence of an electric field offset through recti-

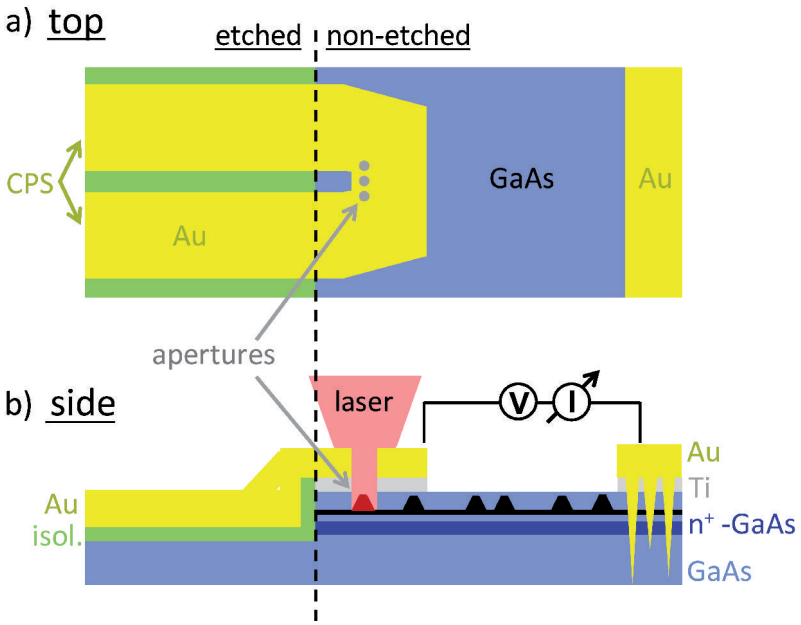

Figure 6.1. *Top and side view of the sample design proposed to circumvent perturbation of the microwave propagation along the stripline by the buried n^+ doped layer as reported by Kroner et al. [Kro12]. The conductive layer forming the back contact can be removed by site selective etching before the CPS structure is evaporated onto the surface. Additionally, an electrically insulating layer introduced between parts of the stripline and the sample could improve the performance of the device due to a reduction of the RC time constant allowing for faster voltage switching.*

fication of the electric field component of the microwave do not represent fundamental problems but rather result in an inconvenient extension in time and complication of the measurement procedure.

However, very recent work by *Kroner et al.* revealed an effect that, if confirmed, will make a modification of the sample design necessary. In contrast to assumptions made based on the skin depth of microwaves at a frequency of several GHz, the 100 nm thin n^+ doped layer that forms the back contact buried 140 nm beneath the sample surface and thus also below the CPS structure, seems to represents an unexpectedly strong perturbation to the microwave, hindering propagation along the stripline [Kro12]. This type of problem would not have been observable in the experiments presented in chapter 5 since the EDMR test measurement were performed on a a-Si:H sample using a planar contact geometry without a buried back contact.

A possible solution to this problem would be the local removal of the n^+ doped layer below the stripline. This can be achieved by lithographically defined etching of the sample before the CPS structure is formed on the surface as depicted in figure 6.1. The figure shows a schematic of the sample structure in top (6.1a) and side (6.1b) view. The CPS is positioned such that the back contact and the QDs are only removed underneath the stripline but not in the area of the termination where the QDs spectroscopy is

supposed to be carried out. This geometry would allow unperturbed propagation of the microwave along the stripline delivering a mw field to the location of the QD underneath the short.

A further improvement of the sample performance can be achieved by introducing an electrically insulating layer between the CPS and the sample surface as illustrated in figure 6.1 (green area). A configuration as presented in the schematic would result in a reduction of the capacity of the structure. This allows for faster voltage switching due to the smaller RC time constant τ_{RC} without having any negative influence on the use as electrical contacts as gates are only necessary in the area where QD spectroscopy is performed, i.e. the termination of the CPS where the in plane B_1 component of the mw field is maximum.

6.2 Nuclear magnetic resonance

6.2.1 Prospects

Performing nuclear magnetic resonance (NMR) on the nuclear spin system of a quantum dot is a very desirable task as it provides a second partially complementary approach for manipulation of the mesoscopic spin ensemble in addition to the hyperfine coupling to electron spins. Furthermore, it represents a tool that is expected to yield new insights into the structural properties of semiconductor quantum dots. As NMR is very challenging in strained materials due to the quadrupole-induced broadening of the NMR spectra [O'D08; Tan08; Sie05] until now, corresponding experiments on quantum dots have almost exclusively be achieved in strain free natural dots formed by fluctuations at the interface of lattice matched layers [Gam97; Bro98; Mak10; Mak11] or large QD ensembles where quadrupole broadening introduced an uncertainty to the interpretation of the data [Fli10]. Only very recently, NMR could be successfully demonstrated on single strained InGaAs/GaAs and InP/GaInP QDs. This was made possible through the development of a novel so-called 'inverse' spectroscopy technique [Che11a].

In the work of *Chekhovich et al.*, detection of nuclear magnetic resonance via the Overhauser splitting of purely optically detected excitonic states in the QD allowed to estimate the strain and material distribution within the volume occupied by the electron as well as to deduce the decoherence time of the nuclear spin ensemble [Che11a]. The samples used in this work did not have any electric gates, hence, neither electric fields could be applied to the QDs nor detection of photocurrent signals was possible. However, application of electric fields could be used to shift the electron wave function as indicated schematically in figure 6.2(a). This would allow to probe different areas within the quantum dot. If a spatial shift of sufficiently large amplitude can be generated, this approach would open the possibility to perform 3D tomography of the inhomogeneous strain and chemical distribution within a self-assembled semiconductor nanostructure such as a QD.

Due to their different gyromagnetic ratios, every isotope present in InGaAs/GaAs (cf.

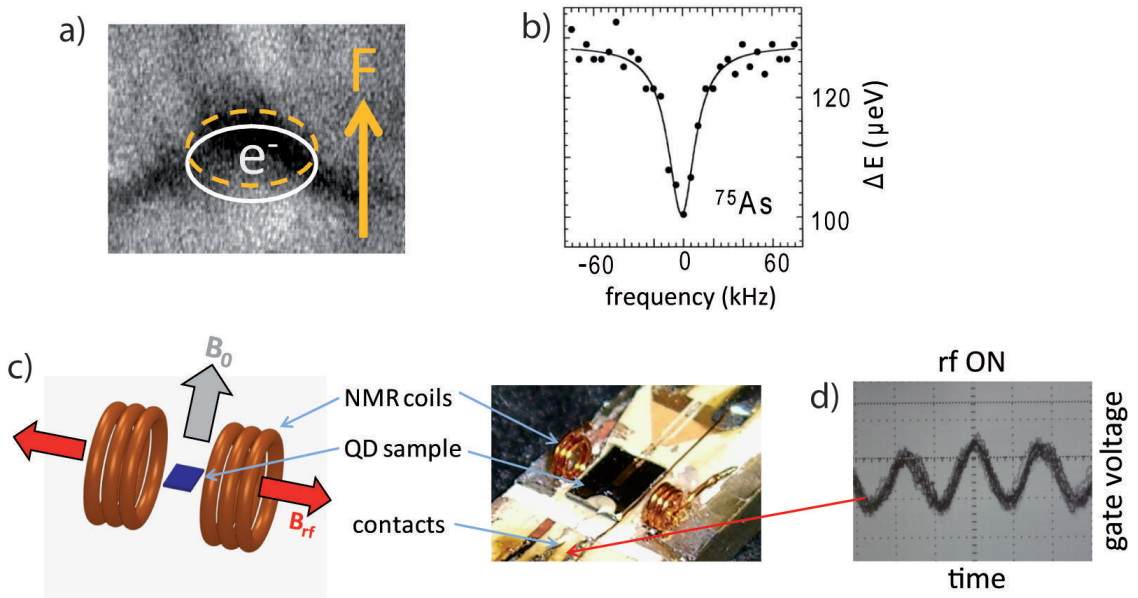

Figure 6.2. *(a) Schematic illustration of the electric field-induced shift of the electron wavefunction, illustrating the working principle of QD tomography via NMR experiments based on DNP. (b) Optically detected NMR resonance of the ^{75}As isotope in a strain-free GaAs/$Al_{0.3}Ga_{0.7}$As interface QD. Adapted from [Gam97; Bro98]. (c) Left: Schematic of a possible experimental configuration to perform NMR measurements on a nuclear spin ensemble in a QD similar to the setup recently used in Refs. [Mak10; Mak11]. Right: First attempt of a quantum dot NMR setup fabricated in the framework of this thesis. The coils were later added to an already exiting and measured single QD sample. On the photograph, the CPW-CPS structure on the sample holder discussed in chapter 5 can also be recognized. (d) Oscillation of the voltage applied to the sample due to inductive pickup of the rf signal by the PC detection circuitry.*

table 2.2) can be addressed individually in NMR experiments as demonstrated exemplarily in figure 6.2(a) where the NMR resonance of ^{75}As recorded in an AlGaAs/GaAs interface dot is presented [Gam97; Bro98; Mak10; Mak11]. This allows to study the influence of different subensembles on nuclear spins in QDs to dynamic nuclear polarization effects as the contribution of a certain species of nuclei to the Overhauser shift can be manipulated separately. Very recently, coherent control of the nuclear spin bath in a single QD was achieved for the first time using strain-free interface dots [Mak11]. This technique was demonstrated to allow fast reorientation of the polarization of a nuclear subensemble in a dot on timescales of $\sim 10\ \mu$s, much faster than manipulation times based on hyperfine assisted optical pumping.

6.2.2 Challenges

A possible sample design to perform NMR experiments based on DNP discussed in chapter 4 is schematically illustrated on the left side of figure 6.2(c). The layout is similar

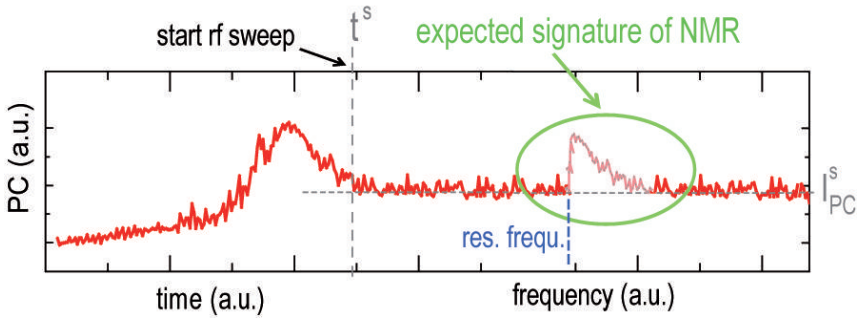

Figure 6.3. *Schematic illustration of the expected signature of NMR in a time resolved PC measurement as discussed in the text.*

to the one used in the NMR experiments on single QDs in Refs. [Mak10; Mak11] and consists of a pair of parallel rf coils. The QD sample is positioned in the center between the two coils. In this configuration, application of MHz ac signals to the coils generates rf fields at the site of a quantum dot with an oscillating magnetic component along the symmetry axis between the coils, i.e. in the plane of the sample surface. Consequently, this geometry is suitable to induce nuclear spin flips and perform NMR experiments for external magnetic fields B_{ext} applied in Faraday geometry (cf. requirements for ESR in chapter 5).

A picture of a first realization of such a structure fabricated in the framework of this thesis is displayed on the right side of figure 6.2(c). The coils were added later to the sample on which the DNP measurement presented in chapter 4 were performed. Since the magnetic field along the symmetry axis perpendicular to the plane of a loop carrying a current is proportional to $\left(r^2\right) \,/\, \left(x^2+r^2\right)^{2/3}$ (r = radius of the loop; x = distance from the center) [Tip91], a position of the sample as close as possible to the coils is desirable to achieve large B_1 field amplitudes at the site of the QD. However, the preset geometry demanded a positioning of the coils in a non-ideal configuration with a distance from the area of the diode for QD spectroscopy (located in the center of the sample) determined by the large sample size of $\sim 4 \times 3$ mm (cf. figure 6.2c). As a result, it was not possible to generate magnetic field strengths of the rf field large enough to induce any detectable NMR at the rf powers used. In order to overcome this problem, new samples of reduced size have to be fabricated that allow to realize an more favorable arrangement of all components necessary for NMR.

A second issue inhibiting the use of the device shown on the right side of figure 6.2(c) for NMR experiments was caused by inductive pickup of the rf signal by the electric circuitry used to contact the sample and detect the photocurrent signal. This resulted in a sinusoidal variation of the voltage applied to the sample at the frequency of the rf signal that could be measured with an oscilloscope as depicted in figure 6.2(d). This superimposed oscillation of the electric field within the sample results in a periodic shift of the QD states due to the QCSE, hindering the performance of resonant PC measurements. Although shielded cables were used for most of the wiring, the pickup

was found to be substantial even for moderate rf powers of several tens of mW. This problem could be tackled by an optimization of the electrical shielding and introduction of effective low pass filters to the detection circuitry as close as possible to the sample, preferably implemented into the sample structure directly. Since for the PC measurements only dc voltages have to be applied to the sample, suppression of perturbing high frequency oscillations via low pass filtering should be possible. In this aspect, the all-optical approach as used in Refs. [Mak10; Mak11] is more advantageous as no electric control or detection of photocurrent is applied.

Since the recording of steady state PC bias sweeps to measure the Overhauser shift of the exciton states is a time consuming task, it is not an appropriate method to perform NMR experiments since this would require to carry out a complete bias sweep for every step of the rf or magnetic field sweep. However, the time-resolved detection scheme of the PC signal as introduced in section 4.3.1 provides a suitable technique to detect a NMR-induced variation of the Overhauser shift. The altered measurement scheme is illustrated in figure 6.3. First, a regular time-resolved PC trace is recorded as described in section 4.3.1. After the nuclear spin ensemble has been pumped to steady state, detection of the PC signal is not stopped but continued. Simultaneously, the rf signal is switched on and swept across the frequency range where the NMR resonance is expected. In case a NMR resonance is hit, partial depolarization of the spin bath takes place due to the manipulation of the addressed subensemble of nuclear spins. The resulting reduction of the Overhauser shift would manifest itself as a 'jump back' to an earlier point in the measurement, i.e. on the PC trace, where the corresponding degree of polarization was reached during the buildup of B_n. After the NMR resonance is passed, optical pumping of the exciton state drives the system back to the steady state as had taken place before. The expected shape of the experimental response in such a measurement is sketched in figure 6.3. This scheme would allow to perform rf sweeps to trace NMR resonances in reasonable time.

Optimization of the electric circuitry for PC detection with regard to rf pickup and fabrication of smaller samples allowing a more favorable positioning with respect to the rf coils together with application of the 'inverse' rf technique should allow to perform NMR experiments on the nuclear spin ensemble of a single QD using the detection schemes for the Overhauser shifts developed in chapter 4. This would open access to a type of experiment where only very few successful measurements have been reported until now [Che11a] in the otherwise intensively and widely studied field of self-assembled QDs.

6.3 Dynamic nuclear polarization

6.3.1 DNP in single quantum dot molecules

Prospects

Many open question and possible applications are still associated with the rich and complex system of coupled dots forming a quantum dot molecule. Here, an experiment with regard to DNP shall be suggested as a continuation of the work carried out in this thesis. As demonstrated in section 4.4, nuclear spin pumping via resonant optical excitation in the photocurrent regime which was intensively studied for individual QDs (cf. chapter 4) can also be achieved in a single QD forming one half of a QDM.

A quantum dot molecule, i.e. two dots with an electrically tunable coupling positioned at a well defined distance provides an ideal system to study nuclear spin diffusion in strained nanostructures. When tuned to the non-coupling regime, pumping of the nuclear spin bath in one and simultaneously detecting the buildup of nuclear polarization as a function of time in the other dot would allow to study diffusion of the nuclear spin polarization out of the area where it was generated into the surrounding material. A more advanced version of this experiment would employ a column of several stacked QDs [Bru03] representing a whole system of nuclear polarization sensors all lined up in one direction which would allow to measure the diffusion profile along this axis.

Another type of experiment can be performed in the coupling regime. Measuring DNP as a function of the energy detuning from the anticrossing yields information on the dependence of nuclear spin pumping on the electron wavefunction being gradually shifted from being confined in one dot to being delocalized across the whole molecule. First measurements of this kind have been started recently at the Walter Schottky Institut in a work following up the project of this thesis.

Challenges

In order to perform the experiments on nuclear spin diffusion described above, the direct neutral exciton states of both dots of the molecule have to identified unambiguously. This is a non-trivial task due to the large number of states in a QDM that lead to a complicated level spectrum (cf. figure 2.25). Due to the characteristic tunnel anticrossing signature, the X^0_{dir} states of the upper dot as well as the X^0_{ind} are easy to recognize in a standard PLV image plot where PL spectra are recorded as a function of the electric field (cf. figure 2.25) [Kre05b]. However, a comprehensive set of PL, PLE and PC characterization measurements is necessary to identify the neutral exciton states of the lower dot. Obviously, this task would become significantly more complex for a QD column consisting of many vertically stacked QDs. In order not to generate DNP during readout of the Overhauser shift in the sensor dot either very low excitation powers and short detection times or, if available in the corresponding magnetic field regime,

detection of the state inactive with regard to DNP have to be employed. Note that the randomization procedure cannot be applied selectively to only one of the dots but would always result in a randomization of the nuclear spin polarization in the whole molecule.

6.3.2 DNP in single quantum dots

Experiments on DNP in single self-assembled have been performed extensively in the framework of this thesis based resonant pumping of the neutral exciton ground states in the photocurrent regime. Further measurements to continue research along this line could be conducted using the same approach, however, applied to excited states of the neutral exciton. Nuclear spin pumping via these QD transitions might turn out to be qualitatively different from ground state excitation due to the altered energy spectrum of the involved bright and dark exciton states, the possibility for the state to decay to the ground state via relaxation and the different shape of the electron wave function of the *p*-, *d*-, ... shells. Investigation of these effects appears to be a promising task that might allow to observe novel nuclear spin pumping phenomena and gain further insight into DNP-related phenomena.

In the current model describing the experimental data on DNP, no effects based on the coupling between holes and nuclei are considered when simulating the dynamics of the system. Although expected to be significantly weaker than the hyperfine assisted electron-nuclear processes [Fis08; Tes09; Ebl09; Fal10; Che11b; Che11c], a future more sophisticated model could try to include polarization and depolarization effects of the nuclear spin bath caused by holes in order to derive a more complete and realistic picture.

Another still open question is the nature of the depolarization processes or other underlying mechanisms in DNP that limit the maximum Overhauser shift achieved in this thesis to $\approx 135\ \mu$eV, corresponding to a degree of nuclear spin polarization of ≈ 54 %, a value that is in agreement with numerous other studies reported in literature [Bra06b; Urb07; Mal09; Klo10a; Che10b; Urb12]. Although the numerical simualtions allow to successfully reproduce many experimental observations, the use of a constant depolarization rate as currently done is a strong simplification as becomes clear when the whole set of empirical results is compared. Therefore, further theoretical investigations should be conducted that include depolarization effects based on physical processes taking place in the system. This might allow to derive predictions for different scenarios which can then be tested in experiment. A better understanding of these processes is essential to develop strategies in order to extend the lifetime of nuclear spin polarization and increase the maximum degree of polarization achievable.

List of Constants and Abbreviation

Table 6.1. *List abbreviations used in this thesis*

QD	quantum dot
QDM	quantum dot molecule
MBE	molecular beam epitaxy
X-STM	cross-sectional scanning transmission microscopy
X-TEM	cross-sectional transmission electron microscopy
AFM	atomic force microscopy
DNP	dynamical nuclear polarization
hf	hyperfine
hh	heavy hole
lh	light hole
mw	microwave
rf	radio frequency
cw	continuous wave
ESR	electron spin resonance
EDMR	electrically detected magnetic resonance
NMR	nuclear magnetic resonance
CPS	coplanar stripline
CPW	coplanar waveguide
PCB	printed circuit board
BCB	benzocyclobutene
He	helium
In	indium
Ga	gallium
As	arsenide
Ti	titanium
Au	gold
Ag	silver

Table 6.2. *List of important symbols used in this thesis*

$mX^{\pm n}$	QD state formed by m excitons and n excess electrons (-) or holes (+)
$\|E_1\rangle$ ($\|E_3\rangle$)	energetically higher bright (dark) state of X^0
$\|E_2\rangle$ ($\|E_4\rangle$)	energetically lower bright (dark) state of X^0
ΔE_{i-j}	energy difference between $\|E_i\rangle$ and $\|E_j\rangle$
$\Delta E_{i-j}^{\mathrm{s,n}}$	ΔE_{i-j} in the presence of steady state Overhauser field
Δ_0	natural linewidth of QD transitions
$\delta_{\mathrm{n}}; \delta_{\mathrm{n}}^{\mathrm{s}}$	Overhauser shift; steady state Overhauser shift
δ_1^{b} (δ_1^{d})	exchange splitting of the two bright (dark) exciton states from another
δ_0	exchange splitting between bright and dark excitons
$g_{\mathrm{e}}; g_{\mathrm{h}}; g_{\mathrm{n}}$	electron; hole; nuclear g-factor
$g_{\mathrm{ex}}^{\mathrm{b}}; g_{\mathrm{ex}}^{\mathrm{d}}$	bright; dark exciton g-factor
$\boldsymbol{J}_{\mathrm{e}}; J_{\mathrm{e}}; J_{\mathrm{e},z}$	electron spin with quantum number and z-projection
$\boldsymbol{J}_{\mathrm{ex}}; J_{\mathrm{ex}}; J_{\mathrm{ex},z}$	exciton spin with quantum number and z-projection
$\boldsymbol{J}_{\mathrm{hh}}; J_{\mathrm{hh}}; J_{\mathrm{hh},z}$	heavy hole spin with quantum number and z-projection
$\boldsymbol{J}_{\mathrm{lh}}; J_{\mathrm{lh}}; J_{\mathrm{lh},z}$	light hole spin with quantum number and z-projection
$\boldsymbol{I}; I; I_z$	nuclear spin spin with quantum number and z-projection
$m_{\mathrm{e}}^*; m_{\mathrm{hh}}^*; m_{\mathrm{lh}}^*$	effective mass for electron; heavy hole; and light hole
$\boldsymbol{B}_{\mathrm{n}}$; $B_{\mathrm{n},z} \equiv B_{\mathrm{n}}$	Overhauser field; z-component of $\boldsymbol{B}_{\mathrm{n}}$
$\boldsymbol{B}_{\mathrm{e}}$; $B_{\mathrm{e},z} \equiv B_{\mathrm{e}}$	Knight field; z-component of $\boldsymbol{B}_{\mathrm{e}}$
$\boldsymbol{B}_{\mathrm{ext}}$; $B_{\mathrm{ext},z} \equiv B_{\mathrm{ext}}$	externally applied magnetic field; z-component of $\boldsymbol{B}_{\mathrm{ext}}$
$D_{\mathrm{n,diff}}$	nuclear spin diffusion constant
Γ_{exc}	optical excitation rate (given by $\frac{1}{e} \cdot PC\ peak\ height\ [A]$)
P^{ff}	probability for an e-n spin flip-flop process to occur
A_i	hyperfine coupling constant of the nucleus i
$I^{\pm}$; $J_{\mathrm{e}}^{\pm}$	nuclear; electron spin rising and lowering operators
$A^{\pm}$	$\sum_i A_i I_i^{\pm}$
$\boldsymbol{F}$; $F_z \equiv F$	electric field applied to quantum do; z-component of $\boldsymbol{F}$
β	exciton polarizability
$\boldsymbol{p}_{\mathrm{int}}$	intrinsic exciton dipole moment
t^s	time until steady state nuclear spin polarization is reached
I^s	PC signal in steady state at fixed F
γ_2	diamagnetic coefficient of diamagnetic shift of QD states
d_{QD}	quantum dot diameter
h_{QD}	quantum dot height
η_{In}	indium content

Table 6.3. *List of important constants used in this thesis*

$\mu_B = 5.788 \cdot 10^{-5}$ eV/T	Bohr magneton
$\mu_n = 3.152 \cdot 10^{-8}$ eV/T	nuclear magneton
$\mu_0 = 4\pi \cdot 10^{-7}\ N/A^2$	permeability of free space
$\hbar = 6.58 \cdot 10^{-16}$ eVs ´	reduced Planck´s constant
1 eV $= 1.6 \cdot 10^{-19}$ J	1 electronvolt
$k_B = 8.62 \cdot 10^{-5}$ eV/K	Boltzmann constant
$e = 1.6 \cdot 10^{-19}$ A·s	elementary charge
$m_0 = 9.12 \cdot 10^{-31}$ kg	free electron mass
$g_0 = 2.002319$	free electron g-factor

Table 6.4. *List of subscripts/superscripts with a particular meaning used in this thesis*

s	steady state
n	nuclear
h	hole
lh	heavy hole
hh	light hole
e	electron
ex	exciton
exc	excitation
ext	external
det	detection
hf	hyperfine
ff	flip-flop
Z	Zeeman
rand	randomization
depol	depolarization
dir	direct
ind	indirect

Bibliography

[Abr61] A. Abragam, *The principles of nuclear magnetism*. Clarendon Press, Oxford, (1961).

[Abr78] A. Abragam and M. Goldman, *Principles of Dynamic Nuclear Polarisation*, Rep. Prog. Phys. **41**(3), 395 (1978).

[Ale06] T. P. Mayer Alegre, F. G. G. Hernández, A. L. C. Pereira, and G. Medeiros-Ribeiro, *Landé g Tensor in Semiconductor Nanostructures*, Phys. Rev. Lett. **97**(23), 236402 (2006).

[Ali96] A. P. Alivisatos, *Semiconductor clusters, nanocrystals, and quantum dots*, Science **271**(5251), 933–937 (1996).

[Ana08] D.E. Anagnostou, M. Morton, J. Papapolymerou, and C.G. Christodoulou, *A 0 - 55-GHz Coplanar Waveguide to Coplanar Strip Transition*, IEEE Transactions on Microwave Theory and Techniques **56**(1), 1–6 (2008).

[And93] A.V. Andreev, V.I. Emelyanov, and Yu.A. Ilinski, *Cooperative effects in optics: Superradiance and phase transitions*. IOP Publishing, Bristol, (1993).

[And07] M. Anderlini, P.J. Lee, B.L. Brown, J. Sebby-Strabley, W.D. Phillips, and J.V. Porto, *Controlled exchange interaction between pairs of neutral atoms in an optical lattice*, Nature **448**(7152), 452–456 (2007).

[And08] T. Andlauer, R. Morschl, and P. Vogl, *Gauge-invariant discretization in multiband envelope function theory and g factors in nanowire dots*, Phys. Rev. B **78**(7), 075317 (2008).

[And09a] T. Andlauer, *Optoelectronic and spin-related properties of semiconductor nanostructures in magnetic fields*. Ph.D. Thesis, Walter Schottky Institut, Technische Universität München, (2009).

[And09b] T. Andlauer and P. Vogl, *Electrically controllable g tensors in quantum dot molecules*, Phys. Rev. B **79**(4), 045307 (2009).

[Ara82] Y. Arakawa and H. Sakaki, *Multidimensional quantum well laser and temperature dependence of its threshold current*, Appl. Phys. Lett. **40**(11), 939–941 (1982).

[Ash96] R. C. Ashoori, *Electrons in artifcial atoms*, Nature **379**(6564), 413–419 (1996).

[Ata00] M. Atature, J. Dreiser, A. Badolato, and A. Imamoğlu, *Observation of Faraday rotation from a single confined spin*, Nature Physics **3**(2), 101–106 (200).

[Ata06] M. Atature, J. Dreiser, A. Badolato, A. Hogele, K. Karrai, and A. Imamoğlu, *Quantum-dot spin-state preparation with near-unity fidelity*, Science **312**(5773), 551–553 (2006).

[Ban99] U. Banin, Y. Cao, D. Katz, and O. Millo, *Identification of atomic-like electronic states in indium arsenide nanocrystal quantum dots*, Nature **400**(6744), 542–544 (1999).

[Bar00] J.A. Barker and E.P. O'Reilly, *Theoretical analysis of electron-hole alignment in InAs-GaAs quantum dots*, Phys. Rev. B **61**(20), 13840–13851 (2000).

[Baw90] M.G. Bawendi, M.L. Steigerwald, and L.E. Brus, *The Quantum-Mechanics of Larger Semiconductor Clusters (Quantum Dots)*, Annual Review of Physical Chemistry **41**, 477–496 (1990).

[Bay98] M. Bayer, S.N. Walck, T.L. Reinecke, and A. Forchel, *Exciton binding energies and diamagnetic shifts in semiconductor quantum wires and quantum dots*, Phys. Rev. B **57**(11), 6584–6591 (1998).

[Bay99a] M. Bayer, A. Kuther, A. Forchel, A. Gorbunov, V. B. Timofeev, F. Schäfer, J. P. Reithmaier, T. L. Reinecke, and S. N. Walck, *Electron and Hole g Factors and Exchange Interaction from Studies of the Exciton Fine Structure in $In_{0.60}Ga_{0.40}As$ Quantum Dots*, Phys. Rev. Lett. **82**(8), 1748–1751 (1999).

[Bay99b] M. Bayer, A. Kuther, F. Schäfer, J.P. Reithmaier, and A. Forchel, *Strong variation of the exciton g factors in self-assembled $In_{0.60}Ga_{0.40}As$ quantum dots*, Phys. Rev. B (R) **60**(12), 8481–8484 (1999).

[Bay99c] M. Bayer, O. Stern, A. Kuther, and A. Forchel, *Spectroscopic study of dark excitons in* $In_xGa_{1-x}As$ *self-assembled quantum dots by a magnetic-field-induced symmetry breaking*, Phys. Rev. B **61**(12), 7273–7276 (1999).

[Bay00] M. Bayer, O. Stern, P. Hawrylak, S. Fafard, and A. Forchel, *Hidden symmetries in the energy levels of excitonic 'artificial atoms'*, Nature **405**(6789), 923–926 (2000).

[Bay01] M. Bayer, P. Hawrylak, K. Hinzer, S. Fafard, M. Korkusinski, Z.R. Wasilewski, O. Stern, and A. Forchel, *Coupling and entangling of quantum states in quantum dot molecules*, Science **291**(5503), 451–453 (2001).

[Bay02a] M. Bayer and A. Forchel, *Temperature dependence of the exciton homogeneous linewidth in* $In_{0.60}Ga_{0.40}As/GaAs$ *self-assembled quantum dots*, Phys. Rev. B **65**(4), 041308 (2002).

[Bay02b] M. Bayer, G. Ortner, O. Stern, A. Kuther, A. A. Gorbunov, A. Forchel, P. Hawrylak, S. Fafard, K. Hinzer, T. L. Reinecke, S. N. Walck, J. P. Reithmaier, F. Klopf, and F. Schäfer, *Fine structure of neutral and charged excitons in self-assembled In(Ga)As/(Al)GaAs quantum dots*, Phys. Rev. B **65**(19), 195315 (2002).

[Beh00] E. Beham, A. Zrenner, and G. Böhm, *STM-photocurrent-spectroscopy on single self-assembled InGaAs quantum dots*, Physica E: Low-dimensional Systems and Nanostructures **7**(3-4), 359–362 (2000).

[Beh01] E. Beham, A. Zrenner, F. Findeis, M. Bichler, and G. Abstreiter, *Nonlinear ground-state absorption observed in a single quantum dot*, Applied Physics Letters **79**(19), 2808–2810 (2001).

[Beh02] E. Beham, A. Zrenner, F. Findeis, M. Bichler, and G. Abstreiter, *Level bleaching in a single quantum dot observed by photocurrent spectroscopy*, Physica E-Low-Dimensional Systems & Nanostructures **13**(2-4), 139–142 (2002).

[Bel09] T. Belhadj, C.-M. Simon, T. Amand, P. Renucci, B. Chatel, O. Krebs, A. Lemaitre, P. Voisin, X. Marie, and B. Urbaszek, *Controlling the Polarization Eigenstate of a Quantum Dot Exciton with Light*, Phys. Rev. Lett. **103**(8), 086601 (2009).

[Ben00] O. Benson, C. Santori, M. Pelton, and Y. Yamamoto, *Regulated and entangled photons from a single quantum dot*, Phys. Rev. Lett. **84**(11), 2513–2516 (2000).

[Ber08] J. Berezovsky, M.H. Mikkelsen, N.G. Stoltz, L.A. Coldren, and D.D. Awschalom, *Picosecond Coherent Optical Manipulation of a Single Electron Spin in a Quantum Dot*, Science **320**(5874), 349–352 (2008).

[Bes00] L. Besombes, K. Kheng, and D. Martrou, *Exciton and biexciton fine structure in single elongated islands grown on a vicinal surface*, Phys. Rev. Lett. **85**(2), 425–428 (2000).

[Bes04] G. Bester, J. Shumway, and A. Zunger, *Theory of Excitonic Spectra and Entanglement Engineering in Dot Molecules*, Phys. Rev. Lett. **93**(4), 047401 (2004).

[Bes05] G. Bester, A. Zunger, and J. Shumway, *Broken symmetry and quantum entanglement of an exciton in $In_xGa_{1-x}As/GaAs$ quantum dot molecules*, Phys. Rev. B **71**(7), 075325 (2005).

[Bev08] L.H. Willems van Beveren, H. Huebl, D.R. McCamey, T. Duty, A.J. Ferguson, R.G. Clark, and M.S. Brandt, *Broadband electrically detected magnetic resonance of phosphorus donors in a silicon field-effect transistor*, Appl. Phys. Lett. **93**(7), 072102 (2008).

[Bin86] G. Binnig, C. F. Quate, and Ch. Gerber, *Atomic Force Microscope*, Phys. Rev. Lett. **56**(9), 930–933 (1986).

[Bjo05] M.T. Bjork, A. Fuhrer, A.E. Hansen, M.W. Larsson, L.E. Fröberg, and L. Samuelson, *Tunable effective g factor in InAs nanowire quantum dots*, Phys. Rev. B **72**(20), 201307 (2005).

[Bla08] R. Blatt and D. Wineland, *Entangled states of trapped atomic ions*, Nature **453**(7198), 1008–1015 (2008).

[Blu11] H. Bluhm, S. Foletti, I. Neder, M. Rudner, D. Mahalu, V. Umansky, and A. Yacoby, *Dephasing time of GaAs electron-spin qubits coupled to a nuclear bath exceeding 200 μs*, Nature Physics **7**(2), 109–113 (2011).

[Box07] F. Boxberg and J. Tulkki, *Theory of the electronic structure and carrier dynamics of strain-induced (Ga, In)As quantum dots*, Rep. Prog. Phys. **70**(8), 1425–1471 (2007).

[Bra05a] A.S. Bracker, E.A. Stinaff, D. Gammon, M.E Ware, J.G. Tischler, A. Shabaev, A.L. Efros, Park, D. D. Gershoni, V.L. Korenev, and I.A. Merkulov, *Optical pumping of the electronic and nuclear spin of single charge-tunable quantum dots*, Phys. Rev. Lett. **94**(4), 047402 (2005).

[Bra05b] P.-F. Braun, X. Marie, L. Lombez, B. Urbaszek, T. Amand, P. Renucci, V. K. Kalevich, K. V. Kavokin, O. Krebs, P. Voisin, and Y. Masumoto, *Direct Observation of the Electron Spin Relaxation Induced by Nuclei in Quantum Dots*, Phys. Rev. Lett. **94**(11), 116601 (2005).

[Bra06a] A.S. Bracker, M. Scheibner, M.F. Doty, E.A. Stinaff, I.V. Ponomarev, J.C. Kim, L.J. Whitman, T.L. Reinecke, and D. Gammon, *Engineering electron and hole tunneling with asymmetric InAs quantum dot molecules*, Appl. Phys. Lett. **89**(23), 233110 (2006).

[Bra06b] P.-F. Braun, B. Urbaszek, T. Amand, X. Marie, O. Krebs, B. Eble, A. Lemaitre, and P. Voisin, *Bistability of the nuclear polarization created through optical pumping in $In_{1-x}Ga_xAs$ quantum dots*, Phys. Rev. B **74**(24), 245306 (2006).

[Bra08] A.S. Bracker, D. Gammon, and V.L. Korenev, *Fine structure and optical pumping of spins in individual semiconductor quantum dots*, Semicond. Sci. Technol. **23**(11), 114004 (2008).

[Bra05] T. Brandes, *Coherent and collective quantum optical effects in mesoscopic systems*, Phys. Rep. **408**(5-6), 315–474 (205).

[Bri26] L. Brillouin, *La mécanique ondulatoire de Schrödinger: une méthode générale de resolution par approximations successives*, Comptes Rendus de l'Academie des Sciences **183**, 24–26 (1926).

[Bro96] S.W. Brown, T.A. Kennedy, D. Gammon, and E.S.) Snow, *Spectrally resolved overhauser shifts in single GaAs/$Al_xGa_{1-x}As$ quantum dots*, Phys. Rev. B **54**(24), 17339–17342 (1996).

[Bro98] S.W. Brown, T.A. Kennedy, and D. Gammon, *Optical NMR from single quantum dots*, Solid State Nuclear Magnetic Resonance **11**(1-2), 49–58 (1998).

[Bru84] L.E. Brus, *Electron-electron and electron-hole interactions in small semiconductor crystallites: The size dependence of the lowest excited electronic state*, Journal of Chemical Physics **80**(9), 4403–4409 (1984).

[Bru91] L. Brus, *Quantum Crystallites and Nonlinear Optics*, Applied Physics A - Materials Science & Processing **53**(6), 465–474 (1991).

[Bru02] D.M. Bruls, J.W.A.M. Vugs, P.M. Koenraad, H.W.M. Salemink, J.H. Wolter, M. Hopkinson, M.S. Skolnick, Fei Long, and S.P.A. Gill, *Determination of the shape and indium distribution of low-growth-rate InAs quantum dots by cross-sectional scanning tunneling microscopy*, Applied Physics Letters **81**(9), 1708–1710 (2002).

[Bru03] D.M. Bruls, P.M. Koenraad, H.W.M. Salemink, J.H. Wolter, M. Hopkinson, and M.S. Skolnick, *Stacked low-growth-rate InAs quantum dots studied at the atomic level by cross-sectional scanning tunneling microscopy*, Applied Physics Letters **82**(21), 3758–3760 (2003).

[Bru09] D. Brunner, B.D. Gerardot, P. A. Dalgarno, G. Wuest, K. Karrai, N.G. Stoltz, P.M. Petroff, and R.J. Warburton, *A Coherent Single-Hole Spin in a Semiconductor*, Science **325**(5936), 70–72 (2009).

[Bur92] M.G. Burt, *The justification for applying the effective-mass approximation to microstructures*, J. Phys.: Condens. Matter **4**(32), 6651 (1992).

[Bur99a] G. Burkard, D. Loss, and D.P. DiVincenzo, *Coupled quantum dots as quantum gates*, Phys. Rev. B **59**(3), 2070–2078 (1999).

[Bur99b] M.G. Burt, *Fundamentals of envelope function theory for electronic states and photonic modes in nanostructures*, J. Phys.: Condens. Matter **11**(9), 53 (1999).

[Bur08] G. Burkard, *Quantum information: Positively spin coherent*, Nature Materials **7**(2), 100–101 (2008).

[But04] A. Butrym and S. Pivnenko, *CPW to CPS Transition for feeding UWB Antennas*, IEEE Aerospace and Electronic Systems Magazine, Second International Workshop on Ultrawideband and Ultrashort Impulse Signals, 107-108 (2004).

[Car53] T.R. Carver and C.P. Slichter, *Polarization of nuclear spins in metals*, Phys. Rev. **92**(1), 212–213 (1953).

[Car56] T.R. Carver and C.P. Slichter, *Experimental Verification of the Overhauser Nuclear Polarization Effect*, Phys. Rev. **102**(4), 975–980 (1956).

[Che59] P.L. Chebyshev, *Sur le développment des fonctions a une seule variable*, Bull. Acad. Sci. St. Petersb. **I**, 193–200 (1859).

[Che10a] E.A. Chekhovich, M.N. Makhonin, A.B. Kavokin, Krysa, M.S. Skolnick, and Tartakovskii A.I., *Pumping of nuclear spins by optical excitation of spin-forbidden transitions in a quantum dot*, Phys. Rev. Lett. **104**(6), 066804 (2010).

[Che10b] E.A. Chekhovich, M.N. Makhonin, J. Skiba-Szymanska, A.B. Krysa, V.D. Kulakovskii, M.S. Skolnick, and A.I. Tartakovskii, *Dynamics of optically induced nuclear spin polarization in individual $InPGa_xIn_{1-x}P$ quantum dots*, Phys. Rev. B **81**(24), 245308 (2010).

[Che11a] E.A. Chekhovich, K.V Kavokin, J. Puebla, A.B. Krysa, M. Hopkinson, A.D. Andreev, A.M. Sanchez, R. Beanland, M.S. Skolnick, and A.I. Tartakovskii, *High resolution nuclear magnetic resonance spectroscopy of highly-strained quantum dot nanostructures*, arXiv:1112.4079v1 (2011).

[Che11b] E.A. Chekhovich, A.B. Krysa, , M.S. Skolnick, and A.I. Tartakovskii, *Direct Measurement of the Hole-Nuclear Spin Interaction in Single InP/GaInP Quantum Dots Using Photoluminescence Spectroscopy*, Phys. Rev. Lett. **106**(2), 027402 (2011).

[Che11c] E.A. Chekhovich, A.B. Krysa, M. Hopkinson, P. Senellart, A. Lemaître, M.S. Skolnick, and A.I. Tartakovskii, *Isotope sensitive measurement of the hole-nuclear spin interaction in quantum dots*, arXiv:1109.0733v1 (2011).

[Che11d] E.A. Chekhovich, A.B. Krysa, M.S. Skolnick, and A.I. Tartakovskii, *Light-polarization-independent nuclear spin alignment in a quantum dot*, Phys. Rev. B **83**(12), 125318 (2011).

[Chi03] I. Chiorescu, Y. Nakamura, C.J.P.M. Harmans, and J.E. Mooij, *Coherent quantum dynamics of a superconducting flux qubit*, Science **299**(5614), 1869–1871 (2003).

[Cho70] A.Y. Cho, *Morphology of Epitaxial Growth of GaAs by a Molecualr Beam Method: The Observation of Surface Structures*, Journal of Applied Physics **41**(7), 2780–2786 (1970).

[Cho71] A.Y. Cho, *GaAs Epitaxy by a Molecular Beam Method: Observation of Surface Structure on the (001) Face*, Journal of Applied Physics **42**(5), 2074–2081 (1971).

[Chr07] H. Christ, J.I. Cirac, and G. Giedke, *Quantum Description of Nuclear Spin Cooling in a Quantum Dot*, Phys. Rev. B **75**(15), 155324 (2007).

[Chu98] I.I. Chuang, I.M.K. Vandersypen, X. Zhou, D.W. Leung, and S. Lloyd, *Experimental realization of a quantum algorithm*, Nature **393**, 143–146 (1998).

[Chu99] L. Chu, M. Arzberger, G. Böhm, and G. Abstreiter, *Influence of growth conditions on the photoluminescence of self-assembled InAs/GaAs quantum dots*, Journal of Applied Physics **85**(4), 2355 (1999).

[Cio00] M. Ciorga, A. S. Sachrajda, P. Hawrylak, C. Gould, P. Zawadzki, S. Jullian, Y. Feng, and Z. Wasilewski, *Addition spectrum of a lateral dot from Coulomb and spin-blockade spectroscopy*, Physical Review B **61**(24), 16315–16318 (2000).

[Cla76] A.H. Clark, R.D. Burnham, D.J. Chadi, and R.M. White, *Spin Relaxation of Conduction Electrons in GaAs*, Solid State Communications **20**(4), 385–387 (1976).

[Cla09] E. Clark, *private communications* (2009).

[Cle98] R. Cleve, A. Ekert, C. Macchiavello, and M. Mosca, *Quantum algorithms revisited*, Proceedings of the Royal Society A **454**(1969), 339–354 (1998).

[Cli08] J.P. Clifford, G. Konstantatos, K.W. Johnston, S. Hoogland, and E.H. Levina, L. Sargent, *Fast, sensitive and spectrally tuneable colloidal-quantum-dot photodetectors*, Nature Nanotechnology **4**(1), 40–44 (2008).

[Coi04] W.A. Coish and D. Loss, *Hyperfine interaction in a quantum dot: Non-Markovian electron spin dynamics*, Phys. Rev. B **70**(19), 195340 (2004).

[Coi09] W.A. Coish and J. Baugh, *Nuclear spins in nanostructures*, Phys. Status Solidi B **246**(10), 2203–2215 (2009).

[Col94] V.L. Colvin, M.C. Schlamp, and A.P. Alivisatos, *Light-emitting diodes made from cadmium selenide nanocrystals and a semiconducting polymer*, Nature **370**(6488), 354–357 (1994).

[Cyw09a] L Cywinski, W.M. Witzel, and S. Das Sarma, *Electron Spin Dephasing due to Hyperfine Interactions with a Nuclear Spin Bath*, Phys. Rev. Lett. **102**(5), 057601 (2009).

[Cyw09b] L Cywinski, W.M. Witzel, and S. Das Sarma, *Pure quantum dephasing of a solid-state electron spin qubit in a large nuclear spin bath coupled by long-range hyperfine-mediated interactions*, Phys. Rev. B **79**(24), 245314 (2009).

[Dal06] P.A. Dalgarno, J. McFarlane, B.D. Gerardot, R.J. Warburton, K. Karrai, A. Badolato, and P.M. Petroff, *Decay dynamics of the positively charged exciton in a single charge tunable self-assembled quantum dot*, Applied Physics Letters **89**(4), 043107 (2006).

[daS97] S. W. daSilva, Y. A. Pusep, J. C. Galzerani, D. I. Lubyshev, P. P. GonzalezBorrero, and P. Basmaji, *Photoluminescence study of spin-orbit-split bound electron states in self-assembled InAs and $In_{0.5}Ga_{0.5}As$ quantum dots*, Journal of Physics-Condensed Matter **9**(1), L13–L17 (1997).

[DE08] M.I. Dyakonov (Ed.), *Spin Physics in Semiconductors*. Springer-Verlag, Berlin, (2008).

[Dea11] R.S. Deacon, Y. Kanai, S. Takahashi, A. Oiwa, K. Yoshida, K. Shibata, K. Hirakawa, Y. Tokura, and S. Tarucha, *Electrically tuned g tensor in an InAs self-assembled quantum dot*, Phys. Rev. B **84**(4), 041302 (2011).

[Dek00] E. Dekel, D.V. Regelman, D. Gershoni, E. Ehrenfreund, W.V. Schoenfeld, and P.M. Petroff, *Cascade evolution and radiative recombination of quantum dot multiexcitons studied by time-resolved spectroscopy*, Phys. Rev. B **62**(16), 11038–11045 (2000).

[Der83] H. Dersch, L. Schweitzer, and J. Stuke, *Recombination processes in a-Si-H spin-dependent photoconductivity*, Phys. Rev. B **28**(8), 4678–4684 (1983).

[deS03] R. deSousa and S. Das Sarma, *Theory of nuclear-induced spectral diffusion: Spin decoherence of phosphorus donors in Si and GaAs quantum dots*, Phys. Rev. B **58**(11), 115322 (2003).

[Deu92] D. Deutsch and R. Jozsa, *Rapid Solution of Problems by Quantum Computation*, Proceedings of the Royal Society A **439**(1907), 553–558 (1992).

[Din74] R. Dingle, W. Wiegmann, and C. Henry, *Quantum states of confined carriers in very thin $Al_xGa_{1-x}As$-GaAs-$Al_xGa_{1-x}As$ Heterostructures*, Phys. Rev. Lett. **33**(14), 827–830 (1974).

[DiV00] D.P. DiVincenzo, *The physical implementation of quantum computation*, Fortschr. Phys. **48**(9-11), 771–783 (2000).

[Dob88] M. Dobers, K. v. Klitzing, and G. Weimann, *Electron-spin resonance in the two-dimensional electron gas of GaAs- $Al_xGa_{1-x}As$ heterostructures*, Phys. Rev. B **38**(8), 5453–5456 (1988).

[Dot06] M. F. Doty, M. Scheibner, I. V. Ponomarev, E. A. Stinaff, A. S. Bracker, V. L. Korenev, T. L. Reinecke, and D. Gammon, *Electrically Tunable g Factors in Quantum Dot Molecular Spin States*, Phys. Rev. Lett. **97**(19), 197202 (2006).

[Dre94] H. Drexler, D. Leonard, W. Hansen, J. P. Kotthaus, and P. M. Petroff, *Spectroscopy of Quantum Levels in Charge-Tunable Ingaas Quantum Dots*, Physical Review Letters **73**(16), 2252–2255 (1994).

[Dre11] L. Dreher, T. A. Hilker, A. Brandlmaier, S. T. B. Goennenwein, H. Huebl, M. Stutzmann, and M. S. Brandt, *Electroelastic Hyperfine Tuning of Phosphorus Donors in Silicon*, Phys. Rev. Lett. **106**(3), 037601 (2011).

[Duc04] Y. Ducommun, M. Kroutvar, J. J. Finley, M. Bichler, A. Zrenner, and G. Abstreiteir, *Dynamics of optically stored charges in InGaAs quantum dots*, Physica E-Low-Dimensional Systems + Nanostructures **21**(2-4), 886–891 (2004).

[Dzh07] R.I. Dzhioev and V.L. Korenev, *Stabilization of the Electron-Nuclear Spin Orientation in Quantum Dots by the Nuclear Quadrupole Interaction*, Phys. Rev. Lett. **99**(3), 037401 (2007).

[Eag90] D. J. Eaglesham and M. Cerullo, *Dislocation-free Stranski-Krastanow growth of Ge on Si(100)*, Phys. Rev. Lett. **64**(16), 1943–1946 (1990).

[Ebl06] B Eble, O. Krebs, A. Lemaitre, K. Kowalik, A. Kudelski, P. Voisin, B. Urbaszek, X. Marie, and T Amand, *Dynamic nuclear polarization of a single charge-tunable InAs/GaAs quantum dot*, Phys. Rev. B **74**(8), 081306 (2006).

[Ebl09] B. Eble, C. Testelin, P. Desfonds, F. Bernardot, A. Balocchi, T. Amand, A. Miard, A. Lemaître, X. Marie, and M. Chamarro, *Hole-Nuclear Spin Interaction in Quantum Dots*, Phys. Rev. Lett. **102**(14), 146601 (2009).

[Efr82] Al.L. Efros and A. L. Efros, *Interband absorption of light in a semiconductor sphere*, Soviet Physics Semiconductors Ussr **16**(7), 772–775 (1982).

[Eis11] T. Eissfeller and P. Vogl, *Real-space multiband envelope-function approach without spurious solutions*, Phys. Rev. B **84**(19), 195122 (2011).

[Eis12a] T. Eisfeller, *private communications* (2012).

[Eis12b] T. Eisfeller, *Theory of the Electronic Structure of Quantum Dots in External Fields*. Ph.D. Thesis, Walter Schottky Institut, Technische Universität München, (2012).

[Eke96] A. Ekert and R. Jozsa, *Quantum computation and Shor's factoring algorithm*, Rev. Mod. Phys. **68**(3), 733–753 (1996).

[Eki81] A.I. Ekimov and A.A. Onushchenko, *Quantum size effect in three-dimensional microscopic semiconductor crystals*, JEPT Letters **34**(6), 363–366 (1981).

[Elz03] J. M. Elzerman, R. Hanson, J.S. Greidanus, L.H.W. van Beveren, S. De Franceschi, L.M.K. Vandersypen, S. Tarucha, and L.P. Kouwenhoven, *Few-electron quantum dot circuit with integrated charge read out*, Phys. Rev. B **67**(16), 161308 (2003).

[Elz04] J. M. Elzerman, R. Hanson, L. H. W. van Beveren, B. Witkamp, L. M. K. Vandersypen, and L. P. Kouwenhoven, *Single-shot read-out of an individual electron spin in a quantum dot*, Nature **430**(6998), 431–435 (2004).

[Erl01] S.I. Erlingsson, Y.V. Nazarov, and V.I. Fal'ko, *Nucleus-mediated spin-flip transitions in GaAs quantum dots*, Phys. Rev. B **64**(19), 195306 (2001).

[Eto97] M. Eto, *Electronic Structures of Few Electrons in a Quantum Dot under Magnetic Fields*, Jpn. J. Appl. Phys **36**(6B), 3924–3927 (1997).

[Faf99] S. Fafard, Z. R. Wasilewski, C. Ni. Allen, D. Picard, M. Spanner, J. P. McCaffrey, and P. G. Piva, *Manipulating the energy levels of semiconductor quantum dots*, Phys. Rev. B **59**(23), 15368–15373 (1999).

[Fal10] P. Fallahi, S.T. Yilmaz, and A. A. Imamoğlu, *Measurement of a Heavy-Hole Hyperfine Interaction in InGaAs Quantum Dots Using Resonance Fluorescence*, Phys. Rev. Lett. **105**(25), 257402 (2010).

[Feh11] M. Fehr, A. Schnegg, B. Rech, K. Lips, O. Astakhov, F. Finger, G. Pfanner, C. Freysoldt, J. Neugebauer, R. Bittl, and C. Teutloff, *Combined multifrequency EPR and DFT study of dangling bonds in a-Si:H*, Phys. Rev. B **84**(24), 245203 (2011).

[Fer30] E. Fermi, *Über die magnetischen Momente der Atomkerne*, Zeitschrift für Physik **60**(5-6), 320–333 (1930).

[Fey82] R. Feynman, *Simulating physics with computers*, International Journal of Theoretical Physics **21**(6-7), 467–488 (1982).

[Fin00] F. Findeis, A. Zrenner, G. Böhm, and G. Abstreiter, *Optical spectroscopy on a single InGaAs/GaAs quantum dot in the few-exciton limit*, Solid State Communications **114**(4), 227–230 (2000).

[Fin01a] F. Findeis, M. Baier, E. Beham, A. Zrenner, and G. Abstreiter, *Photocurrent and photoluminescence of a single self-assembled quantum dot in electric fields*, Appl. Phys. Lett. **78**(19), 2958–2960 (2001).

[Fin01b] F. Findeis, M. Baier, A. Zrenner, M. Bichler, G. Abstreiter, U. Hohenester, and E. Molinari, *Optical excitations of a self-assembled artificial ion*, Physical Review B **63**(12), 121309 (2001).

[Fin01c] J. J. Finley, P. W. Fry, A. D. Ashmore, A. Lemaitre, A. I. Tartakovskii, R. Oulton, D. J. Mowbray, M. S. Skolnick, M. Hopkinson, P. D. Buckle, and P. A. Maksym, *Observation of multicharged excitons and biexcitons in a single InGaAs quantum dot*, Physical Review B **63**(16), 161305 (2001).

[Fin01d] J.J. Finley, A.D. Ashmore, A. Lemaître, D.J. Mowbray, M.S. Skolnick, I.E. Itskevich, P.A. Maksym, M. Hopkinson, and T.F. Krauss, *Charged and neutral exciton complexes in individual self-assembled In(Ga)As quantum dots*, Physical Review B **63**(7), 073307 (2001).

[Fis08] J. Fischer, W.A. Coish, D.V. Bulaev, and D. Loss, *Spin decoherence of a heavy hole coupled to nuclear spins in a quantum dot*, Phys. Rev. B **78**(15), 155329 (2008).

[Fla09] E. B. Flagg, A. Muller, J. W. Robertson, S. Founta, D. G. Deppe, M. Xiao, W. Ma, G. J. Salamo, and C. K. Shih, *Resonantly driven coherent oscillations in a solid-state quantum emitter*, Nature Physics **5**(3), 203–207 (2009).

[Fli10] K. Flisinski, I.Ya. Gerlovin, I.V. Ignatiev, M.Yu. Petrov, S.Yu. Verbin, D.R. Yakovlev, D. Reuter, A.D. Wieck, and M. Bayer, *Optically detected magnetic resonance at the quadrupole-split nuclear states in (In,Ga)As/GaAs quantum dots*, Phys. Rev. B **82**(8), 081308 (2010).

[For88] A. Forchel, H. Leier, B.E. Maile, and R. Germann, *Fabrication and optical spectroscopy of ultra small III - V compound semiconductor structures*, Advances in Solid State Physics **28**, 99–119 (1988).

[For00] B.A. Foreman, *Theory of the effective Hamiltonian for degenerate bands in an electric field*, J. Phys.: Condens. Matter **12**(34), R435 (2000).

[Fry00a] P. W. Fry, J. J. Finley, L. R. Wilson, A. Lemaitre, D. J. Mowbray, M. S. Skolnick, M. Hopkinson, G. Hill, and J. C. Clark, *Electric-field-dependent carrier capture and escape in self-assembled InAs/GaAs quantum dots*, Applied Physics Letters **77**(26), 4344–4346 (2000).

[Fry00b] P. W. Fry, I. E. Itskevich, D. J. Mowbray, M. S. Skolnick, J. J. Finley, J. A. Barker, E. P. O'Reilly, L. R. Wilson, I. A. Larkin, P. A. Maksym, M. Hopkinson, M. Al-Khafaji, J. P. R. David, A. G. Cullis, G. Hill, and J. C. Clark, *Inverted electron-hole alignment in InAs-GaAs self-assembled quantum dots*, Physical Review Letters **84**(4), 733–736 (2000).

[Fry00c] P. W. Fry, I. E. Itskevich, S. R. Parnell, J. J. Finley, L. R. Wilson, K. L. Schumacher, D. J. Mowbray, M. S. Skolnick, M. Al-Khafaji, A. G. Cullis, M. Hopkinson, J. C. Clark, and G. Hill, *Photocurrent spectroscopy of InAs/GaAs self-assembled quantum dots*, Physical Review B **62**(24), 16784 (2000).

[Fuc09] G.D. Fuchs, V.V. Dobrovitski, D.M. Toyli, F.J. Heremans, and D.D. Awschalom, *Gigahertz Dynamics of a Strongly Driven Single Quantum Spin*, Science **326**(5959), 1520–1522 (2009).

[Gam96a] D. Gammon, E.S. Snow, B.V. Shanabrook, D.S. Katzer, and D. Park, *Fine structure splitting in the optical spectra of single GaAs quantum dots*, Phys. Rev. Lett. **76**(16), 3005–3008 (1996).

[Gam96b] D. Gammon, E.S. Snow, B.V. Shanabrook, D.S. Katzer, and D. Park, *Homogenous linewidths in the optical spectrum of a single gallium arsenide quantum dot*, Science **273**(5271), 87–90 (1996).

[Gam97] D. Gammon, S.W. Brown, E.S. Snow, T.A. Kennedy, D.S. Katzer, and D. Park, *Nuclear Spectroscopy in Single Quantum Dots: Nanoscopic Raman Scattering and Nuclear Magnetic Resonance*, Science **277**(5322), 85–88 (1997).

[Gam01] D. Gammon, A.L. Efros, T.A. Kennedy, M. Rosen, D.S. Katzer, D. Park, S.W. Brown, V.L. Korenev, and I.A. Merkulov, *Electron and nuclear spin interactions in the optical spectra of single GaAs quantum dots*, Phys. Rev. Lett. **86**(22), 5176 (2001).

[Gar97] J. M. García, G. Medeiros-Ribeiro, K. Schmidt, T. Ngo, J. L. Feng, A. Lorke, J. Kotthaus, and P. M. Petroff, *Intermixing and shape changes during the formation of InAs self-assembled quantum dots*, Applied Physics Letters **71**(14), 2014–2016 (1997).

[Ger89] D. Gershoni, J. M. Vandenberg, S. N. G. Chu, H. Temkin, T. Tanbunek, and R. A. Logan, *Excitonic Transitions in Strained-Layer $In_xGa_{1-x}As/GaAs$ Quantum Wells*, Physical Review B **40**(14), 10017–10020 (1989).

[Ger08] B. Gerardot, D. Brunner, P.A. Dalgarno, P. Ohberg, S. Seidl, M. Kroner, K. Karrai, N.G. Stoltz, P.M. Petroff, and R.J. Warburton, *Optical pumping of a single hole spin in a quantum dot*, Nature (London) **451**(7177), 441–444 (2008).

[Gie12] G. Giedke, *private communications* (2012).

[GM31] M. Göppert-Mayer, *Über Elementarakte mit zwei Quantensprüngen*, Ann. d. Physik **9**, 273 (1931).

[Goe83] K.-H. Goetz, D. Bimberg, H. Jurgensen, J. Selders, A.V. Solomonov, G.F. Glinskii, and M. Razeghi, *Optical and crystallographic properties and impurity incorporation of $Ga_xIn_{1-x}As$ ($0.44 < x < 0.49$) grown by liquid phase epitaxy, vapor phase epitaxy, and metal organic chemical vapor deposition*, Journal of Applied Physics **54**(8), 4543–4552 (1983).

[Gol85] L. Goldstein, F. Glas, J. Y. Marzin, M. N. Charasse, and G. Leroux, *Growth by Molecular-Beam Epitaxy and Characterization of Inas/Gaas Strained-Layer Superlattices*, Applied Physics Letters **47**(10), 1099–1101 (1985).

[Gol88] J.E. Golub, P.F. Liao, D.J. Eilenberger, J.P. Harbison, L.T. Florez, and Y. Prior, *Type I-type II anticrossing and enhanced Stark effect in asymmetric coupled quantum wells*, Applied Physics Letters **53**(26), 2584–2586 (1988).

[Gol99] Y.A. Goldberg and N.M. Schmidt, *Handbook Series on Semiconductor Parameters*. volume 2, pages 153-179, World Scientific, London, (1999).

[Gor36] C.J. Gorter, *Negative result of an attempt to detect nuclear magnetic spins*, Physica **3**(9), 995–998 (1936).

[Gra72] D.E. Gray, (Editor), *American Institute of Physics Handbook,* 3rdedn. McGraw-Hill, New York, (1972).

[Gre03] B.A. Gregg and M.C. Hanna, *Comparing organic to inorganic photovoltaic cells: Theory, experiment, and simulation*, J. Appl. Phys. **93**(6), 3605 (2003).

[Gre06] A. Greilich, D. R. Yakovlev, A. Shabaev, A. L. Efros, I. A. Yugova, R. Oulton, V. Stavarache, D. Reuter, A. Wieck, and M. Bayer, *Mode locking of electron spin coherences in singly charged quantum dots*, Science **313**(5785), 341–345 (2006).

[Gre07] A. Greilich, A. Shabaev, D.R. Yakovlev, I.A. Efros, Al.L. Yugova, D. Reuter, A.D. Wieck, and M. Bayer, *Nuclei-Induced Frequency Focusing of Electron Spin Coherence*, Science **317**(5846), 1896–1899 (2007).

[Gro96] L.K. Grover, *A fast quantum mechanical algorithm for database search*. Proceedings of the twenty-eighth annual ACM symposium on Theory of computing, STOC '96, Philadelphia, Pennsylvania, United States, (1996).

[Gru95] M. Grundmann, N. N. Ledentsov, R. Heitz, L. Eckey, J. Christen, J. BÃ¶hrer, D. Bimberg, S. S. Ruvimov, P. Werner, U. Richter, J. Heydenreich, V. M. Ustinov, A. Yu. Egorov, A. E. Zhukov, P. S. Kopev, and Zh. I. Alferov, *InAs/GaAs quantum dots radiative recombination from zero-dimensional state*, physica status solidi B **188**(1), 249–258 (1995).

[Gru97] A. Gruber, A. Dräbenstedt, C. Tietz, L. Fleury, J. Wrachtrup, and v.C. Borczyskowsk, *Scanning confocal optical microscopy and magnetic resonance on single defect centers*, Science **276**(5321), 2012–2014 (1997).

[Gul03] S. Gulde, M. Riebe, G.P. Lancaster, C. Becher, J. Eschner, H. Häffner, F. Schmidt-Kaler, IL. Chuang, and Blatt R., *Implementation of the Deutsch-Jozsa algorithm on an ion-trap quantum computer*, Nature **421**(6918), 48–50 (2003).

[Gur05] I. Gur, N.A. Fromer, M.L. Geier, and A.P. A. Paul Alivisatos, *Air-Stable All-Inorganic Nanocrystal Solar Cells Processed from Solution*, Science **310**(5747), 462–465 (2005).

[Gyw09] O. Gywat, H.J. Krenner, and J. Berezovsky, *Spins in Optically Active Quantum Dots: Concepts and Methods*. John Wiley & Sons, Hoboken, New Jersey, (2009).

[Hah50] E.L. Hahn, *Spin Echoes*, Physical Review **80**(4), 580–594 (1950).

[Han05] R. Hanson, L. H. W. van Beveren, I. T. Vink, J. M. Elzerman, W. J. M. Naber, F. H. L. Koppens, L. P. Kouwenhoven, and L. M. K. Vandersypen, *Single-shot readout of electron spin states in a quantum dot using spin-dependent tunnel rates*, Phys. Rev. Lett. **94**(19), 196802 (2005).

[Han07] R. Hanson, L.P. Kouwenhoven, J.R. Petta, S. Tarucha, and L.M.K. Vandersypen, *Spins in few-electron quantum dots*, Reviews of Modern Physics **79**(4), 1217–1265 (2007).

[Han08] R. Hanson and D.D. Awschalom, *Coherent manipulation of single spins in semiconductors*, Nature **453**(7198), 1043–1049 (2008).

[Har00] A. Hartmann, Y. Ducommun, E. Kapon, U. Hohenester, and E. Molinari, *Few-Particle Effects in Semiconductor Quantum Dots: Observation of Multicharged Excitons*, Phys. Rev. Lett. **84**(24), 5648–5651 (2000).

[Har06] J. Harrison, M.J. Sellars, and N.B. Manson, *Measurement of the optically induced spin polarisation of N-V centres in diamond*, Diamond Related Mater. **15**(4-8), 589–588 (2006).

[Haw98] P. Hawrylak and A. Wojs, *Quantum Dots*. Springer-Verlag, Berlin, (1998).

[Haw03] P. Hawrylak and M. Korkusinski, *Electronic Properties of Self-Assembled Quantum Dots in in Single Quantum Dots: Fundamentals, Applications, and New Concepts*, Topics in Applied Physics, edited by P. Michler, Springer Verlag Berlin Heidelberg **90**, 25–92 (2003).

[Hei27] Werner Heisenberg, *Über den anschaulichen Inhalt der quantentheoretischen Kinematik und Mechanik*, Zeitschrift für Physik **43**(3), 172–198 (1927).

[Hei97] R. Heitz, M. Veit, N. N. Ledentsov, A. Hoffmann, D. Bimberg, V. M. Ustinov, P. S. Kopev, and Z. I. Alferov, *Energy relaxation by multiphonon processes in InAs/GaAs quantum dots*, Physical Review B **56**(16), 10435–10445 (1997).

[Hei08a] D. Heiss, V. Jovanov, M. Bichler, G. Abstreiter, and J. J. Finley, *Charge and spin readout scheme for single self-assembled quantum dots*, Phys. Rev. B **77**(23), 235442 (2008).

[Hei08b] D. Heiss, S. Schaeck, H. Huebl, M. Bichler, G. Abstreiter, J.J. Finley, D.V. Bulaev, and D. Loss, *Observation of extremely slow hole spin relaxation in self-assembled quantum dots*, Phys. Rev. B **76**(24), 241306 (2008).

[Hei09a] D. Heiss, *Spin storage in Quantum Dot Ensembles and Single Quantum Dots*. Ph.D. Thesis, Walter Schottky Institut, Technische Universität München, (2009).

[Hei09b] D. Heiss, V. Jovanov, M. Caesar, M. Bichler, G. Abstreiter, and J.J. Finley, *Selective optical charge generation, storage, and readout in a single self-assembled quantum dot*, Appl. Phys. Lett. **94**(7), 072108 (2009).

[Hei10] D. Heiss, V. Jovanov, F. Klotz, D. Rudolph, M. Bichler, G. Abstreiter, M.S. Brandt, and J. J. Finley, *Optically monitoring electron spin relaxation in a single quantum dot using a spin memory device*, Phys. Rev. B **82**(24), 245316 (2010).

[Her64] C. Hermite, *Sur un nouveau développment en série de fonctions*, C. R Acad. Sci. Paris **58**, 93–100 (1864).

[Hoe04] A. Hoegele, S. Seidl, M. Kroner, K. Karrai, R.J. Warburton, B.D. Gerardot, and P.M. Petroff, *Voltage-Controlled Optics of a Quantum Dot*, Phys. Rev. Lett. **93**(21), 217401 (2004).

[Hoe12] A. Hoegele, M. Kroner, C. Latta, M. Claassen, I. Carusotto, C. Bulutay, and A. Imamoğlu, *Dynamic Nuclear Spin Polarization in the Resonant Laser Excitation of an InGaAs Quantum Dot*, Phys. Rev. Lett. **108**(19), 197403 (2012).

[Hsu01] T.M. Hsu, W.-H. Chang, C.C. Huang, N.T. Yeh, and J.-I. Chyi, *Quantum-confined Stark shift in electroreflectance of InAs/$In_xGa_{1-x}As$ self-assembled quantum dots*, Applied Physics Letters **78**(12), 1760–1762 (2001).

[H.Y54] Carr H.Y. and E.M. Purcell, *Effects of Diffusion on Free Precession in Nuclear Magnetic Resonance Experiments*, Physical Review **94**(3), 630–638 (1954).

[Ima03] A. Imamoğlu, E. Knill, L. Tian, and P. Zoller, *Optical Pumping of Quantum-Dot Nuclear Spins*, Phys. Rev. Lett. **91**(1), 017402 (2003).

[Ivc97] E.L. Ivchenkoa, A.A. Kiseleva, and M. Willanderb, *Electronic g factor in biased quantum wells*, Solid State Communications **102**(5), 375–378 (1997).

[Jel04] F. Jelezko, T. Gaebel, I. Popa, A. Gruber, and J. Wrachtrup, *Observation of Coherent Oscillations in a Single Electron Spin*, Phys. Rev. Lett. **92**(7), 076401 (2004).

[Jia01] H.W. Jiang and E. Yablonovitch, *Gate-controlled electron spin resonance in* $GaAs/Al_xGa_{1-x}As$ *heterostructures*, Phys. Rev. B **64**(4), 041307 (2001).

[Joh05] A.C. Johnson, J.R. Petta, J.M. Taylor, A. Yacoby, M.D. Lukin, C.M. Marcus, M.P. Hanson, and A.C. Gossard, *Triplet-singlet spin relaxation via nuclei in a double quantum dot*, Nature (London) **435**(7044), 925–928 (2005).

[Jov10] V. Jovanov, *private communications* (2010).

[Jov11] V. Jovanov, T. Eissfeller, S. Kapfinger, E.C. Clark, F. Klotz, M. Bichler, J.G. Keizer, P.M Koenraad, G. Abstreiter, and J.J. Finley, *Observation and explanation of strong electrically tunable exciton g factors in composition engineered In(Ga)As quantum dots*, Phys. Rev. B **83**(16), 161303 (2011).

[Jov12a] V. Jovanov. Ph.D. Thesis, Walter Schottky Institut, Technische Universität München, (2012).

[Jov12b] V. Jovanov, T. Eissfeller, S. Kapfinger, E. C. Clark, F. Klotz, M. Bichler, J. G. Keizer, P. M. Koenraad, M.S. Brandt, G. Abstreiter, and J. J. Finley, *Highly nonlinear excitonic Zeeman spin splitting in composition-engineered artificial atoms*, Phys. Rev. B **85**(16), 165433 (2012).

[Jov12c] V. Jovanov, S. Kapfinger, M. Bichler, G. Abstreiter, and J.J. Finley, *Direct observation of metastable hot trions in an individual quantum dot*, Phys. Rev. B **84**(23), 235321 (2012).

[Kan98] B.E. Kane, *A silicon-based nuclear spin quantum computer*, Nature **393**(6681), 133–137 (1998).

[Kap78] D. Kaplan, I. Solomon, and N.F. Mott, *Explanation of large spin-dependent recombination effect in semiconductors*, J. Phys. (Paris) Lett. **39**(4), L51–L54 (1978).

[Kap11] S. Kapfinger, *Spin Physics in Single Self-Assembled Quantum Dots*. Diploma Thesis, Walter Schottky Institut, Technische Universität München, (2011).

[Kat03] Y. Kato, R. C. Myers, D. C. Driscoll, A. C. Gossard, J. Levy, and D. D. Awschalom, *Gigahertz Electron Spin Manipulation Using Voltage-Controlled g-Tensor Modulation*, Science **299**(5610), 1201–1204 (2003).

[Kaw97] G. Kawachi, C.F.O. Graeff, M.S. Brandt, and M. Stutzmann, *Saturation measurements of electrically detected magnetic resonance in hydrogenated amorphous silicon based thin-film transistors*, Jpn. J. Appl. Phys. **36**(1A), 121–125 (1997).

[Keg01] I. Kegel, T. H. Metzger, A. Lorke, J. Peisl, J. Stangl, G. Bauer, K. Nordlund, W. V. Schoenfeld, and P. M. Petroff, *Determination of strain fields and composition of self-organized quantum dots using x-ray diffraction*, Phys. Rev. B **63**(3), 035318 (2001).

[Kei10] J.G. Keizer, E.C. Clark, M. Bichler, G. Abstreiter, J.J. Finley, and P.M. Koenraad, *An atomically resolved study of InGaAs quantum dot layers grown with an indium flush step*, Nanotechnology **21**(21), 215705 (2010).

[Kes90] H. W. van Kesteren, E. C. Cosman, W. A. J. A. van der Poel, and C. T. Foxon, *Fine structure of excitons in type-II GaAs/AlAs quantum wells*, Phys. Rev. B **41**(8), 5283–5292 (1990).

[Kes10] E.M. Kessler, S. Yelin, M.D. Lukin, J.I. Cirac, and G. Giedke, *Optical Superradiance from Nuclear Spin Environment of Single Photon Emitters*, Phys. Rev. Lett. **104**(14), 143601 (2010).

[Kes12] E.M. Kessler, *Generalized Schrieffer-Wolff Formalism for Dissipative Systems*, arXiv:1205.5440v1 (2012).

[Kha01] A.V. Khaetskii and Y.V. Nazarov, *Spin-flip transitions between Zeeman sublevels in semiconductor quantum dots*, Phys. Rev. B **64**(12), 125316 (2001).

[Kha02] A.V. Khaetskii and L. Loss, D.and Glazman, *Electron spin decoherence in quantum dots due to interaction with nuclei*, Phys. Rev. Lett. **88**(18), 186802 (2002).

[Kie10] J. Kierig, *Dynamic Nuclear Polarisation in a Single Selfassembled Quantum Dot*. Diploma Thesis, Walter Schottky Institut, Technische Universität München, (2010).

[Kim02] S. Kim, S. Jeong, Y.T. Lee, D.H. Kim, J.S. Lim, K.S. Seo, and S. Nam, *Ultra-wideband (from DC to 110GHz) CPW to CPS transition*, Electronics Letters **38**(13), 622–623 (2002).

[Kim09] D. Kim, W. Sheng, P.J. Poole, D. Dalacu, J. Lefebvre, J. Lapointe, M.E. Reimer, G.C. Aers, and R. A.L. Williams, *Tuning the exciton g factor in single InAs/InP quantum dots*, Phys. Rev. B **79**(4), 045310 (2009).

[Kis98] A.A. Kiselev, E.L. Ivchenko, and U. Rössler, *Electron g factor in one- and zero-dimensional semiconductor nanostructures*, Phys. Rev. B **58**(24), 16353–16359 (1998).

[Kla06] D. Klauser, W.A. Coish, and D. Loss, *Nuclear spin state narrowing via gatecontrolled Rabi oscillations in a double quantum dot*, Phys. Rev. B **73**(20), 205302 (2006).

[Kle09] N. A. J. M. Kleemans, J. van Bree, M. Bozkurt, P. J. van Veldhoven, P. A. Nouwens, R. Nötzel, A. Yu. Silov, P. M. Koenraad, and M. E. Flatté, *Size-dependent exciton g factor in self-assembled InAs/InP quantum dots*, Phys. Rev. B **79**(4), 045311 (2009).

[Klo10a] F. Klotz, V. Jovanov, J. Kierig, E. Clark, G. Bichler, M. Abstreiter, H. Schwager, G. Giedke, M.S. Brandt, and J.J. Finley, *Asymmetric optical nuclear spin pumping in a single uncharged quantum dot*, Phys. Rev. B. **82**(12), 121307(R) (2010).

[Klo10b] F. Klotz, V. Jovanov, J. Kierig, E.C. Clark, D. Rudolph, D. Heiss, G. Bichler, M. Abstreiter, M.S. Brandt, and J.J. Finley, *Observation of an electrically tunable exciton g factor in InGaAs/GaAs quantum dots*, Appl. Phys. Lett. **96**(5), 053113 (2010).

[Klo11a] C. Kloeffel, P.A. Dalgarno, B. Urbaszek, B.D. Gerardot, D. Brunner, P.M. Petroff, D. Loss, , and R.J. Warburton, *Controlling the interaction of electron and nuclear spins in a tunnel-coupled quantum dot*, Phys. Rev. Lett **106**(4), 046802 (2011).

[Klo11b] F. Klotz, H. Huebl, D. Heiss, K. Klein, J.J. Finley, and M. S. Brandt, *Coplanar stripline antenna design for optically detected magnetic resonance on semiconductor quantum dots*, Rev. Sci. Instrum. **82**(7), 074707 (2011).

[Klo12] F. Klotz, V. Jovanov, J. Kierig, P.-L. Ardelt, , G. Bichler, M. Abstreiter, H. Schwager, G. Giedke, M.S. Brandt, and J.J. Finley, *A comprehensive experimental and theoretical study of asymmetric optical nuclear spin pumping in single neutral InGaAs quantum dots*, in course of prepration (2012).

[Kni49] W.D. Knight, *Nuclear magnetic resonance shifts in metals*, Phys. Rev. **76**(8), 1259–1260 (1949).

[Kni01] E. Knill, R. Laflamme, and G.J. Milburn, *A scheme for efficient quantum computation with linear optics*, Nature **409**(6816), 46–52 (2001).

[Koe09] T. Koeppen, D. Franz, A. Schramm, C. Heyn, D. Heitmann, and T. Kipp, *Resonant Raman Transitions into Singlet and Triplet States in InGaAs Quantum Dots Containing Two Electrons*, Phys. Rev. Lett **103**(3), 037402 (2009).

[Kog04] A. Kogan, S. Amasha, D. Goldhaber-Gordon, G. Granger, M. A. Kastner, and H. Shtrikman, *Measurements of Kondo and Spin Splitting in Single-Electron Transistors*, Phys. Rev. Lett. **93**(16), 166602 (2004).

[Kom08] Y. Komijani, M. Csontos, T. Ihn, K. Ensslin, D. Reuter, and A. D. Wieck, *Observation of excited states in a p-type GaAs quantum dot*, EPL **84**(5), 57004 (2008).

[Kon06] G. Konstantatos, I. Howard, A. Fischer, S. Hoogland, J. Clifford, E. Klem, L. Levina, and E.H. Sargent, *Ultrasensitive solution-cast quantum dot photodetectors*, Nature **442**(7099), 180–183 (2006).

[Kop05] F.H.L. Koppens, J.A. Folk, J.M. Elzerman, R. Hanson, L.H.W. van Beveren, I.T. Vink, H.P. Tranitz, W. Wegscheider, L.P. Kouwenhoven, and L.M.K. Vandersypen, *Control and detection of singlet-triplet mixing in a random nuclear field*, Science **309**(5739), 1346–1350 (2005).

[Kop06] F. H. L. Koppens, C. Buizert, K. J. Tielrooij, I. T. Vink, K. C. Nowack, T. Meunier, L. P. Kouwenhoven, and L. M. K. Vandersypen, *Driven coherent oscillations of a single electron spin in a quantum dot*, Nature **442**(7104), 766–771 (2006).

[Kop08] F. H. L. Koppens, K. C. Nowack, and L. M. K Vandersypen, *Spin echo of a single electron spin in a quantum dot*, Phys. Rev. Lett. **100**(23), 236802 (2008).

[Kor99] V.L. Korenev, *Dynamic self-polarization of nuclei in low-dimensional systems*, JETP Lett. **70**(20), 129–134 (1999).

[Kor07] V.L. Korenev, *The Nuclear Spin Nanomagnet*, Phys. Rev. Lett. **99**(25), 256405 (2007).

[Kot01] R. Kotlyar, T.L. Reinecke, M. Bayer, and A. Forchel, *Zeeman spin splittings in semiconductor nanostructures*, Phys. Rev. B **63**(8), 085310 (2001).

[Kou91] L. P. Kouwenhoven, A. T. Johnson, N. C. van der Vaart, C. J. P. M. Harmans, and C. T. Foxon, *Quantized current in a quantum-dot turnstile using oscillating tunnel barriers*, Phys. Rev. Lett. **67**(12), 1626–1629 (1991).

[Kow06] K. Kowalik, O. Krebs, P. Senellart, A. LemaÃ®tre, B. Eble, A. Kudelski, J. Gaj, and P. Voisin, *Stark spectroscopy of Coulomb interactions in individual InAs/GaAs self-assembled quantum dots*, Phys. Stat. Sol. C **3**(11), 3890 – 3894 (2006).

[Kow07] K. Kowalik, O. Krebs, A. LemaÃ®tre, B. Eble, A. Kudelski, P. Voisin, S. Seidl, and J. A. Gaj, *Monitoring electrically driven cancellation of exciton fine structure in a semiconductor quantum dot by optical orientation*, Applied Physics Letters **91**(18), 183104 (2007).

[Kra26] H.A. Kramers, *Wellenmechanik und halbzählige Quantisierung*, Zeitschriftür Physik A - Hadrons and Nuclei **39**(10), 828–840 (1926).

[Kre05a] H. Krenner, *Coherent Quantum Coupling of Excitons in Single Quantum Dots and Quantum Dot Molecules*. Ph.D. Thesis, Walter Schottky Institut, Technische Universität München, (2005).

[Kre05b] H.J. Krenner, M. Sabathil, E.C. Clark, A. Kress, D. Schuh, M. Bichler, G. Abstreiter, and J.J. Finley, *Direct Observation of Controlled Coupling in an Individual Quantum Dot Molecule*, Phys. Rev. Lett. **94**(5), 057402 (2005).

[Kre05c] H.J Krenner, S. Stufler, M. Sabathil, E.C. Clark, P. Ester, M. Bichler, G. Abstreiter, J.J. Finley, and A. Zrenner, *Recent advances in exciton-based quantum information processing in quantum dot nanostructures*, New Journal of Physics **7**(1), 184 (2005).

[Kre05d] A. Kress, F. Hofbauer, N. Reinelt, M. Kaniber, H. J. Krenner, R. Meyer, G. Bohm, and J. J. Finley, *Manipulation of the spontaneous emission dynamics of quantum dots in two-dimensional photonic crystals*, Physical Review B **71**(24), 241304 (2005).

[Kro03] M. Kroutvar, Y. Ducommun, J. J. Finley, M. Bichler, G. Abstreiter, and A. Zrenner, *Wavelength selective charge storage in self-assembled InGaAs/GaAs quantum dots*, Applied Physics Letter **83**(3), 443–445 (2003).

[Kro04] M. Kroutvar, Y. Ducommun, D. Heiss, M. Bichler, D. Schuh, G. Abstreiter, and J. J. Finley, *Optically programmable electron spin memory using semiconductor quantum dots*, Nature **432**(7013), 81–84 (2004).

[Kro08a] M. Kroner, *Resonant photon-exciton interaction in semiconductor quantum dots*. Ph.D. Thesis, Ludwig-Maximilans-München, (2008).

[Kro08b] M. Kroner, K. M. Weiss, B. Biedermann, S. Seidl, S. Manus, A. W. Holleitner, A. Badolato, P. M. Petroff, B. D. Gerardot, R. J. Warburton, and K. Karrai, *Optical detection of single-electron spin resonance in a quantum dot*, Phys. Rev. Lett. **100**(15), 156803 (2008).

[Kro12] M. Kroner, *private communications* (2012).

[Kul99] V.D. Kulakovskii, G. Bacher, R. Weigand, T. Kümmell, A. Forchel, E. Borovitskaya, K. Leonardi, and D. Hommel, *Fine structure of biexciton emission in symmetric and asymmetric CdSe/ZnSe single quantum dots*, Phys. Rev. Lett. **82**(8), 1780–1783 (1999).

[Kuo00] D.M.-T. Kuo and Y.C. Chang, *Electron tunneling rate in quantum dots under a uniform electric field*, Phys. Rev. B **61**(16), 11051–11056 (2000).

[Kut98] A. Kuther, M. Bayer, A. Forchel, A. Gorbunov, V. B. Timofeev, F. Schäfer, and J. P. Reithmaier, *Zeeman splitting of excitons and biexcitons in single In0.60Ga0.40As/GaAs self-assembled quantum dots*, Phys. Rev. B (R) **58**(11), 7508–7511 (1998).

[Kwa12] J. Kwak, W.K. Bae, D. Lee, I. Park, J. Lim, M. Park, H. Cho, H. Woo, D.Y. Yoon, K. Char, S. Lee, and C. Lee, *Bright and Efficient Full-Color Colloidal Quantum Dot Light-Emitting Diodes Using an Inverted Device Structure*, Nano Lett. **12**(5), 2362–2366 (2012).

[Lad10] T. D. Ladd, F. Jelezko, R. Laflamme, Y. Nakamura, C. Monroe, and J. L. O'Brien, *Quantum computers*, Nature **464**(7285), 45–53 (2010).

[Lai06] C.W. Lai, P. Maletinsky, A. Badolato, and A. Imamoğlu, *Knight-Field-Enabled Nuclear Spin Polarization in Single Quantum Dots*, Phys. Rev. Lett. **96**(16), 167403 (2006).

[Lan04] W. Langbein, P. Borri, U. Woggon, V. Stavarache, D. Reuter, and A.D. Wieck, *Control of fine-structure splitting and biexciton binding in* $In_xGa_{1-x}As$ *quantum dots by annealing*, Physical Review B(R) **69**(16), 161301 (2004).

[Lan07] B.P. Lanyon, T.J. Weinhold, N.K. Langford, M. Barbieri, D.F.V. James, A. Gilchrist, and A.G. White, *Experimental Demonstration of a Compiled Version of Shor's Algorithm with Quantum Entanglement*, Physical Review Letters **99**(25), 250505 (2007).

[Lat09] C. Latta, A. Högele, Y. Zhao, A.N. Vamivakas, P. Maletinsky, M. Kroner, J. Dreiser, I. Carusotto, A. Badolato, D. Schuh, W. Wegscheider, M. Atature, and A. Imamoğlu, *Confluence of resonant laser excitation and bidirectional quantum-dot nuclear-spin polarization*, Nature Physics **5**, 758–763 (2009).

[Lat11] C. Latta, A. Srivastava, and A. Imamoğlu, *Hyperfine Interaction-Dominated Dynamics of Nuclear Spins in Self-Assembled InGaAs Quantum Dots*, Phys. Rev. Lett. **107**(16), 167401 (2011).

[Led96] N.N. Ledentsov, V.A. Shchukin, M. Grundmann, N. Kirstaedter, J. Böhrer, O. Schmidt, D. Bimberg, V.M. Ustinov, A. Yu. Egorov, A.E. Zhukov, P.S. Kop'ev, S.V. Zaitsev, N. Yu. Gordeev, Zh.I. Alferov, A.I. Borovkov, A.O. Kosogov, S.S. Ruvimov, P. Werner, U. Gösele, and J. Heydenreich, *Direct formation of vertically coupled quantum dots in Stranski-Krastanow growth*, Phys. Rev. B **54**(12), 8743–8750 (1996).

[Lem01] A. Lemaître, A.D. Ashmore, J.J. Finley, D.J. Mowbray, M.S. Skolnick, M. Hopkinson, and T.F. Krauss, *Enhanced phonon-assisted absorption in single InAs/GaAs quantum dots*, Phys. Rev. B **63**(16), 161309 (2001).

[Leo93] D. Leonard, M. Krishnamurthy, C.M. Reaves, S.P. Denbaars, and P.M. Petroff, *Direct formation of quantum-sized dots from uniform coherent islands of InGaAs on GaAs surfaces*, Appl. Phys. Lett. **63**(23), 3203–3205 (1993).

[Leo94] D. Leonard, K. Pond, and P.M. Petroff, *Critical layer thickness for self-assembled InAs islands on GaAs*, Phys. Rev. B **50**(16), 11687–11692 (1994).

[Leo95] M. Leon, P. M. Petroff, D. Leonard, and S. Fafard, *Spatially resolved visible luminescence of selfassembled semiconductor quantum dots*, Science **267**(5206), 1966–1968 (1995).

[Lev96] M.E. Levinshtein, S. Rumyantsev, and M. Shur, *Handbook Series on Semiconductor Parameters*. volume 2, pages 77-103, World Scientific, London, (1996).

[Lia98] G.D. Lian, J. Yuan, L.M. Brown, G.H. Kim, and D.A. Ritchie, *Modification of InAs quantum dot structure by the growth of the capping layer*, Applied Physics Letters **73**(1), 49–51 (1998).

[Liu00] N. Liu, J. Tersoff, O. Baklenov, A. L. Holmes, and C. K. Shih, *Nonuniform Composition Profile in* $In_{0.5}Ga_{0.5}As$ *Alloy Quantum Dots*, Phys. Rev. Lett. **84**(2), 334–337 (2000).

[Lom85] G. Lommer, F. Malcher, and U. Rössler, *Reduced g factor of subband Landau levels in AlGaAs/GaAs heterostructures*, Phys. Rev. B **32**(10), 6965–6967 (1985).

[Los98] D. Loss and D. P. DiVincenzo, *Quantum computation with quantum dots*, Phys. Rev. A **57**(1), 120–126 (1998).

[Lou73] Rodney Loudon, *The quantum theory of light*. Oxford University Press, Oxfod, (1973).

[Lu07] C.-Y. Lu, D.E. Browne, T. Yang, and J.-W. Pan, *Demonstration of a Compiled Version of Shor's Quantum Factoring Algorithm Using Photonic Qubits*, Physical Review Letters **99**(25), 250504 (2007).

[Mad87] O. Madelung, W. von der Osten, and U. Rössler, *Intrinsic Properties of Group IV Elements and III-V, II-VI and I-VII Compunds*, volumeofa *Landolt-Börnstein: Numerical Data and Functional Relationships in Science and Technology - New Series, Group3: Condensed Matter, Subseries: Semiconductors*. Springer-Verlag, Berlin, (1987).

[Mai12] A.D.B. Maia, E.C.F. da Silva, A.A. Quivy, V. Bindilatti, V.M. de Aquino, and I.F.L Dias, *The influence of different indium-composition profiles on the electronic structure of lens-shaped $In_xGa_{1-x}As$ quantum dots*, J. Phys. D: Appl. Phys. **45**(22), 225104 (2012).

[Mak08a] M.N. Makhonin, K.V. Kavokin, P. Senellart, A. Lemaitre, A.J. Ramsay, M.S. Skolnick, and A.I. Tartakovskii, *Long nuclear spin polarization decay times controlled by optical pumping in individual quantum dots*, Phys. Rev. B **77**(12), 125307 (2008).

[Mak08b] M.N. Makhonin, A.I. Tartakovskii, A. Ebbens, M.S. Skolnick, A. Russell, V.I. Fal'ko, and M. Hopkinson, *Nuclear spin pumping under resonant optical excitation in a quantum dot*, Appl. Phys. Lett. **93**(7), 073113 (2008).

[Mak10] M.N. Makhonin, E.A. Chekhovich, P. Senellart, A. Lemaitre, M.S. Skolnick, and A.I. Tartakovskii, *Optically tunable nuclear magnetic resonance in a single quantum dot*, Phys. Rev. B **82**(16), 161309 (2010).

[Mak11] M.N. Makhonin, A.I. Tartakovskii, A.B. Van'kov, I. Drouzas, T. Wright, J. Skiba-Szymanska, A. Russell, V.I. Fal'ko, M.S. Skolnick, H.-Y. Liu, , and M. Hopkinson, *Fast control of nuclear spin polarization in an optically pumped single quantum dot*, Nature Materials **10**(11), 844–848 (2011).

[Mal01] A. Malinowski, M.A. Brand, and R.T. Harley, *Nuclear effects in ultrafast quantum-well spin-dynamics*, Physics E **10**(1-3), 13–16 (2001).

[Mal07] P. Maletinsky, A. Badolato, and A. Imamoğlu, *Dynamics of Quantum Dot Nuclear Spin Polarization Controlled by a Single Electron*, Phys. Rev. Lett. **99**(5), 056804 (2007).

[Mal08] P. Maletinsky, *Polarization and Manipulation of a Mesoscopic Nuclear Spin Ensemble Using a Single Confined Electron Spin*. Ph.D. Thesis, ETH Zürich, (2008).

[Mal09] P. Maletinsky, M. Kroner, and A. Imamoğlu, *Breakdown of the nuclear-spin-temperature approach in quantum-dot demagnetization experiments*, Nature Physics **5**(6), 407–411 (2009).

[Mar94] J.Y. Marzin, J.-M. Gerard, A. Izrael, D. Barrier, and G. Bastard, *Photoluminescence of Single InAs Quantum Dots Obtained by Self-Organized Growth on GaAs*, Phys. Rev. Lett. **73**(5), 716–719 (1994).

[Mar02] J.M. Martinis, S. Nam, J. Aumentado, and C. Urbina, *Rabi oscillations in a large Josephson-junction qubit*, Phys. Rev. Lett. **89**(11), 117901 (2002).

[McF09] J. McFarlane, P. A. Dalgarno, B. D. Gerardot, R. H. Hadfield, R. J. Warburton, K. Karrai, A. Badolato, and P. M. Petroff, *Gigahertz bandwidth electrical control over a dark exciton-based memory bit in a single quantum dot*, Applied Physics Letters **94**(9), 093113 (2009).

[Mei84] F. Meier and B.P. Zakharchenya, *Electron spin dynamics in quantum dots and related nanostructures*. Elsevier Science Ltd, Amsterdam, (1984).

[Mer98] I.A Merkulov, *Formation of a nuclear spin polaron under optical orientation in GaAs-type semiconductors*, Phys. Solid State **40**(6), 930–933 (1998).

[Mer02] I.A. Merkulov, A.L. Efros, and M. Rosen, *Electron spin relaxation by nuclei in semiconductor quantum dots*, Phys. Rev. B **65**(20), 205309 (2002).

[Mes61] A. Messiah, *Quantum Mechanics, Volume 1 & 2*. North-Holland Publishing Company, Amsterdam, (1961).

[Mic00] P. Michler, C. Kiraz, A. Becher, W.V. Schoenfeld, P.M. Petroff, E. Lidong Zhang, Hu, and A. Imamoğlu, *A Quantum Dot Single-Photon Turnstile Device*, Science **290**(5500), 2282 – 2285 (2000).

[Mig02] M.A. Migliorato, A.G. Cullis, M. Fearn, and J.H. Jefferson, *Atomistic simulation of strain relaxation in $In_xGa_{1-x}As$ / GaAs quantum dots with nonuniform composition*, Phys. Rev. B **65**(11), 115316 (2002).

[Mil84] D. A. B. Miller, D. S. Chemla, T. C. Damen, A. C. Gossard, W. Wiegmann, T. H. Wood, and C. A. Burrus, *Band-Edge Electroabsorption in Quantum Well Structures: The Quantum-Confined Stark Effect*, Phys. Rev. Lett. **53**(22), 2173–2176 (1984).

[Mir97] R.P. Mirin, I.P. James, J.E. Bowers, and A.C. Gossard, *Overgrowth of InGaAs quantum dots formed by alternating molecular beam epitaxy*, Journal of Crystal Growth **75-176, Part 2**, 696–701 (1997).

[Moh00] P.J. Mohr and B.N. Taylor, *CODATA recommended values of the fundamental physical constants: 1998*, Reviews of Modern Physics **72**(2), 351–495 (2000).

[Moi94] J. M. Moison, F. Houzay, F. Barthe, L. Leprince, E. AndrÃ©, and O. Vatel, *Self-organized growth of regular nanometer-scale InAs dots on GaAs*, Applied Physics Letters **64**(2), 196–198 (1994).

[Mor10] A. Morello, , J.J. Pla, , F.A. Zwanenburg, , K.W. Chan, , K.Y. Tan, , H. Huebl, M. Mottonen, C.D. Nugroho, C. Yang, J.A. van Donkelaar, A.D.C Alves, D.N. Jamieson, C.C. Escott, L.C.L. Hollenberg, R.G. Clark, and A.S. Dzurak, *Single-shot readout of an electron spin in silicon*, Nature **467**(7316), 687–691 (2010).

[Mos09] E.S. Moskalenko, L.A. Larsson, and P.O. Holtz, *Spin polarization of the neutral exciton in a single InAs quantum dot at zero magnetic field*, Phys. Rev. B **80**(19), 193413 (2009).

[Mue10] K. Mueller, *private communications* (2010).

[Mue11] K. Mueller, G. Reithmaier, E. C. Clark, V. Jovanov, M. Bichler, H. J. Krenner, M. Betz, G. Abstreiter, and J. J. Finley, *Excited state quantum couplings and optical switching of an artificial molecule*, Phys. Rev. B **84**(8), 081302 (2011).

[Mue12a] K. Mueller, A. Bechtold, C. Ruppert, M. Zecherle, G. Reithmaier, M. Bichler, H.J. Krenner, G. Abstreiter, A.W. Holleitner, J.M. Villas-Boas, and J.J. Finley, *Electrical control of inter-dot electron tunneling in a quantum dot molecule*, Phys. Rev. Lett. **108**(19), 197402 (2012).

[Mue12b] K. Mueller, F. Klotz, P.-L. Ardelt, A. Waeber, M. Bichler, H. Krenner, M.S. Brandt, G. Abstreiter, and J.J. Finley, *Observation of Coulomb couplings in the optical spectrum of quantum dot molecules*, in course of prepration (2012).

[Nag06] M. Nagy and S.G Akl, *Quantum computation and quantum information*, The International Journal of Parallel, Emergent and Distributed Systems, **21**(1), 1–59 (2006).

[Nak99] Y. Nakamura, Yu.A. Pashkin, and Tsa, *Coherent control of macroscopic quantum states in a single-Cooper-pair box*, Nature **398**(6730), 786–788 (1999).

[Nak04] T. Nakaoka, T. Saito, J. Tatebayashi, and Y. Arakawa, *Size, shape, and strain dependence of the g factor in self-assembled In(Ga)As quantum dots*, Phys. Rev. B **70**(23), 235337 (2004).

[Nak05] T. Nakaoka, T. Saito, J. Tatebayashi, S. Hirose, T. Usuki, N. Yokoyama, and Y. Arakawa, *Tuning of g-factor in self-assembled In(Ga)As quantum dots through strain engineering*, Phys. Rev. B **71**(20), 205301 (2005).

[Nak07] T. Nakaoka, S. Tarucha, and Y. Arakawa, *Electrical tuning of the g factor of single self-assembled quantum dots*, Phys. Rev. B **76**(4), 041301 (2007).

[Nan10] J. Nannen, T. Kümmell, M. Bartsch, K. Brunner, and G. Bacher, *Ultrafast electrical charging and discharging of a single InGaAs quantum dot*, Appl. Phys. Lett. **97**(17), 173108 (2010).

[Nan12] J. Nannen, W. Quitsch, S. Eliasson, T. Kümmell, and G. Bacher, *High-frequency electrical charge and spin control in a single InGaAs quantum dot*, Phys. Rev. B **85**(3), 035325 (2012).

[Neg06] C. Negrevergne, T.S. Mahesh, C.A. Ryan, M. Ditty, F. Cyr-Racine, W. Power, N. Boulant, T. Havel, D.G. Cory, and R. Laflamme, *Benchmarking quantum control methods on a 12-qubit system*, Phys. Rev. Lett. **96**(17), 170501 (2006).

[Nic09] N.A. Nick Vamivakas, Y. Zhao, C.-Y. Lu, and M. Atature, *Spin-resolved quantum-dot resonance fluorescence*, Nature Physics **5**(3), 198–202 (2009).

[Niz04] A.P. Nizovtsev, S.Ya. Kilin, F. Jelezko, T. Gaebal, I. Popa, A. Gruber, and J. Wrachtrup, *A quantum computer based on NV centers in diamond: Optically detected nutations of single electron and nuclear spins*, Optics and Spectroscopy **99**(2), 233–244 (2004).

[Nor96] D.J. Norris and M.G. Bawendi, *Measurement and assignment of the size-dependent optical spectrum in CdSe quantum dots*, Phys. Rev. B **53**(24), 16338–16346 (1996).

[Now07] K.C. Nowack, F.H.L. Koppens, Y.V. Nazarov, and L.M.K. Vandersypen, *Coherent control of a single electron spin with electric fields*, Science **318**(5855), 1430–1433 (2007).

[NSM] *NSM: NSM archive - physical properties of semiconductors, www.ioffe.rssi.ru/ /SVA/NSM/Semicond/ (8^{th} June, 2012)*.

[O'B07] J.L. O'Brien, *Optical quantum computing*, Science **318**(5856), 1567–1570 (2007).

[O'D08] L.A. O'Dell and R.W. Schurko, *QCPMG using adiabatic pulses for faster acquisition of ultra-wideline NMR spectra*, Chemical Physics Letters **464**(1-3), 97–102 (2008).

[Off05] P. Offermans, P.M. Koenraad, J.H. Wolter, K. Pierz, M. Roy, and P.A. Maksym, *Atomic-scale structure and photoluminescence of InAs quantum dots in GaAs and AlAs*, Phys. Rev. B **72**(16), 165332 (2005).

[Ort03] G. Ortner, M. Bayer, A. Larionov, V.B. Timofeev, A. Forchel, Y.B. Lyanda-Geller, T.L. Reinecke, P. Hawrylak, S. Fafard, and Z. Wasilewski, *Fine structure of excitons in InAs/GaAs coupled quantum dots: A sensitive test of electronic coupling*, Phys. Rev. Lett. **90**(8), 086404 (2003).

[Ort04] G. Ortner, M. Schwab, P. Borri, W. Langbein, U. Woggon, M. Bayer, S. Fafard, Z. Wasilewski, P. Hawrylak, Y.B. Lyanda-Geller, T.L. Reinecke, and A. Forchel, *Exciton states in self-assembled InAs/GaAs quantum dot molecules*, Physica E- Low Dimensional Systems & Nanostructures **25**(2-3), 249–260 (2004).

[Osh94] J . Oshinowo, M. Nishioka, S. Ishida, and Y. Arakawa, *Highly uniform InGaAs/GaAs quantum dots ($\sim$ 15 nm) by metalorganic chemical vapor deposition*, Appl. Phys. Lett. **65**(11), 1421–1423 (1994).

[Oul07] R Oulton, A Greilich, S.Yu Verbin, R.V. Cherbunin, T. Auer, D.R. Yakovlev, M. Bayer, I.A. Merkulov, V. Stavarache, D. Reuter, and A.D. Wieck, *Subsecond spin relaxation times in quantum dots at zero applied magnetic field due to a strong electron-nuclear interaction.*, Phys. Rev. Lett. **98**(10), 107401 (2007).

[Ove53] A.W. Overhauser, *Polarization of nuclei in metals*, Phys. Rev. **92**(2), 411–415 (1953).

[Pag77] D. Paget, G. Lampel, B. Sapoval, and V.I. Safarov, *Low Field Electron-Nuclear Spin Coupling in Gallium-Arsenide under Optical-Pumping Conditions*, Phys. Rev. B **15**(12), 5780–5796 (1977).

[Pag82] D. Paget, *Optical-Detection of NMR in High-Purity GaAs - Direct Study of the Relaxation of Nuclei Close to Shallow Donors*, Phys. Rev. B **24**(7), 4444–4451 (1982).

[Pat00] A. Patane, A. Levin, A. Polimeni, F. Schindler, P.C. Main, L. Eaves, and M. Henini, *Piezoelectric effects in $In_{0.5}Ga_{0.5}As$ self-assembled quantum dots grown on (311)B GaAs substrates*, Applied Physics Letters **77**(19), 2979–2981 (2000).

[Pet94] P. M. Petroff and S. P. Denbaars, *MBE and MOCVD Growth and Properties of Self-Assembling Quantum-Dot Arrays in III-V Semiconductor Structures*, Superlattices and Microstructures **15**(1), 15–21 (1994).

[Pet05] J.R. Petta, A.C. Johnson, J.M. Taylor, E.A. E. A. Laird, A. Yacoby, M.D. Lukin, C.M. Marcus, M.P. Hanson, and A.C. Gossard, *Coherent Manipulation of Coupled Electron Spins in Semiconductor Quantum Dots*, Science **309**(5744), 2180 – 2184 (2005).

[Pfe90] L. Pfeiffer, K.W West, H.L. Stormer, J.P. Eisenstein, K.W. Baldwin, D. Gershoni, and J. Spector, *Formation of a high quality two-dimensional electron gas on cleaved GaAs*, Appl. Phys. Lett **56**(17), 1697–1699 (1990).

[Pin08] J. Pingenot, C.E. Pryor, and M.E. Flatté, *Method for full Bloch sphere control of a localized spin via a single electrical gate*, Applied Physics Letters **92**(22), 222502 (2008).

[Pin11] J. Pingenot, C.E. Pryor, and M.E. Flatté, *Electric-field manipulation of the Landé g tensor of a hole in an $In_{0.5}Ga_{0.5}As$/GaAs self-assembled quantum dot*, Phys. Rev. B **84**(19), 195403 (2011).

[Pj25] W. Pauli jr., *Über den Zusammenhang des Abschlusses der Elektronengruppen im Atom mit der Komplexstruktur der Spektren*, Zeitschrift für Physik **31**(10), 765–783 (1925).

[Pol99] A. Polimeni, A. Patanè, M. Henini, L. Eaves, and P.C. Main, *Temperature dependence of the optical properties of* $InAs/Al_yGa_{1-y}As$ *self-organized quantum dots*, Phys. Rev. B **59**(7), 5064–5058 (1999).

[Pol09] A. Politi, J.C.F. Matthews, and J.L. O'Brien, *Shor's quantum factoring algorithm on a photonic chip*, Science **325**(5945), 1221 (2009).

[Poo83] C.P. Poole, *Electron Spin Resonance: A Comprehensive Treatise on Experimental Techniques*. 2nd ed., Wiley, New York, (1983).

[Pot03] R. M. Potok, J. A. Folk, C. M. Marcus, V. Umansky, M. Hanson, and A. C. Gossard, *Spin and Polarized Current from Coulomb Blockaded Quantum Dots*, Phys. Rev. Lett. **91**(1), 016802 (2003).

[Pre10] D. Press, K. De Greve, P. L. McMahon, T. D. Ladd, B. Friess, C. Schneider, M. Kamp, S. Hofling, A. Forchel, , and Y. Yamamoto, *Ultrafast optical spin echo in a single quantum dot*, Nature Photonics **4**(6), 367–370 (2010).

[Pry98] C. Pryor, *Eight-band calculations of strained InAs/GaAs quantum dots compared with one-, four-, and six-band approximations*, Phys. Rev. B **57**(12), 7190–7195 (1998).

[Pry06] C.E. Pryor and M.E. Flatté, *Lande g factors and orbital momentum quenching in semiconductor quantum dots*, Phys. Rev. Lett **96**(2), 026804 (2006).

[Ram08] C. Ramanathan, *Dynamic nuclear polarization and spin diffusion in nonconducting solids*, Applied magnetic resonance **34**(3-4), 409–421 (2008).

[Rea94] C.M. Reaves, V. Bresslerhill, M. Krishnamurthy, S. Varma, P.M. Petroff, W.H. Weinberg, and S.P. DenBaars, *InP islands on GaAs substrates - MOCVD growth of quantum-sized structures*, IEEE 6th International Conference on Indium Phosphide and Related Materials: Conferenence Proceedings, 611-614 (1994).

[Ree86] M.A. Reed, R.T. Bate, K. Bradshaw, M.W. Duncan, W.R. Frensley, J.W. Lee, and H.D. Shih, *Spatial quantization in GaAs/AlGaAs multiple quantum dots*, Journal of Vacuum Science & Technology B **4**(1), 358–360 (1986).

[Ree88] M. A. Reed, J. N. Randall, R. J. Aggarwal, R. J. Matyi, T. M. Moore, and A. E. Wetsel, *Observation of discrete electronic states in a zero-dimensional semiconductor nanostructure*, Phys. Rev. Lett. **60**(6), 535–537 (1988).

[Rei08] D.J. Reilly, J.M. Taylor, J.R. Petta, C.M. Marcus, M.P. Hanson, and A.C. Gossard, *Suppressing Spin Qubit Dephasing by Nuclear State Preparation*, Science **321**(5890), 817–821 (2008).

[Rie08] J.H.H. Rietjens, G.W.W. Quax, C.A.C. Bosco, R. Nötzel, A.Y. Silvo, and B. Koopmans, *Optical control over electron g factor and spin decoherence in (In,Ga)As/GaAs quantum dots*, J. Appl. Phys **103**(7), 07B116 (2008).

[Ros83] R. Rossetti, S. Nakahara, and L.E. Brus, *Quantum Size Effects in the Redox Potentials, Resonance Raman Spectra, and Electronic Spectra of CdS Crystallites in Aqueous Solutions*, J. Chem. Phys. **79**(2), 1086–1088 (1983).

[Rot59] L.M. Roth, B. Lax, and S. Zwerdling, *Theory of Optical Magneto-Absorption Effects in Semiconductors*, Phys. Rev. **114**(1), 90–104 (1959).

[Rud09] D. Rudolph, *Optical Spin Storage and Readout in a Single Self-assembled Quantum Dot*. Diploma Thesis, Walter Schottky Institut, Technische Universität München, (2009).

[Sal01] G. Salis, Y. Kato, K. Ensslin, D. C. Driscoll, A. C. Gossard, and D. D Awschalom, *Electrical control of spin coherence in semiconductor nanostructures*, Nature **414**(6864), 619–622 (2001).

[San00] S. Sanguinetti, M. Gurioli, E. Grilli, M. Guzzi, and M. Henini, *Piezoelectric effects in InAs/GaAs(N11) self-assembled quantum dots*, Thin Solid Films **380**(1-2), 198–200 (2000).

[Sch83] W.J. Schaffer, M.D. Lind, S.P. Kowalczyk, and R.W. Grant, *Nucleation and strain relaxation at the InAs/GaAs(100) heterojunction*, Journal of Vacuum Science and Technology B **1**(3), 688–695 (1983).

[Sch97] G. Schedelbeck, W. Wegscheider, M. Bichler, and G. Abstreiter, *Coupled Quantum Dots Fabricated by Cleaved Edge Overgrowth: From Artificial Atoms to Molecules*, Science **278**(5344), 1792–1795 (1997).

[Sch98a] K. H. Schmidt, U. Kunze, G. Medeiros-Ribeiro, J. M. Garcia, P. Wellmann, and P. M. Petroff, *Field dependent carrier dynamics and charged excitons in InAs self-assembled quantum dots*, Physica E: Low-dimensional Systems and Nanostructures **2**(1-4), 627–631 (1998).

[Sch98b] K. H. Schmidt, G. Medeiros-Ribeiro, and P. M. Petroff, *Photoluminescence of charged InAs self-assembled quantum dots*, Phys. Rev. B **58**(7), 3597–3600 (1998).

[Sch03] J. Schliemann, A. Khaetskii, and D. Loss, *Electron spin dynamics in quantum dots and related nanostructures due to hyperfine interaction with nuclei*, J. Phys.: Condens. Matter **15**(50), 1809–1833 (2003).

[Sch07] D. Schroer, A.D. Greentree, L. Gaudreau, K. Eberl, L.C.L. Hollenberg, J.P. Kotthaus, and S. Ludwig, *Electrostatically defined serial triple quantum dot charged with few electrons*, Phys. Rev. B **76**(7), 075306 (2007).

[Sch08] M. Scheibner, M. Yakes, A.S. Bracker, I.V. Ponomarev, M.F. Doty, C.S. Hellberg, L.J. Whitman, T.L. Reinecke, and D. Gammon, *Optically mapping the electronic structure of coupled quantum dots*, Nature Physics **4**(4), 291–295 (2008).

[She07] W. Sheng and A. Babinski, *Zero g factors and nonzero orbital momenta in self-assembled quantum dots*, Phys. Rev. B **75**(3), 033316 (2007).

[She08] W. Sheng, S. J. Xu, and Pawel Hawrylak, *Electron g-factor distribution in self-assembled quantum dots*, Phys. Rev. B **77**(24), 241307 (2008).

[She09] W. Sheng, *Electrical tuning of exciton g factors in quantum dot molecules: Effect of hole localization*, Appl. Phys. Lett. **95**(11), 113105 (2009).

[She10] W. Sheng, *g-factor tuning in self-assembled quantum dots*, Appl. Phys. Lett. **96**(13), 133102 (2010).

[Sho94] P. Shor, *Proc. 35th Annu. Symp. on the Foundations of Computer Science (ed. Goldwasser)*. IEEE Computer Society Press, Los Alamitos, California, (1994).

[Sho97] P. Shor, *Polynomial-time algorithms for prime factorization and discrete logarithms on a quantum computer*, SIAM J. Comput. **26**(5), 1484–1509 (1997).

[Shu01] J. Shumway, A. J. Williamson, A. Zunger, A. Passaseo, M. DeGiorgi, R. Cingolani, M. Catalano, and P. Crozier, *Electronic structure consequences of In/Ga composition variations in self-assembled $In_xGa_{1-x}As/GaAs$ alloy quantum dots*, Physical Review B **6412**(12), 125302 (2001).

[Sie05] R. Siegel, T.T. Nakashima, and R.E. Wasylishen, *Sensitivity enhancement of NMR spectra of half-integer quadrupolar nuclei in the solid state via population transfer*, Concepts in Magnetic Resonance Part A **26A**(2), 47–61 (2005).

[Sim51] A. Simon, M.E. Rose, and J.M. Jauch, *Polarization and alignement of nuclei*, Phys. Rev. **84**(6), 1155–1159 (1951).

[Sli80] C.P. Slichter, *Principles of Magnetic Resonance*. Springer-Verlag, Berlin, (1980).

[Sne92] M.J. Snelling, E. Blackwood, C.J. McDonagh, R.T. Harley, and C.T.B. Foxon, *Exciton, heavy-hole, and electron g factors in type-I $GaAsAl_xGa_{1-x}As$ quantum wells*, Phys. Rev. B **45**(7), 3922–3925 (1992).

[Sol77] I. Solomon, D. Biegelsen, and J.C. Knights, *Spin-dependent photoconductivity in n-type and p-type amorphous silicon*, Solid State Comm. **22**(8), 505–508 (1977).

[Sol95a] G.S. Solomon, J.A. Trezza, and J.S. Harris Jr., *Effects of monolayer coverage, flux ratio, and growth-rate on the island density of InAs Islands on GaAs*, App. Phys. Lett. **66**(23), 3161–3163 (1995).

[Sol95b] G.S. Solomon, J.A. Trezza, and J.S. Harris Jr., *Substrate-temperature and monolayer coverage effects on epitaxial ordering of InAs and InGaAs islands on GaAs*, App. Phys. Lett. **66**(8), 991–993 (1995).

[Sol96] G. S. Solomon, J. A. Trezza, A. F. Marshall, and J. S. Harris, *Vertically aligned and electronically coupled growth induced InAs islands in GaAs*, Physical Review Letters **76**(6), 952–955 (1996).

[Sou99] J. Soubusta, R. Grill, P. Hlídek, M. Zvàra, L. Smrča, S. Malzer, W. Geißelbrecht, and G. H. Döhler, *Excitonic photoluminescence in symmetric coupled double quantum wells subject to an external electric field*, Phys. Rev. B **60**(11), 7740–7743 (1999).

[Sta04] J. Stangl, V. Holy, and G. Bauer, *Structural properties of self-organized semiconductor nanostructures*, Reviews of Modern Physics **76**(3), 725 (2004).

[Ste06] R.M. Stevenson, R.J. Young, P. Atkinson, K. Cooper, D.A. Ritchie, and A.J. Shields, *A semiconductor source of triggered entangled photon pairs*, Nature **439**(7073), 179–182 (2006).

[Sti99] O. Stier, M. Grundmann, and D. Bimberg, *Electronic and optical properties of strained quantum dots modeled by 8-band k·p theory*, Phys. Rev. B **59**(8), 5688–5701 (1999).

[Sti06] E.A. Stinaff, M. Scheibner, A.S. Bracker, I.V. Ponomarev, V.L. Korenev, M.E. Ware, M.F. Doty, T.L. Reinecke, and D. Gammon, *Optical signatures of coupled quantum dots*, Science **311**(5761), 636–639 (2006).

[Str37] I.N. Stranski and L. Krastanow, *Zur Theorie der orientierten Ausscheidung von Ionenkristallen aufeinander*, Monatshefte Für Chemie **146**(1), 351–364 (1937).

[Str38] I.N. Stranski and L. Krastanow, *Zur Theorie der orientierten Ausscheidung von Ionenkristallen aufeinander*, Sitzungsberichte der Akademie der Wissenschaften Wien, Mathematisch-naturwissenschaftliche Klasse, Abteilung IIb **146**, 797–810 (1938).

[Str82] R.A. Street, *Spin-dependent photoconductivity in undoped a-Si-H*, Phil. Mag. B **46**(3), 273–278 (1982).

[Stu86] M. Stutzmann and D.K. Biegelsen, *Electron-nuclear double-resonance experiments in hydrogenated amorphous-silicon*, Phys. Rev. B **34**(5), 3093–3107 (1986).

[Stu89] M. Stutzmann and D.K. Biegelsen, *Microscopic nature of coordination defects in amorphous-silicon*, Phys. Rev. B **40**(14), 9834–9840 (1989).

[Sze06] S.M. Sze and K.K. Ng, *Physics of Semiconductor Devices*. 3rd ed., John Wiley & Sons, New Jersey, (2006).

[Tan08] J.A. Tang, L.A. O'Dell, P.M. Aguiar, B.E. Lucier, D. Sakellariou, and R. W Schurko, *Application of static microcoils and WURST pulses for solid-state ultra-wideline NMR spectroscopy of quadrupolar nuclei*, Chemical Physics Letters **466**(4-6), 227–234 (2008).

[Tar04] A. I. Tartakovskii, J. Cahill, M. N. Makhonin, D. M. Whittaker, J.-P. R. Wells, A. M. Fox, D. J. Mowbray, M. S. Skolnick, K. M. Groom, M. J. Steer, and M. Hopkinson, *Dynamics of Coherent and Incoherent Spin Polarizations in Ensembles of Quantum Dots*, Phys. Rev. Lett. **93**(5), 057401 (2004).

[Tar07] A.I. Tartakovskii, T. Wright, A. Russell, A.B. Fal'ko, Van'kov, J. Skiba-Szymanska, I. Drouzas, R.S. Kolodka, M.S. Skolnick, P.W. Fry, H.Y. Tahraoui, Liu, and M. Hopkinson, *Nuclear spin switch in semiconductor quantum dots*, Phys. Rev. Lett. **98**(2), 026806 (2007).

[Tay03] J.M. Taylor, C.M. Marcus, and M.D. Lukin, *Long-lived memory for mesoscopic quantum bits*, Phys. Rev. Lett. **90**(20), 206803 (2003).

[Tes08] C. Testelin, E. Aubry, B. Eble, F. Bernardot, M. Chamarroa, and A. Lemaître, *Anisotropy of the electron Lande g factor in InAs/GaAs self-assembled quantum dots*, Physica E **40**(6), 2072–2074 (2008).

[Tes09] C. Testelin, F. Bernardot, B. Eble, and M. Chamarro, *Hole-spin dephasing time associated with hyperfine interaction in quantum dots*, Phys. Rev. B **79**(19), 195440 (2009).

[Tip91] P.A. Tipler, *Physics for Scientists and Engineers, Third edition, Extended Version*. Worth Publishers Inc., New York, (1991).

[Tra95] N. J. Traynor, R. T. Harley, and R. J. Warburton, *Zeeman splitting and g factor of heavy-hole excitons in $In_xGa_{1-x}As$/GaAs quantum wells*, Phys. Rev. B **51**(11), 7361–7364 (1995).

[Urb07] B. Urbaszek, P.-F. Braun, T. Amand, O. Krebs, T. Belhadj, A. Lemaitre, P. Voisin, and X. Marie, *Efficient dynamical nuclear polarization in quantum dots: Temperature dependence*, Phys. Rev. B **76**(20), 201301 (2007).

[Urb12] B. Urbaszek, X. Marie, T. Amand, O. Krebs, P. Voisin, P. Maletinsky, A. Högele, and A. Imamoğlu, *Nuclear spin physics in quantum dots: an optical investigation*, arXiv:1202.4637v1 (2012).

[Vam10] A. N. Vamivakas, C.-Y. Lu, C. Matthiesen, Y. Zhao, S. Falt, A. Badolato, and M. Atature, *Observation of spin-dependent quantum jumps via quantum dot resonance fluorescence*, Nature **467**(7313), 297–300 (2010).

[Van01] L.M.K. Vandersypen, M. Steffen, G. Breyta, C.S. Yannoni, M.H. Sherwood, and I.L. Isaac, *Experimental realization of Shor's quantum factoring algorithm using nuclear magnetic resonance*, Nature **414**(6866), 883–887 (2001).

[Via87] L. Via, R.T. Collins, E.E. Mendez, Wang, and W.I., *Excitonic coupling in GaAs/GaAlAs quantum wells in an electric field*, Phys. Rev. Lett. **58**(8), 832–835 (1987).

[Vin79] G. Vincent, A. Chantre, and D. Bois, *Electric field effect on the thermal emission of traps in semiconductor junctions*, Journal of Applied Physics **50**(8), 5484–5487 (1979).

[Vin09] I.T. Vink, K.C. Nowack, F.H.L. Koppens, J. Danon, Y.V. Nazarov, and L.M.K. Vandersypen, *Locking electron spins into magnetic resonance by electron-nuclear feedback*, Nature Physics **5**(10), 764–768 (2009).

[Vri01] R. Vrijen and E. Yablonovitch, *A spin-coherent semiconductor photo-detector for quantum communication*, Physica E **10**(4), 569 (2001).

[Wae12] A.M. Waeber, *Optical and Magneto-Optical Spectroscopy in Coupled Quantum Dots*. Diploma Thesis, Walter Schottky Institut, Technische Universität München, (2012).

[Wal98] S. N. Walck and T. L. Reinecke, *Exciton diamagnetic shift in semiconductor nanostructures*, Phys. Rev. B **57**(15), 9088–9096 (1998).

[Wan99] L.-W. Wang, J. Kim, and A. Zunger, *Electronic structure of 110-faceted self-assembled pyramidal InAs/GaAs quantum dots*, Phys. Rev. B **59**(8), 5678–5687 (1999).

[War93] R. J. Warburton, R. J. Nicholas, S. Sasaki, N. Miura, and K. Woodbridge, *Superlattice modification of the valence-band spin splitting in $In_xGa_{1-x}As/GaAs$ superlattices up to 45 T*, Phys. Rev. B **48**(16), 12323–12325 (1993).

[War98] R.J. Warburton, B.T. Miller, C.S. Dürr, C. Bödefeld, K. Karrai, J.P. Kotthaus, Medeiros-Ribeiro G., P.M. Petroff, and S. Huant, *Coulomb interactions in small charge-tunable quantum dots: A simple model*, Phys. Rev. B **58**(24), 16221–16231 (1998).

[War00] R. J. Warburton, C. Schaflein, D. Haft, F. Bickel, A. Lorke, K. Karrai, J. M. Garcia, W. Schoenfeld, and P. M. Petroff, *Optical emission from a charge-tunable quantum ring*, Nature **405**(6789), 926–929 (2000).

[War05] M.E. Ware, E.A. Stinaff, D. Gammon, M.F. Doty, A.S. Bracker, D. Gershoni, V.L. Korenev, S.C. Badescu, Y. Lyanda-Geller, and T.L. Reinecke, *Polarized Fine Structure in the Photoluminescence Excitation Spectrum of a Negatively Charged Quantum Dot*, Phys. Rev. Lett. **95**(17), 177403 (2005).

[Was99] Z.R. Wasilewski, S. Fafard, and J.P. McCaffrey, *Size and shape engineering of vertically stacked self-assembled quantum dots*, Journal of Crystal Growth **201-202**, 1131–1135 (1999).

[Wei07] J.A. Weil and J.R. Bolton, *Electron Paramagnetic Resonance: Elementary Theory and Practical Applications*. 2nd ed., John Wiley & Sons, Hoboken, New Jersey, (2007).

[Wen26] G. Wentzel, *Eine Verallgemeinerung der Quantenbedingungen für die Zwecke der Wellenmechanik*, Zeitschrift für Physik **38**(6-7), 518–529 (1926).

[Wil12] A. Wild, J. Kierig, J. Sailer, J.W. Ager III, E.E. Haller, G. Abstreiter, S. Ludwig, and D. Bougeard, *Few electron double quantum dot in an isotopically purified ^{28}Si quantum well*, Applied Physics Letters **100**(14), 143110 (2012).

[Win98] D.J. Wineland, C. Monroe, W.M. Itano, D. Leibfried, B.E. King, and D.M. Meekhof, *Experimental issues in coherent quantum-state manipulation of trapped atomic ions*, J. Res. Natl. Inst. Stand. Technol. **103**(3), 259–328 (1998).

[Win03] R. Winkler, *Spin-Orbit Coupling Effects in Two-Dimensional Electron and Hole Systems*. Springer-Verlag, Berlin, (2003).

[Wit11] B.J. Witek, R.W. Heeres, U. Perinetti, E.P.A.M. Bakkers, L.P. Kouwenhoven, and V. Zwiller, *Measurement of the g-factor tensor in a quantum dot and disentanglement of exciton spins*, Phys. Rev. B **84**(19), 195305 (2011).

[Woj97] A. Wojs and P. Hawrylak, *Theory of photoluminescence from modulation-doped self-assembled quantum dots in a magnetic field*, Phys. Rev. B **55**(19), 13066–13071 (1997).

[Xie94] Q. Xie, P. Chen, and A. Madhukar, *InAs island-induced-strain driven adatom migration during GaAs overlayer growth*, Applied Physics Letters **65**(16), 2051–2053 (1994).

[Xie95] Q. Xie, A. Madhukar, P. Chen, and N.P. Kobayashi, *Vertically Self-Organized InAs Quantum Box Islands on GaAs(100)*, Phys. Rev. Lett. **75**(13), 2542–2545 (1995).

[Xu09] X. Xu, Y. Wang, B. Sun, D.G. Steel, A.S. Bracker, D. Gammon, and L.J. Sham, *Optically controlled locking of the nuclear field via coherent dark-state spectroscopy*, Nature **459**(7250), 1105–1109 (2009).

[Yaf61] Y. Yafet, *Hyperfine interaction due to orbital magnetic moment of electrons with large g-factors*, J. Phys. Chem. Solids **21**(1-2), 99–104 (1961).

[Yan10] W. Yang and L.J. Sham, *Hole-induced Dynamic Nuclear Polarization in Quantum Dots*, arXiv:1012.0060v2 (2010).

[Yok05] T. Yokoi, S. Adachi, H. Sasakura, S. Muto, H.Z. Song, T. Usuki, and S. Hirose, *Polarization-dependent shift in excitonic Zeeman splitting of self-assembled $In_{0.75}Al_{0.25}As/Al_{0.3}Ga_{0.7}As$ quantum dots*, Phys. Rev. B **71**(4), 041307 (2005).

[Yua02] Z. Yuan, B.E. Kardynal, R.M. Stevenson, A.J. Shields, C.J. Lobo, K. Cooper, N.S. Beattie, D.A. Ritchie, and M. Pepper, *Electrically Driven Single-Photon Source*, Science **295**(5552), 102–105 (2002).

[Zav45] E. Zavoisky, J. Phys. UdSSR **9**, 211 (1945).

[Zhu05] J.-L. Zhu, W. Chu, Z. Dai, and D. Xu, *Exciton states and their entanglement in coupled quantum dots*, Phys. Rev. B **72**(16), 165346 (2005).

[Zre90] A. Zrenner, J.M. Worlock, L.T. Florez, and J.P. Harbison, *Exciton tunneling in in asymmetric coupled quantum wells with spatially separated electron and hole injection*, Proceedings of the 20th International Conference on the Physics of Semiconductors (ICPS-20), Thessaloniki, August 6-10 1990, E.M. Anastasskis and J.D. Joannopoulos, editors pages 1493–1496 (1990).

[Zre94] A. Zrenner, L. V. Butov, M. Hagn, G. Abstreiter, G. Böhm, and G. Weimann, *Quantum dots formed by interface fluctuations in AlAs/GaAs coupled quantum well structures*, Phys. Rev. Lett. **72**(21), 3382–3385 (1994).

[Zre02] A. Zrenner, *A close look on single quantum dots*, Journal of Chemical Physics **418**(6898), 612–614 (2002).

[Zut04] I. Zutic, J. Fabian, and S. Das Sarma, *Spintronics: Fundamentals and applications*, Reviews of Modern Physics **76**(2), 323–410 (2004).

List of Publications

Published

1. *All optical preparation, storage, and readout of a single spin in an individual quantum dot*
   V. Jovanov, F. Klotz, S. Kapfinger, D. Heiss, S. Spiga, D. Rudolph, M. Bichler, M. S. Brandt, G. Abstreiter, J. Finley – Proc. SPIE, **8272**, 827211 (2012).

2. *Highly nonlinear excitonic Zeeman spin splitting in composition-engineered artificial atoms*
   V. Jovanov, T. Eissfeller, S. Kapfinger, E. C. Clark, F. Klotz, M. Bichler, J. G. Keizer, P. M. Koenraad, M. S. Brandt, G. Abstreiter, and J. J. Finley – Phys. Rev. B **85**, 165433 (2012).

3. *Coplanar stripline antenna design for optically detected magnetic resonance on semiconductor quantum dots*
   F. Klotz, H. Huebl, D. Heiss, K. Klein, J. J. Finley, and M. S. Brandt – Rev. Sci. Instrum. **82**, 074707 (2011).

4. *Observation and explanation of strong electrically tunable exciton g factors in composition engineered In(Ga)As quantum dots*
   V. Jovanov, T. Eissfeller, S. Kapfinger, E. Clark, F. Klotz, M. Bichler, J. G. Keizer, P. M. Koenraad, G. Abstreiter, and J. Finley – Phys. Rev. B **83**, 161303(R) (2011).

5. *Asymmetric optical nuclear spin pumping in a single uncharged quantum dot*
   F. Klotz, V. Jovanov, J. Kierig, E. C. Clark, M. Bichler, G. Abstreiter, M. S. Brandt, and J. J. Finley – Phys. Rev. B **82**, 121307(R) (2010).

6. *Observation of an electrically tunable exciton g factor in InGaAs/GaAs quantum dot*
   F. Klotz, V. Jovanov, J. Kierig, E. Clark, D. Rudolph, D. Heiss, M. Bichler, G. Abstreiter, M. S. Brandt, and J. Finley – Appl. Phys. Lett. **96**, 053113 (2010).

7. *Optically monitoring electron spin relaxation in a single quantum dot using a spin memory device*
   D. Heiss, V. Jovanov, F. Klotz, D. Rudolph, M. Bichler, G. Abstreiter, M. S. Brandt, and J. Finley – Phys. Rev. B **82**, 245316 (2010).

In preparation

1. *Dynamic nuclear spin pumping in resonantly pumped neutral quantum dots: An experimental and theoretical study*
   F. Klotz, V. Jovanov, J. Kierig, P.L. Ardelt, M. Bichler, G. Abstreiter, M. S. Brandt, and J. J. Finley

2. *Observation of Coulomb couplings in the optical spectrum of quantum dot molecules*
   K. Müller, F. Klotz, P.-L. Ardelt, A. Waeber, M. Bichler, H. Krenner, M.S. Brandt, G. Abstreiter, and J.J. Finley

Danksagung

Auch wenn die Mundart lehrt, dass „net g'motzt g'lobt gnug isch", so soll an dieser Stelle doch all den Personen gedankt werden, die zum Gelingen dieser Arbeit beigetragen haben und meine Zeit am WSI bereichert haben. Besonderer Dank geht an:

Prof. Martin Brandt und **Prof. Jonathan Finley** dafür, dass sie ein $(\alpha\,|E24\rangle + \beta\,|E25\rangle)$ Projekt zum Thema Spinkontrolle in Einzelquantenpunkten gewagt haben und für die Chance dieses bearbeiten zu dürfen - die Betreuung durch eine Doppelspitze hat sich als durchgängig positiv erwiesen. Die Möglichkeit, Ideen, Feedback und Know-how aus verschiedenen Perspektiven zu erhalten, hat diese Arbeit auf jeden Fall bereichert und vorangebracht. Potentiell mögliche Schwierigkeiten, die sich aus einer solchen Konstellation ergeben können, waren hingegen nicht existent. Ich möchte mich bei beiden für ihre Unterstützung, Motivation sowie ihre immer offene Tür und Bereitschaft zur Diskussion bedanken. Selbiges gilt für das Schaffen einer angenehmen und produktiven Arbeitsatmosphäre sowie der exzellenten Rahmenbedingungen für das Projekt im Speziellen und wissenschaftliches Arbeiten im Allgemeinen, aber auch für so manch nicht-wissenschaftliche Unternehmung während der letzten Jahre.

Prof. Gerhard Abstreiter für die Unterstützung des Projekts, sein konstruktives Interesse und natürlich für das zur Verfügung stellen des Magnetlabors.

Alle Beteiligten des QD-Spinner Teams, in wechselnder Besetzung bestehend aus **Vase Jovanov, Dominik Heiss, Kai Müller, Alexander Bechtold, Johannes Kierig, Pelle Ardelt, Andreas Waeber, Stephan Kapfinger** und **Daniel Rudolph** für die super Zusammenarbeit.

Dominik Heiss und **Vase Jovanov** für die Einführung ins Magnetlabor und die Vorarbeiten am Setup. **Konrad Klein** für das Ätzen der a:Si-H Proben und die ESR-Beratung. **Andre Stegner** für die Hilfe bei der (fast) erfolgreichen Reparatur der Wiltron-Quelle. **Markus Trautwein** für eine erste Einweisung in COMSOL. **Hubert Krenner** für die langlebigen und ertragreichen QDM-Proben MS1 und MS2. **Kai Müller** für den kreativen Netzwerk-Workaround im Magnetlabor und das zur Verfügung stellen seines Kannensticks. **Vase** für das allweihnachtliche Tanken des Magneten.

Hannes Kierig, der als Diplomand Mitglied der ersten Stunde des DNP-Projekts war und dieses durch seinen Einsatz stets mit vorangebracht hat.
Andreas Waeber und **Pelle Ardelt** für die vielen Messungen an den Quantenpunkt-Molekülen - auch wenn das Thema letztlich nur noch bedingt in diese Arbeit eingeflossen ist - sowie **Kai Müller** für das exzellente Zusammenarbeiten und seine hilfreiche und umfassende Expertise auf dem Gebiet der Moleküle. Außerdem **Pelle** viel Erfolg beim Weiterführen der Experimente und des Labors N107.

Dr. Geza Giedke und **Heike Schwager** für die gute und fruchtbare Zusammenarbeit im DNP-Projekt beim gemeinsamen Erarbeiten eines Modells zum Verständnis der experimentellen Daten sowie für die Durchführung der numerischen Simulationen und das gemeinsame Schreiben der Manuskripte für die entsprechenden Veröffentlichungen.

Thomas Eisfeller für seine Berechnungen und theoretischen Arbeiten zum g-Faktor Tuning.

Dr. Hans Hübl für den Input hinsichtlich des Designs der CPW-CPS Strukturen sowie deren Integration in die Quantenpunktspektroskopie.

Max Bichler für das Wachsen der Quantenpunkt-Proben und die Unterstützung rund um den Magneten.

Wolfgang Bendak, Fritz Sedlmeier und **Hannes Seitz** für den Werkstatt-Support und das Anfertigen diverser Teile für das neue Tieftemperaturmikroskop.

Dr. Friedhelm Finger und **Dr. Oleksandr Astakhov** für das Wachsen der a-Si:H Proben.

Die Office-Crew **Konrad Klein, Susanne Schäfer** und **Tobias Antesberger** für die angenehme Büroatmosphäre, viele Gespräche auch über nicht-physikalische Themen sowie das Ertragen meiner stilsicheren Zimmerdekoration.

All diejenigen, die mit dafür verantwortlich waren, dass ich (fast immer) gerne täglich ins WSI gekommen bin und meine Doktorandenzeit zu einer erlebnisreichen und lehrreichen Zeit gemacht haben, die ich sehr genossen habe und auf die ich gerne zurückblicke. Dafüer verantwortlich waren insbesondere (E24): **Arne Laucht** (dafür, dass ich jetzt gefühlte 100 Kicker-Bars von München bis Tokio kenne), **Norman Hauke** (+ seinen Pokerkoffer), **Vase** (für mazedonische Weinkunde und sein immerfröhliches Gemüt - see you at Intel), **Kai** (fürs Jammen, das zur Verfügung stellen der Garage und das konsequente Ignorieren von political correctness), **Hagen Langhuth** (für seinen unglaublichen Unterhaltungswert), **Hannes**, **Dominik**, **Michael Kaniber**, **Gregor Bracher**, **Alexander**, **Günther Reithmaier** (fürs Jammen), **Daniel**, **Thomas Zabel** (aka Weißwurstfrühstückorganisator), **Emily Clark**, **Malte Huck**, **Ilaria Zardo**, **Pelle**, **Andre-**

as, **Stephan** (fürs Solieren beim Jammen) und **Simon Frederick** (für das Schokobananenrezept und den New Mexico-Roadtrip). (E25): **Konrad** (für die immer kompetente und enthusiastische Beratung rund ums Rad), **Susanne**, **Lukas Dreher**, **Felix Höhne**, **Andre Stegner**, **Markus Trautwein**.
...und natürlich auch für all die anderen Aktivitäten wie BBQs, Partys, Junggesellenabschiede, Pokerabende, Seminarraum-Movie-Nights, Biergartenbesuche, Radtouren, und vieles mehr.

Die NTT-School-Reisegruppe **Arne, Kai, Norman, Heike** und **Hagen** für eines der außerwissenschaftlichen Highlights der Doktorarbeit. Außerdem **Jon, Alex, Thomas, Simon, Vase, Kai, Norman, Arne, Hagen, Heike** und **Andreas Wild** für die tolle Zeit auf diversen Konferenzen und Workshops sowie den **E25ern** für die alljährliche DPG-Tagung.

Die **TUM Graduate School** für die Möglichkeit des Austausches mit Doktoranden anderer Fachrichtungen, die finanzielle Unterstützung durch Internationalisierungsgutscheine sowie das Bereitstellen einer umfassenden Auswahl von Seminaren zur überfachlichen Qualifizierung,

Meine **Eltern** für die Unterstützung nicht nur während der Doktorarbeit sondern des gesamten Studiums.

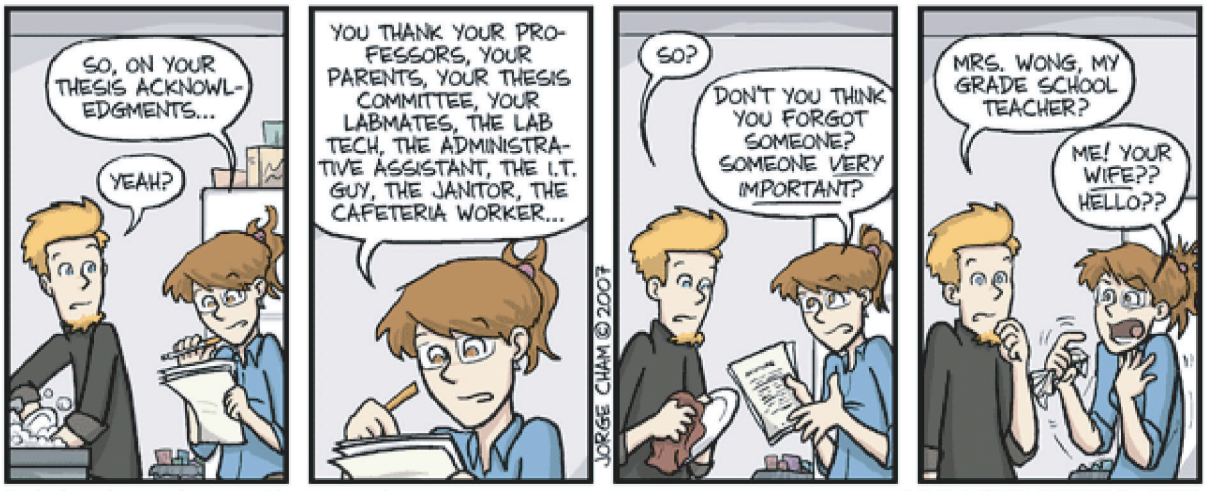

"Piled Higher and Deeper" by Jorge Cham

...und natürlich an **Anna** für ihren Humor ◡̈ sowie den Rückhalt und das Verständnis während der vergangen Jahre.

Diese Arbeit wurde finanziell unterstützt durch die Deutsche Forschungsgemeinschaft im Rahmen des Sonderforschungsbereichs 631, Teilprojekt C6 sowie von der Deutschen Exzellenz-Initiative durch den Forschungscluster „Nanosytems Initiative Munich“. Das Wachstum der a:Si-H Proben am Forschungszentrum Jülich wurde finanziell unterstützt durch das Projekt EPR-Solar des Bundesministerium für Bildung und Forschung.